Ice Scour and Gouging Effects with Respect to Pipeline and Wellhead

Prepared for: BSEE
Doc Ref: 100100.01.PL.REP.004
Rev: 0
Date: July 2015

Final Report

This study was funded by the Bureau of Safety and Environmental Enforcement (BSEE), U.S. Department of the Interior, Washington, D.C. under Contract E14PC00011.

WOOD GROUP KENNY

Client
BSEE
Document Title
Ice Scour and Gouging Effects with Respect to Pipeline and Wellhead

WG Reference Number	Client Reference Number (if applicable)
100100.01.PL.REP.004	E14PC00011

Contact

Jorge L. Alba, Senior Consultant
Jorge.alba@woodgroupkenny.com
Tel: +1 281 646 4160

Wood Group Kenny
15115 Park Row
3rd Floor
Houston, TX 77084

Tel +1 281 675 1000
http://www.woodgroupkenny.com

Revision	Date	Reason for Issue	Prepared	Checked	Approved
0	07/14/15	For Client Approval	KH/MS	AA/RC	JA 07/14/15
B	06/19/15	For Client Review	KH/MS	AA	JA
A	05/15/15	For Internal Review	KH/MS	AA	JA

Executive Summary

Researchers use several approaches to generate information on scouring phenomena and gain understanding of seabed response to ice gouging. These approaches can be divided into two categories: observations of real events and artificial simulations.

Observation of real events involves performing extensive site surveys (seabed scanning), identifying gouging characteristics, and locating areas with high gouging occurrence rates. Surveying has challenging technical and economical limitations, as discussed in the first task of this study.

Artificial simulations can be useful tools to bridge the knowledge gaps and provide better understanding of the complexity of gouging processes. The advantage of simulations over field observations is that simulations allow full control of the test parameters (e.g., soil type, keel width and depth, attack angle, ice and subsea structure properties) that dictate the ice gouging response.

Artificial simulations are classified into two types:

- Physical testing
- Numerical simulation

Physical tests are conducted in the field or in laboratory settings using small– or large–scale instrumental setups. Physical testing can be performed under two different types of testing conditions:

- The first type is ice gouge testing at normal gravity (1–g). This test can be performed indoors (laboratory) or outdoors (large–scale), depending on the size of the keel pushed into the soil bed to induce the gouge. Primary issues are associated with the range of confining stresses, uncertainty related to scaling laws, contact mechanics, interface conditions, and strain localization.
- The second type of testing is performed in a centrifuge facility. The centrifuge applies an increased ‘gravitational’ acceleration to physical models to produce identical self–weight stresses in the model and prototype. Centrifuge testing has practical limitations related to the level of acceleration that can be applied and the size of the scale model used.

Current computational capabilities make numerical simulation models cost effective. Simulations using finite element (FE) models have proven to be a fast–paced track for improving understanding of ice gouging.

FE models used for simulating ice keel–soil–pipeline interactions mainly fall into two categories:

- Structural FE models – The structural models assume that it is possible to decouple the interaction between ice and soil and the interaction between soil and pipe. In general, comparisons of pipe response predicted by the structural FE models and those measured in reduced scale physical tests have been reasonable but conservative. Feasibility studies or early phases of design can use structural FE models.
- Continuum FE models – The continuum models resolve the coupled interactions between ice, soil, and pipe more accurately and therefore allow more realistic representations of the ice gouging process. These models, which usually predict lower subgouge soil displacements and lower pipeline strain demand compared to the structural models, have the potential to reduce burial depth requirements.

The advantage of numerical simulations is their versatility and control over the parameters involved. However, the use of these simulations for design requires rigorous validation.

Recommendations

The following areas, which are discussed in detail in Section 8.0, should be addressed through combined multidisciplinary efforts:

1. Reduce uncertainty in input parameters.
2. Improve the numerical process through advancements in software package capabilities.
3. Reduce uncertainty in output parameters through validation.

Revision History (Optional)		
Revision	**Date**	**Comments**
A	05/15/2015	Issued for Internal Review
B	06/19/2015	Issue for Client Review
0	07/14/2015	Issue for Client Approval

HOLDS		
No.	**Section**	**Comment**

Signatory Legend		
Revision	**Role**	**Comments**
0	Prepared	Khaled Mostafa,Staff Consultant
		Markella K. Spari, Staff Specialist
	Checked	Aiman Al–Showaiter, Staff Consultant
		Ronda Cavender, Senior Technical Editor
	Approved	Jorge Alba, Senior Consultant

Table of Contents

List of Figures

List of Tables

1.0 Introduction

1.1 General

This report meets part of the requirements included in the Statement of Work in Contract No. E14PC00011 between the Bureau of Safety and Environmental Enforcement (BSEE) and Wood Group Kenny (WGK). The project is titled, *Ice Scour and Gouging Effects with Respect to Pipeline and Wellhead Placement and Design*.

The work for this contract is a result of a proposal that was submitted in response to the Broad Agency Announcement (BAA) E14PS00019 titled, *Arctic Safety of Oil and Gas Operations in the U.S. Outer Continental Shelf*.

Refer to Appendix A for definitions of many of the terms used in this report.

1.2 Report Objectives

The objective of this report is to identify and present knowledge gaps in ice scour and gouging effects on pipeline and wellhead placement and design in the Beaufort Sea.

This report includes a review of:

- Collected field data.
- Physical test data.
- Research programs conducted to date.
- Numerical modeling techniques that have been developed.

1.3 Abbreviations

Abbreviations that are used throughout this report include the following.

ALE	Arbitrary Lagrangian–Eulerian
ALIE	Abnormal Level Ice Event
ASCE	American Society of Civil Engineers
APOA	Arctic Petroleum Operator's Association
BAA	Broad Agency Announcement
BSEE	(U.S.) Bureau of Safety and Environmental Enforcement
CARA	Circum–Arctic Resource Appraisal

C–CORE	Centre for Cold Ocean Resources Engineering
CEL	Coupled Eulerian–Lagrangian
CSR	Canadian Seabed Research Ltd.
EDC	Excavated Drill Center
ESRF	Environmental Studies Research Funds
FE	Finite Element
GIS	Geographic Information System
GPS	Global Positioning System
HP/HT	High Pressure/High Temperature
IIP	International Ice Patrol
JIP	Joint Industry Project
MMS	(U.S.) Minerals Management Service
NOAA	National Oceanic and Atmospheric Administration
OCR	Overconsolidation Ratio
PIC	Particle–In–Cell
PIRAM	Pipeline Ice Risk Assessment and Mitigation
PRISE	Pressure Ridge Ice Scour Experiment
ROV	Remotely Operated Vehicle
SCL	Shear Connection Link
SGD	Subgouge Deformation
SPH	Smoothed Particle Hydrodynamics
USGS	United States Geological Survey
WGK	Wood Group Kenny

2.0 The Arctic

2.1 Arctic Oil and Gas Reserves

As conventional oil reserves decline, the oil and gas industry is focusing on difficult–to–access and unconventional oil and gas reserves throughout the world. As a result, the industry is increasingly interested in exploring the Arctic region. Based on recent estimates, about $100 billion could be invested in the next decade in the development of production fields in the Arctic [34].

The Arctic contains vast amounts of oil and natural gas reserves. The United States Geological Service (USGS) Circum–Arctic Resource Appraisal (CARA) estimates Arctic oil and gas reserves to be 1,670 trillion cubic feet (tcf) of natural gas and 90 billion barrels of crude oil [126], which represents approximately 30% of the gas and 13% of the oil reserves around the world. With the increasing decline in oil and gas production from conventional reservoirs, oil and gas production in the Arctic region is gaining an economic advantage.

Some observers consider oil and gas exploration in the Arctic region to be among the most technically challenging environments to date. However, climate change, technological development, and volatile oil prices have played an important role in making Arctic exploration feasible and attractive [49].

2.2 Arctic Regions of Interest

The Arctic is defined as the region above the Arctic Circle, an imaginary line that circles the globe at latitude 66° 32" N. At the North Pole, the sun rises and sets once a year to produce six months of continuous daytime and six months of continuous nighttime conditions. In addition to the region within the Arctic Circle, the Arctic includes any locations in high latitudes where the average daily summer temperature does not exceed 50°F (10°C) [87].

Geographically, the Arctic covers approximately 10 million square miles (26 million square kilometers), or 5% of the earth's surface. This region includes onshore and offshore areas that may or may not be covered in ice. Related to oil and gas exploration, extremely low winter temperatures, long–term ice coverage, deep seas, very large fields, and extremely sensitive ecosystems characterize the Arctic. This report broadly refers to the Arctic as any territory with Arctic–like conditions.

Arctic areas of interest include Barents Sea, the Russian Arctic region, onshore Russia, Chukchi Sea, Beaufort Sea, the Canadian Arctic islands, northern Canada, Alaska, and the east coast of Greenland. Exploration activities in the Beaufort and Chukchi Seas

(between the 1950s and 1980s and the 1990s and 2000s) indicated that these areas are promising for oil and gas production. Each area has its challenges, mostly related to climatic and environmental conditions.

Figure 2.1 illustrates the Arctic area.

Figure 2.1: Arctic Map [87]

2.3 Key Arctic Challenges

The extreme climatic conditions in the Arctic pose serious challenges that limit the window of opportunity for oil and gas field development.

Ice covers the Arctic region approximately eight months of the year, and access to the seabed is possible only during the spring and summer seasons. Climate conditions generate ice gouging by pressure ridges or icebergs in shallow water depths, strudel scour, and permafrost thaw.

Arctic exploration and development requires expensive tailored technologies as well as safeguards that are adapted to the extreme climatic conditions. The severe Arctic conditions can present challenges for construction, installation (trenching and well interventions), and maintenance operations such as leak detection, monitoring, inspection pigging, pipeline repair, and flow assurance.

Figure 2.2 summarizes key Arctic challenges.

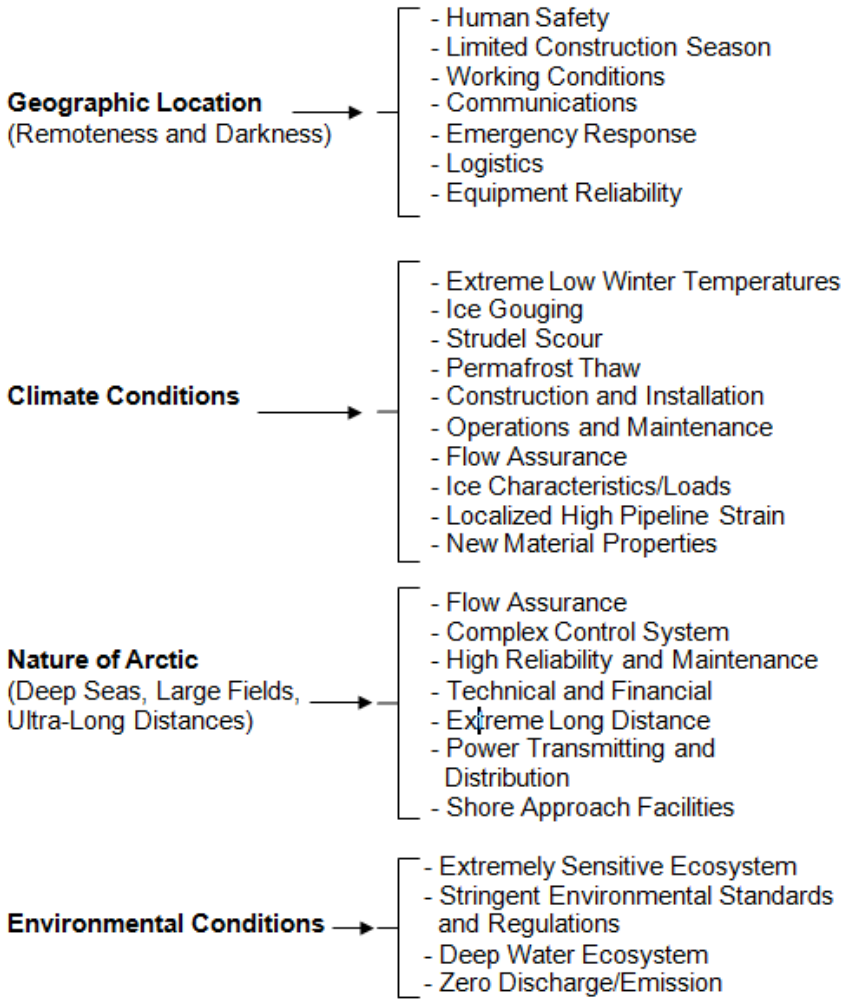

Figure 2.2: Key Arctic Challenges

2.4 Ice Gouge Protection

General agreement in the industry is that the most significant risk to subsea structures in cold waters is seabed gouging by ice features (Abdalla et al., 2009 [1]; Konuk, 2009 [62]; Barrette and Sudom, 2012 [11]). Ice gouging can exert considerable loads on the seabed, jeopardizing the integrity of structures on or below the seabed.

Consequences of an ice gouging event may include extensive structural damage to subsea components or severing of subsea pipelines. Both operators and regulators are concerned with the monetary and environmental risks associated with ice gouging events. Designing subsea components to withstand the loads associated with an ice gouging event is impractical.

Alternative methods to protect against ice features include:

- Ice management.
- Shielding.
- Trenching or burial.

Ice management implies that ice features are monitored and towed away from their drifting course when they pose a threat to subsea structures. This approach may not be practical in many cases, given the extensive length of pipelines and the costs associated with detection and vessel operation.

Shielding refers to the installation of a protective structure that can withstand a direct impact and divert the ice feature from its destructive course. Barriers made of rocks or concrete can be used for wellheads and conductor casings. Mattresses and rock berms can be used for pipelines, but they can be cost prohibitive for long pipelines.

The most practical and cost effective protection against ice gouging is achieved by trenching or burying the structure below the seafloor to avoid direct interaction with an ice feature. Trenching and burying techniques are typically applied to pipelines. However, wellheads and manifolds can be placed inside glory holes, which are holes deep enough to avoid contact with the ice feature.

The biggest unknown factor related to pipeline burial is the burial depth required to achieve adequate protection and an economical solution. The answer is not straightforward. The choice of burial depth relies on a proper understanding of complex ice gouging processes. These processes involve the interactions between ice features, pipelines, seabed soils, and other hydro–meteorological factors.

In the past 20 years, a considerable amount of research has been conducted to advance the industry's understanding of ice gouging. The following sections summarize the accumulated experience and knowledge of state–of–the–art practices related to ice gouging, ice gouge testing, and ice gouge analysis.

3.0 Ice Gouging

3.1 Definition

Wind and currents are environmental factors that drive icebergs. The gouging process starts when the tip of the keel at the bottom of the iceberg interacts with the seabed. The pressure that the keel applies on the seabed forms a zone of overconsolidated soil. The soil resistance on the iceberg's keel may cause the iceberg to tilt upward, which will decrease the interaction between the keel and the soil, thus facilitating the iceberg's movement forward. Fracture of the keel tip may occur, which results in a smaller iceberg that can travel farther toward shallower water depths.

Ice gouging can be classified into single and multiple keel events, as shown in Figure 3.1.

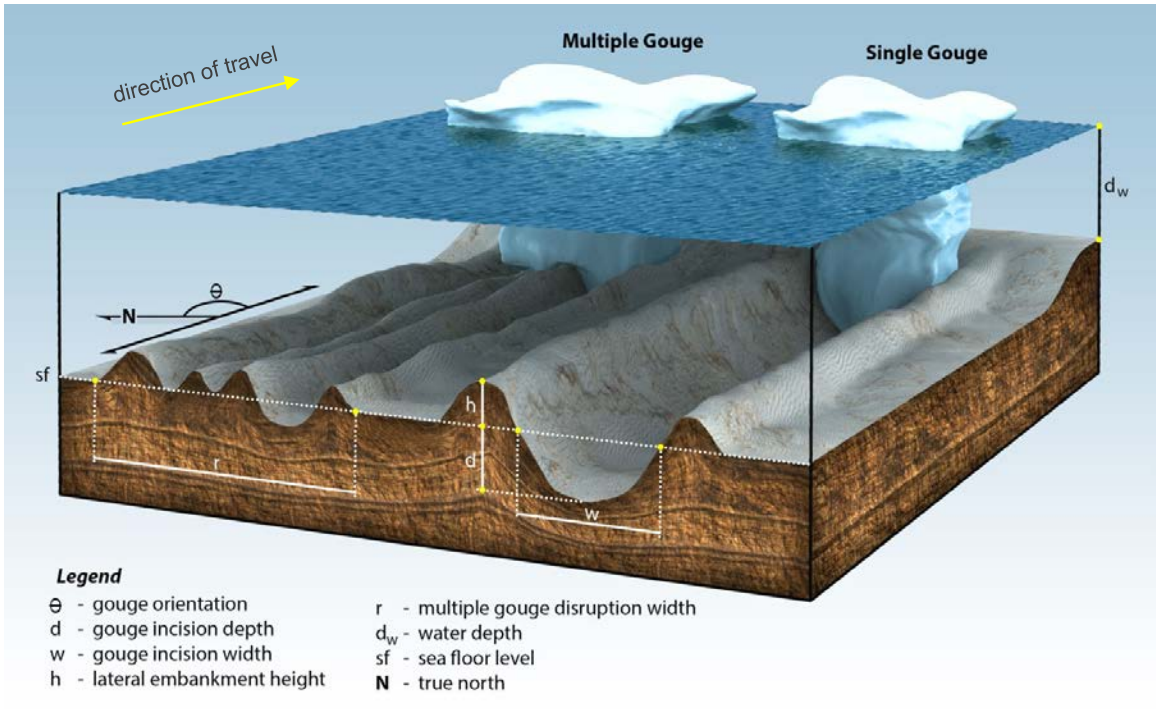

Figure 3.1: Single and Multiple Keel Icebergs (Modified by WGK) [112]

A single keel event occurs when a single keel iceberg disturbs the seabed and creates a gouge in the soil. The soil on each side of the gouge is pushed up and away from the iceberg to form berms. Alternatively, a multiple keel event involves the interaction of multiple keels with the seabed. Ice gouge events caused by multi–keeled icebergs are called 'multiplet' events.

Gouge dimensions may be estimated by analyzing trends of other gouges observed in the area of interest. The most important parameters for ice gouge risk assessment are the gouge dimensions (depth and width) and gouge rate. Gouge depth, also referred to as the incision depth, is measured from the seabed before the disturbance to the deepest point in the gouge. Gouge width is measured between two points inside the gouge at a level that is equivalent to the seabed before disturbance. Gouge rate is expressed as the number of gouges passing per mile (kilometer) per year. Periodic mapping by surveying the seafloor is essential to record the new gouge events and estimate the return period of similar gouge events.

3.2 Considerations

3.2.1 Ice Keel

Ice features are generally characterized by type as icebergs or ice ridges. Ice features observed in the Beaufort Sea and Arctic islands are primarily sea ice ridges, while ice features observed in the eastern Arctic, offshore Labrador, and Newfoundland are icebergs. Design criteria must consider the gouging features that are most relevant at the location of interest.

3.2.2 Icebergs

Icebergs are large, floating fragments of ice that are detached from ice sheets or glacier edges. According to the National Oceanic and Atmospheric Administration (NOAA), to be classified as an ‘iceberg,’ an ice sheet must be greater than 16 ft. (4.8 m) above sea level, 98–164 ft. (29.8–49.9 m) thick, and cover an area of at least 5,382 sq ft. (500 m^2).

International Ice Patrol (IIP) [50] estimated that about 40,000 medium–to–large–sized icebergs are breaking off, or calving, from the Greenland glaciers. Only about 400–800 of the icebergs make it as far south as St. John's, Newfoundland; but these numbers can vary significantly from year to year.

The mass of an iceberg can exceed 4.5 million tons. The shape and size of icebergs can vary because of melting, flipping, or breaking into smaller masses. Depending on the density and temperature of the ice and water, the keel, which is the submerged portion of an iceberg, can be eight to nine times the volume of the sail, which is the portion of the iceberg above the water line.

Characteristics and crossings of icebergs are difficult to predict. Ocean currents carry some icebergs more than 2,000 mi (3,200 km) from their origins. Icebergs present the biggest threat to subsea structures in the Arctic region. Icebergs weighing several thousand tons may impact subsea structure several hundred times in the structure's field life.

Table 3.1 lists possible iceberg shapes. Table 3.2 shows the IIP's iceberg characterization based on dimension and mass.

Table 3.1: Iceberg Shapes [48]

Shape	Description
Block	Flat–topped with steep sides.
Dome	Smooth and rounded on top.
Dry–dock	Eroded such that a U–shaped slot is formed near, or at, water level with two or more pinnacles or columns.
Pinnacle	Features a central spire or pyramid. May have additional spires.
Tabular	Flat–topped. Most show horizontal banding. The width is usually greater than five times their height.
Wedge	Flat surfaces, steep on one side, and gradually sloped to the water on the other side, forming a wedge shape.

Table 3.2: Iceberg Characterization [50]

Size Category	Height		Length		Approx. Weight (metric tons)
	(ft.)	(m)	(ft.)	(m)	
Growler	less than 3.28	less than 1	less than 16.40	less than 5	<53
Bergy Bit	4.92–16.40	1.5–5	16.40–49.21	5–15	< 1,400
Small	16.40–49.21	5–15	49.21–196.85	15–60	91,000
Medium	49.21–164.04	15–50	196.85–393.70	60–120	730,000
Large	164.04–328.08	50–100	393.70–721.78	120–220	4,500,000
Very Large	> 328.08	> 100	> 721.78	> 220	> 4,500,000

3.2.3 Sea Ice Ridges

Sea ice forms a 'perennial' ice cover over a large portion of the Arctic Basin. Currents and winds compress pieces of the ice cover together and rework them to form sea ice ridges. Flat pieces of ice or ice floes are driven into each other and form ice fragments of various size along the suture line (Figure 3.2).

Ice ridges may extend several miles. The component ice fragments, known as ice rubble, vary in shape, size, and degree of refreezing (consolidation) at the waterline.

Multi–year ridges, which have survived longer than one summer, are typically stronger and thicker than first–year ice ridges.

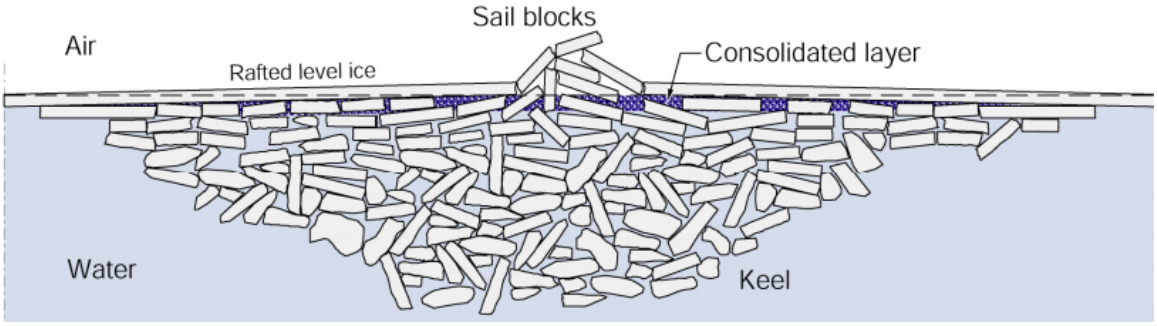

Figure 3.2: Cross–section of a First–year Ice Ridge (Liferov, 2005 [75])

3.2.4 Seabed

Although ice features cause ice gouging, it can be considered a geotechnical phenomenon. The keel of the ice feature exerts pressure on the seabed. The seabed response to keel pressure is intrinsically dependent on local soil conditions, including soil type, soil properties, and stratigraphy (alternation of layers).

These soil characteristics are obtained by drilling and extracting cylindrical core samples at the location of interest. A geotechnical investigation of the core samples provides information on the types of soil encountered at various depths.

Soil is divided into two categories: cohesionless and cohesive.

3.2.4.1 Cohesionless Soil

Cohesionless soil is a coarse grain material consisting of sand or gravel whose strength depends on the friction between its particles. The angle of internal friction (φ) is a standard parameter that is used to characterize the strength of a cohesionless soil.

Cohesionless soil allows for quick water drainage; therefore, loading conditions associated with this type of soil are usually referred to as drained loading conditions. However, because load application is relatively fast during ice gouging, undrained responses can be assumed for sandy seabeds.

3.2.4.2 Cohesive Soil

Cohesive soil is a finely grained material consisting of clay, silt, or a combination of the two. Cohesive soils have low permeability, which affects water drainage and pore water dissipation. The pore pressure of cohesive soil increases when it is loaded. This soil behavior is often referred to as undrained response. The strength of cohesive soil is a measure of the undrained shear strength, typically symbolized by Su (or cu).

The geotechnical conditions (soil shear strength and resistance to ice keel penetration), morphology, and local seabed bathymetry influence gouge attributes. Therefore, gouge attributes may vary along the length of a gouge with changing seabed conditions.

Research shows that seabed soil conditions influence the ice gouging processes, with deeper gouge depths generally occurring in weak marine silts and clays.

3.2.5 Pipeline Design

Offshore oil and gas production systems use pipelines to transport crude oil and natural gas at water depths greater than 1.25 mi (2,000 m). Export pipelines, which transport natural resources (oil or gas) from the offshore production facility to land–based facilities, may extend over long distances.

The offshore Arctic environment imposes several unique loading conditions on subsea pipelines, including ice gouging, strudel scour, and marine permafrost. This study focuses only on the effects of ice gouging on pipelines.

Pipeline design relies on stress–related criteria that guide material selection and welding requirements. Typically, internal pressure from the contained fluid and external pressure from the water column are the most significant loads considered in pipeline design.

When there is a risk of ice gouging, the load from the gouge event becomes the significant design load, and the stress–based approach becomes impractical and ineffective. Designing a pipeline with the strength to withstand deformation from an ice mass is cost prohibitive and impractical. Instead, designers use strain–based principles in which the design of the pipeline allows for some permanent or plastic strain.

3.2.5.1 Northstar Project

One example of an operational subsea pipeline in the Alaskan Beaufort Sea is BP Exploration's Northstar project. This project was the first development in the Arctic to incorporate subsea pipelines. (Refer to Lanan and Ennis, 2001 [71], and Nogueira and Paulin, 1999 [92].)

The Northstar project incorporated two 10–inch pipelines extending six miles offshore into the Beaufort Sea. Trenches were used to provide safety from seabed ice gouging and loads from permafrost thaw settlement. At the time, it was believed that a pipeline would be safe if it were trenched deeply enough for the ice to pass over it.

The design of the Northstar offshore Arctic field development was based on this principle. During the design of the Northstar pipelines, displacement–controlled soil loading conditions and seabed ice gouging scenarios were applied. This design requirement was addressed by using limit–state bending analysis to verify the integrity of the pipelines during their service life.

Later, as the ice gouge study advanced through analytical and experimental phases, it was determined that intense soil deformations could occur beneath a gouge depth. The studies concluded that a pipeline could be damaged in an ice gouge event as a result of being dragged with the seabed soil below a gouging ice mass, even if the ice mass itself does not touch the pipeline.

3.2.5.2 Other Projects

The Oooguruk oilfield offshore the North Slope of Alaska, which is described in Lanan et al., 2008 [70], is the second Beaufort Sea oilfield using a subsea pipeline. The Nikaitchuq system is another example of pipelines operating in Arctic environments. These examples provide valuable information on design, construction, and operability of pipelines in Arctic environments.

3.2.6 Wellhead Design

One of the biggest challenges in the Arctic environment is the design and placement of subsea wellheads while assuming potential damage from icebergs. Full control of a well (e.g., maintenance, shut–in, injection, production) is achieved through a subsea tree that is installed on top of a well in the final stage of well completion. There are two types of trees: horizontal and vertical. Unlike pipelines, wellheads are vertical structures that extend several feet (meters) above the seabed. This makes them vulnerable to damage from gouging and floating icebergs (also known as near–gouge events).

Several design techniques are used to protect wellheads from ice damage [41] [79]. The techniques are classified as preventive, protective, and sacrificial.

A preventive technique assesses the characteristics and frequency of a potential gouge event and minimizes the risk of contact by selecting an area with the lowest risk.

A protective technique uses fabricated structures to prevent iceberg contact with the wellheads.

3.2.6.1 Sacrificial Technique

A sacrificial technique is based on a probabilistic design approach. According to this approach, if the estimated probability of exceedance meets an acceptable risk criterion, then a design may be adopted. For example, if contact between the wellhead and an iceberg keel is likely to occur, then shearing of the wellhead by the advancing keel is also likely to occur. (Refer to Figure 3.3.)

Assuming that the probability of the occurrence exceeds the acceptability criteria limit, the wellhead design must incorporate a mechanical shear connection link (SCL). In the event of extreme loading by an iceberg, the SCL will isolate displacement of the wellhead system to a zone near the mud line while maintaining the integrity of the downhole safety barriers.

Ralph et al. (2012) [110] explains how a shear link, or failure joint, acts as a mechanical fuse that is designed to fail in a combination of shear, tension, and buckling from a load event. The failure joint minimizes downhole structural response during a load event on the production tree. The designed failure mechanism allows the well to be re–entered by protecting the well casing from damage. Safety shut down valves are installed below the anticipated gouge depth to prevent the release of hydrocarbons in a load and disconnect event.

Sacrificial techniques require information about icebergs' keel draft, keel angles, and near gouging keel distributions to determine the possibility of contact with floating and gouging icebergs. Unfortunately, survey data from seabed scanning is limited to induced gouges over a period of time, and the crossing frequencies provided in the literature do not include near–gouging events. This is a serious limitation to the level of detail required for a sacrificial design approach. Furthermore, there is a significant risk of malfunction of the involved safety valves. The sacrificial technique is not a recommended approach.

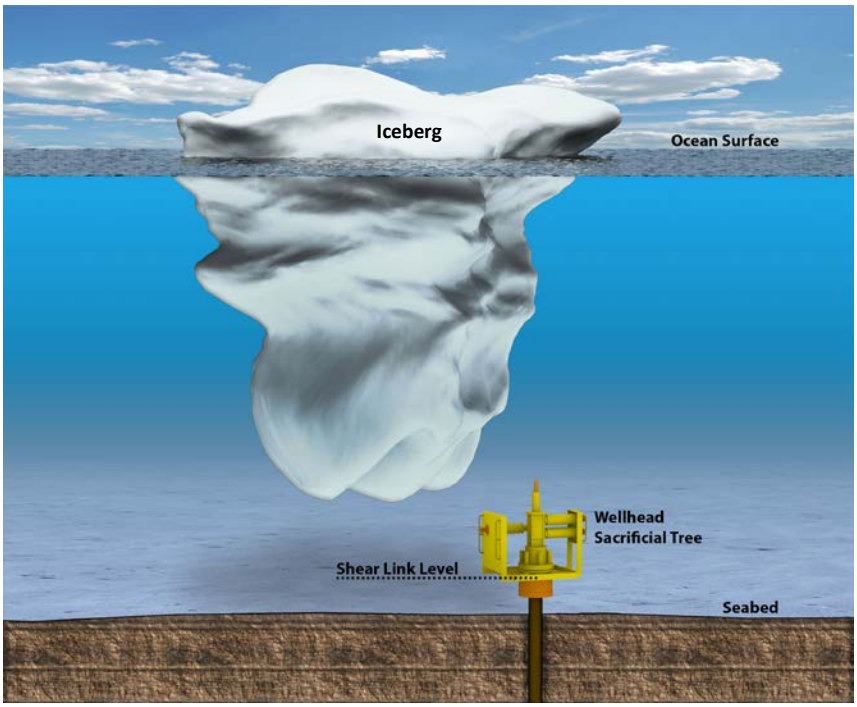

Figure 3.3: Threat of Ice Gouging to Wellhead Integrity

The design techniques described in this sub–section apply to wellheads installed above the mud line. Ralph et al. (2011) [110] presents three alternatives:

- Excavated Drill Centers (EDCs), also known as mud line cellars or glory holes
- Protective, truncated cone structures installed above the mud line
- Sub–seafloor protective structures

The following sub–sections describe these techniques.

3.2.6.2 Excavated Drill Centers

EDCs, also known as mud line cellars or glory holes, allow the installation of subsea equipment below the seafloor at depths greater than the anticipated gouge depth. Figure 3.4 and Figure 3.5 show schematics of cased and uncased drill holes, respectively.

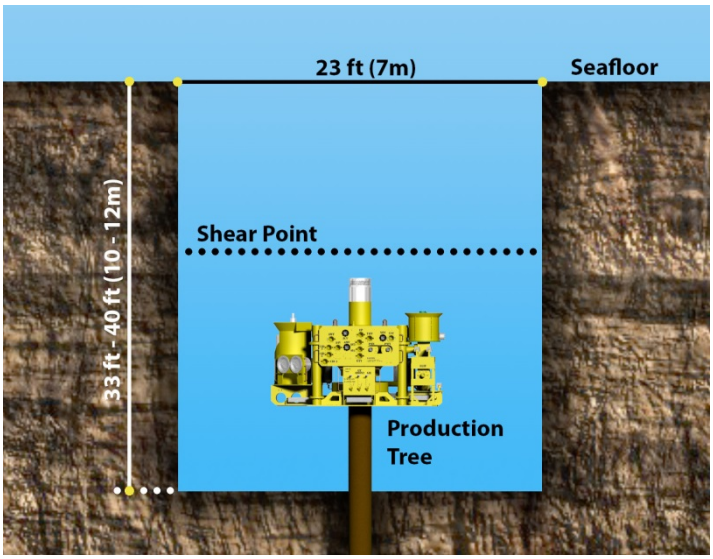

Figure 3.4: Cased Excavated Drilling Center Arrangement

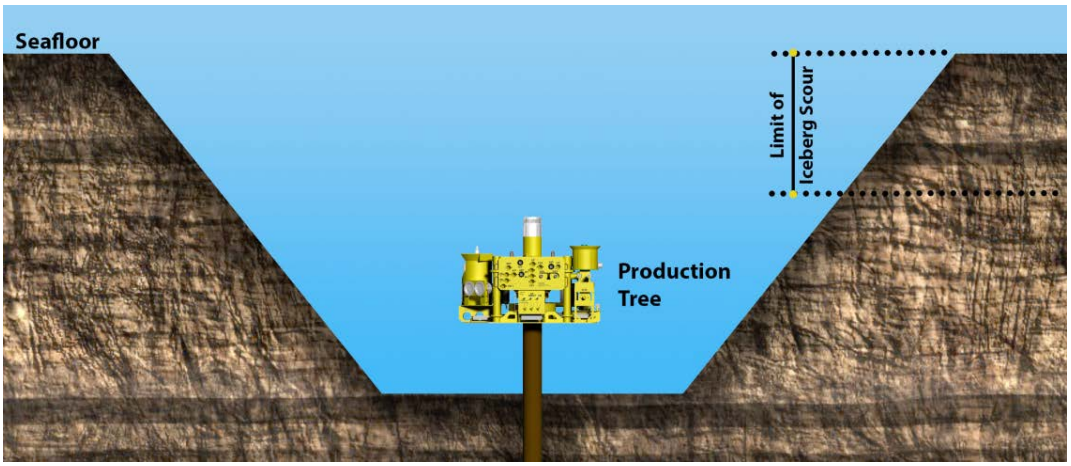

Figure 3.5: Uncased Excavated Drilling Center Arrangement

This method requires excavating the drill center and placing all subsea equipment at the bottom of the excavation. The depth of the EDC takes into account the expected depth of the gouge from passing ice keels and the height of the subsea equipment. This technique requires the removal of a substantial portion of the seabed and is costly from financial and environmental perspectives.

3.2.6.3 Protective Cone Structure

The second technique uses a protective structure at the mud line that sits over the top of a single wellhead system, shielding it from direct interaction with an iceberg keel. The

protective structure absorbs energy by crushing the ice keel and diverting the iceberg around and over the structure. The protective structure design uses ultimate limit state, accounting for energy absorption through elastic and plastic deformation of the structure. The protective structure is designed using loads that correspond to an Abnormal Level Ice Event (ALIE) with an annual exceedance probability of 10^{-4}. The size of the frame is governed by the size of the wellhead and tree system, Remotely Operated Vehicle (ROV) access requirements, and the minimum slope required to achieve iceberg keel deflection.

3.2.6.4 Sub–seafloor Protective Structure

The third technique is applicable to single and small well cluster systems. Compared to the conventional EDCs, it requires relatively smaller but more precise seabed excavation. King et al. (2012) [60] investigated the feasibility of protecting wellhead systems by housing them in a buried rectangular caisson.

While some of the design techniques described here may eliminate environmental impact, these complex systems may be cost prohibitive for exploration wells and marginal field tie–in wells.

3.3 Ice Gouge Processes

3.3.1 Keel Motion

Following contact with the seabed, an ice keel will continue to scour until the initial kinetic energy and the work done by the driving forces are expended, or until the soil resistance exceeds the strength of the ice keel, causing ice fracture. Depending on the characteristics of the ice feature and seabed, the ice mass may rotate, tilt, or lift during the scouring process. The ice keel itself may be subject to breakage and abrasion.

In the Beaufort Sea, sea ice ridges and associated keels are typically contained within ice sheets of considerable lateral extent. Resistance to uplift depends on the forces generated between the ice ridge and the seabed, and between the ice ridge and the surrounding ice sheets. Movement of the keel is predominantly horizontal, and the parent floe controls the keel almost entirely. The ploughing face may have a very low angle to the horizontal, generally less than a 30° angle. The width of an ice keel is generally much larger than its depth.

During the ice gouge process, various vertical uplift scenarios may occur:

- As the keel progresses, vertical forces exerted by the seabed will cause the ice feature to lift. Rotation of the ice feature may occur because of the unbalanced moments.

- If the vertical movements of the keel are small, low vertical forces are generated between the ice ridge and the surrounding ice sheets. In this scenario, the ice ridge may deflect without breaking through the surrounding ice sheet.
- If the vertical movements of the keel are large, high vertical forces are generated between the ice ridge and the surrounding ice sheets. In this scenario, the ice ridge may induce a bearing failure of the surrounding ice sheets. Depending on the bond between the ice ridge and the surrounding ice sheets, the ice ridge moves downward to restore vertical equilibrium and generates a bearing failure in the seabed. As bearing failure occurs in either the ice sheet or seabed, the vertical loads decrease rapidly and the vertical movements become smaller.
- If the uplift of the ice ridge generates extreme loads (greater than those forces that normally cause bearing failure), the ice ridge will separate from the surrounding ice sheets. However, the ice ridge will still be confined by the parent floe. Separation from the ice sheets will have little effect on the horizontal movement of the ice ridge, but the scour depth will be significantly reduced because of the reduction in uplift resistance.

In the Canadian Arctic, significant lifting of ice ridges caused by interactions with the seabed has been reported. In these instances, the vertical force component exerted by the seabed is as large as the horizontal force component. In other locations, such as the Grand Banks offshore Newfoundland and the Labrador Sea, the gouging process involves icebergs instead of ice ridges.

Based on the keel movement scenarios described in this sub–section, it is clear that the soil failure mechanism during gouging may vary across regions within the Arctic.

3.3.2 Soil Failure Mechanism

The parameter of interest during the ice gouging process is the soil mass displacement. The extent of soil deformation (the deformation profile) is important to determine the probability of damage to the structure.

If a pipeline or wellhead structure lies within a zone of large soil displacement, load transfer from the displaced soil is likely to damage the structure. Buried pipeline, which is generally considered to be a flexible structure, will be carried along with the displaced soil if the soil stiffness is high (relative to the pipe stiffness). If the soil stiffness is low (relative to the pipe stiffness), the displaced soil will flow around the pipeline.

Unlike pipelines, wellheads are vertical structures that extend several feet (meters) above the seabed. This makes them more sensitive to lateral soil movements.

For the previously mentioned reasons, it is important to understand the mechanism of soil failure and soil displacements when performing an integrity assessment of subsea structures. Figure 3.6 illustrates the dominant scour mechanism.

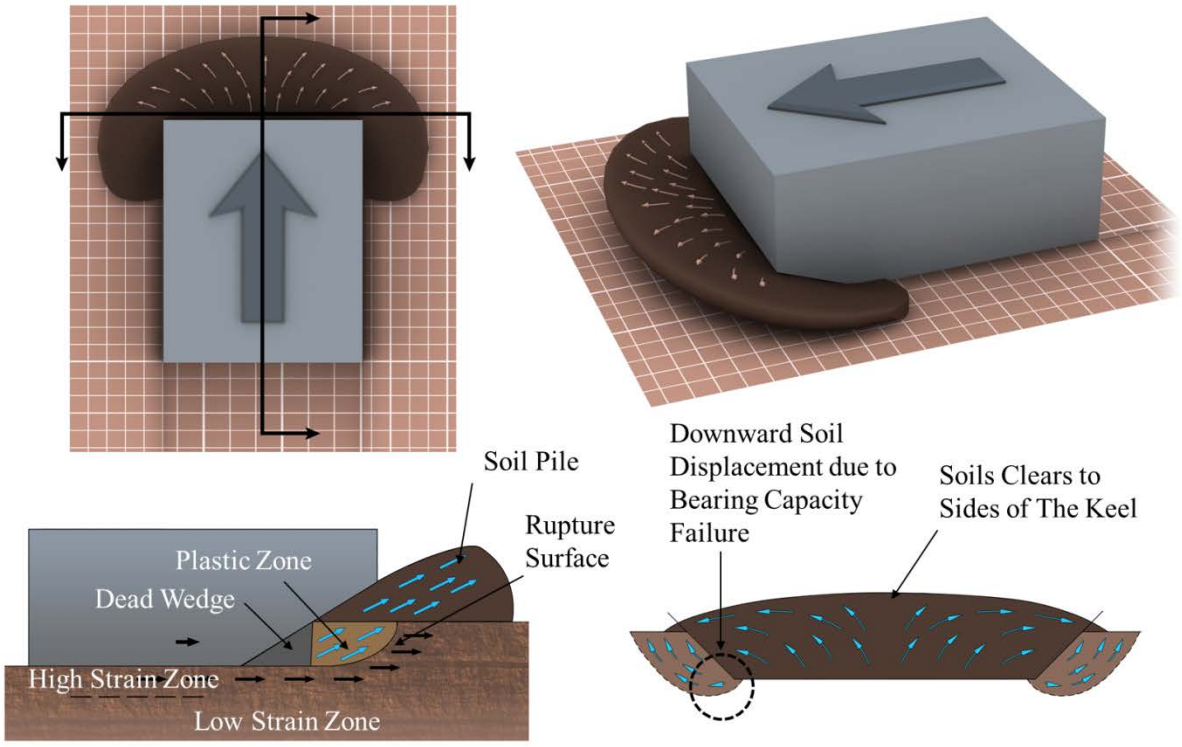

Figure 3.6: Gouge Mechanism Diagrams for Horizontally Moving Ice (Been et al., 1990 [14])

Figure 3.6 illustrates a soil failure zone in front of an advancing ice feature. The failure zone typically includes a dead wedge, a plastic zone, and a soil pile. A dead wedge forms in front of the ice keel and is carried along as scouring advances. The dead wedge has small or negligible relative motion with the ice keel. Soil wedges of this type, which are commonly observed in soil cutting experiments, have the effect of increasing the cutting angle. It is assumed that friction between the ice feature and the soil mass is fully mobilized.

As scouring begins, soil is pushed up and away in front of the advancing ice keel. As scouring continues, the mass of the displaced soil reaches a stable configuration—a steady state. Additional soil feeds in from the failure zone. Soil is cleared progressively from the scour path to form berms on both sides of the gouge.

Greater lateral movements are possible at the edges of the ice keel. The dead wedge becomes unstable and may erode as soil is pushed sideways because of transverse forces. These edge effects, combined with the ploughing motion in front of the dead wedge in the central portion of the keel, form a spoon–shaped failure zone, as illustrated in Figure 3.6.

According to Been et al., 1990 [14], the two mechanisms of soil failure are:

- Bearing capacity and passive earth pressure failure – the synergy of these mechanisms develops a rupture surface where soil undergoes large strains. An illustration of bearing capacity and passive pressure failure mechanisms is presented in Figure 3.7.
- Shear dragging – occurs when shearing loads drag the soil adjacent to the rupture surface in the direction of the scour. Refer to Figure 3.8.

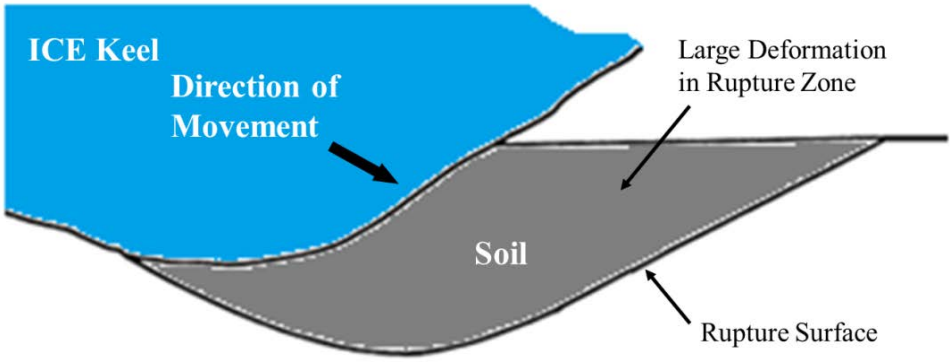

Figure 3.7: Rupture Surface Caused by Passive or Bearing Capacity Failure (Been et al., 1990 [14])

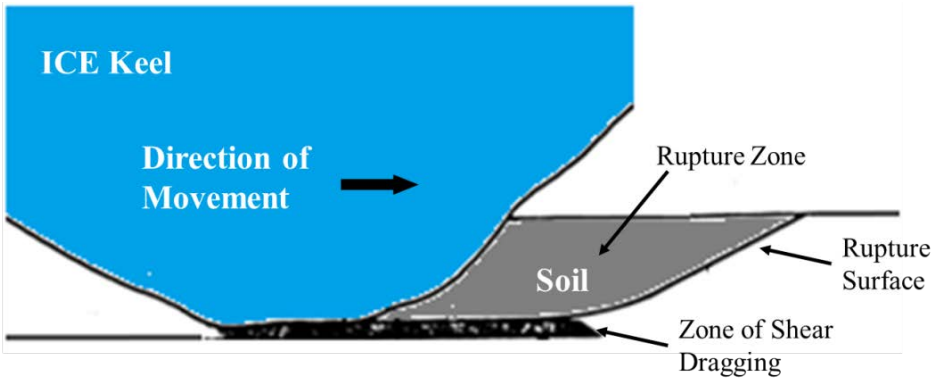

Figure 3.8: Shear Dragging Adjacent to Ice or Rupture Surface (Been et al., 1990 [14])

Bearing capacity and passive pressure solutions do not fully explain the development and propagation of a rupture surface. The motion of the ice feature also plays a significant role in the characterization of the rupture surface. An inclined plate moving through soil in a direction that is not perpendicular to the plate can characterize the reaction of the soil to the motion of an ice feature.

Been et al., 1990 described a solution for this general problem based on the method of characteristics and finite differences, as outlined by Sokolovski, 1965 [123]. Similarly, Hettiarachi and Reece, 1975 [46] calculated the size and orientation of the dead wedge. An alternate analytical approach is to use the upper bound theorem of plasticity and generate velocity field solutions as described by Palmer et al., 1989 [94]; James and Bransby, 1971 [51]; Chen and Rosenfarb, 1973 [30]; and Golder and Associates, 1990 [42].

These studies indicate that the rupture planes caused by horizontally moving features do not extend below the edge of the moving feature. This conclusion has also been proven experimentally.

There is evidence of the rupture planes extending below the edge of the moving feature when:

- Soils are non–homogeneous (i.e., soil shear strength varies with depth).
- The feature moves from stiff to soft soil (e.g., trench).
- There is a significant vertical movement of the ice feature.

Researchers also observed that quasi–dead zones of soil could form within the failure zone, as illustrated in Figure 3.9 and Figure 3.10.

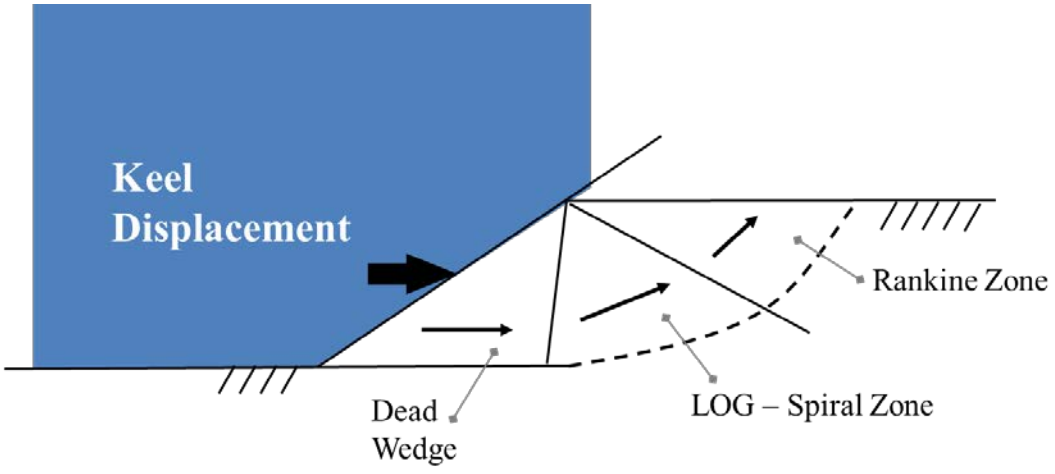

Figure 3.9: Typical Rupture Surface and Dead Zone in Dense Sands (Been et al., 1990 [14])

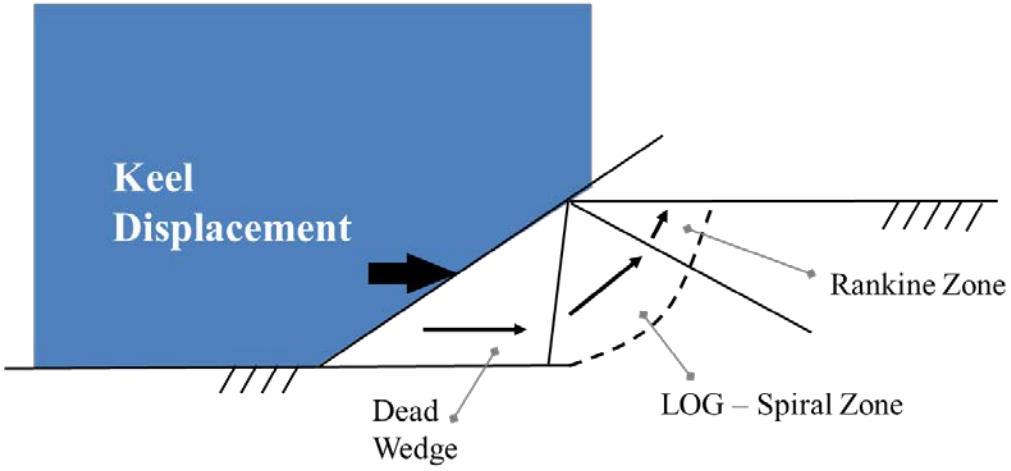

Figure 3.10: Typical Rupture Surface and Dead Zone in Clays (Been et al., 1990 [14])

Alternatively, trends in subgouge soil deformation were inconsistent between analytical and experimental results. The term ‘subgouge’ refers to the zone below the edge of the gouging ice feature. Experiments show that subgouge soil displacements are greater in loose sands and soft clays than in dense sands and stiff clays. Conversely, analyses have suggested that the dense and dilatant sands tend to exhibit greater subgouge soil disturbances. This inconsistency was later attributed to the shear dragging mechanism.

Been et al., 1990 [14] was among the first to recognize the potential for subgouge disturbance attributed to shear drag. Been et al. concluded that shear drag causes soil displacements outside of the rupture surface. Soil adjacent to a rupture surface or a rigid body sliding will displace along the direction of the shear. The ‘ploughing’ motion of the keel mobilizes significant soil mass underneath it, forcing the soil to flow and deform around the moving keel.

A zone of soil with a shear profile is formed below the scour. The depth of this zone is controlled by the stress strain behavior of the soil. A strain hardening soil (e.g., loose sands and soft clays) will develop a thicker band of dragging disturbance as the soil close to the scour surface strain hardens. Stress in the hardened material will be transmitted to the softer soil below. On the other hand, a strain softening soil (e.g., dense sands and stiff clays) close to the scour surface will fail, and a weaker material will form.

Further, the shearing will remain concentrated in the shear drag zone because it is weaker than the surrounding soil. This type of shear band localization can be shown using the theory of plasticity and bifurcation (Drescher and Vardoulakis, 1982 [33]).

3.3.3 Subgouge Deformations

Palmer et al. [94] reported that buried pipes are vulnerable to damage even if they are below the maximum expected gouge depth. Gouging introduces high levels of strain to soil layers that may penetrate deeper than the expected burial depth. Pressure loads are transferred through the soil to the pipe. Therefore, soil deformation and the pressure transferred to the pipe must be investigated.

Based on Palmer et al.'s observations of gouging events, the seabed can be split into three zones:

- Zone 1: This uppermost seabed sustains very large strains and soil deformation as the ice keel passes through the seabed. It would be reasonable to assume that the integrity of pipeline in this zone would be compromised. This zone is often delineated at the basal plane of the ice keel, as presented in Figure 3.11. However, not all of the soil above the basal plane moves upward.
- Zone 2: This soil, which is below the ice keel, is subjected to substantial disturbance. Within this intermediate zone, it is likely that the pipeline would deform plastically. The spatial extent and magnitude of soil deformation in this zone is uncertain.
- Zone 3: The soil extending beneath Zone 2 is subject to much less disturbance. It is likely that the pipeline would only deform elastically.

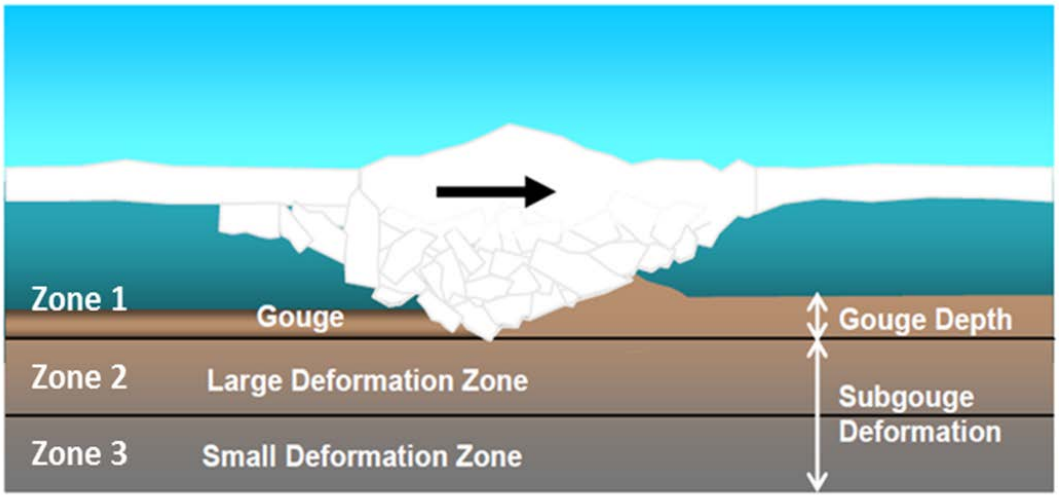

Figure 3.11: Seabed Gouging Schematic (Palmer et al., 1990 [95]) (Modified by WGK)

3.4 Knowledge and Understanding of Ice Scouring

Researches use several approaches to generate information on scouring phenomena and gain understanding of seabed response to ice gouging. These approaches can be divided into observations of real events and artificial simulations. Figure 3.12 presents a diagram prepared by Barrette and Sudom, 2012 [11] that describes the current approaches used to study ice gouging.

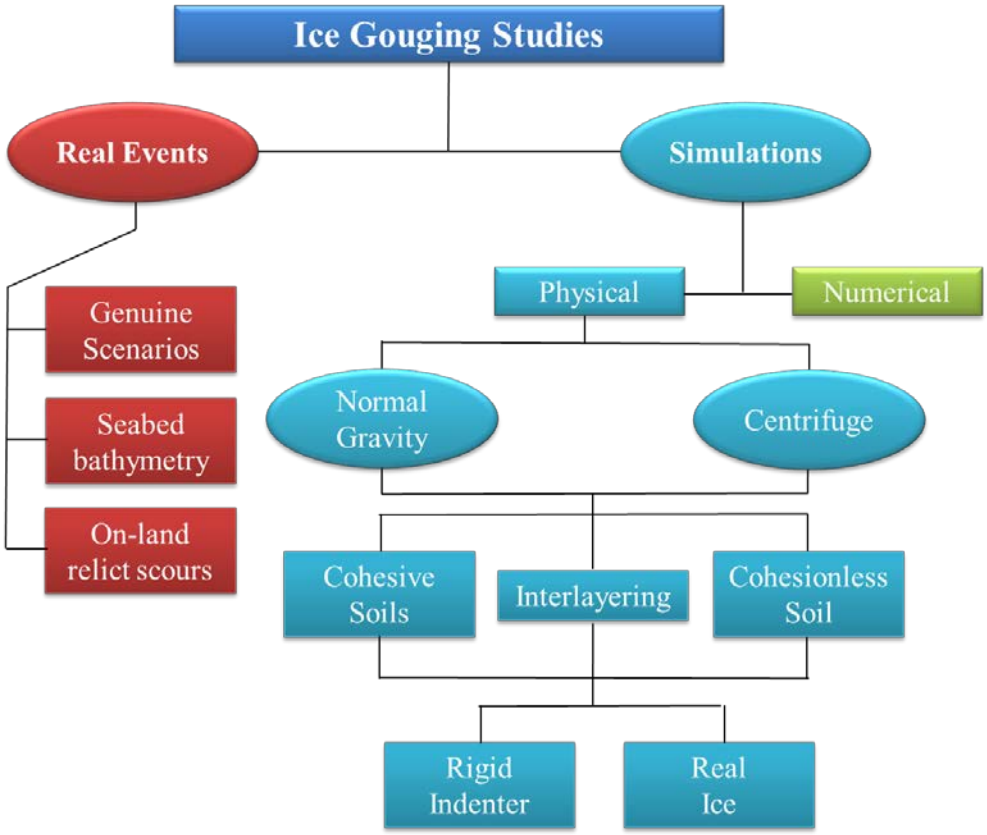

Figure 3.12: Current Knowledge Base on Scouring (Barrette and Sudom, 2012 [11])

3.4.1 Real Events

In the early 1960s, the need to account for the inherent uncertainty of ice gouging led to the development of design guidance and recommended practices that focused on extensive site surveys and seabed scanning at identified sites of interest.

The pipeline design philosophy is based on the development of strain–based criteria. For this reason, prediction of the maximum possible gouge depth and soil deformation is essential to determining the optimum burial depth required to ensure integrity. Surveys in

the Arctic region focused on identifying gouging characteristics and locating areas with a high rate of gouging events.

Seabed mapping allows an observation of real–scale scour activity. Repetitive mapping of the same seabed distinguishes recent scours from old ones to collect information on scour depth, width, length, orientation, and density; and it determines scour frequency. Developing accurate models that correlate all of these factors requires a thorough review of a large database of gouge records and statistical analyses. Surveys provide the data required to calibrate the models that are used to predict the minimum required burial depth, which affects design considerations for cost and safety.

The data obtained from surveys is valuable; however, experience and technical and economic limitations must be considered. Data collection must be performed on a recurring basis to establish scour frequency. With an average period of five years between surveys, data collection is very time consuming. Furthermore, the observations are site dependent and cannot be generalized for other locations. Another limitation is that surveys do not provide information on keel geometry, which studies have proven to have a significant effect on subgouge soil deformations.

3.4.2 Simulations

Physical and numerical simulations of ice gouging are alternative approaches to provide insight to the complexity of the gouging processes.

The advantage of physical tests over surveys is that physical tests allow for full control of the gouging test parameters. All of the aspects involved in ice gouging (e.g., soil failure, contact mechanics, and ice–structure interaction) can be broken down into separate processes and closely monitored. Likewise, tailored experimental simulations can investigate the influence of each parameter thoroughly and independently. For example, the influence of ice–keel attack angle on a specific soil type can be accurately investigated using indenters of varying cutting face angles.

Another advantage of simulation is the integration of the structure of interest (the pipe or wellhead), which enables a better understanding of the keel–structure interaction. Researches can perform simulations through physical or numerical (computational) tests.

Figure 3.13 presents the inputs and outputs of typical ice gouging simulations.

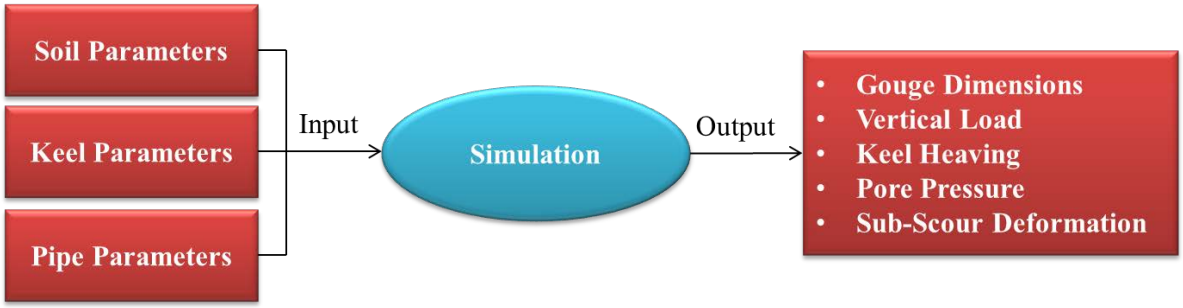

Figure 3.13: Inputs and Outputs of Simulation Tests

3.4.2.1 Physical Tests

Physical tests are conducted in the field or in laboratory settings, indoors or outdoors, using small– or large–scale instrumentation. Physical testing can be performed under two types of conditions:

- Ice gouge testing at normal gravity (1–g) – Normal gravity facilities mimic real gouging events. Depending on the size and setup of the test facility, soil failure can be observed inside or outside the range of in-situ confinement stresses.
- In a centrifuge facility – The centrifuge applies an increased 'gravitational' acceleration to physical models in order to produce identical self–weight stresses in the model and prototype.

Section 6.0 provides a literature review on the physical testing of ice gouging.

3.4.2.2 Numerical Simulation

Numerical simulation is used to study a wide range of engineering problems. With the increasing computational capacity of processors and enhancements in commercial software, simulation of ice gouging is now possible.

Numerical simulations that use finite element (FE) methods provide useful information about the seabed response to gouging, such as soil deformation profiles and seabed stress distributions. In addition, numerical simulations provide local stresses and strain demands in the structure (the pipe or wellhead).

The scope of numerical simulations is limited. Further developments are required to reduce computational time and overcome the shortcomings of the constitutive models to simulate multi–phase materials of time–dependent, stress–strain behavior.

Section 7.0 provides a literature review on the numerical modeling of ice gouging.

3.4.3 Comparison of Approaches for Ice Gouging Studies

Table 3.3 provides a comparison of the available approaches to studying ice gouging. Each approach has advantages and limitations.

The key advantage of physical testing is that it allows full control of the test parameters. In addition, physical tests can be performed on all soil types under dry or saturated conditions. Large–scale testing is preferred, but finding full–scale test facilities that account for all the processes and physics observed in a gouge event is challenging. These processes and physics include:

- Ice keel kinematics (e.g., vertical stiffness, heave, pitch, or rotation).
- Pull or tow forces (i.e., to overcome the seabed reaction forces).
- Testbed preparation (e.g., consolidation of cohesive seabed, placement of cohesionless seabed, saturation).
- Measurements during the test (e.g., real time monitoring of subgouge soil deformations, pipe strain, and pore pressures).

Centrifuge experiments can be less complicated, but the cost of the appropriate instrumentation to provide real time measurements (e.g., vertical and horizontal reaction loads, stress distributions, and displacements) can be prohibitive. The scale of centrifuge tests may not be representative of real ice gouging events, particularly when dense, cohesionless soil and overconsolidated clay testbeds, which require full–scale verification, are used.

Table 3.3: Comparison of Approaches for Ice Gouging Studies

Source	Real Event	Physical Testing	Numerical
Soil	Site dependent	Cohesive and cohesionless	Cohesive and cohesionless
Saturation	Saturated Only	Saturated or Dry	Dry Only
Keel information	Not available	Available	Available
Pipeline	Not applicable	Applicable	Applicable
Site	Site dependent	Not site dependent	Not site dependent
Study output	Gouging location, prediction of gouge dimensions	Gouge dimensions, forces acting on keel, force acting on pipe, pore pressure	Gouge dimensions, forces acting on keel, force acting on pipe, pore pressure

4.0 Geotechnical Investigations

4.1 Beaufort Sea

The Beaufort Sea is located at the far edges of the Arctic Ocean to the north of the Alaska and Yukon shores. The shore of the U.S. Beaufort Sea extends from Point Barrow, Alaska to the southwestern edge of Prince Patrick Island. The deepest point of the Beaufort Sea is approximately 15,360 ft. (approximately 5000 m). The estimated surface area of the sea is 184,000 sq mi (476,000 sq km).

Located in the north portion of the Arctic Sea, the Beaufort Sea is characterized by severe weather conditions. It is covered with ice approximately nine months of the year and is partially covered (5% to 30%) with ice during the summer. The continental shelf extends approximately 36 to 72 miles (58 to 116 km) away from the shore at a water depth interval ranging from 200 to 230 ft. (61 to 70 m). Barrier islands extend several meters above sea level and form a chain of islands parallel to the shoreline at shallow waters (30 to 60 ft. [9 to 18 m]). Figure 4.1 shows the location and bathymetry of the Alaskan Beaufort Sea.

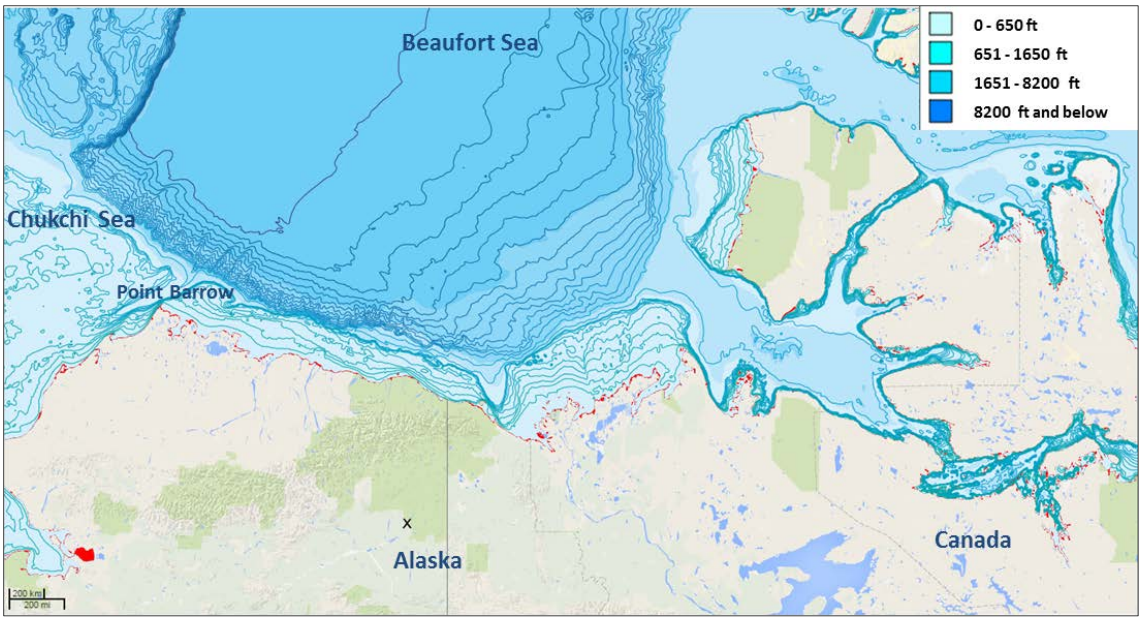

Figure 4.1: Alaskan Beaufort Sea Plan and Bathymetry [35]

The surficial sediments of the Alaskan Beaufort Sea continental shelf consist predominantly of clayey to silty soils. In the near–shore zones near the barrier islands, on shoals and along the shelf break, more coarsely grained soils of sedimentary origin

sediments are present. The seabed sediments are mainly overconsolidated because of glacial consolidation. Another typical characteristic is erosion caused by currents and permafrost thaw cycles.

Intensive geotechnical surveys were performed to investigate the geotechnical profile of the seabed. A summary of research findings are included in the following sub–sections.

4.1.1 Barnes and Reimnitz (1974)

Barnes and Reimnitz [10] described soil characteristics in the Beaufort Sea based on vibracore samples and in situ testing collected at 23 locations. Figure 4.2 shows locations of vibracore samples and in situ testing.

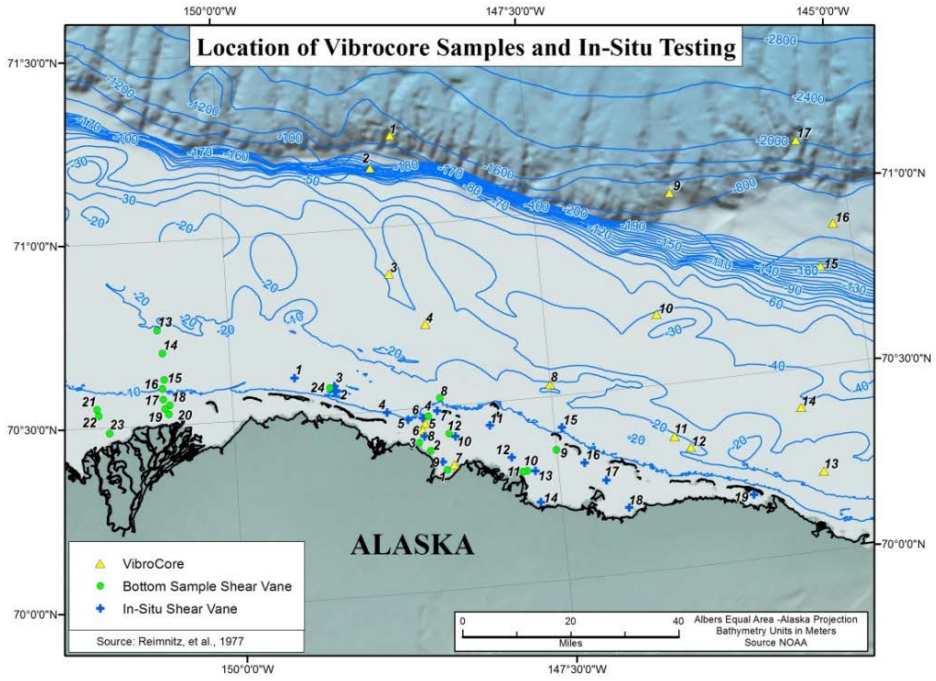

Figure 4.2: Location of Vibracore Samples and In Situ Testing (Reimnitz et al., 1977 [114])

Figure 4.3, Figure 4.4, and Figure 4.5 show the mean diameter of grain size distribution, sorting of sediment samples, and distribution of gravel in surface sediments. Figure 4.6 provides an additional location map that the U.S. Minerals Management Service (MMS) [82] prepared to show the sea surficial sediments in the near–shore areas.

Barnes and Reimnitz [10] reported that soils in the Beaufort Sea seabed surface can be classified into three main categories: poorly sorted; fairly well–sorted fine grained

sediments; and moderate to well–sorted sand and silts. The poorly sorted soils are located along the shelf break and on the central shelf off Prudhoe Bay. The central shelf is characterized by fairly well–sorted, fine–grained sediments. The inner shelf contains well–sorted sand and silt.

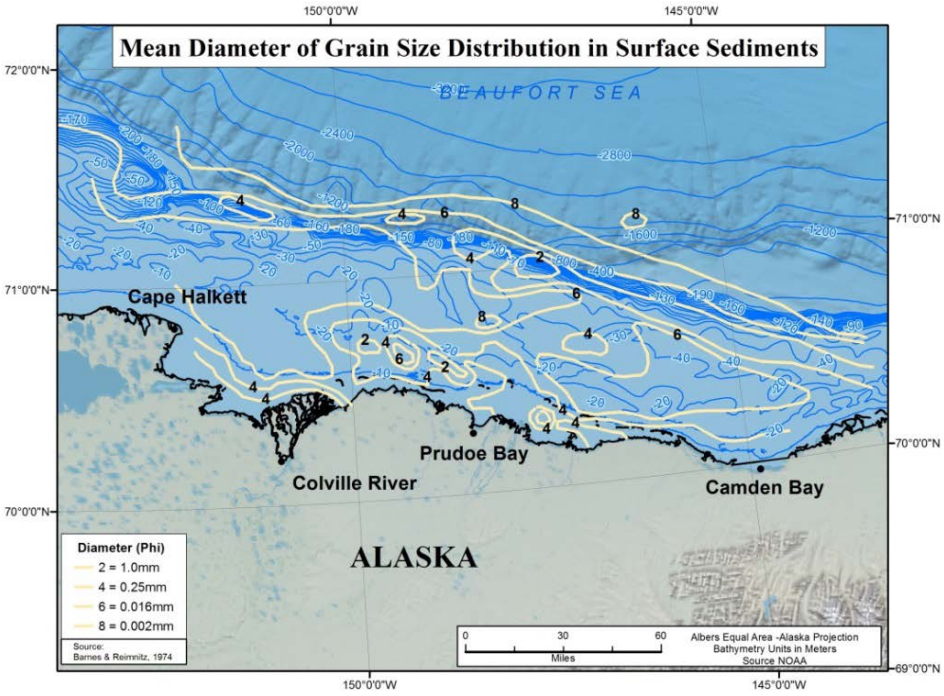

Figure 4.3: Mean Diameter of Grain Size Distribution in Surface Sediments (Barnes and Reimnitz, 1974 [10])

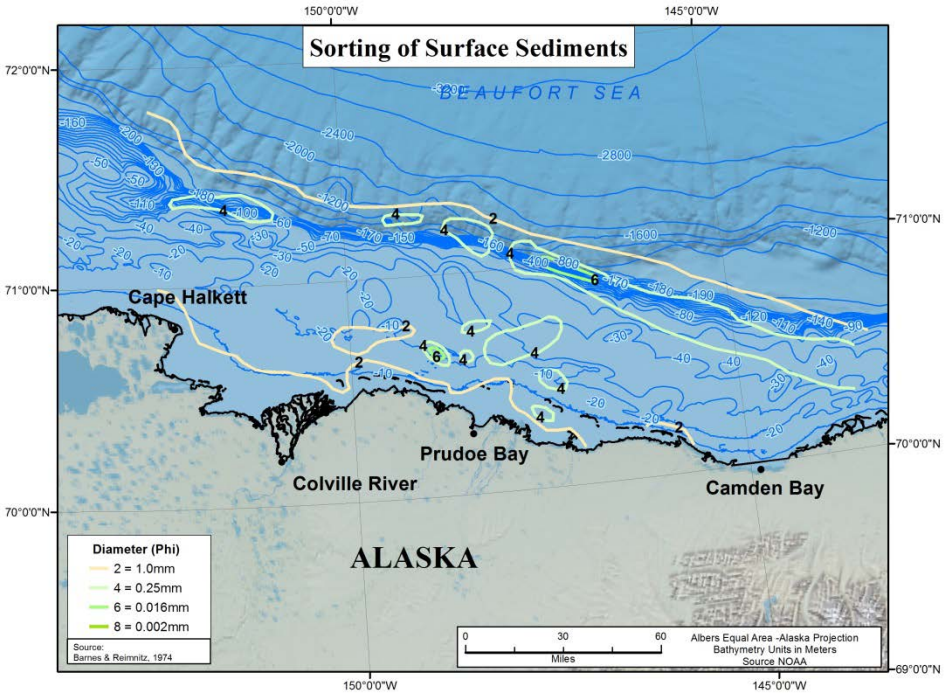

Figure 4.4: Sorting of Surface Sediment Samples (Barnes and Reimnitz, 1974 [10])

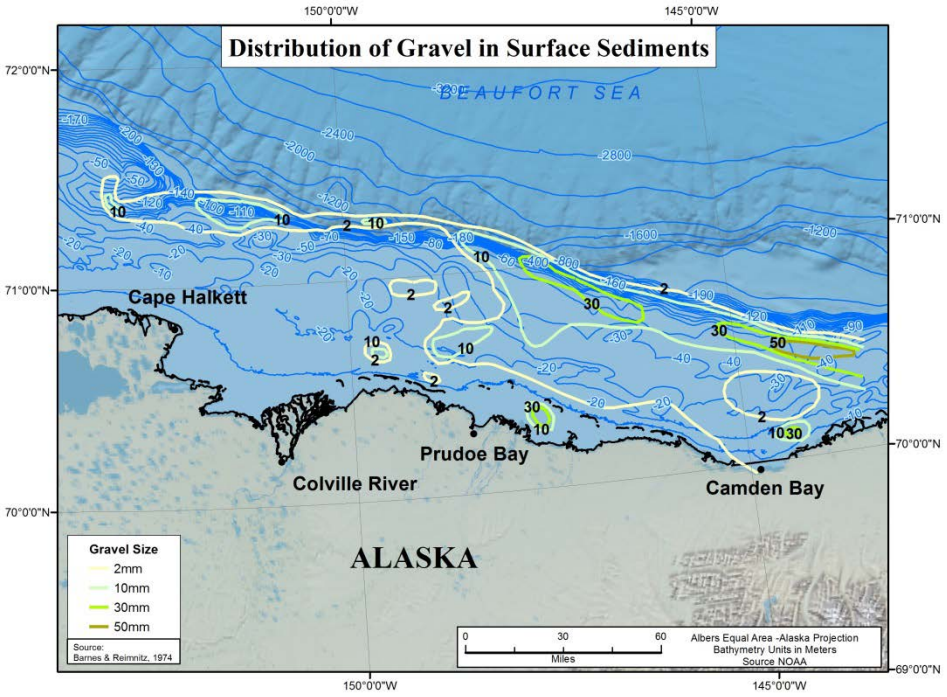

Figure 4.5: Distribution of Gravel in Surface Sediments (Barnes and Reimnitz, 1974 [10])

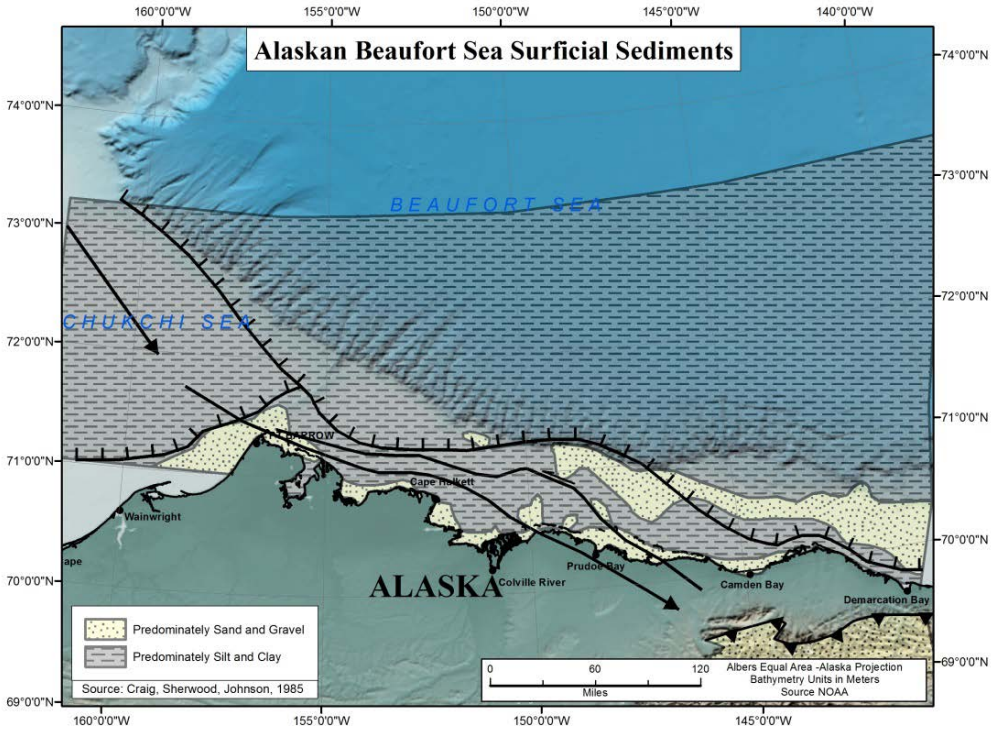

Figure 4.6: Alaskan Beaufort Sea Surficial Sediments (MMS, 1990 [82])

4.1.2 Reimnitz et al. (1977)

Reimnitz et al. [114] performed investigations that analyzed the pore fluid salinity and temperature profiles in areas of interest of the Beaufort Sea. The goal of the study was to learn the temperatures at which the sediments were most likely to freeze.

Reimnitz et al. reported soil sample properties at the top 3.0 ft. (0.9 m) of the seabed. Samples collected at the surface had very low shear strength, indicating a very soft seabed at the test locations, because the samples were collected from gouged areas and may have been remolded by frequent gouging. Temperature profiles and soil samples were used to investigate the existence of ice–bonded permafrost. Borehole samples indicated that permafrost was limited to the Pleistocene deposits between 50 ft. and 200 ft. (15 m and 60 m) below the seabed. Reimnitz proposed four soil categories, based on shear strength, for the top 165 ft. (50 m) of seabed soils. Table 4.1 provides a brief description of each category.

Table 4.1: Beaufort Seabed Soil Categories (Reimnitz et al., 1977 [114])

#	Category	Composition	Material Strength	Location
1	Soft to medium stiff	Fine grained Holocene deltaic	Approximately 3 psi	Shoreward of the barrier islands in Prudhoe Bay and Mikkelsen Bay
2	Medium dense to very dense	Uniform fine sand with particle size ranging from 0.11 to 0.19 mm	Measured internal angle of friction of 41° to 47°	Offshore, the barrier islands are linked with underwater shoals
3	Stiff to hard	Silt and clay deposits	Undrained shear strengths measured in the range of 7.25 to 43.5 psi, with an average value of 18.85 psi	Between Cross Island and Stefansson Sound, and to the east of the Maguire Islands
4	Dense	Well graded Pleistocene sand and gravel	Reasonably well graded, maximum of 50-mm (2-inch) diameter particle size	Not specified

4.1.3 Miller and Bruggers (1980)

Miller and Bruggers [81] investigated the soil profile at 20 drilled boreholes with the intent to determine geotechnical and permafrost properties of the borehole locations. Figure 4.2 shows the locations of the drilled holes and a summary soil profile for each sample. Figure 4.7 shows the data that Millers and Bruggers developed and used to create the stratigraphic sections (AA, BB, and CC. Borehole locations are plotted in Figure 4.8 and are summarized in Appendix B in Table B–1. Figure 4.9 shows the borehole logs for borehole numbers A to D.

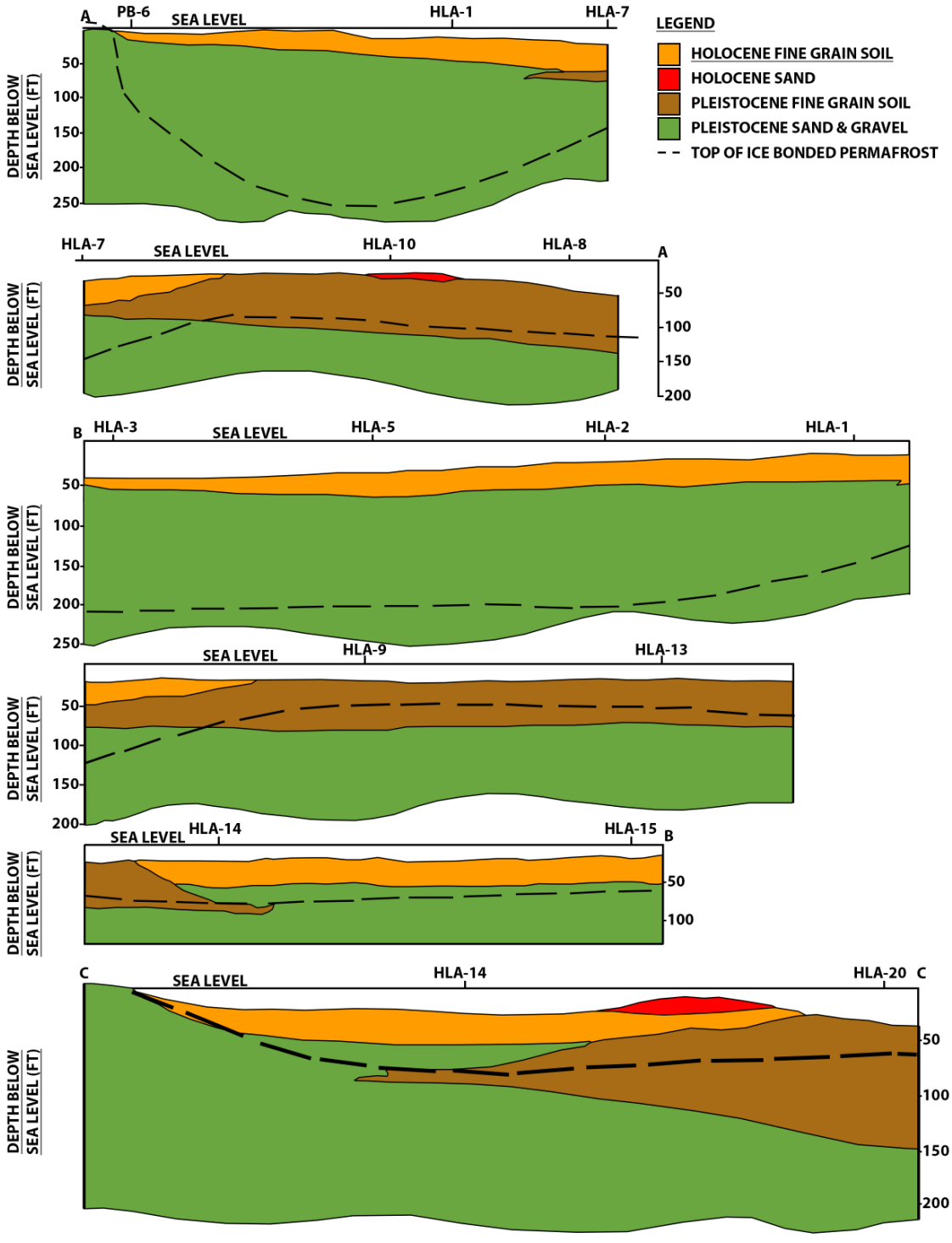

Figure 4.7: Stratigraphic Sections AA, BB and CC (Miller and Bruggers, 1980 [81])

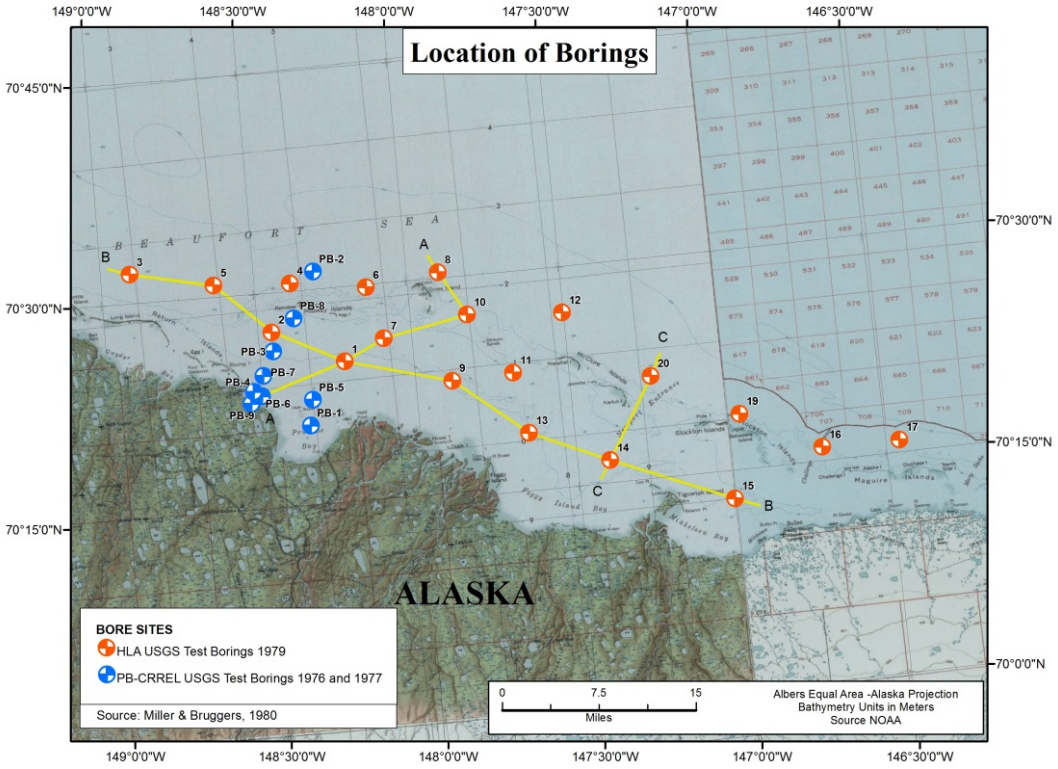

Figure 4.8: Locations of Borings (Miller and Bruggers, 1980 [81])

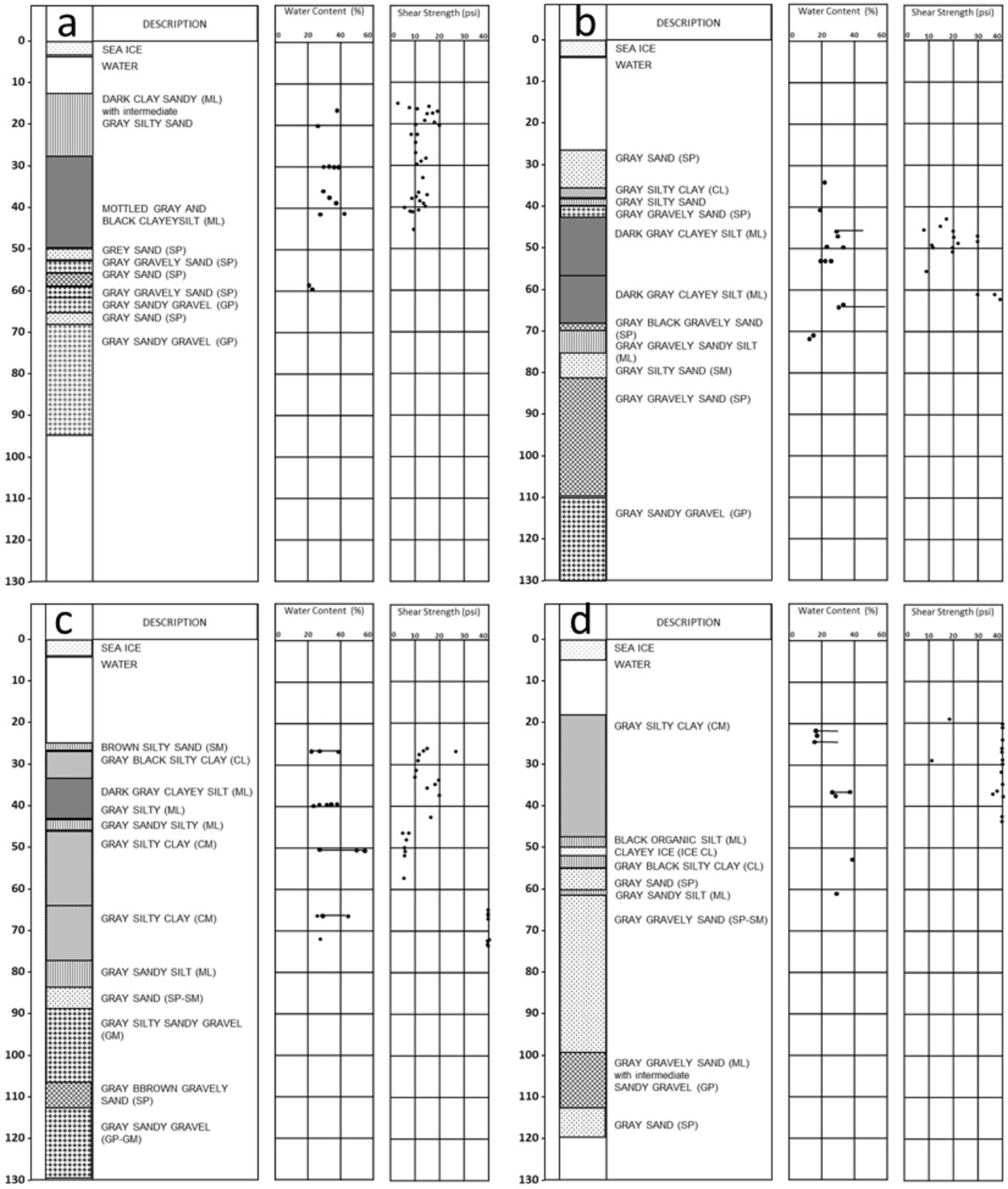

Figure 4.9: Borehole Logs (Miller and Bruggers, 1980 [81]) (Reproduced by WGK)

4.2 Chukchi Sea

The U.S. Chukchi Sea is located at the northwest section of the Alaskan coast, between Point Barrow to the east and Cape Prince of Wales to the west. Like most of the Arctic area, the Chukchi Sea is covered with ice most of the year (approximately eight months). The total approximate area of the Chukchi Sea is 230,000 sq mi (595,000 sq km). A number of islands can be found in the area; in general, the sea is considered shallow. Figure 4.10 shows the location and bathymetry of the Chukchi Sea.

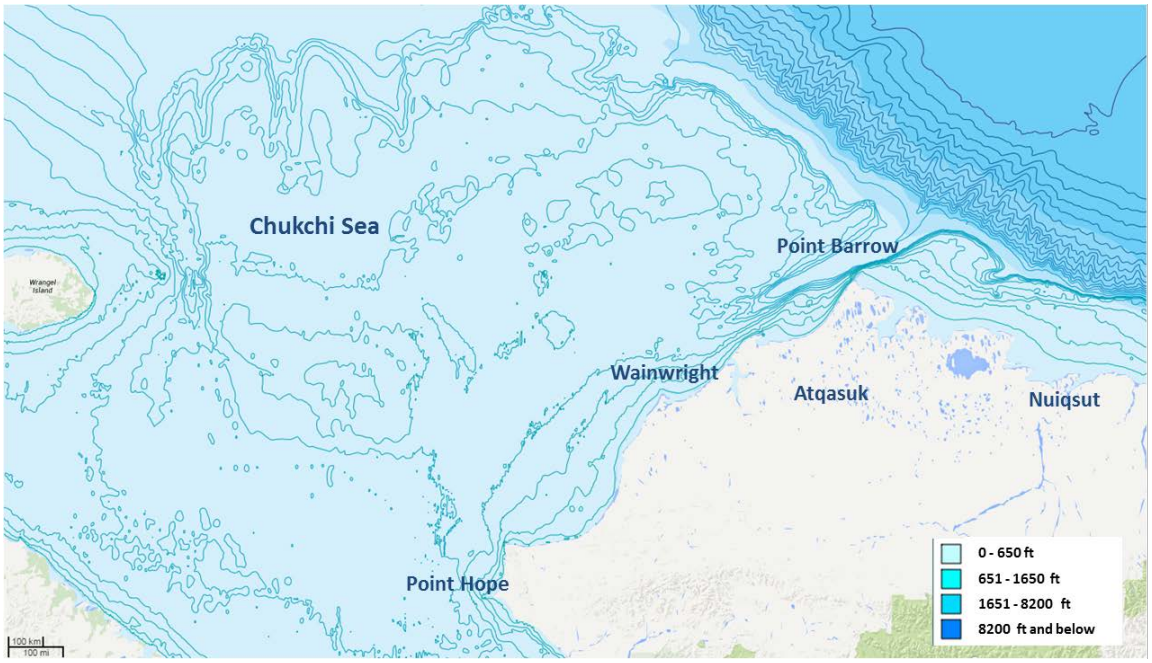

Figure 4.10: Chukchi Sea Bathymetry [35]

The most common sea depths are less than 164 ft. (50 m). The depth drops sharply to more than 9,842 ft. (approximately 3,000 m) close to the northern limits of the study region. The eastern area of the sea has a deep channel that is 300 ft. deep (91 m) at the Barrow Valley. The west border is relatively shallow, with a water depth of 164 ft. (50 m). Some shoals exist at the shelf area, which extends 66 ft. (20 m) within the sea surface. There are additional shoals near the shore side, along the northwest coast.

The surficial sediments of the Chukchi Sea are predominantly silts, sands, and gravel across the shelf (MMS, 2006 [84]). Silt and clay are considered to be modern sediments (from the Yukon River and others) that have been carried north through the Bering Strait.

The predominant sediments on the inner shelf range from gravelly muddy sand, gravelly sand, sand, and muddy sand to sandy mud.

4.2.1 McManus et al. (1969)

McManus et al. [78] investigated the surficial characteristics of the Chukchi Sea sediments. The researchers obtained the relative distribution of silts, sands, and gravel across the shelf. MMS 2006 [84] presented McManus' work and prepared a soil–type location map, which is shown in Figure 4.11.

The following points summarize the McManus et al. (1969) [78] findings:

- Sandy soils are generally found over the shoal areas and may have been transported from eroded sea cliffs along the north Alaskan coast.
- Sand waves have been observed in water depths ranging from 49 ft. to 213 ft. (15 m to 65 m) and are considered to be active features because of their asymmetric form.
- Gravel deposits occur on the Herald Shoal and along the coast north of the Lisburne Peninsula.

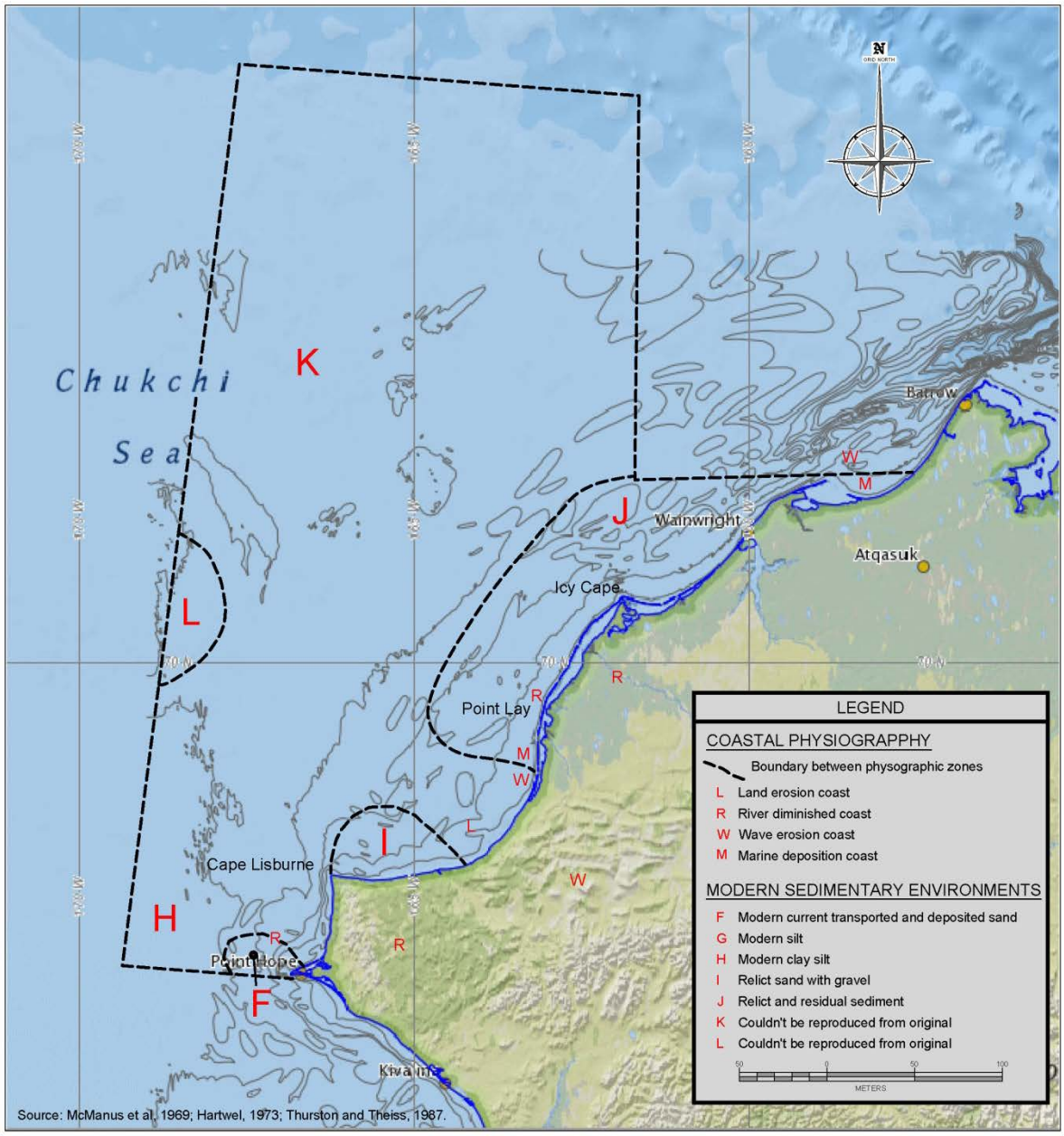

Figure 4.11: Distribution of Surficial Sediments (MMS, 2006 [84])

4.2.2 Winters and Lee (1984)

Winters and Lee (1984) [133] used results from geotechnical testing performed on samples collected from seven boreholes in the Chukchi Sea and estimated the shear strength properties of the seabed soils. Water depth at the borehole drilling locations ranged from 154 ft. to 177 ft. (47 m to 54 m). Table B–2 lists these boring locations.

Testing results showed that the surficial layer had a thickness between 3 ft. and 27 ft. (0.9 m and 8 m) with a low shear strength of 2.9 ksi (20 kPa) and an underlying layer of stiff soils. The thickness of the soft layer was correlated with the water depth. The shear strength of the stiff layer was 29 ksi (200 kPa). The depth of the bedrock line was not identified in the study. The shear strength profile for the seven boreholes is presented in Figure 4.12

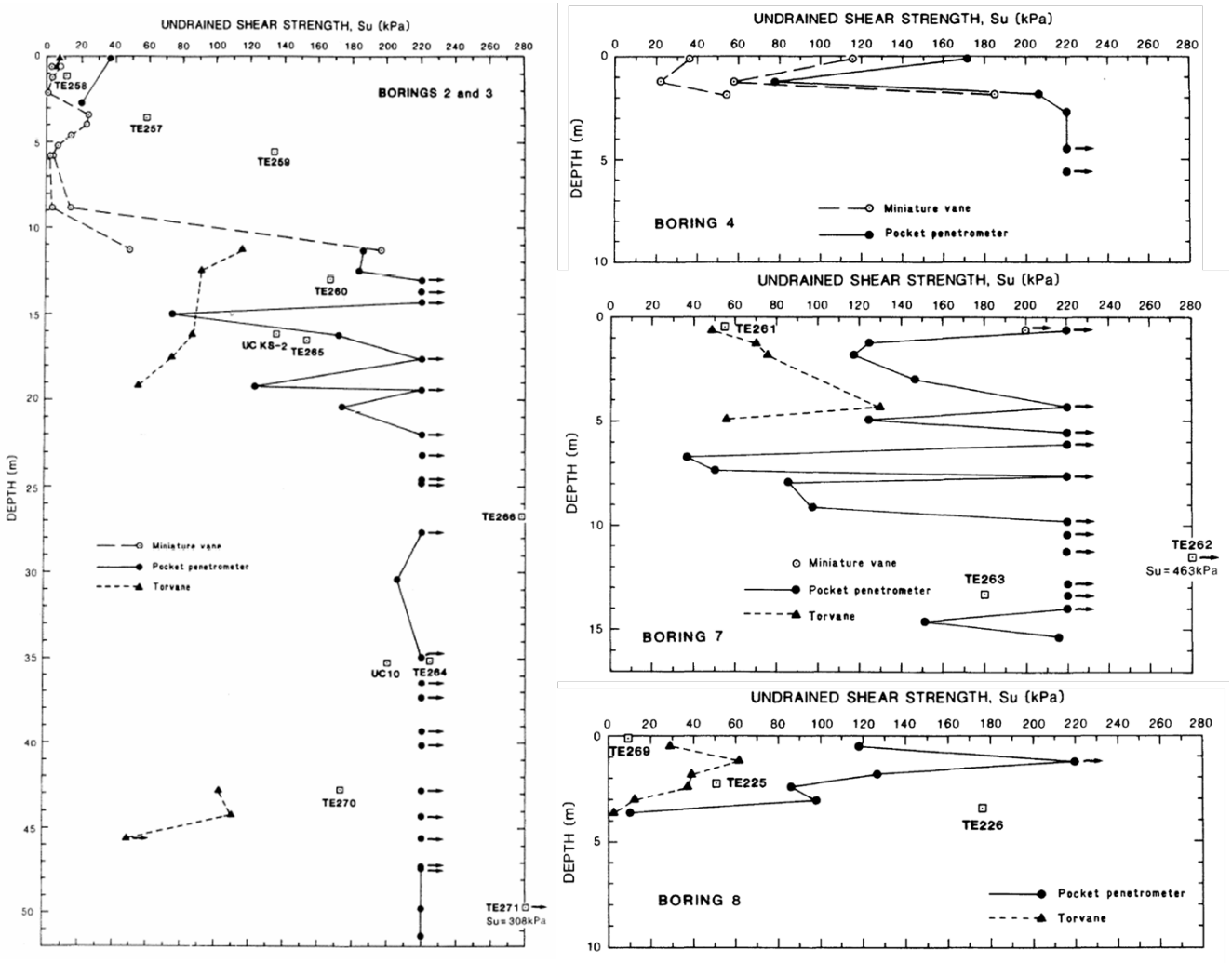

Figure 4.12: Undrained Shear Strength Profiles (Winters and Lee, 1984 [133])

4.2.3 Miley and Barnes (1986)

The objective of a geological survey conducted by Milley and Barnes [80] was to establish the sedimentary and geotechnical characteristics of ice and current affected sediments in the Chukchi Sea and the Beaufort Sea. Vibracore and gravity core samples were collected in water depths between 59 ft. (18 m) and 1,033 ft. (315 m). Figure 4.13 and Figure 4.14 show the map locations of the samples.

The study revealed that the majority of core samples are overconsolidated materials and, in some cases, samples may be considered mudstone. Layers of consolidated or overconsolidated muds and sandy muds underlie the Chukchi Sea central and inner shelf regions.

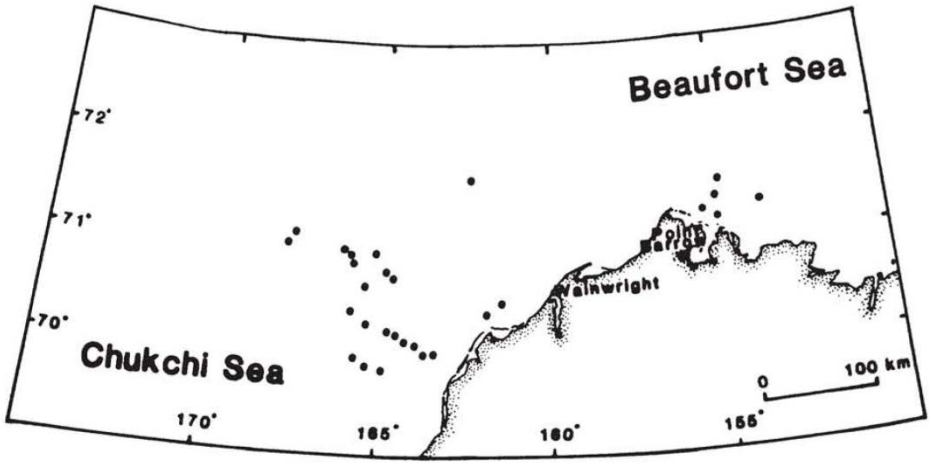

Figure 4.13: Locations of Gravity Core (Miley and Barnes, 1986 [80])

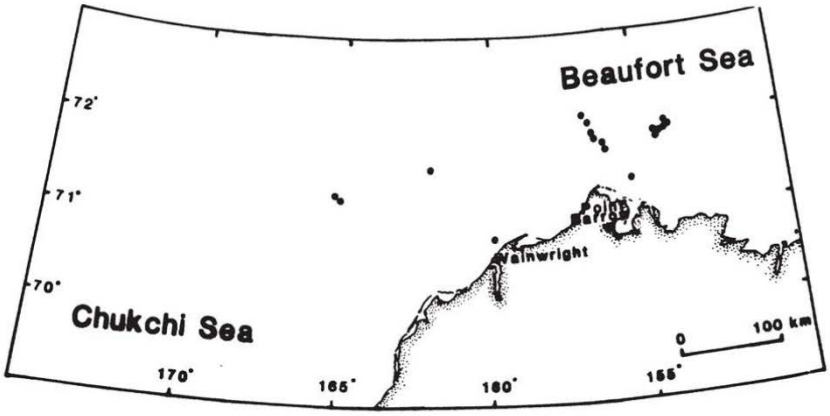

Figure 4.14: Locations of Vibracore Cores (Miley and Barnes, 1986 [80])

4.2.4 Phillips et al. (1988)

Phillips et al. (1988) [105] investigated the surficial sediment. The work of these scientists, which was limited to the inner shelf of the Chukchi Sea, identified a number of facies.

Sedimentary facies are mappable subdivisions of a designated stratigraphic unit. These subdivisions reflect the depositional environment and are distinguished from adjacent subdivisions by lithology sediment bodies that are recognizably different from adjacent sediments. Generally, facies are distinguished by the type of the rock or sediment that is being studied. Thus, facies that are based on petrological characters such as grain size and mineralogy are called lithofacies, while facies based on fossil content are called biofacies.

Figure 4.15 shows the distribution of the surficial sediment. Sediment thickness varied from 3.2 ft. (1.0 m) to 16.4 ft. (5.0 m) and was classified into four major facies:

- Outer sand facies – Occur in water depths varying from 137.8 ft. (42 m) to 157.5 ft. (48 m) at the western flank of the Barrow Sea Valley. This facies is bounded from the eastern side of the Barrow Sea Valley with a large gravel field.
- Outer gravel facies – Occur in water depths varying from 131 ft. (40 m) west of the ice cape to 197 ft. (60 m) in the north. This geological formation is a layer of gravel 13.1 ft. (4 m) thick that lies on top of other layers of overconsolidated mud.
- Coastal current sand facies – Lie to the east of the outer gravel facies. (Refer to Figure 4.15.) Phillips et al. (1988) [105] reported that this facies is distinct, containing abundant echinoids and recording active northward sediment transport represented by sand wave fields. Box core samples indicated that the sand content of the coastal current sand facies varies from 82% to 98%. The texture of the sand ranges from slightly gravelly muddy sand to sand.
- Inner gravel facies – Reside at the east side of the coastal current sand facies at relatively shallow water depths (ranging from approximately 94.4 ft. [29 m] to less than 16.4 ft. [5 m] near shore).

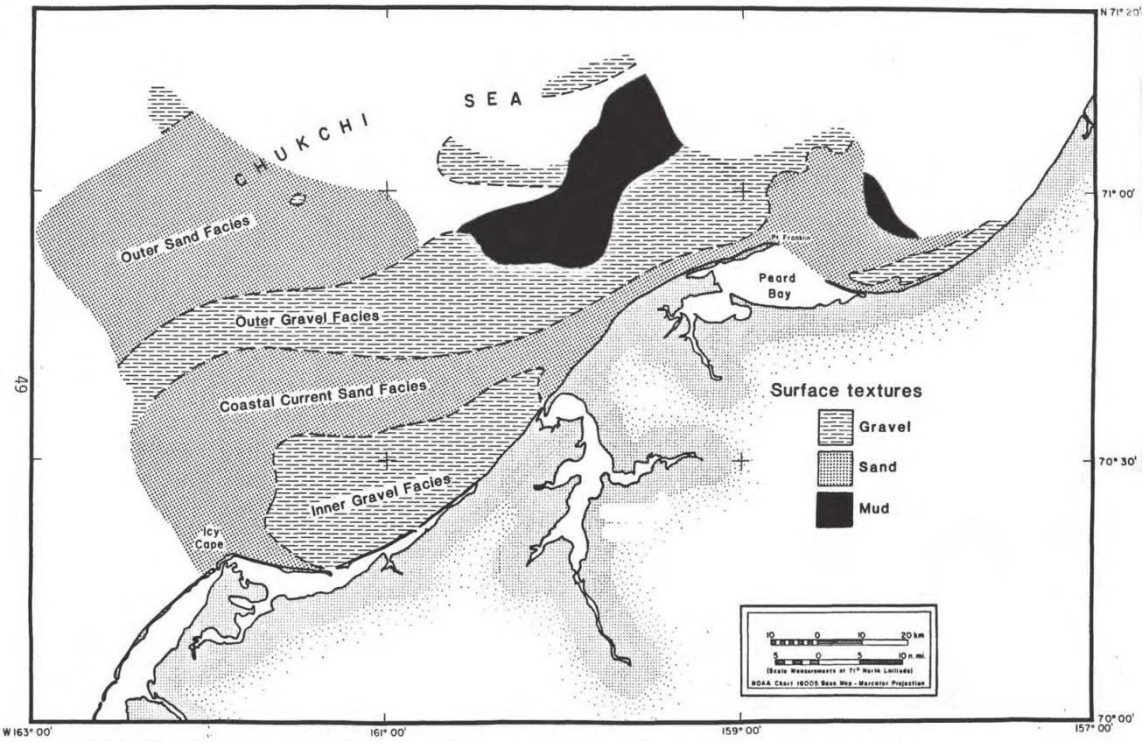

Figure 4.15: Major Surficial Sediment Types (Phillips et al., 1988 [105])

4.3 Summary

Researchers have performed intensive geotechnical surveys to investigate the geotechnical characteristics of the Beaufort and Chukchi seabeds. The USGS documents describe the ice gouging and geotechnical investigation surveys in both the Chukchi and Beaufort Seas during a two–decade timeframe between the 1970s and 1980s.

The surficial sediments of the Beaufort Sea continental shelf consist predominantly of clayey to silty soils. In the near–shore zones near the barrier islands and on shoals and along the shelf break, coarsely grained soils of sedimentary origin are present. The seabed sediments are mainly overconsolidated because of glacial consolidation. Another typical characteristic is erosion caused by currents and permafrost thaw cycles. Shear strength estimates of the test locations, based on shallow sampling of the seabed, suggest that the seabed is predominately very soft (approximately 5.07 psi or 35 kPa).

The surficial sediments of the Chukchi Sea are predominantly silts, sands, and gravel across the shelf (C–CORE, 1995 [18] [19]). Silt and clay are considered to be modern sediments, from the Yukon River and others, that have been carried north through the Bering Strait. The predominant sediments on the inner shelf range from gravelly muddy sand, to gravelly sand, sand, muddy sand, and sandy mud. Gravel deposits are present

along Herald Shoal and along the coast north of the Lisburne Peninsula. Test results have shown that the surficial layer, with a thickness varying from 3 to 30 ft. (0.9 to 9 m), has a low shear strength of 3.0 psi (20 kPa) with an underlying layer of stiff soils.

The geotechnical conditions (seabed–soil shear strength and resistance to ice keel penetration), morphology, and localized bathymetry of the seabed influence gouge characteristics. Therefore, gouge attributes may vary along the length of an ice gouge with changing seabed conditions. Research indicates that seabed soil conditions limit ice gouging processes, with deeper gouge depths generally occurring in weak marine silts and clays.

5.0 Ice Gouging Surveys

Seabed mapping aids in the evaluation of gouging activity. Seabed mapping involves conducting geophysical surveys at a location using ship–borne instruments such as single– or multiple–beam echo sounders (refer to Figure 5.1), side–scan sonars, and sub–bottom profilers. The information that can be acquired by a single survey includes gouge depth, width, length, orientation, and density.

Sediment deposition, called infill, causes a reduction of the measured gouge depth and width. Gouge infilling thus introduces a non–conservative bias in the data. Although a correction factor can be applied (e.g., Kenny et al., 2007 [57]), this issue is generally addressed by repeatedly mapping the seabed over a number of years. Repetitive mapping also helps to distinguish young gouges from old ones and to determine gouging frequency.

In the absence of reliable, repetitive seabed surveying data, estimates of ice gouge or near ice gouge event recurrence rates may be determined through the application of alternative methods, including analyses of:

- Ice feature drift rates.
- Keel draft to sail height ratios.
- Upward looking sonar.

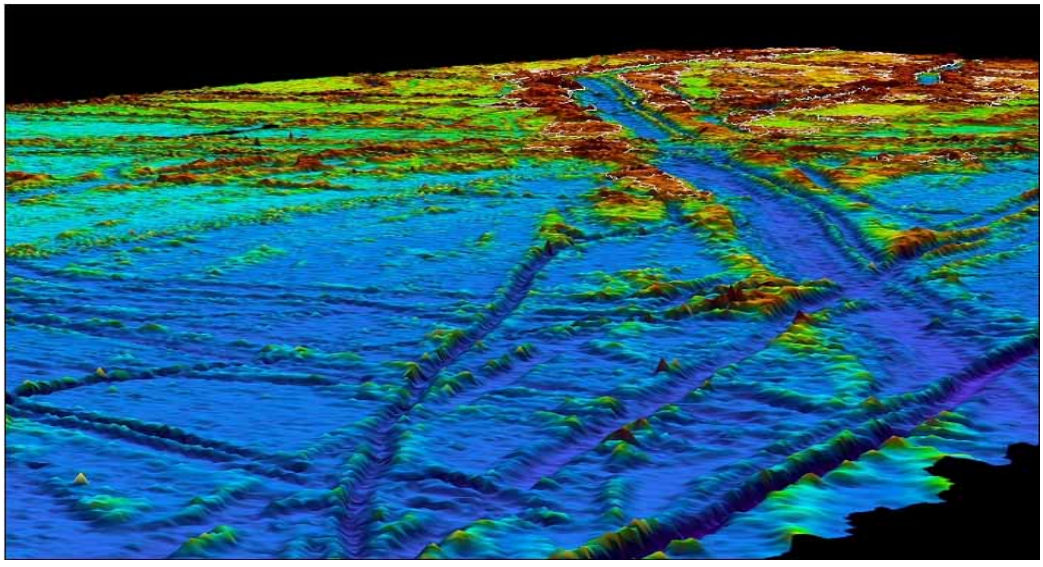

Figure 5.1: Seabed Scour Image from Multi–beam Echo Sounder (USGS [16])

5.1 Analysis of Data and Models

The United States Geological Survey (USGS) has collected a significant amount of ice gouge data through numerous seabed survey programs conducted in the American Beaufort and Chukchi Seas.

The collected data is categorized according to water depth and location. Then, probability distributions are fitted to each of the characteristics of interest. Therefore, the collected data from ice gouging records is analyzed separately with respect to gouge depth, gouge width, crossing density, and crossing frequency.

The burial depth required to protect subsea structures against interaction with gouging ice keels is a function of the maximum gouge depth, the rate of ice gouge occurrence in a specific area, and the specified level of acceptable risk. Burial depth depends on the design ice gouge depth and the design gouge depth return period.

The width of the gouge is used to estimate the length of pipe that may be subjected to damage in an ice gouge event. For wellheads, the seabed area that is subject to a gouging hazard is used to predict damage.

Ice gouge crossing density or crossing rate is the number of gouges observed per surveyed area. If the survey is performed along a vessel track line, the crossing density is reported as a linear density. If a scan of a seabed area is performed, a spatial density is used.

A common analysis approach is to generate exceedance probability plots and estimate the extreme design parameters at a certain level of risk (i.e., for a given probability of exceedance). This approach considers ice gouge depth data and fitted probability function while ignoring a number of factors related to the data acquisition process. However, fitting distributions over a wide class range can mask otherwise distinct occurrence trends and can sometimes lead to over–conservative designs. For this reason and the data acquisition uncertainties outlined in this sub–section of this report, exceedance probability assessments cannot solely be relied on for ice gouge design.

Several uncertainties are related to the detection of gouges and their identified characteristics (e.g., depth). One related uncertainty is the degradation of gouging marks caused by sedimentation, infilling, and reworking of the seabed. Another uncertainty related to the measurement technology is the resolution cut–off and the sensitivity of the instruments to sea state conditions.

Additionally, some survey methods do not allow for a distinction between single and multiplet events. For example, survey programs conducted in U.S. Arctic seas recorded each ice gouge in a multi–tracked seabed as an individual ice gouge, regardless of

whether it was created by a single keel or a multiplet gouging event. If a multiplet gouge event is reported as more than one gouge track in one survey and as one gouge track in another survey, correlations between the two surveys will not be accurate. This inconsistency prevents comparisons between repetitive surveys of the same areas.

The ice gouge crossing rate is commonly presented for single seabed surveys and does not present updated gouge occurrence data. The surveys count the number of crossings along a track line or area of survey, but they usually do not identify the orientation of the pipeline relative to the gouging heading and the potentially exposed pipeline length unless they are performed along the pipeline route.

Early investigators (Lewis, 1977 [74]; Weeks et al., 1983 [130]; Lanan et al., 1986 [69]) recommended the single–parameter exponential distribution as an effective and conservative probabilistic ice gouge model. In addition, three–parameter gamma or Weibull distributions can be fitted to ice gouge depth data. Both of these distributions may be reduced to the exponential form under specific conditions.

The findings of Nessim and Hong, 1992 [88] suggest that the Weibull distribution provides the better fit to Canadian Beaufort Sea ice gouge depth data across the full range of available water depths. The two–parameter exponential and three–parameter gamma distributions tended to under–predict the amount of shallow gouge depth data.

When analyzing the available data sets, researchers can draw some general correlations between gouge features, seabed type, and bathymetry.

A correlation between ice gouge depth and soil strength properties is that the soil's shear strength seems to be a limiting factor, which is supported by two observations:

- Maximum gouge depths are recorded in areas with weaker surficial sediments.
- Shallower gouges are traced in areas with stronger soil or bedrock near the surface (e.g., western Beaufort Sea, northwest and northeast Shoal regions of Chukchi Sea)

Seabed bathymetry (Figure 5.2) also affects gouge depths, but it does so in a more complicated way. The general trend shows that gouge depths increase with water depth. To support this observation, Wilson, 1982 [131] shows that the maximum gouge depths observed in the Chukchi Sea are shallower than those observed in the Beaufort Sea. In the Beaufort Sea, high–frequency occurrence rates are observed for depths between 49.2 ft. (15 m) and 147.6 ft. (45 m). The 49.2–ft. (15–m) isobaths coincide with the shoreward boundary of the dynamic shear ice zone. In the Chukchi Sea, the Alaskan Coastal Current strongly influences the ice gouge process as ice features tend to drift parallel to the bathymetric contours. Therefore, the frequency of ice gouge events increases with increasing latitude and seafloor slope but decreases with increasing water depth (Toimil, 1978 [124] and MMS, 1990 [82]; 2008 [85]).

Table B–9 presents a summary of gouge depths as reported by Toimil.

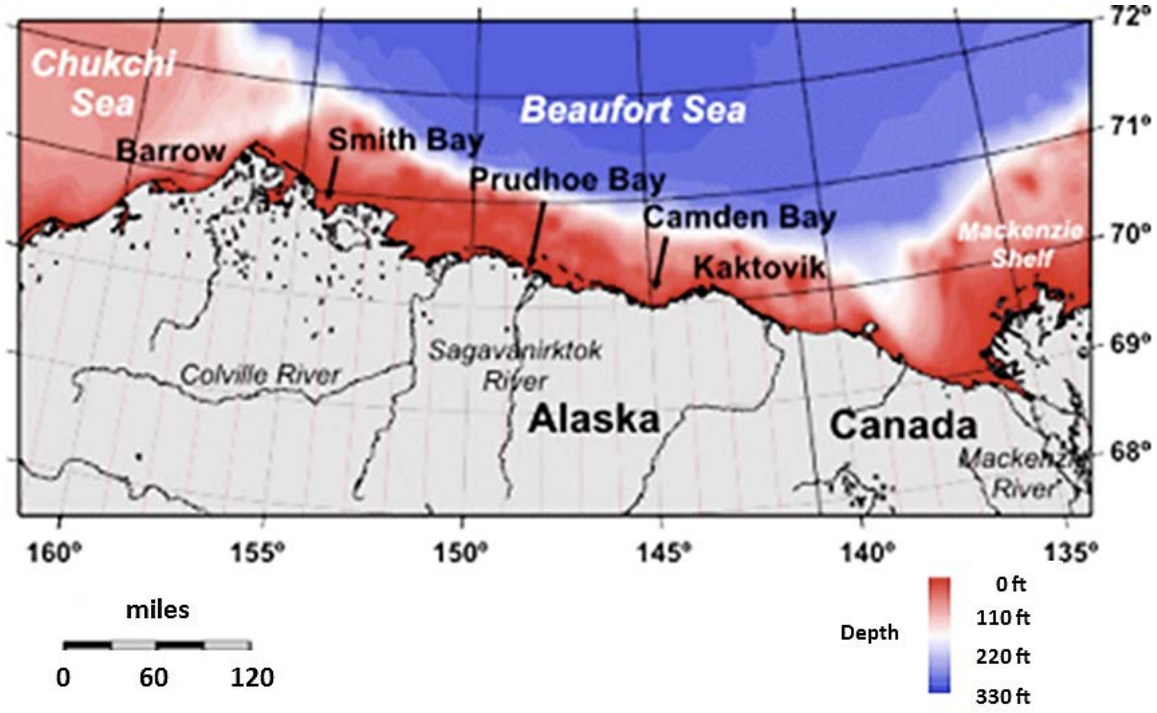

Figure 5.2: Alaskan Beaufort Sea and Chukchi Sea Plan and Bathymetry [47]

The following sub–sections present the data sets collected from the Beaufort Sea and the Chukchi Sea as well as correlations among ice gouge characteristics as reported in the literature.

5.2 Surveys in the Beaufort Sea

The USGS provides two primary documents, which are available to the public, that present adequate survey data for the U.S. Beaufort Sea: Rearic and McHendrie (1983) [111] and Weber et al., (1989) [129]. An additional survey by MMS (2002) [83] provides usable data sets for ice gouges. Several studies have been conducted to develop ice gouging rate prediction models. The following sub–sections describe the available data sets. An additional section, which has been added to summarize MMS (2008) [85], presents a brief comparison between the available data sets.

5.2.1 Rearic and McHendrie (1983)

Rearic and McHendrie (1983) [111] combined the data obtained by their earlier surveys, which were reported in Rearic et al. (1981) [112] and Reimnitz et al. (1982) [113]. Rearic and McHendrie conducted the surveys for the Alaskan Beaufort Sea to study size,

density, orientation, and location of ice gouges. The study provides extensive information about gouge dimensions (i.e., width, depth, and length). The data was included in USGS report numbers 81–950 and 82–972.

The files contain 2,071 records for the Beaufort Sea shelf west of the Canning River (longitude 146° West) and provide survey data for 1,394 miles (2,243 km) of track lines. The authors identified 132,183 gouges in the data, and they discussed both single and multiple gouges in the study. However, data tabulated by Rearic and McHendrie (1983) [111] does not distinguish between single and multiple events because only the maximum number of incisions per gouge interval was provided (refer to Figure 5.3).

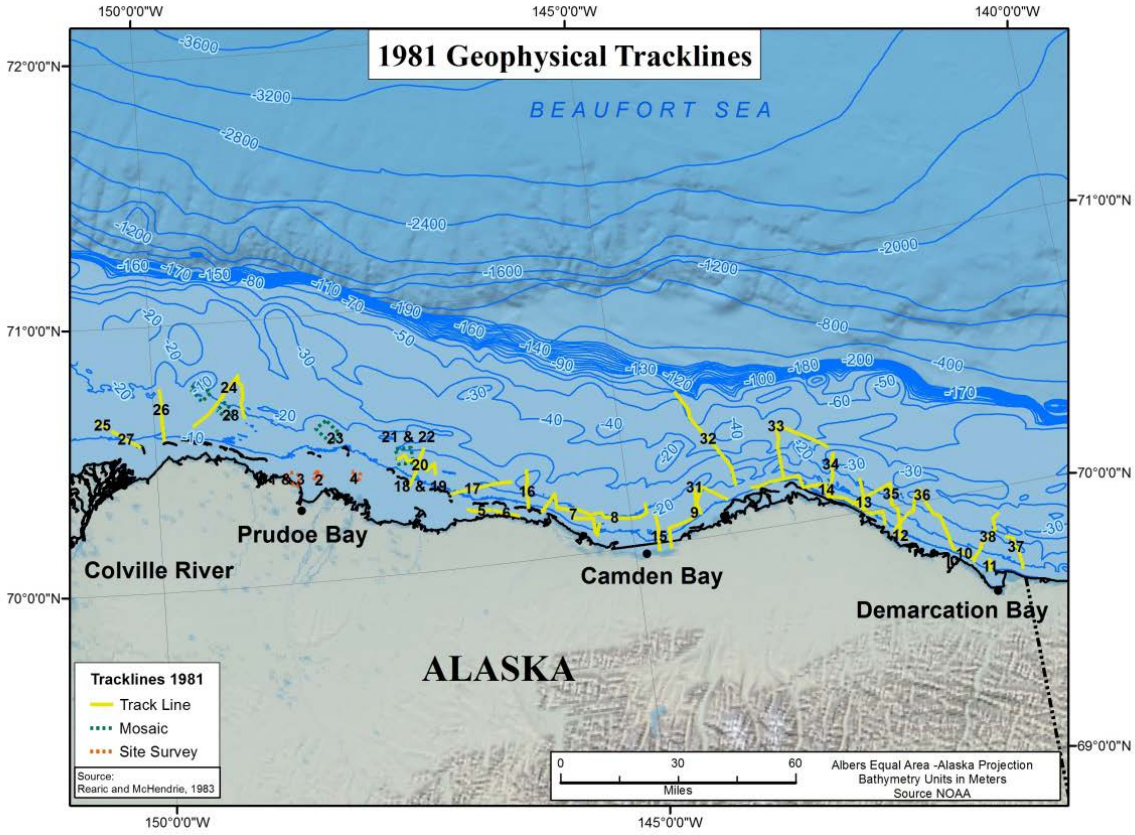

Figure 5.3: 1981 Geophysical Track Lines (Rearic and McHendrie, 1983 [111])

5.2.2 Weber et al. (1989)

Weber et al. (1989) [129] tabulated repetitive surveys collected from nine sites between 1977 and 1985. Figure 5.4 shows a map of corridor locations.

Weber et al. surveyed a total of 1,077 ft. (316 m) of track lines, in which 19,327 gouges were located. The study provides gouge data per segment (measured in km) and indicates the water depth and the total number of existing gouges in each segment. The authors also determined the ages of the gouges by comparing recent surveys with the previous surveys. They recorded multiple gouge events and their dimensions and classified gouges by the depth of occurrence. Unfortunately, accurate coordinates of the gouge records were not provided. However, associations made with the depths and corridor locations of data obtained by Barnes and Rearic, 1985 [9] link the two surveys.

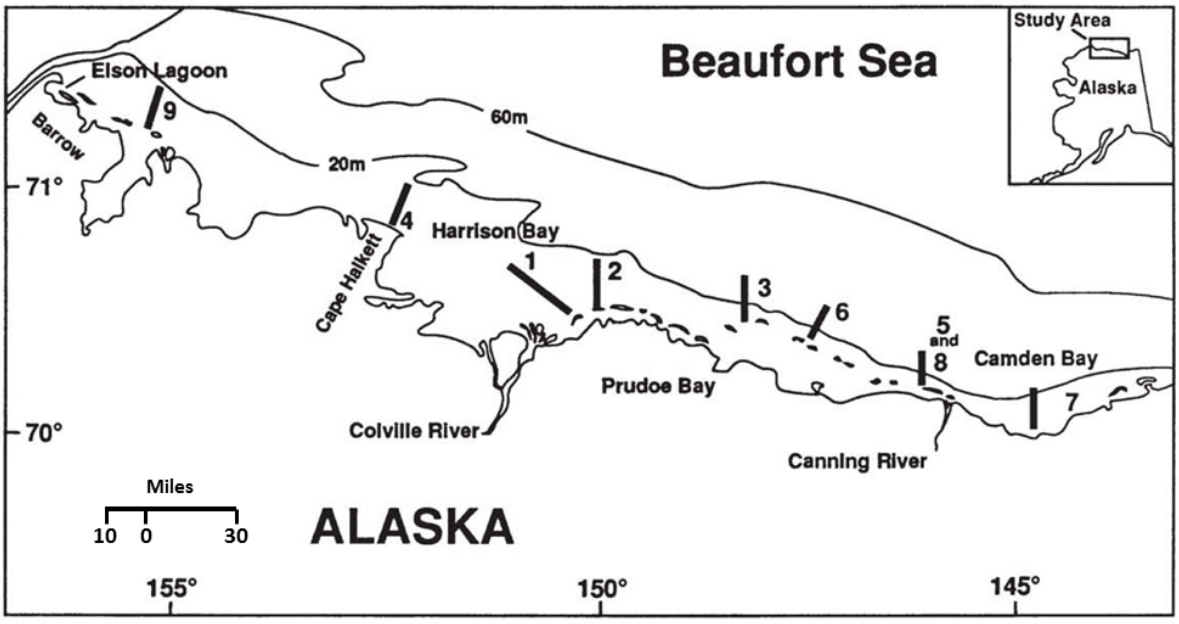

Figure 5.4: Location Map Indicating Corridor Locations and Generalized Bathymetry for the Alaskan Beaufort Sea (Weber et al., 1989 [129])

5.2.3 Nessim and Hong (1992)

Nessim and Hong, 1992 [88] interpreted the available data from the Canadian Beaufort Sea surveys to estimate gouge crossing rates. These surveys included approximately 808 miles (1,300 km) of track lines. The authors noted that the deepest newly induced gouge was at water depths of 125 ft. (38 m). The average number of gouges per mile per year ranged from 1.01 to 1.73 (1.63 to 2.78 gouges per kilometer per year) for a water depth interval of 16.4 to 98.43 ft. (5 to 30 m), with a sudden drop for water depth of more than 100 ft. (30 m). The highest crossing rate that Nessim and Hong noted was for a water depth interval of 65.62 to 82.02 ft. (20 to 25 m). The track length in this water depth interval, in which 35 tracks were surveyed, was 128 miles (206 km). Table 5.1 provides the average number of gouges per mile (or kilometer) per year and the

standard deviation for each water depth interval. The observations of Nessim and Hong, 1982 [88] show a similarity between gouges in the Canadian and U.S. Beaufort Seas.

Table 5.1: Frequency of New Gouges in Canadian Beaufort (Nessim and Hong, 1992 [88])

Water Depth		Average Number of Gouges (north)		Standard Deviation		Number of Tracks	Track Length	
ft.	m	mile/yr	km/yr	mile	km		mile	km
16.40–32.81	5–10	1.26	2.02	1.67	2.68	24	133.33	214.58
32.81–49.21	10–15	1.09	1.75	0.7	1.12	30	167.01	268.78
49.21–65.62	15–20	1.33	2.14	1.22	1.97	32	113.67	182.93
65.62–82.02	20–25	1.73	2.78	1.64	2.64	35	128.32	206.51
82.02–98.43	25–30	1.01	1.63	0.92	1.48	44	122.56	197.24
98.43–114.83	30–35	0.25	0.40	0.31	0.50	19	54.74	88.10

5.2.4 Myers et al. (1996)

Myers et al., 1996 [86] prepared the location map for the track lines in the Canadian Beaufort Sea, as shown in Figure 5.5. The authors obtained the track lines from repetitive surveys performed by Canadian Seabed Research Ltd. (CSR). Funded by the Environmental Studies Research Funds (ESRF) in 1990, the purpose of the research was to update the database. During the 1990 survey, 2,291 new scour events were recorded compared to a prior survey conducted in 1982.

Myers et al. reported that approximately 3% of scours are more than 6.5 ft. (2 m) deep. The combined database from the two surveys has 5,329 scours. The database set contains sufficient information to develop spatial and statistical data distribution. Although the data set represented by Myers et al. was collected for the Canadian Beaufort Sea, it can be used as an indication of the crossing density and gouging dimensions for the entire U.S. Beaufort Section.

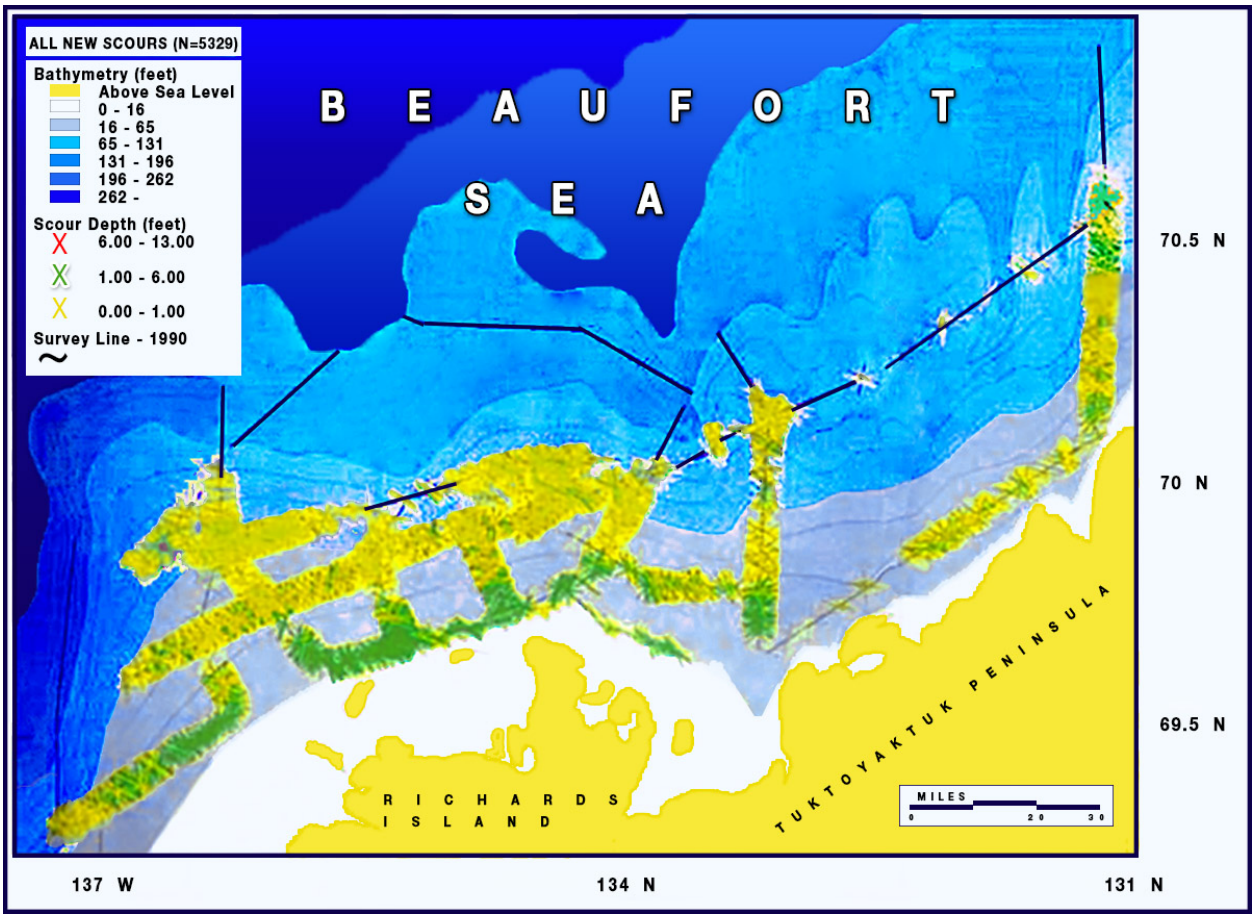

Figure 5.5: Canadian Beaufort Lines with Gouge Crossings (adopted from Myers et al., 1996 [86])

5.2.5 MMS (2002, 2008)

MMS, 2002 [83] performed additional surveys that recorded 836 ice gouge events. MMS, 2008 [85] later prepared a location map for the gouge locations. Refer to Figure 5.6.

MMS, 2002 [83] reported that most of the gouges occurred within shallow waters. The Geographic Information System (GIS) database reported only 307 gouges having meaningful gouge depth and width information, and the surveys did not distinguish between single and multiple gouge events. Table 5.2 summarizes the data set that MMS [85] prepared in 2008.

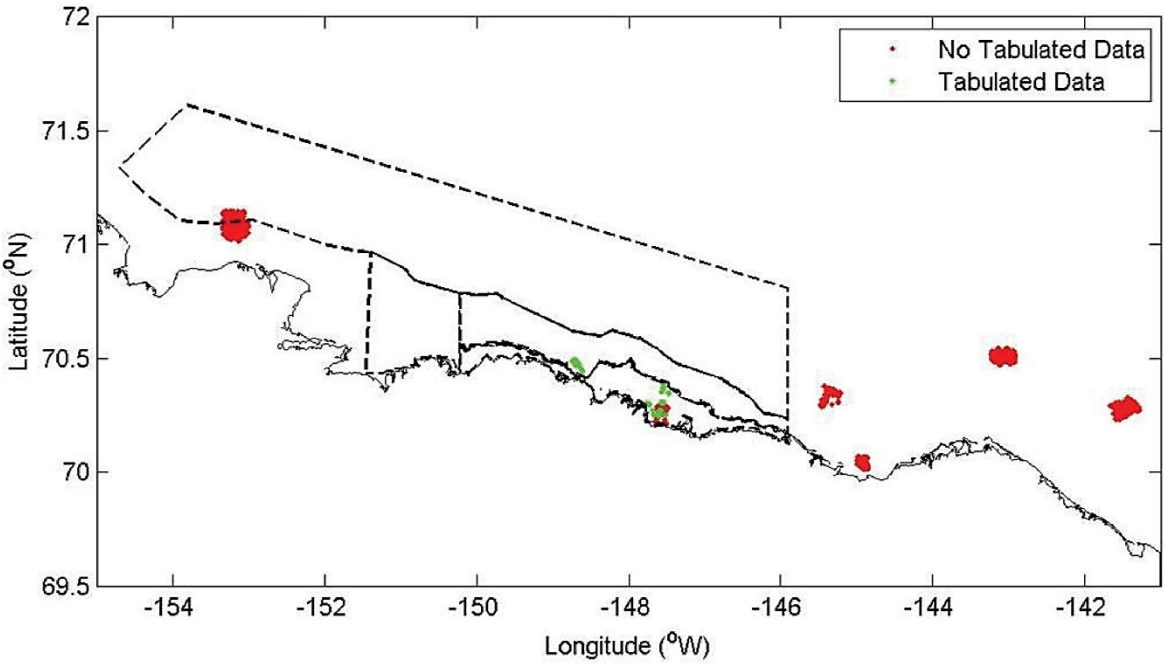

Figure 5.6: GIS Database Ice Gouge Locations MMS, 2002 [83]

Table 5.2: Summary of MMS (2002) Data Sets – Prepared by MMS, 2008 [85]

Parameter	GIS
Dates surveyed	1995–1998
Repetitive mapping used	Yes
Total number of gouges recorded	836
Seabed soil type identified	No
Gouge depths recorded	Yes
Gouge width recorded	Yes
Gouge widths recorded at the Northstar Site	120
Total number of gouges recorded at the Liberty Site	187

The MMS (2008) recommended a division of the area of study in the U.S. Beaufort Sea into four zones (A, B, C, and D). Each zone has its own distinctive environmental conditions and surface texture. The potential hazard for each zone was reported as a function of the bathymetry of each zone. Figure 5.7 shows the proposed zones as reported by MMS (2002).

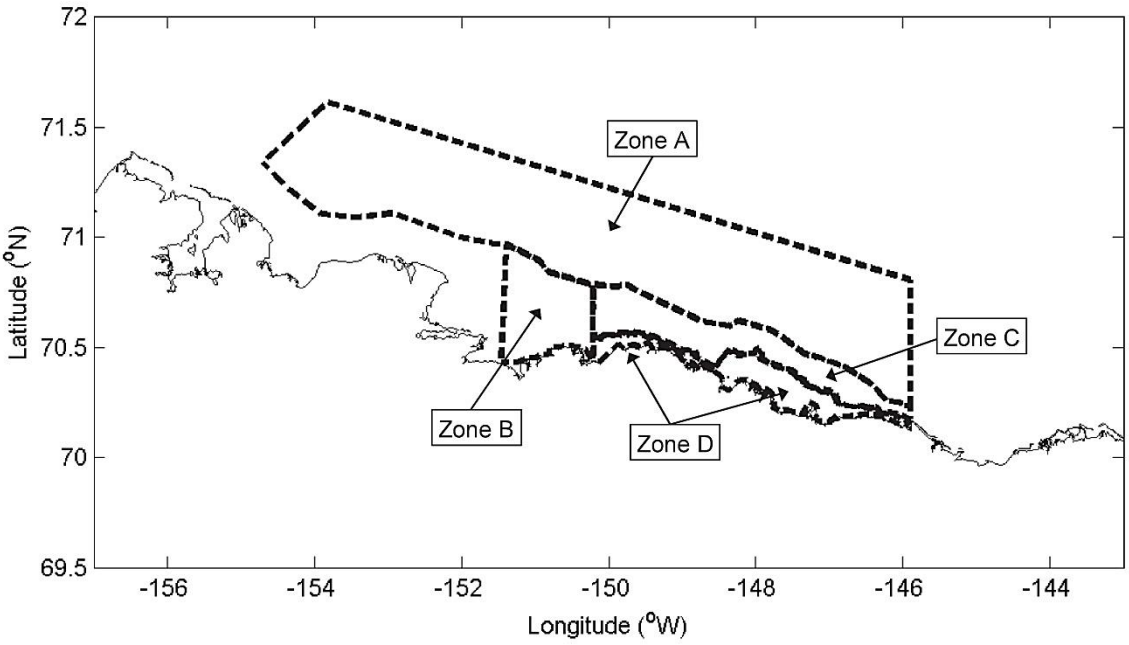

Figure 5.7: Beaufort Sea Case Study Zones (MMS, 2002 [83])

The zones can be summarized as follows:

- Zone A is the largest of the four zones. It represents the outer limits of the continental shelf. Water depth is 60 to 180 ft. (15 to 55 m). The surface soil is primarily soft to stiff clay. Zone A has high ice gouging probability.
- Zone B is located at the north of the Colville River. Soft soils are prevalent throughout this zone. Water depth is relatively shallow, which may attract ice gouging during freeze–up and thaw.
- Zone C consists of mainly dense sand or gravel. Water depth is 60 to 120 ft. (18 to 37 m). Because of the relatively shallow water depth, gouging frequency is between medium and low.
- Zone D is located between the shallow water between the barrier islands and the shoreline. Barrier islands protect the zone from ridge movement. Figure 5.7 shows that Zone D comprises two contiguous sub–zones, which are named D1 and D2.

Table 5.3 lists a summary of the basic characteristics of each zone.

Table 5.3: Environmental Parameters for Beaufort Sea Case Study Zones (MMS, 2008 [85])

Zone	Soil Type	Ice Gouging Frequency
A	Soft to stiff clay 2.90 to 14.50 psi (20 to 100 kPa)	High
B	Soft clay 1.45 to 4.35 psi (10 to 30 kPa)	Low to Medium
C	Dense sand and gravel 40° to 45° (friction angle)	Low to Medium
D	Soft to stiff clay 2.90 to 14.50 psi (20 to 100 kPa)	Low

In addition to the U.S. Beaufort Sea study zones, MMS (2008) [85] provided location maps for the track lines associated with the data set in relation to the specified zones as tabulated by Rearic and McHendrie (1983). These track lines are shown in Figure 5.8. Figure 5.9 shows an additional location map, which was prepared for the repetitive mapping surveys collected from the nine sites based on the tabulated data of Weber et al. (1989).

To understand the significant differences between the available data sets, MMS (2008) conducted a comparison between Rearic and McHendrie (1983) [111] and Weber et al. (1989) [129] data sets as shown in Table B–4. The number of miles (kilometers) surveyed, as well as the total number of gouges recorded, were tabulated separately for each zone. There was no available data for Zone D in the Weber et al. (1989) data set.

The study found clear discrepancies for Zone A data in total gouges recorded, which may be a result of the difference in the surveyed water depths of 30 to 180 ft. (9 to 55 m) versus 50 to 100 ft. (15 to 30 m), and the length of the track line of 370 mi (595 km) versus 10 mi (16 km). Refer to Table 5.3 for the environmental parameters of Zones A through D.

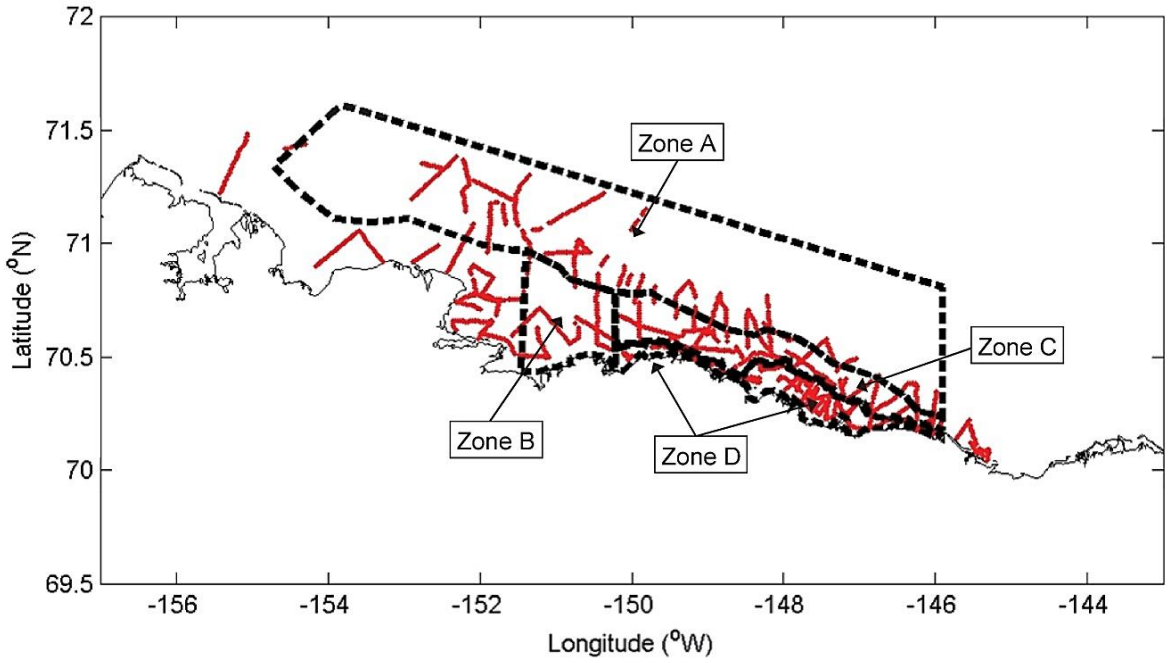

Figure 5.8: Track Lines (Rearic and McHendrie, 1983 [111]) – MMS, 2008 [85]

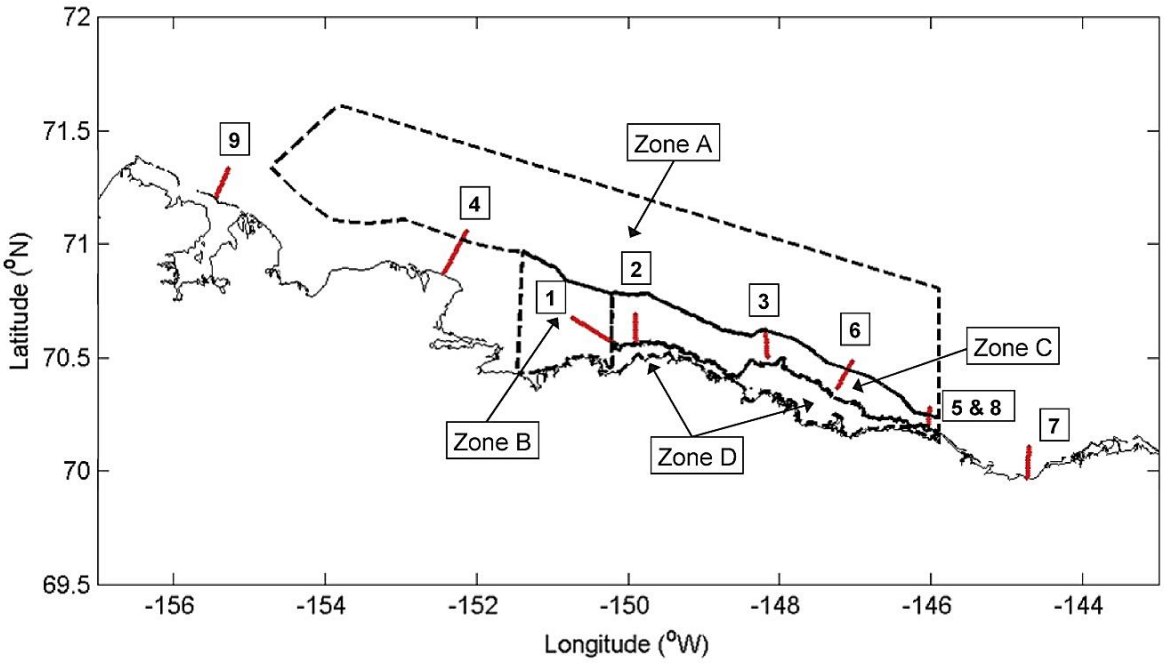

Figure 5.9: Surveyed Corridors (Weber et al., 1989 [129]) – Modified by MMS, 2008 [85]

5.3 Analysis of Data in the Beaufort Sea

This section presents the analyses of data sets and correlations that can be made with respect to ice gouge characteristics (width, depth, and crossing density). MMS (2008) provided a comprehensive statistical analysis of Rearic and McHendrie (1983) and Weber et al. (1989) data sets. The gouge data in each data set were first categorized in four location zones (A, B, C, and D) and classified according to water depth. Later, probability distributions were fitted, focusing on the parameters of interest such as gouge depth, gouging width, crossing density and crossing frequency.

5.3.1 Gouge Depth

5.3.1.1 Rearic and McHendrie (1983)

To allow for the application of distribution functions, MMS (2008) [85] tabulated the data provided by Rearic and McHendrie (1983) [111] for 0.65 ft. (0.2 m) depth intervals and selected a midpoint value for each gouge interval. Therefore, scatter plots in the MMS work have a banded figure. Gouge depth falls within +/– 0.1 m of the tabulated value.

Table B–4 presents the Rearic and McHendrie (1983) data as tabulated in the MMS (2008) report. A total of 24,481 gouges were listed, with Zones A, B, C, and D containing 18,392; 857; 5,204; and 28 gouges, respectively. The deepest gouge for all of the zones, which was 12.8 ft. (3.9 m) deep, occurred within Zone A in the 115–164 ft. (35–50 m) water depth region. The mean value of the gouge depth is 1.6 ft. (0.5 m), which is relatively shallow, but it is comparable to the mean value of gouge depth for each zone.

Rearic and McHendrie performed statistical analysis for each water depth separately and assumed an exponential distribution for each water depth set of data. They calculated maximum gouge depth, mean value, standard deviation, and decay function. The tabulated data represents a useful guide during design processes. An exponential distribution for each water depth or zone of interest may be used if a more conservative approach is adopted during the design phase. Figure 5.10, Figure 5.11, Figure 5.12, and Figure 5.13 show scatter and distribution plots for the four zones.

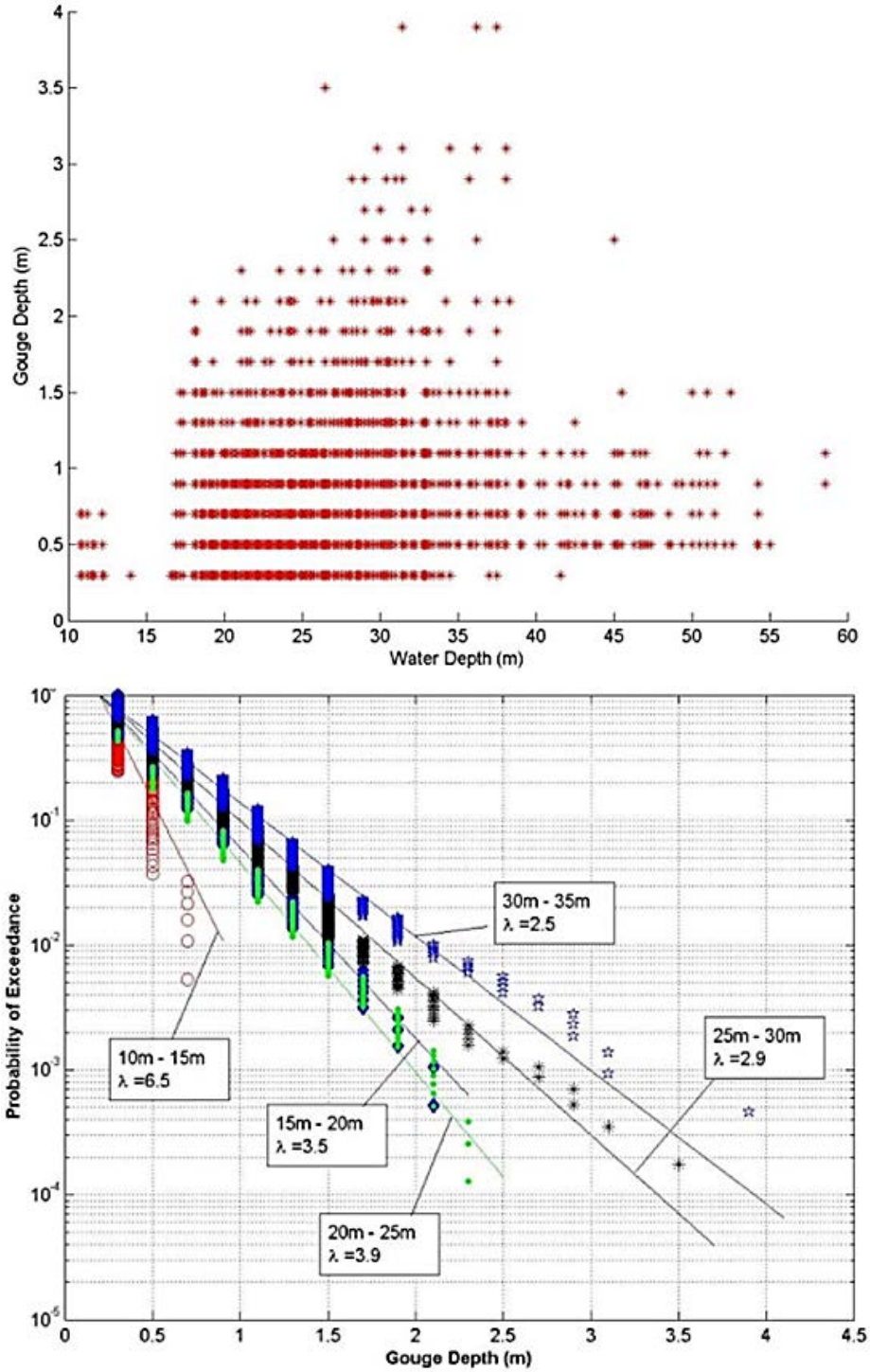

Zone A

Figure 5.10: Gouge Depth Summary (Rearic and McHendrie, 1983 [111]) – MMS, 2008 [85]

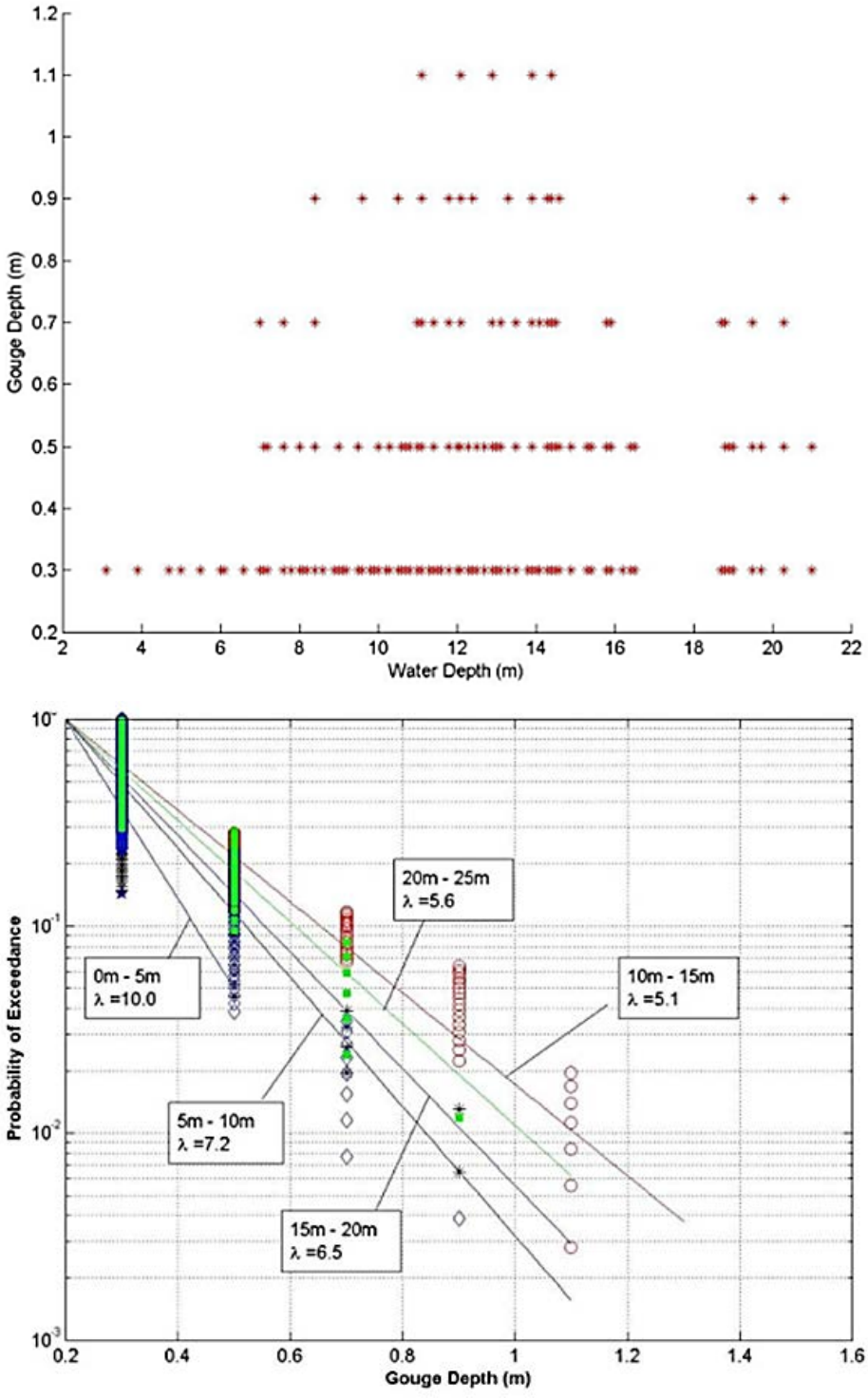

Zone B

Figure 5.11: Gouge Depth Summary (Rearic and McHendrie, 1983 [111]) – MMS, 2008 [85]

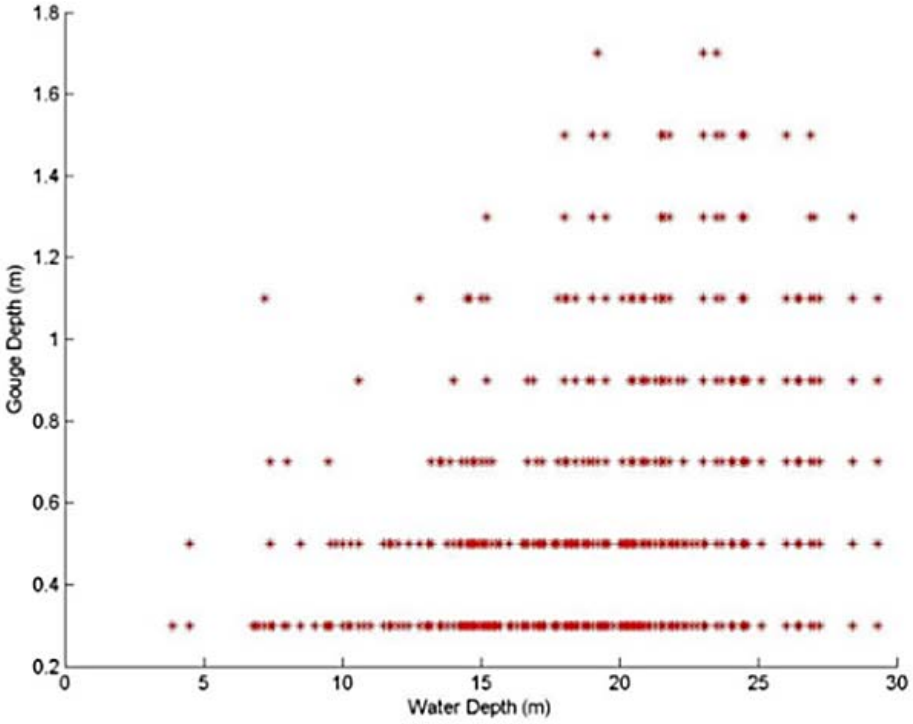

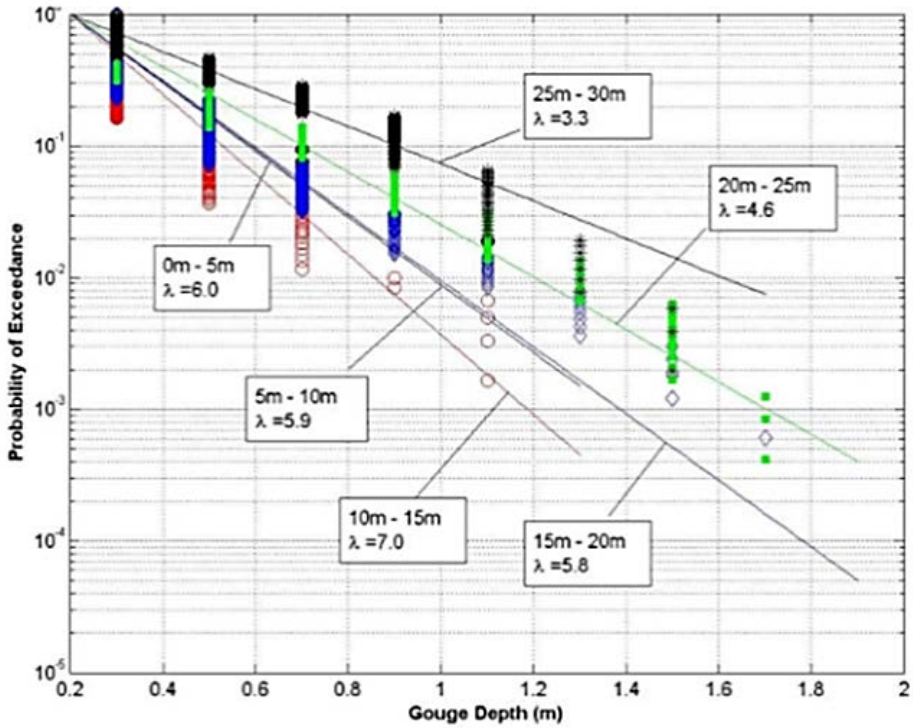

Zone C

Figure 5.12: Gouge Depth Summary (Rearic and McHendrie, 1983 [111]) – MMS, 2008 [85]

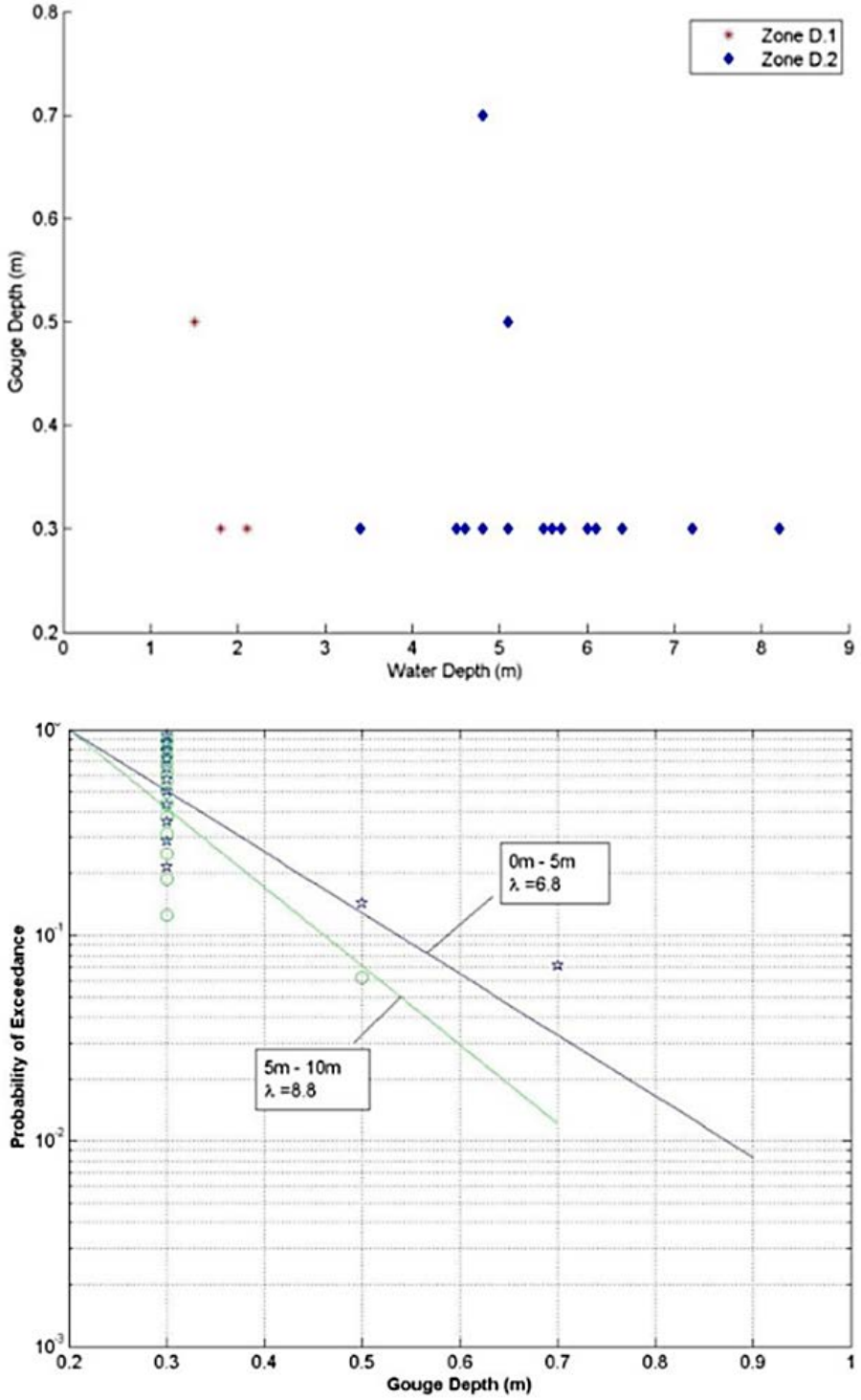

Zone D

Figure 5.13: Gouge Depth Summary (Rearic and McHendrie, 1983 [111]) – MMS, 2008 [85]

5.3.1.2 Weber et al.(1989)

MMS (2008) [85] compiled the gouge data published by Weber et al. [129] in 1989 into a report. Table B–5 summarizes this gouge data as MMS presented it. Totals of 48 single gouges and 38 multiple gouges were observed for all of the zones. The authors noted that the gouge data set population may not have been as comprehensive as the data set provided by Rearic and McHendrie (1983) [111].

The deepest single gouge is within Zone B, in the 33–49 ft. (10–15 m) water depth interval. In general, Zone B was relatively shallow, with water depths of 16.4–65.6 ft. (5–20 m). Only 27 single gouges were identified in Zone B. The deepest single gouges for Zones A and C were less than 1.6 ft. (0.5 m) and 4.6 ft. (1.4 m), respectively. The mean gouge depth for all of the zones falls within a comparable range of 1.0 ft. (0.3 m) to 1.64 ft. (0.5 m). This mean depth may be considered an indication of homogenous gouge depths, excluding some extreme events.

Data for multiple gouges is summarized in Table B–6. The deepest gouge depth, which was 9.8 ft. (3 m), was found in Zone C in the 33–49 ft. (10–15 m) water depth. The mean value and standard deviation for Zone C were calculated using a set of only five gouges. The standard deviation was 3.9 ft. (1.2 m), which was much higher than the standard deviation for Zones A and B, which were 1.0 ft. (0.3 m) and 0.32 ft. (0.1 m), respectively. The analysis for the complete data set indicated that the mean and the standard deviation (38 gouges) were 1.6 ft. (0.5 m) and 1.6 ft. (0.5 m), respectively. Weber and co–workers recommended additional surveys to increase the population of gouges and to improve the prediction of distribution parameters (mean and standard deviation). Figure 5.14 shows the scatter plots for the three zones.

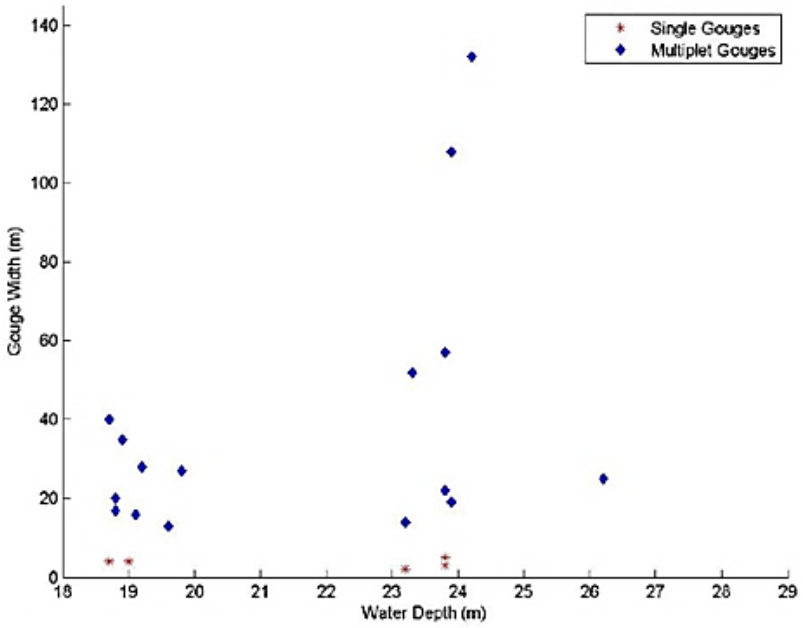
Single Gouges
Multiplet Gouges
Gouge Width (m)
Water Depth (m)
0
20
40
60
80
100
120
140
18
19
20
21
22
23
24
25
26
27
28
29

Zone A

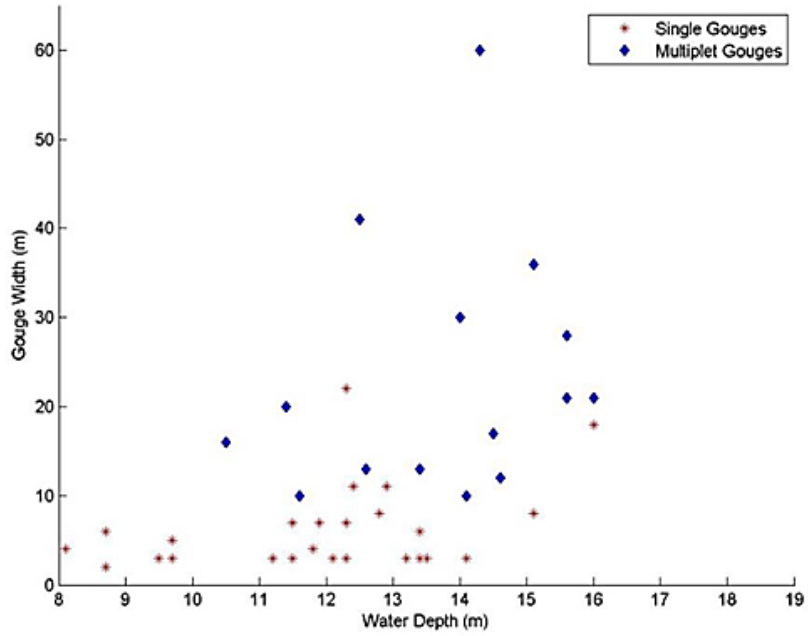
Single Gouges
Multiplet Gouges
Gouge Width (m)
Water Depth (m)
0
10
20
30
40
50
60
8
9
10
11
12
13
14
15
16
17
18
19

Zone B

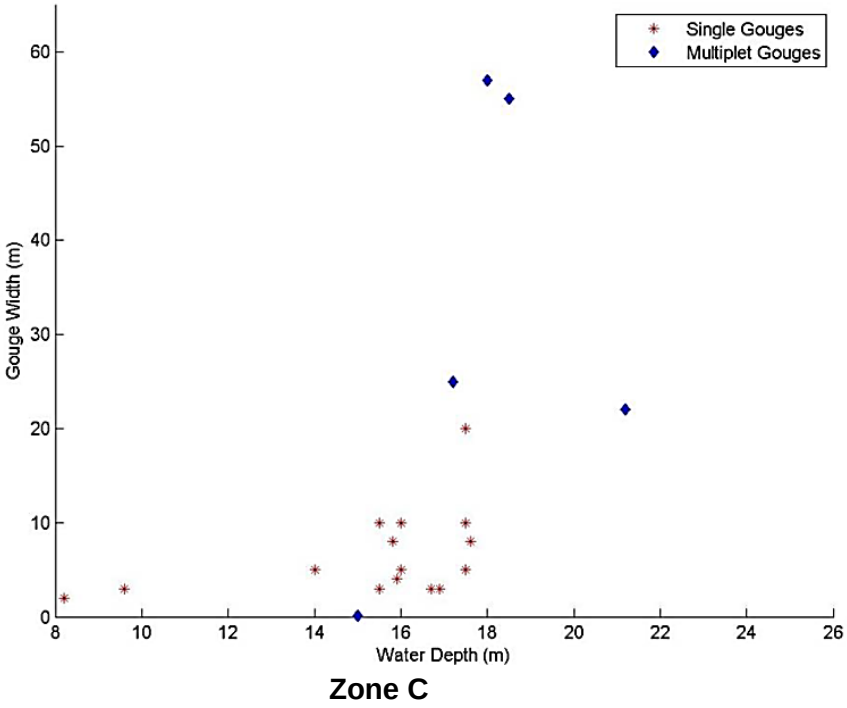

Figure 5.14: Gouge Width Data (Weber et al., 1989 [129]) – MMS, 2008 [85]

5.3.2 Gouge Width

Early analyses focused on gouge depth and considered gouge width to be of secondary importance. As a result, gouge widths were either not reported, or only maximum gouge widths were noted, as in Rearic and McHendrie, 1983 [111].

The general trend is that deeper gouges tend to be wider; conversely, wide gouges are not necessarily the deepest.

5.3.2.1 Rearic and McHendrie (1983)

Rearic and McHendrie (1983) [111] provided a gouge database that tabulated the gouge depths over a wide seabed area. The data set provided the maximum gouge depth for each segment. Unfortunately, the data set did not accurately describe the width of the gouges, and the authors made no distinction between single and multiple gouges Therefore, MMS (2008) reported that the data may not be sufficient for further analysis. However, the data may still be used as an indication of possible gouge widths.

5.3.2.2 Weber et al. (1989)

Weber et al. [129] lists 48 single gouges and 38 multiple gouges, along with gouge width information. MMS (2008) analyzed this data set.

The data for single gouge widths are listed in Table B–7. The data set is categorized for each zone and is divided into depth intervals. The maximum observed width, which is 72.18 ft. (22 m) wide, occurs within Zone B at the 33–49 ft. (10–15 m) water depth interval. Mean value and standard deviation for the entire set are 19.7 ft. (6 m) and 13.12 ft. (4 m), respectively. Most of the gouge depths fall into Zones B and C, which are relatively shallower in depth than Zone A (approximately 88%). In addition, the widths of the gouges in Zones B and C are wider than those in Zone A. Therefore, it may be concluded as a general guideline that an iceberg passing through Zones A, B, and C is wide and shallow. Therefore, the iceberg is captured in the shallow water zones (Zones C and D).

MMS followed the same procedure of analysis for the multiple gouge widths presented in Table B–8, which lists 38 gouges. The maximum gouge widths identified in Zones C and D are 197 ft. (60 m) and 187 ft. (57 m), respectively. The mean values for Zones A, B, and C are 128, 75, and 104 ft. (39, 23, and 32 m), respectively. The average gouge width for the entire width is 31 m. The maximum observed gouge width is 433 ft. (132 m) wide at Zone A, which is six times wider than the maximum width from a single gouge of 72.18 ft. (22 m).

5.3.3 Crossing Density

The data set provided by Rearic and McHendrie, 1983 [111] includes extensive information about the gouge dimensions and locations, although the age of the gouges is unknown. Therefore, a crossing density (mile–1 or km–1) was calculated for each length segment within each zone.

Zone A contained 309.5–mile (498–kilometer) intervals with a maximum crossing density of 237 gouges per mile (147 gouges per kilometer) in a water interval of 65.62–82.01 ft. (20–25 m). There was an average of 60 gouges per mile (37 gouges per km) for the entire zone, with a standard deviation of 59 gouges per mile (35 gouges per km).

Zone B contained 89.48–mile (144–kilometer) intervals with a maximum crossing density of 105 gouges per mile (65 gouges per km) in a water depth of 49.21–65.62 ft. (15–20m). An average of 10 gouges per mile (6 gouges per km) and a standard deviation of 15 gouges per mile (9 gouges per km) were calculated for Zone B.

Zone C contained 243–mile (391–kilometer) intervals with a maximum crossing density of 208 gouges per mile (129 gouges per km) in a water depth range of 65.62–82.01 ft. (20–25m). An average crossing density of 21 gouges per mile (13 gouges per km) and a standard deviation of 39 gouges per mile (24 gouges per km) was also calculated.

MMS, 2008 [85] also investigated the crossing densities using the data provided by Weber et al., 1989 [129]. MMS counted multi–keel events as one event for consistency with other sources.

Table B–9 lists the gouge depths for each zone and categorizes them based on the water depth interval of occurrence. The number of gouges, mean crossing density, maximum crossing density, and standard deviations are listed for each water depth interval.

Zone A contained 10.56–mile (17–kilometer) intervals, with a maximum crossing density of 432 gouges per mile (268 gouges per km) at a water depth of 65.62–82.02 ft. (20–25 m). Mean crossing density and a standard deviation of 198 gouges per mile (123 gouges/km) and 87 gouges per mile (54 gouges/km), respectively, were calculated.

Zone B contained 54.06–mile (87 kilometer) intervals with a maximum crossing density of 275.3 gouges per mile (171 gouges per km) at a water depth of 32.81–49.21 ft. (10–15 m). An average crossing density of 106.3 gouges per mile (66 gouges per km) and a standard deviation of 64.4 gouges per mile (40 gouges per km) were also calculated for the entire zone.

Zone C contained 66.49–mile (107–kilometer) intervals with a maximum crossing density of 213 gouge per mile (132 gouges per km) recorded at a water depth of 49.21–65.62 ft. (15–20 m). Also calculated were a mean of 38.6 gouges per mile (24 gouges per km) and a standard deviation of 46.7 gouges per mile (29 gouges per km) (MMS 2008).

A direct comparison of the crossing densities for Rearic and McHendrie (1983) and Weber et al. (1989) is not possible because of the constraints associated with the original data sets. Rearic and McHendrie (1983) used a gouge depth cut–off of 0.66 ft. (0.2m), while Weber et al. (1989) used a gouge cut–off of 0.33 ft. (0.1m).

Rearic and McHendrie (1983) also counted all the keels of a multiplet as a single event. With the combination of known and unknown gouges of Weber et al. (1989), each keel of a multiplet was counted as an individual event. This could lead to an over–estimation of the number of gouges recorded in each zone.

5.3.4 Crossing Frequency

The MMS (2008) report investigated crossing frequency in the Beaufort Sea using available data sets. The data set prepared by Rearic and McHendrie (1983) [111] did not contain information on the age of the gouges. As a result, the MSS performed a crossing frequency calculation using only the data set provided by Weber et al. (1989) [129].

Zone A contained only two repetitively–mapped kilometer intervals with crossing frequencies of about one gouge per kilometer per year in a water depth of 49.21–65.62 ft. (15–20 m).

Zone B contained 83 repetitively mapped intervals in which a maximum crossing frequency of 4.8 gouges per mile per year (3 gouges per km per year) was recorded in a water depth of 32.81–49.21 ft. (10–15m). An overall zone crossing frequency mean and standard deviation was calculated as 0.8 gouge per mile per year (0.5 gouges per km per year) and 1.29 gouge per mile per year (0.8 gouges per km per year), respectively.

Zone C contained 50.33–mile (81–kilometer) repetitively mapped intervals with a maximum crossing frequency of 9.7 gouges per mile per year (6 gouges per km per year) in a water depth of 49.21–65.62 ft. (15–20 m). A mean of 0.32 gouges per mile per year (0.2 gouges per km per year) and a standard deviation of 1.29 gouges per mile per year (0.8 gouges per km per year) was calculated for this zone.

5.4 Surveys in the Chukchi Sea

This section describes in detail the findings of a field survey conducted in 1974 by members of the Office of Marine Geology of the U.S. Geological Survey in cooperation with the U.S. Coast Guard aboard the U.S.S. Burton Island. Since this survey, no repetitive mapping has been performed. The ages of the gouges were not identified, and the study was limited to the general trend of gouging in the Chukchi Sea.

Toimil (1978) [124] studied ice gouging using the data obtained from the side–scan sonar and bathymetric measurements that were performed during the 1974 field operations. The study reports that furrow–like linear depressions produced by ice gouging of the seabed were noticed along the track lines. The general texture of the seabed was significantly disturbed by single and multiple gouging events. Side–scan sonar studies were conducted over 96,500 square miles (approx. 250,000 sq km) of the Chukchi Sea. Figure 5.15 shows this area of study.

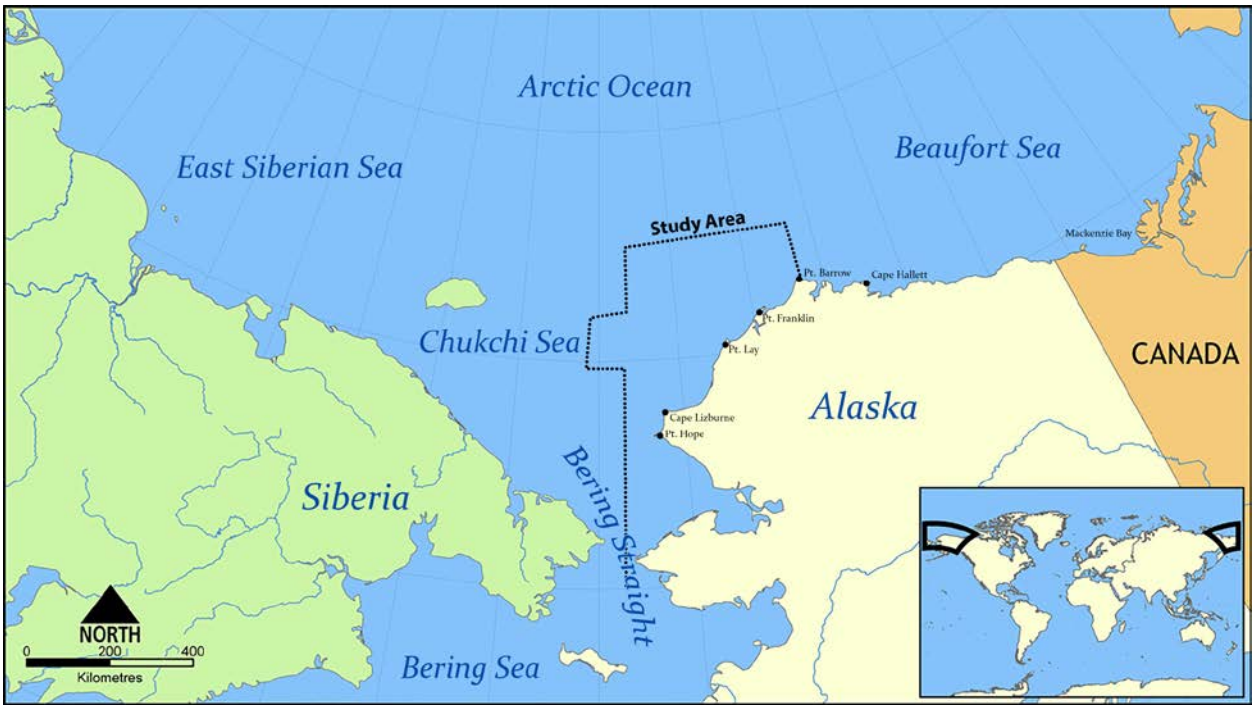

Figure 5.15: Area of Study (Toimil, 1978 [124])

Tomil analyzed survey data to locate ice gouging in the seabed and performed surveys for 1,118 miles (1,800 km) of track line at the eastern Chukchi Sea continental shelf. He identified a large number of individual gouges (10,200) in water depths between 66 and 230 ft. (20 and 70 m). The author also examined gouges to identify potential future gouge orientation, incision depth, width, and relative abundance over the shelf.

Toimil (1978) [124] indicated that the general dominant ice gouge drift is parallel to the bathymetric contours that are shown in Figure 5.16. This is consistent with the sea current that is moving west to east.

Figure 5.17 presents the location of side–scan sonar track lines, as determined by satellite navigation fixes, which were taken by the U.S. Burton Island and are considered accurate within about 0.3 mile (0.5 km).

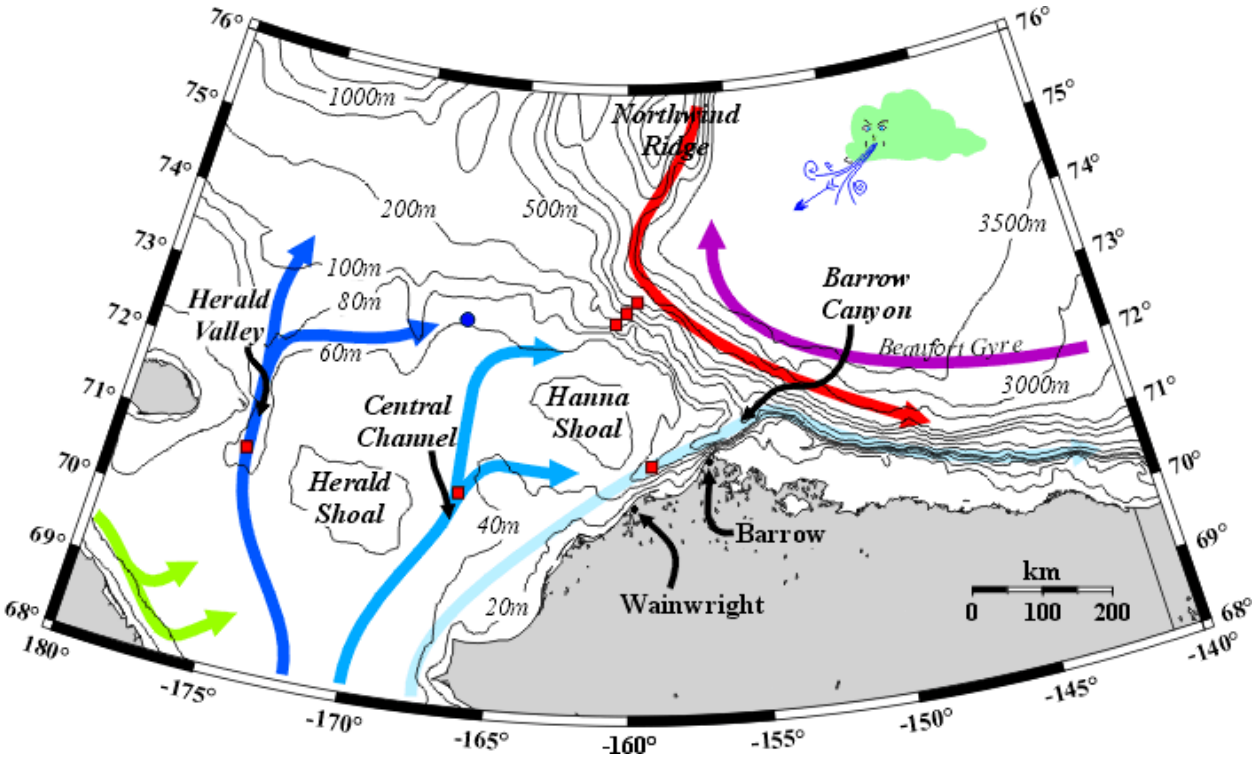

Figure 5.16: Bathymetric Data and Circulation Features [125]

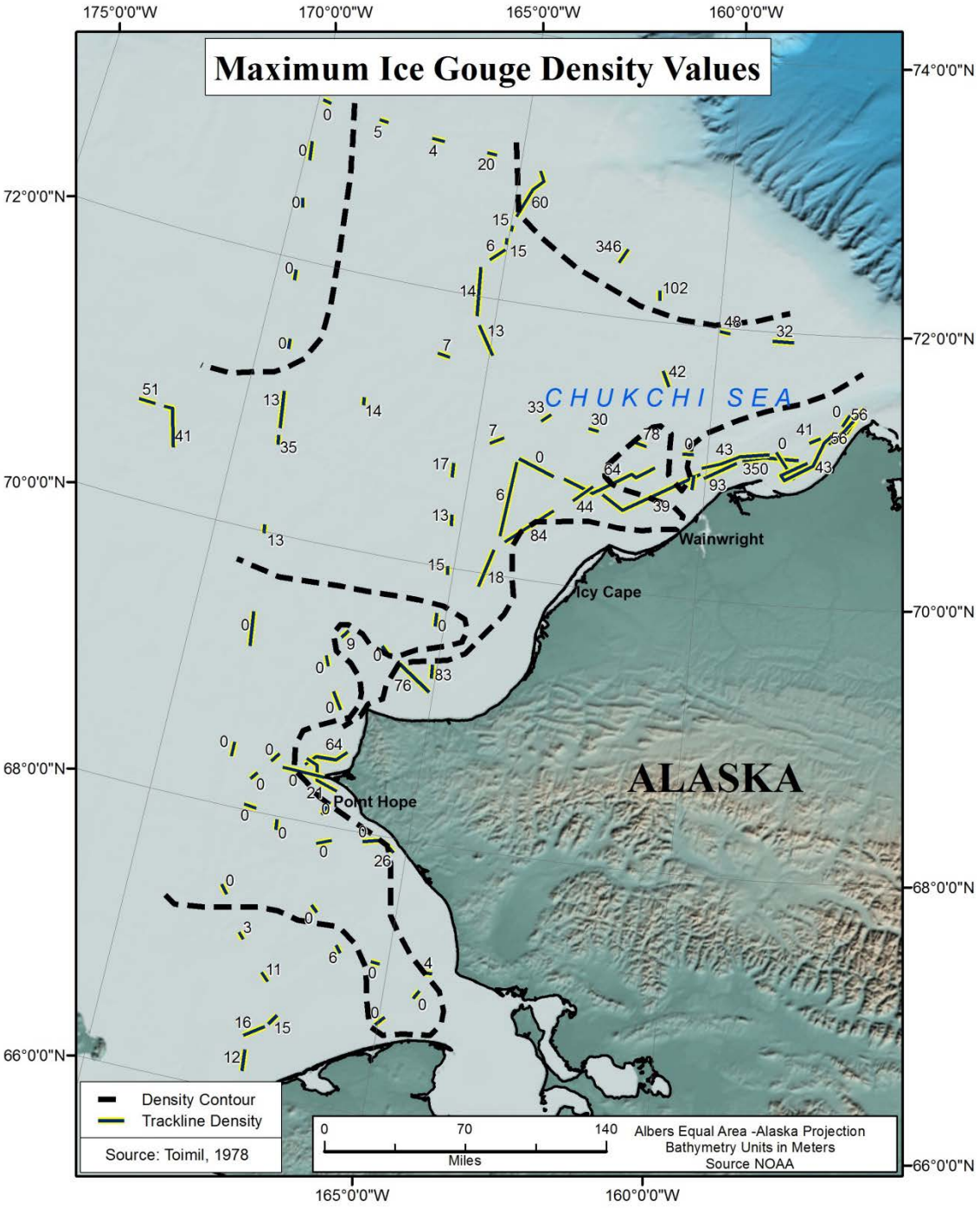

Figure 5.17: Maximum Ice Gouge Density Values over Complete Trackline Segment (Toimil, 1978 [124])

Figure C–1 shows normalized maximum ice gouge mean ice gouge density values plotted over 1–m water depth intervals (Toimil, 1978 [124])

The analysis of survey data shows that the maximum gouge incision depth per kilometer of track line is greatest in water depths between 115 and 164 ft. (35 and 50 m). The maximum noticed incision depth is equal to 14.7 ft. (4.5 m) in the 115 to 164 ft. (35 to 50 m) water depth interval. Tomil identified gouges with depths of 6.6 ft. (2.0 m) in the 69 to 82–ft. (21 to 25–m) water depth intervals. A summary of data, which has been added to Table 5.4, presents a summary of ice gouge densities.

Table 5.4: Summary of Ice Gouge Densities

Water Depth Interval		Max. Ice Gouge Densities		Max. Gouge Depth		Gouge Width	
ft.	m	per mile	per km	ft.	m	ft.	m
68.9–114.82	21–35	124.27	200	14.76	4.5	NA	
118.11–147.64	36–45	NA		NA		> 328.08	> 100
183.73	< 56	6.21	10	3.28	1	NA	
190.29	< 58	None		None		None	

5.5 Analysis of Data in the Chukchi Sea

The MMS (2008) [85] report used the data provided in Toimil (1978) [124] to perform statistical analyses of the ice gouging probabilities to estimate the depth and width of the gouges. The report recommends dividing the Chukchi Sea into three main zones based on environmental conditions such as hazard regime. The MMS studied ice gouges for each zone because each had its own characteristics (e.g., bathymetry, soil, location).

Figure 5.18 shows the three recommended zones:

- Zone A – The first zone, which is the largest area among the three studied areas, represents the seabed of the Chukchi Sea, which is relatively shallow. Water depth in Zone A varies from 98 to 197 ft. (30 to 60 m). Surficial sediments are generally sand and gravel overlaying stiff consolidated clay or dense sand. MMS (2008) [85] reported significant ice gouging in Zone A.

- Zone B – This zone represents the Herald and Hanna Shoals, which are located within Zone A. The bathymetry of the shoals rises up to 131 ft. (40 m) from the surrounding seafloor. At some locations on the shoals, the bathymetry has a maximum height of 82 ft. (25 m). Shoals serve as barriers that protect the seabed from iceberg gouging.
- Zone C – The third zone is the near–shore shallow water with a water depth less than 98 ft. (30 m) and a low rate of ice gouging.

Table 5.5 summarizes soil types/condition and ice gouging frequency, as the MMS (2008) [85] reported for each zone.

Figure 5.18 provides the location of track lines used in the Toimil (1978) study and the study zones as proposed by MMS (2008). A summary of the data set is listed in Table B–10 and Table B–11.

Table 5.5: Environmental Parameters for Chukchi Sea Case Study Zones (MMS, 2008 [85])

Zone	Soil Type	Ice Gouging Freq.
A	Stiff clay 14.50 to 29 psi (100kPa – 200 kPa) and dense sand 40° to 45°	High
B	Stiff clay 14.50 to 29 psi (100–200 kPa) and dense sand 40° to 45°	Low to Medium
C	Dense sand and gravel 40° to 45°	Medium

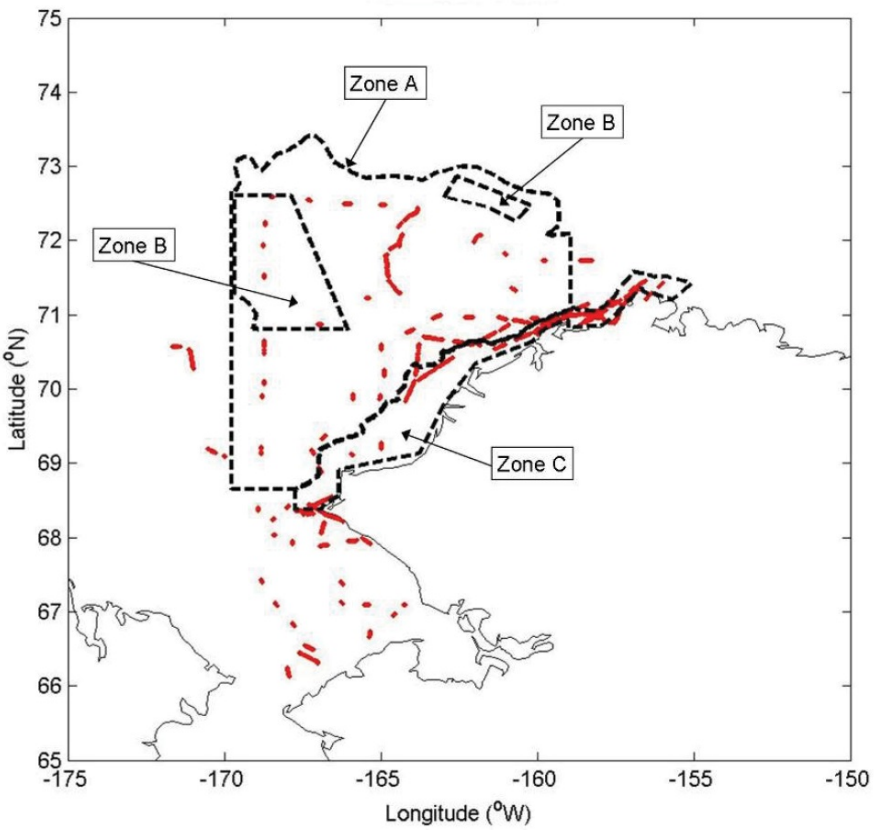

Figure 5.18: Chukchi Sea Case Study Zones (MMS, 2008 [85])

5.5.1 Gouge Depth

In Zone A, which is relatively shallow with a water depth between 98 and 197 ft. (30 to 60 m), 219 gouges were studied. The deepest gouge depth observed was 14.7 ft. (4.5 m), which was recorded within a water depth interval of 115 to 131 ft. (35 to 40 m). Figure 5.19 shows a log–normal distribution, which was recommended for the data set. The calculated mean and standard deviation for the entire zone are 2.6 ft. (0.8 m) and 2 ft. (0.6 m), respectively. The lack of sufficient data limited the usefulness of the proposed distribution. After reviewing Table B–3, the conclusion is that approximately 75% of the gouges occur at a depth interval of 98 to 164 ft. (30 to 50 m). The data can be used to determine the general trend of gouge depth, but with a limited level of confidence.

To understand the general trend of gouging near shore, the gouges in Zone C were investigated. The maximum identified depth was 16.4 ft. (5 m). The observed mean gouge depth was 2.6 ft. (0.8 m). Approximately 83% of the gouges occurred at depth intervals between 98 and 164 ft. (30 and 50 m). The average observed gouge depth was

2.4 ft. (0.73 m). The combined analysis of Zone A and Zone C indicates that approximately 90% of the gouges (out of 494 total gouges) occurred between water depth intervals of 98 and 164 ft. (30 and 50 m).

Figure 5.19 and Figure 5.20 show an analysis gouge depth as prepared by the MMS.

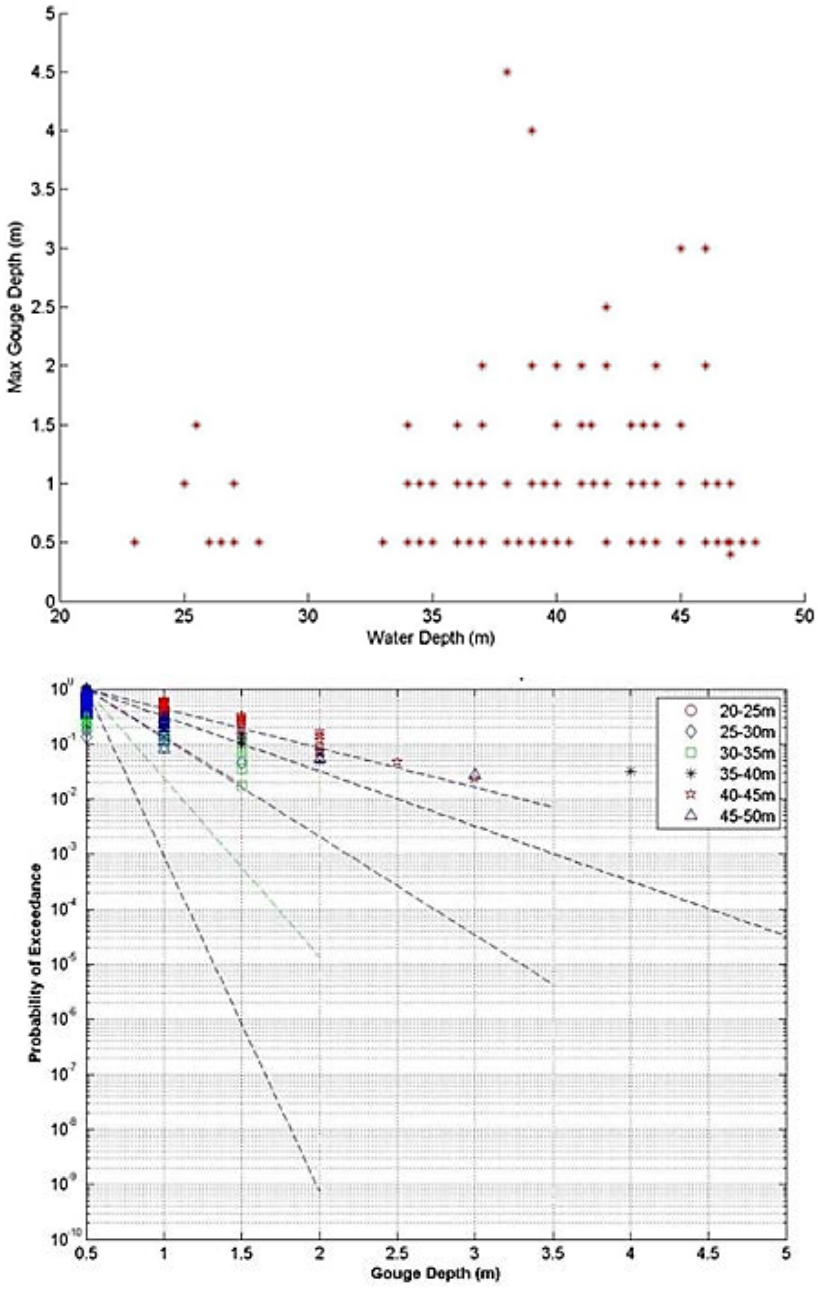

Zone A

Figure 5.19: Analysis of Toimil, 1978 [124] Gouge Depth Data as Prepared by MMS, 2008 [85]

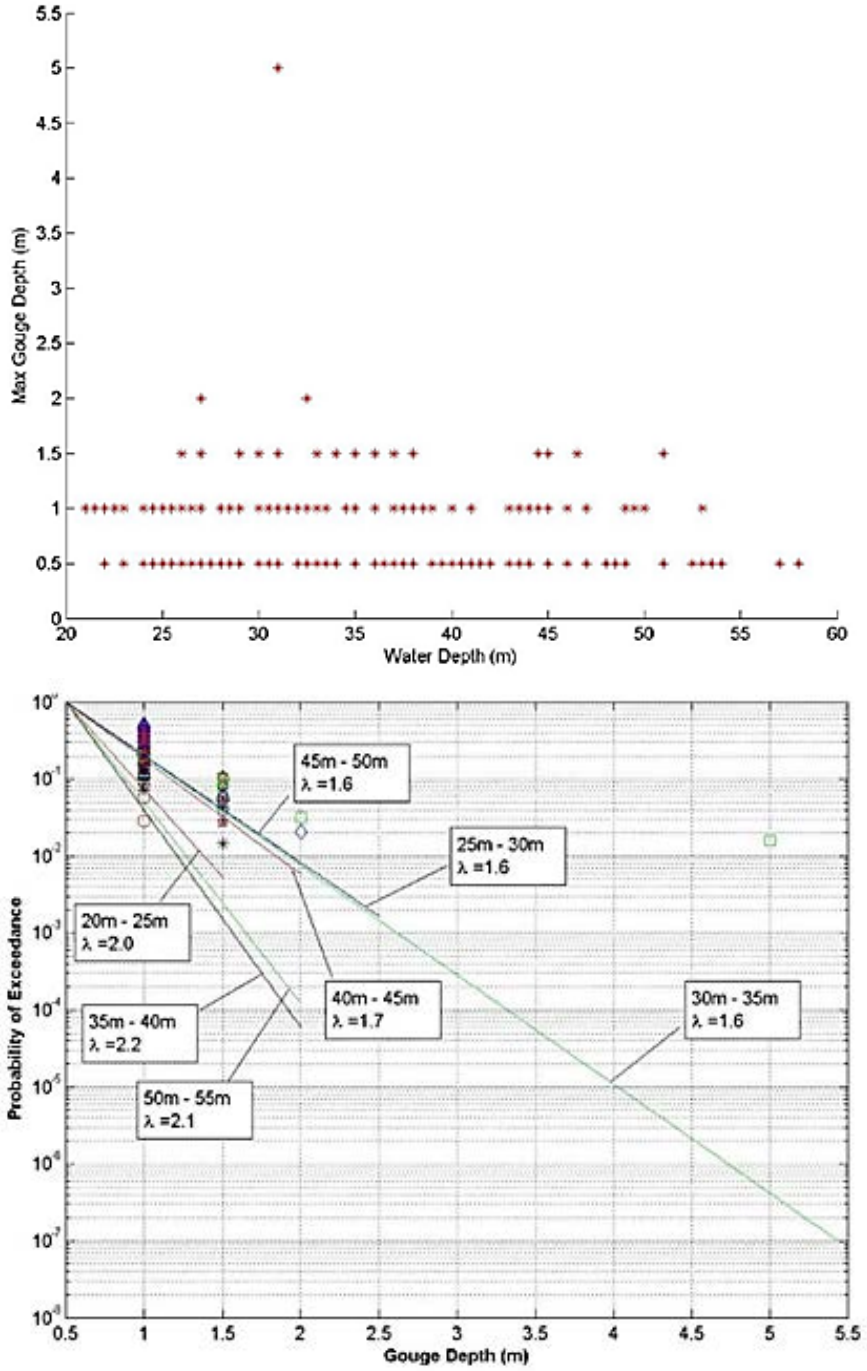

Zone C

Figure 5.20: Analysis of Toimil, 1978 [124] Gouge Depth Data as Prepared by MMS, 2008 [85]

5.5.2 Gouge Width

Similar to the gouge depth analysis in Section 0, MMS (2008) analyzed a set of data that described the gouge width as presented in Toimil (1978). (Table B–12 presents a summary of gouge widths as reported by Toimil.) MMS lists the maximum gouge width for each tracking line segment; the tabulated data also lists whether gouges are single or multiple. Gouge widths are estimated and include a conservative margin of error. The MMS summarized the data in 2008.

MMS (2008) [85] prepared a scatter plot for a set of 86 gouge widths, which were measured in water depth intervals between 82 ft. (25 m) and 165 ft. (50 m) and were identified to fall within Zone A. The analysis found a maximum gouge width of 311 ft. (95 m) in a water depth interval of 115–130 ft. (35–40 m). MMS used a log–normal distribution to fit the gouge width data, and their report states that the distribution match is not definitive because of the lack of data.

The MMS prepared an additional scatter plot using 128 gouge widths in Zone C. A maximum gouge width of 180 ft. (55 m) occurred three times at water depth intervals between 82 and 150 ft. (25 to 46 m). They prepared a log–normal distribution for the data. Zone C had a mean gouge width of 45 ft. (14 m) and a standard deviation of 36 ft. (11 m). The MMS report determined that the lack of sufficient gouge widths data limited fitting the data with high confidence. Figure 5.21 shows the scatter plots for Zones A and C.

The data set provided with the Toimil (1978) report only tabulates the maximum gouge width for each segment; the report makes no reference to a single or multiplet gouge. In Zone A, 86 gouge widths were measured in water depths of 65.62–82.02 ft. (25–50 m). A maximum gouge width of 311.7 ft. (95 m) was measured between 114.83–131.23 ft. (35–40 m) as shown in Figure 5.21, with a zone mean of 105 ft. (32 m) and a standard deviation of 72.18 ft. (22 m). Similar to gouge depths, gouge widths follow more of a log–normal distribution; however, because of the lack of data points, the distribution match is not definitive.

For Zone C, 128 gouge widths were recorded from 65.62–180.45 ft. (20–55 m) water depths. A maximum gouge width of 196.85 ft. (60 m) occurred three times at a water depth of 82.02–147.64 ft. (25–45 m), with a zone mean of 45.93 ft. (14 m) and standard deviation of 36.09 ft. (11 m). Again, because of a lack of data points, it is difficult to fit a distribution with high confidence.

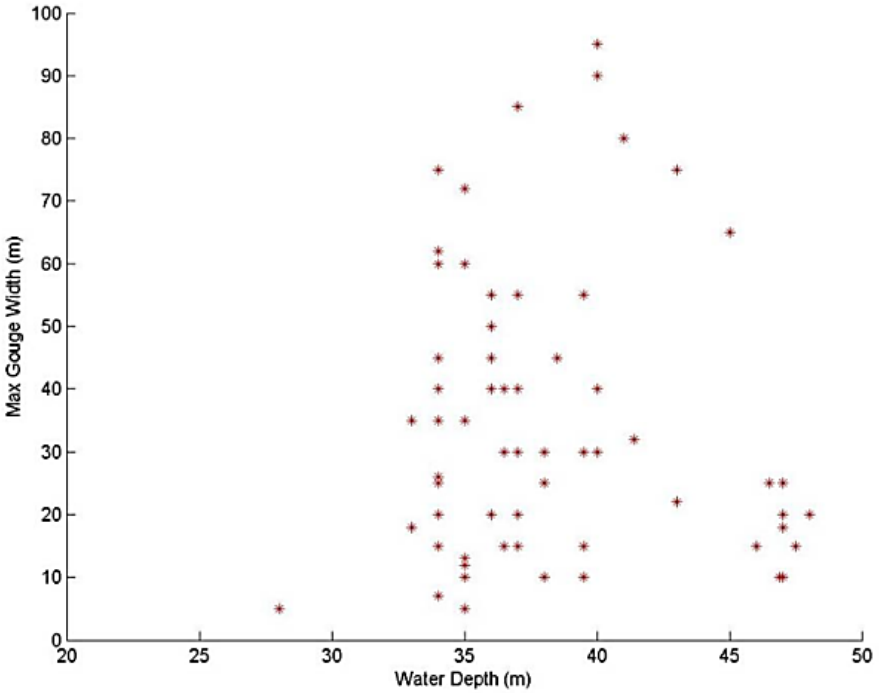

Zone A

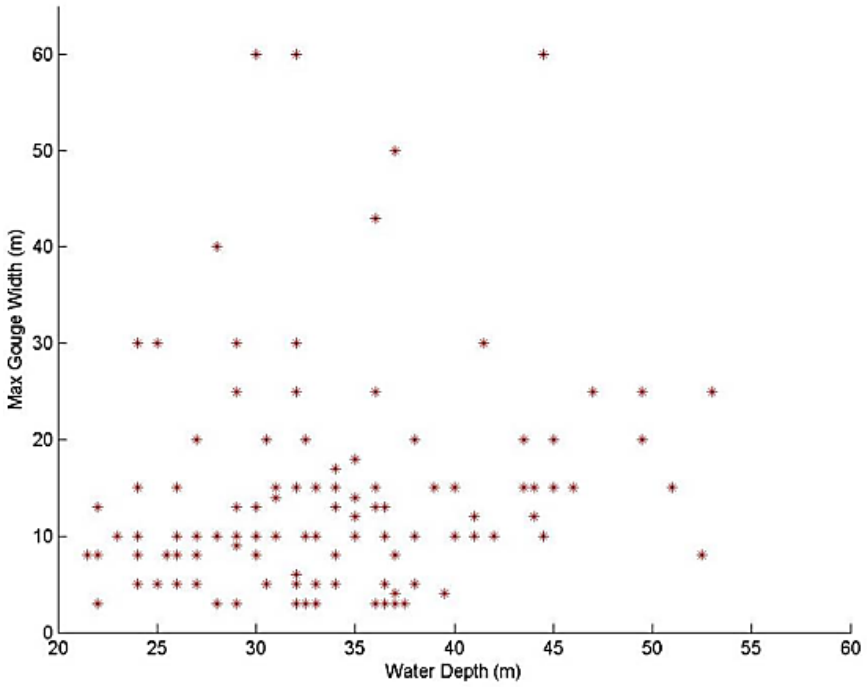

Zone C

Figure 5.21: Analysis of Toimil, 1978 [124] Gouge Width Data as Prepared by MMS, 2008 [85]

5.5.3 Crossing Density

The data tabulated by Toimil (1978) does not include the age of gouges because this information was not collected in the study. Therefore, MMS (2008) estimated the number of gouges/km. (Refer to Table B–13.) Zone A contains 382 intervals with a maximum crossing rate of 140 gouges in a water depth interval of 82–98 ft. (25–30 m). Figure 5.22 shows the scatter plot of the data. The average of the zone is 11 gauges/mi (7.0 gouges per km), and the standard deviation is 25.6 gouges per mile (16 gouges per km). MMS (2008) [85] reported that the crossing density decreases with increasing water depths beyond 98 ft. (30 m); it then becomes nearly constant to a water depth of 164 ft. (50 m).

Obtaining a correlation for Zone B using the available data was not possible. Only 21 intervals were recorded for Zone B, with a maximum crossing density of 5 gouges/mi or 3 gouges/km. During the survey, water depth was not recorded. The mean crossing rate for Zone B is much lower when compared to the other zones. This suggests that the drift direction of the ice is from west to east

A set of 535 intervals, with a maximum crossing rate of 379.2 gouges/mile (237 gouges/km), was noticed for Zone C. The majority of crossings occurred in a water depth range of 115–131 ft. (35–40 m). Figure 5.22 shows a scatter plot of the crossing densities at Zones A and C. Fitting the data to a log–normal distribution shows a mean value of the crossing density that is equal to 18 gouges per mile (11 gouges per km) and a standard deviation of 32 gouges per mile (20 gouges per km).

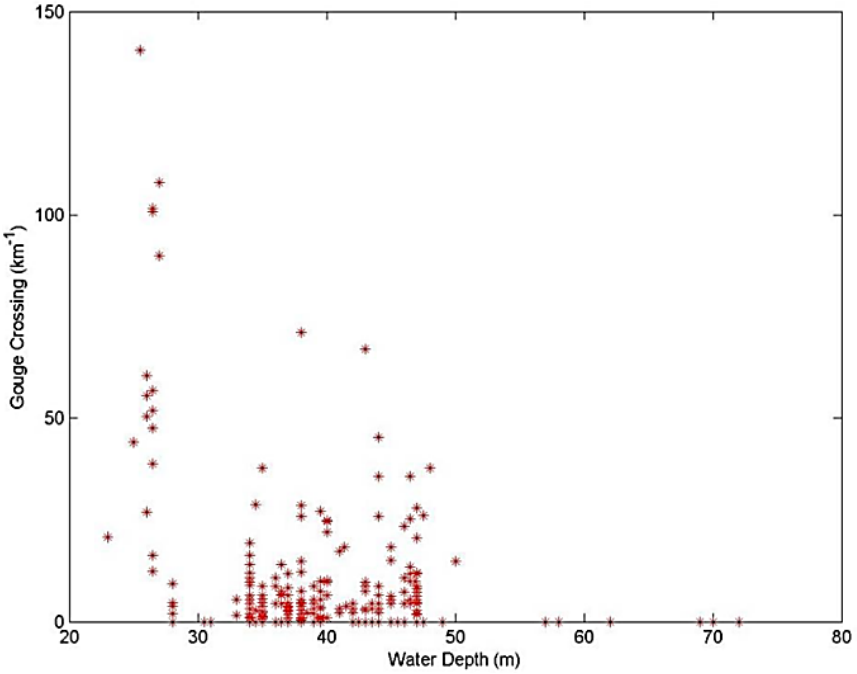

Zone A

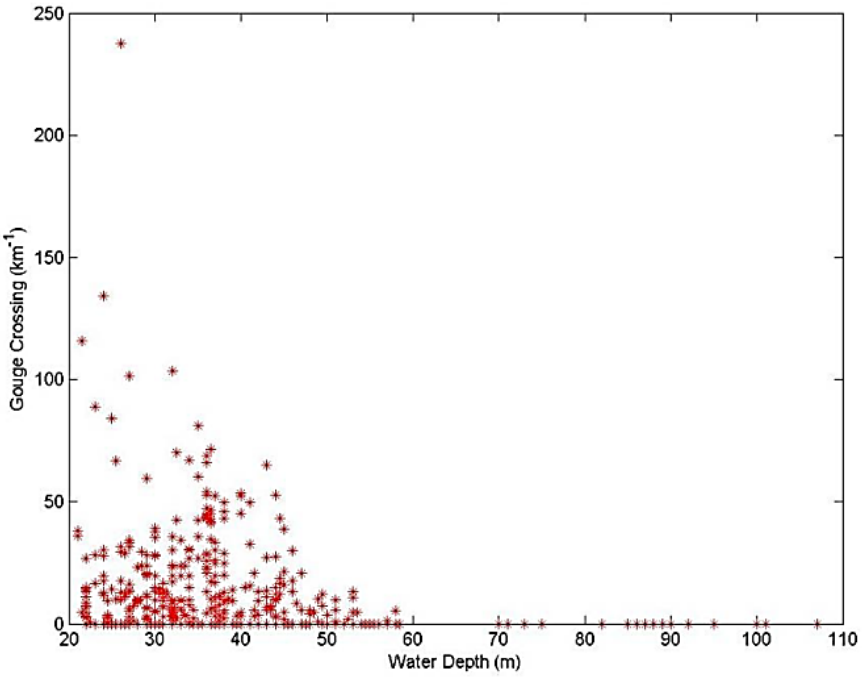

Zone C

Figure 5.22: Analysis of Toimil, 1978 [124] Gouge Crossing Density Data as Prepared by MMS, 2008 [85]

5.5.4 Crossing Frequency

As discussed in the MMS (2008) report, no record has been found of repetitive ice gouge surveying programs conducted in the Chukchi Sea, which has thus led to the scarcity of applicable ice gouge recurrence rate information.

Therefore, in light of the current paucity of regional or site–specific data, American Beaufort Sea ice gouge recurrence rates may be used in Chukchi Sea ice gouge analyses.

5.6 Summary of Findings

Seabed mapping provides an understanding of gouging activity. The information acquired by a single survey includes gouge depth, width, length, orientation, and density. Sediment deposition (called infill) causes a reduction of the measured gouge depth and width. Repetitive mapping helps assess degradation of the recorded characteristics over time. Only repetitive surveys allow the determination of gouging frequency by distinguishing young gouges from old ones.

A common approach is to generate exceedance probability plots and estimate the extreme design parameters at a certain level of risk (i.e., for a given probability of exceedance). This approach considers ice gouge depth data and fitted probability functions while ignoring uncertainties related to the data acquisition process. These uncertainties are related to the detection of gouges and their identified characteristics (e.g., depth). The degradation of gouge marks introduces a non–conservative bias in the design. Additionally, the technology used to perform surveys often has a resolution cut–off range and is sensitive to sea state conditions.

Furthermore, fitting distributions over a wide class range can mask distinct occurrence trends, which can lead to an over–conservative design. For the these reasons, exceedance probability assessments cannot solely be relied on for design against ice gouge.

The USGS provided two relevant documents that are available to the public: Rearic and McHendrie (1983) [111] and Weber et al. (1989) [129]. These studies were performed in the Beaufort Sea. Analysis of the available survey data shows that the deepest identified ice gouge is 13 ft. (3.9 m) deep. The maximum depths for single and multiple gouges were observed at water depths from 72 to 473 ft. (22 to 132 m). The maximum number of gouges occurs in the water depth intervals between 82 and 131 ft. (25 and 40 m). The highest calculated crossing density is 91 gouges per mile (147 gouges per km), which has been observed within the 66 to 82 ft. (20 to 25 m) water depth interval.

At the eastern Chukchi Sea, continental shelf surveys were performed for 1,120 miles (1,802 km) of track line. An estimated 10,200 individual gouges were identified in the water depths interval between 60 and 210 ft. (18 and 64 m). The maximum noticed incision depth is equal to 15 ft. (4.5 m) in the 115 to 130 ft. (35 to 40 m) water depth interval. Two–meter deep gouges were noticed in the 69 to 82 ft. (21 to 25 m) water depth intervals. Gouges wider than 300 ft. (91 m) occurred at 118 to 131 ft. (36 to 40 m) water depths. The maximum occurrence of wide gouges occurs in the water depths interval of 101 to 148 ft. (31 to 45 m).

Early investigators recommended the single–parameter exponential distribution as an effective and conservative probabilistic ice gouge model. Later efforts suggest that the Weibull distribution provides the better fit for the Canadian Beaufort Sea ice gouge depth data across the full range of available water depths. The two–parameter exponential and three–parameter gamma distributions tended to under–predict the amount of shallow gouge depth data. For the Chukchi Sea, log–normal distribution models have been produced, but the lack of sufficient gouge depth and widths data has resulted in limited confidence.

Comparisons of the available data sets show discrepancies and inconsistencies between different surveys. For example, the gouge width was not recorded for all the gouges observed in some studies. In the same way, survey programs conducted in American Arctic oceans characteristically record each individual ice gouge in a multi–tracked seabed as an individual ice gouge, regardless of whether it was created by a single keel or multiplet event. A consistent surveying approach must be followed in future surveys to enable meaningful connections between repetitive surveys of the same areas.

As discussed, no repetitive ice gouge surveying programs were conducted in the Chukchi Sea, which has led to a paucity of information on ice gouge recurrence rate.

Therefore, it is suggested that U.S. Beaufort Sea ice gouge recurrence rates may also be used in Chukchi Sea ice gouge analyses in the absence of regional or site–specific data.

6.0 Physical Testing

6.1 Introduction

Physical tests are conducted in the field or in laboratory settings, indoors or outdoors, using small– or large–scale instrumental setups. Physical testing can be performed under two types of testing conditions:

- The first type of physical testing is ice gouge testing at normal gravity (1–g):
  - Normal gravity facilities mimic real–gouging events. Geotechnical materials have non–linear mechanical properties that depend on the effective confining stress and stress history. Soils are tested under normal confinement stress resulting from the soils' self–weight. Depending on the size of the facility and experimental setup, soil failure can be observed within or outside the range of the confinement stresses that exist in reality.
  - Primary issues are associated with the range of confining stresses, uncertainty on scaling laws, contact mechanics, interface conditions, and strain localization. For example, there are technical difficulties in extrapolating the results from 1–g scale models to full–scale models for extreme ice gouge events (e.g., 10 ft. deep and 30 ft. wide) with respect to bearing pressure, interface behavior, strain localization, and soil behavior, particularly in dense, cohesionless seabeds. It is preferable to perform full–scale tests that do not require full–scale verification. However, whether the testing is conducted in a purpose–built facility or in the field, such tests are costly and have technical constraints. For this reason, most of the ice gouging studies have been performed at normal gravity in indoor facilities.
  - Figure 6.1 shows the typical configuration of a normal gravity experimental facility.
- The second type of physical testing is performed in a centrifuge facility:
  - The centrifuge applies an increased gravitational acceleration ('g–level') to physical models to produce identical self–weight stresses in the model and prototype. The one–to–one scaling of stress enhances the similarity of geotechnical models and makes it possible to obtain accurate data to help solve complex problems.

- During centrifuge testing, the vertical stress in the soil is equal to the self–weight factored by the g–level under which the test is performed (g is the gravity acceleration). For example, if the centrifuge test is performed under 10g, the vertical stress in soils is ten times the vertical stress in normal gravity tests. Therefore, soils can be tested under higher (simulated) vertical stresses. Centrifuge testing has practical limitations related to the level of acceleration that can be applied and the size of the scale model being used.
- The typical configuration of centrifuge testing facility is presented in Figure 6.2.

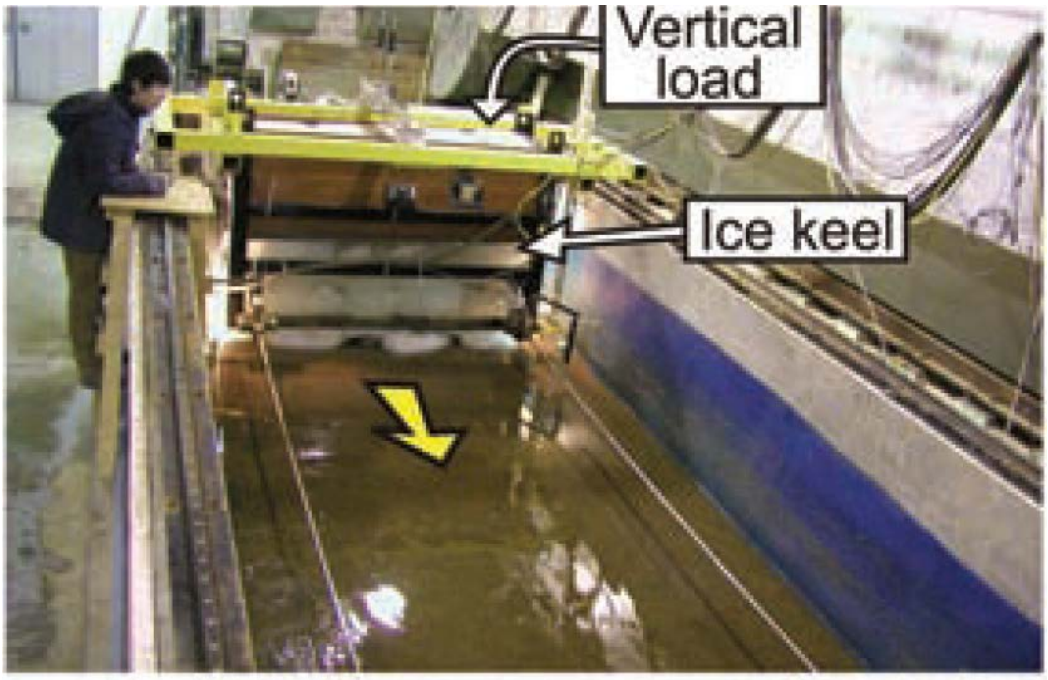

Figure 6.1: Typical Normal Gravity Testing Facility (Barrette and Sudom, 2012 [11])

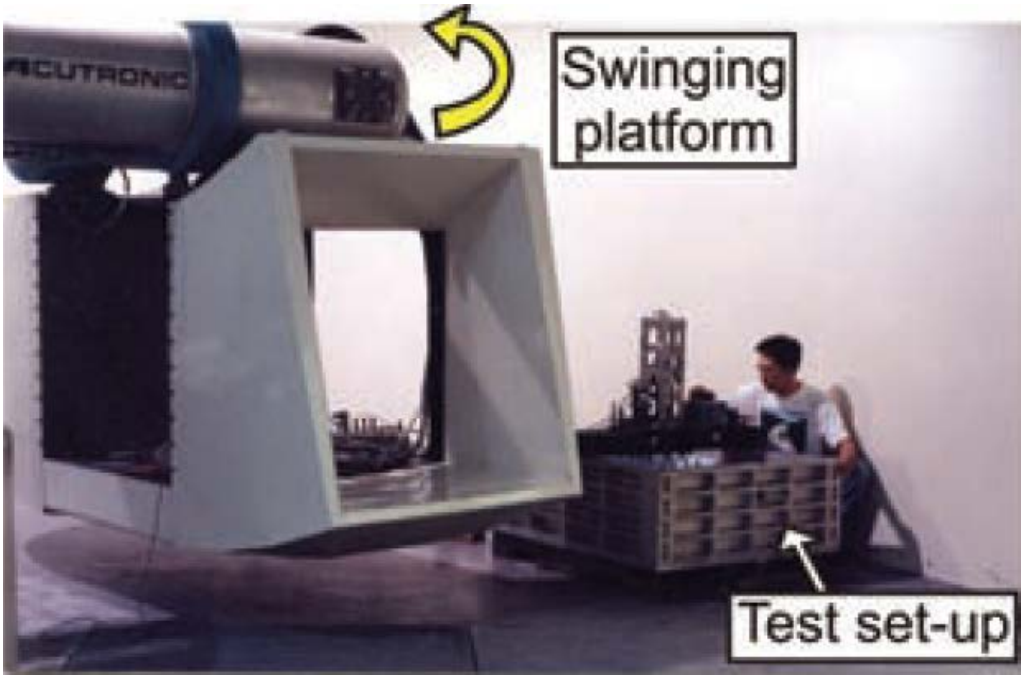

Figure 6.2: Typical Normal Centrifuge Testing Facility (Barrette et al., 2012 [11])

The dimensions of the testing tank vary as a function of the study objectives. Figure 6.3 shows a sketch of the typical tank prepared by Green [44].

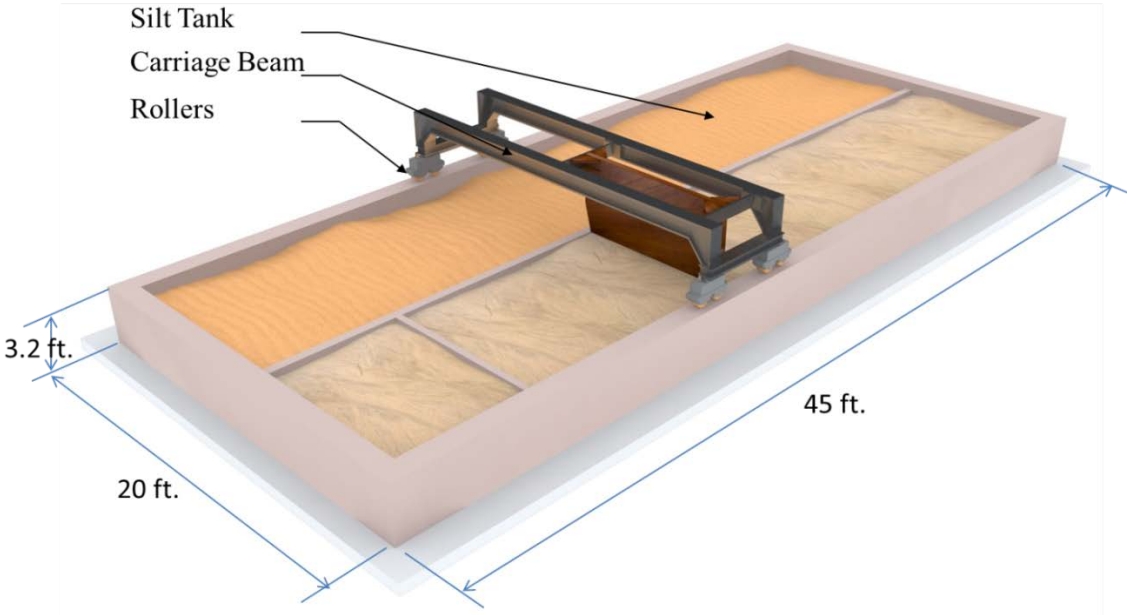

Figure 6.3: Schematic of Typical Ice Gouging Tank (Green, 1983 [44])

6.2 Experimental Setup

During a physical test, the keel is moved horizontally to scour the soil surface. Contact between keel and soil causes disturbances to the soil surface that mobilize soil passive resistance and bearing capacity. As a result, vertical and horizontal reaction forces act on the keel.

In real situations, an ice keel may rupture because of the high–contact loads, or it may lift and reduce the contact pressure with the soil. Two types of physical test setups can be performed to investigate the forces acting on a keel.

The first type of test setup prevents the keel from lifting. Figure 6.4 presents this test. A load cell mounted on top of the keel measures the vertical loads acting on a load cell. The measured load is indicative of the level of pressure applied by the soil on the keel. This type of setup uses a pre–set keel depth.

The second type of test setup, which is presented in Figure 6.5, allows for keel lift; the gouge depth is not pre–set. Resistance to keel motion is caused by the friction between the keel surface and the seabed. A dead load is used to stabilize the keel during contact with the soil.

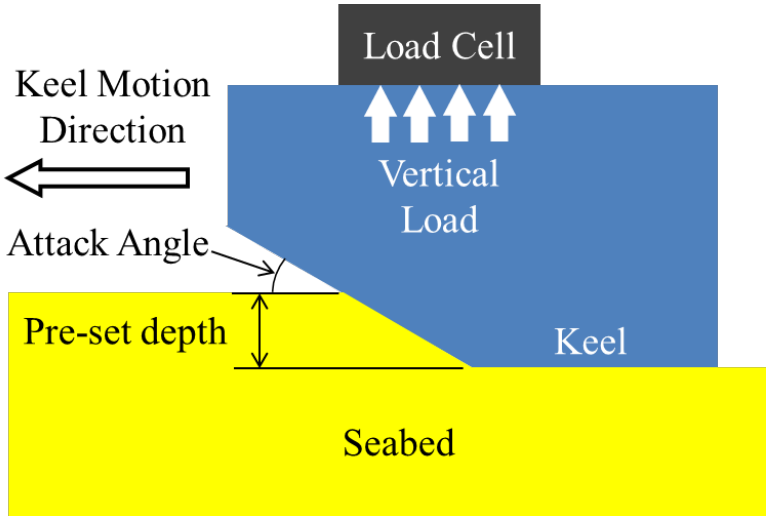

Figure 6.4: Test Setup 1 (Barrette and Sudom, 2012 [11])

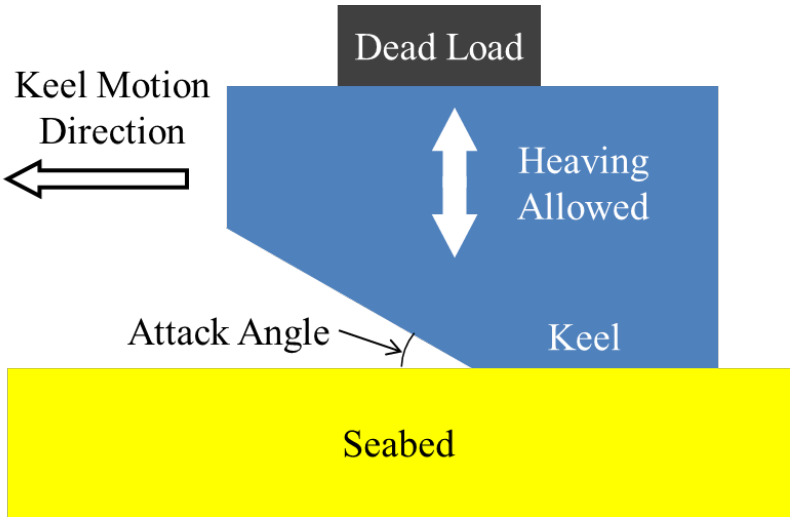

Figure 6.5: Test Setup 2 (Barrette and Sudom, 2012 [11])

Physical testing may be performed for different types of soil under dry or saturated conditions. For saturated conditions, sensors called piezometers can measure pore water pressure and monitor changes in the pore pressure that are generated by the gouging event. Reaction loads (vertical and horizontal), stress distributions, and displacements can be monitored and recorded with the appropriate sensors and data acquisition system.

Because of the difficulties associated with the use of real ice, the keel is modeled using a steel or concrete mass. Only a limited number of experiments use ice ridges of loose and more compacted structures, simulating first year ridges and multi–year icebergs, respectively. In reality, ice keels are highly heterogeneous masses with limited strength that come in a wide range of shapes.

In physical tests, the keel shape is idealized as a block–shaped mass. Several shapes are assumed for the keel face, most of which have a flat smooth surface (with some exceptions where rough surfaces are used). Contact between keel and soil can occur along rounded or rectangular keel faces.

The most influential parameter of the keel shape is the attack angle, which is defined as the angle between the keel face and the contacting soil surface. Several studies investigate the effect of the attack angle on the applied pressure to the soil surface and the induced subgouge deformations.

According to Barrette et al. [11], physical testing parameters can be classified into five categories, the first four of which represent the inputs for the test. These categories include:

1. Soil parameters
2. Keel parameters
3. Pipeline
4. Test conditions.
5. Testing results (e.g., pressure, horizontal and vertical load, pore water pressure)

Table 6.1 presents a summary of the testing parameters proposed by Barrette and Sudom, 2012.

Table 6.1: Summary of Database Parameters (Barrette and Sudom, 2012 [11])

Categories	Parameters
Information on the soil (sediment) bed	• Bathymetry (level or slope) • Soil type (cohesionless, cohesive, others) • Soil density, strength, and other mechanical properties • State: Overconsolidated, saturated • Pipeline trench backfill properties
Information on the keel	• Keel type (rigid indenter versus real ice) • Keel dimensions • Attack angle • Degrees of freedom allowed (e.g., heave, pitch) • Keel surface roughness • Ice type, strength (for keel made from real ice)
Information on the buried pipeline (if applicable)	• Pipe outer diameter and wall thickness • Material properties • Crown depth (below seabed) • Constraints (free to move or anchored) • Instrumentation
Test conditions	• Acceleration (n) level for tests in centrifuge • Normal gravity (1–g) versus centrifuge (ng) • Vertical load on keel (depending on test setup) • Pre–set depth (depending on test setup) • Keel displacement rate • Scour length (i.e., travel distance) • Instrumentation

Categories	Parameters
Test results	• Horizontal load • Vertical load • Assessment of steady–state • Keel heaving (depending on test setup) • Pore pressure • Post–test bathymetry (scour depth, width, side berms, front mound) • Subscour deformation

6.3 Normal Gravity (1–g)

6.3.1 Harrison (1962, 1972)

One of the earliest studies relevant to ice scouring is attributed to Harrison, 1972 [45]. The experimental work observed soil failure on an inclined plane delimiting the edge of a passive soil wedge, using grouser plates up to 1.6 ft. (0.5 m) wide. This study was conducted in a glass–sided flume using three different soil conditions: dry sand, saturated clay, and intermediate loam. Harrison's objective was to verify the conventional theory of soil failure using slip line fields.

6.3.2 Chari (1975, 1979, 1980, 1981, 1982)

Chari [25] [26] [27] [28] [29] was the first researcher to analyze the gouging processes from a detailed, geotechnical perspective. The researcher took into account the bearing and passive resistance failure mechanisms. Figure 6.6, which explains Chari's mechanism of shear plane, presents the idealized keel shape used in this work. Keel movement produces horizontal passive pressure (P) on the soil surface. As a result, shear stress (S) develops at an inclined plane (X1). Soil failure occurs when the shear stress component exceeds the shear strength of the tested soil.

Tests were designed to observe the mechanics of scouring and to illustrate the complexity of the keel/soil interaction model. The experimental program focused on measuring the pressures and forces on the model and monitoring soil displacements near the keel during the scour process.

During the experiment, the model was driven into the sloping testbed while towing forces and pressures were recorded. The primary resistances to the model motion were identified to be passive soil resistance in front of the model, soil movement in front of the model, and soil movement below the model. Chari explained a pattern of failure surfaces originating at the keel toe and concluded that soil fails at an angle of 25° to 30° with respect to the testbed surface (horizontal plane).

The results show that soil mobilization in the testbed occurs far ahead of the model in both sand and clay. The results describe failure surfaces that begin or extend below the maximum scour depth. Unfortunately, Chari did not provide the magnitude of displacements. Figure 6.7 presents soil failure along successive shear planes in front of an earthmoving machine.

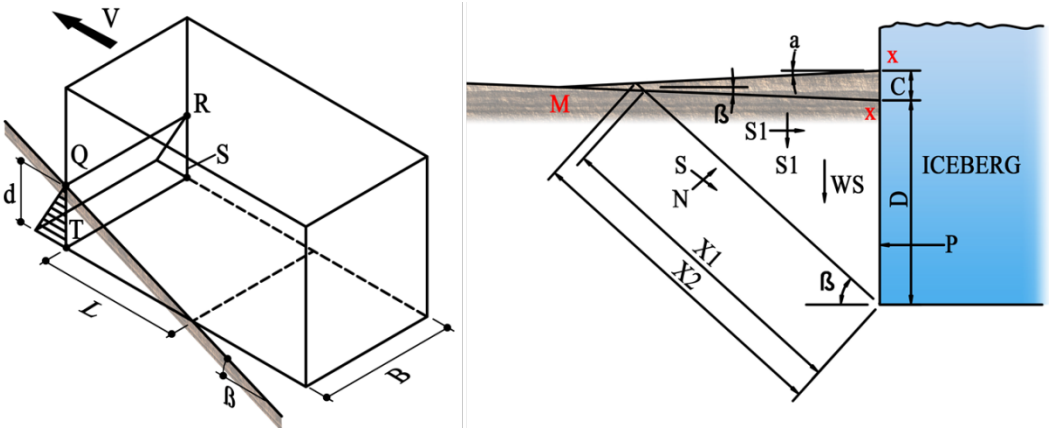

Figure 6.6: Assumed Type of Soil Failure in Front of Idealized Iceberg (Chari, 1982 [29])

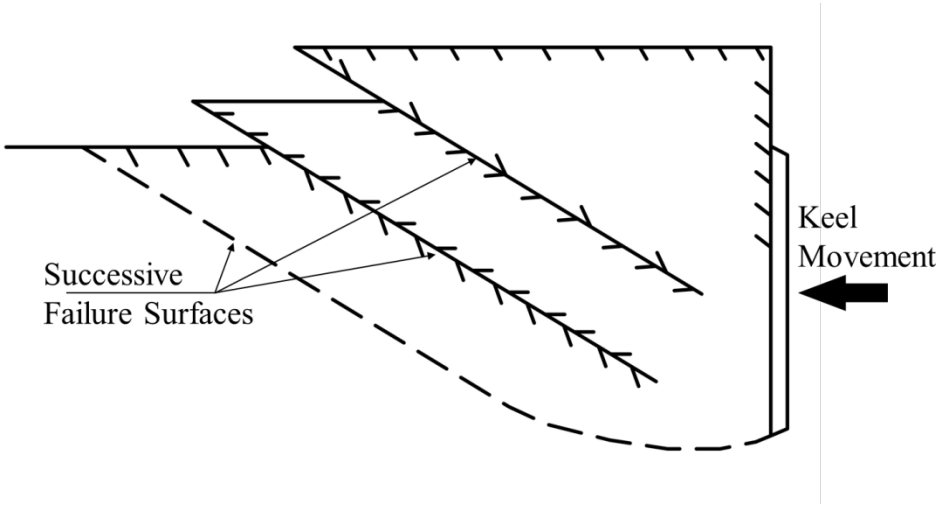

Figure 6.7: Soil Failure along Successive Shear Planes in Front of Earthmoving Machines (Chari, 1982 [29])

6.3.3 Abdelnour (1981, 1984)

Abdelnour [3] [2] conducted extensive tests to understand the soil resistance to keel motion during an ice gouging event. The Arctic Petroleum Operator's Association (APOA) funded this research.

To investigate the influence of each test parameter on the pressure measurements, the test parameters were changed independently for each test setup. A range of modeling parameters such as soil types, model keel shape, model scale, scour cut depth, and towing velocities were used in the tests.

The study comprised 110 runs using two model shapes. The first model was an inverted pyramid shape with 63° angle (measured with the horizontal plane). The second model was a rectangular, prismatic shape with 90° faces. Two model widths were used: 0.85 ft. (26 cm) and 2.7 ft. (52 cm).

Pressure transducers were placed on the face of the model to measure the applied pressure on the soil surface. The pressure measurements were used to calculate the forces acting on the keel mounting frame, and the frame forces were used to determine the soil resistance to keel motion. Adelnour provides detailed information regarding the gouge dimensions for each experiment in his publication.

Abdelnour used the findings of the test program to develop dimensional and non–dimensional semi–empirical relationships. The analysis was extensive and provided deep understanding of the influence of each testing parameter on the resulting contact pressure. However, as Paulin, 1992 [97] reported, information regarding subgouge deformation was not included in the study.

6.3.4 Green et al. (1984)

Green's experiments [43] were a continuation of Chari's work, which focused on the measurement of resistance pressures and the effects of forces by varying keel shapes and sizes. Green conducted physical tests using Chari's model, in which the keel was driven into the sloping testbed to record towing forces and pressures. Because the purpose of the experiments was to study the gouging process in dry sand, the tests were limited to cohesionless sand. Pressures and forces were measured on the keel and on an instrumented pipeline model that was buried in the testbed. The effects of several modeling parameters were investigated using different sized models and keel shapes.

Green conducted the tests in a concrete tank at Memorial University, Newfoundland, Canada, using six different iceberg models of varying sizes and shapes. He used pressure cells and load cells to measure horizontal force on the keel. A plexiglass pipeline model, which was instrumented with pressure transducers, was rigidly mounted in the testbed at predetermined locations below the scouring model.

The primary resistance on the model was attributed to passive earth pressure. During the test, failure planes developed in the soil ahead of the keel. Soil resistance measured during the tests was directly proportional to the width and the slope of the keel. Changing

the slope of the keel face from vertical (90° from horizontal) to sloping (less than 90° from horizontal) increased soil resistance by as much as 35%. The speed of the model test had no effect on the forces measured during testing.

The pipeline model was designed to be very rigid, relative to the soil. The tests could not provide clear information about the pipeline displacements relative to the surrounding soil.

6.3.5 Prasad (1985)

Prasad [108] performed a series of tests to study the effects of the keel shapes on soil resistance and pressures during a gouging event. The tests included observing the failure planes associated with each shape.

Six model shapes were selected for the experiment. The models had a common base of 3.3 ft. (1 m) long, 1.64 ft. (0.5 m) wide, and approximately 2 ft. (0.6 m) high. The length of the keel face varied, depending on its shape. Two angles, 30° and 60°, were used to model a tapered keel. The tip of the keel was modeled as a sharp corner in all cases. Prasad investigated gouging events for a rounded edge and found that the keel pressure was spread out over a larger area. In addition, a semi–cylindrical–shaped keel was tested. Finally, an extreme case of soil penetration was modeled using a front–angled keel shape. Figure 6.8 illustrates the shapes and dimensions used in the study.

Prasad used theoretical methods to correlate the keel face resistance measurements for each model with the computed values. It was shown that the influence of keel shape on the estimated scour depth is within an acceptable range of variation, and the experimental results were extrapolated to the scour model with confidence. The keel–face pressure measurements varied from model to model, but the scouring profile did not. A progression of failures toward the keel surface was observed and attested by the plot of the horizontal load. Prasad correlated the increased face inclination to the increase of soil resistance, but he did not discuss pressure and displacement measurements in his report.

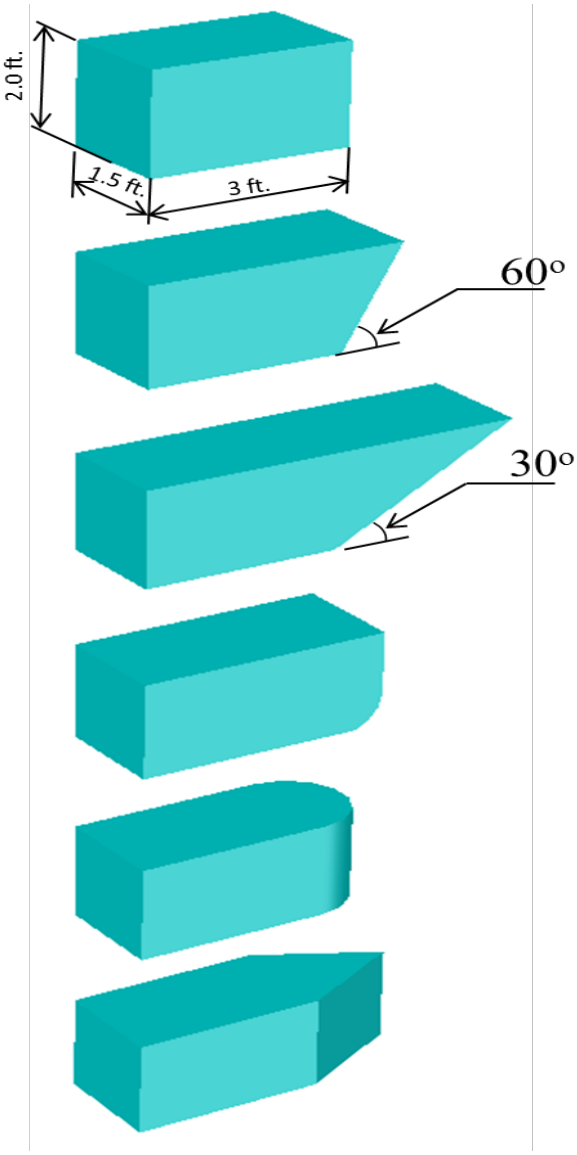

Figure 6.8: Keel Model Shapes Used by Prasad, 1985 [108] (Modified by WGK)

6.3.6 Golder and Associates Ltd. (1989)

To investigate soil movement below the scour [42], Golder and Associates Ltd. used a small indenter to perform 45 tests. Rigid indenters, varying in width and attack angle, were driven into sand and clay testbeds. Displacements and forces on the indenters were measured during the tests.

The failure plane patterns and load measurements were presented for model tests in sands, and the test results were repeatable. Measured pressures and loads were in agreement with the calculated values. The authors observed dead wedges of material,

which were in front of the sloping indenters. The tests showed subgouge displacements below the indenter in the small–scale tests. In medium and dense sand, subgouge soil disturbance extended to a depth of 0.8 in. (2 cm) below the indenter. In loose sand, soil disturbance was observed to a depth of 2.75 in. (7 cm).

These observations were linked to critical state aspects. For example, below the indenter, dilation and strain softening took place in dense soil while contraction and shear strains took place in loose soil. Clay soils behaved similarly to loose sands, although subgouge disturbances were minimal.

This experimental work contributed to identifying the mechanisms involved in soil failure during scouring. Been et al., 1990 [14] attributed the movements below the scour in the Golder and Associates' tests to shear dragging, which provided the missing link in understanding soil failure during ice gouging and explaining the patterns of subgouge deformation. Been's study highlighted the importance of determining the thickness of the shear dragging zone to ensure pipeline safety for the first time.

6.3.7 Poorooshasb et al. (1989)

Poorooshasb et al., 1989 [107] reviewed the work of the Canadian C–CORE (Centre for Cold Ocean Resources Engineering) by using small–scale modeling of ice scours in saturated silt and dry sand. Poorooshasb et al. conducted a series of four scour model tests at the Memorial University sand tank to investigate the size and nature of the deformation zone below a scouring iceberg. In addition, the Poorooshasb study investigated the effects of width and attack angle on subgouge deformation. A force vector was calculated at time points during the driving process. Figure 6.9 presents a sample of total force vectors.

Two factors that significantly affect the magnitude of subgouge deformation were identified: soil density and attack angle.

In dense soils, the zone in which deformation occurs is restricted to a region immediately below the iceberg scour. The Poorooshasb study indicates that soil deformations are larger in loose soils.

The two attack angles (15° and 30°) presented in this study show significantly different results. The 15° attack angle produces very little soil disturbance, which is limited to a shallow zone below the iceberg. The 30° attack angle generates higher levels of soil disturbance over a greater depth. From a force perspective, increasing the attack angle from 15° to 30° decreases the force required to scour and generate subgouge soil deformations.

In low–strength, fine materials (clays and silts), small surface deformations may coincide with significant subgouge deformation and mobilizing shear stresses up to seven times the scour depth. As previously discussed, the deformation of sandy soils decreases with decreasing attack angles. Similarly, soil deformation decreases with higher soil density. The Poorooshasb et al. study emphasizes the limitations when extrapolating small–scale tests results to full–scale models as well as the lack of a correct self–weight stress.

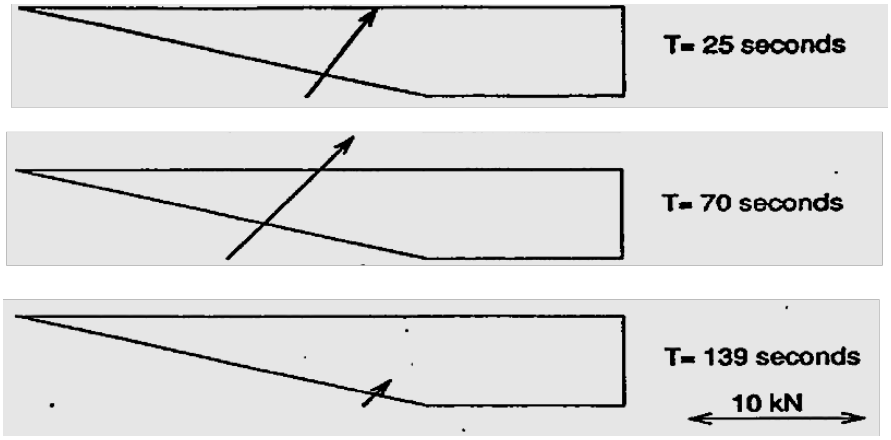

Figure 6.9: Total Force Vectors Acting on Keel During Driving (Poorooshasb et al., 1989 [107])

6.3.8 Barker and Timco (2002, 2003)

Barker and Timco implemented a test program to measure the scouring loads and seabed response (displacement, angular movements, and resulting trenches) to the gouging event using an ice block [7] [8]. They performed 14 tests representing 35 configurations with a variety of seabed types. The study focused on the oil discovery areas within the Jeanne d' Arc Basin area of the northeastern Grand Banks. Figure 6.10 presents a schematic of the experimental setup.

The study was performed using two test setups. In the first test setup, an ice block was mounted on a carriage that traveled along the length of the tank. In the second test setup, the ice model was towed along the tank and was free to move throughout the water column.

Test results showed that the scour profiles are generally uniform along each section of the test channel. The ice did not fail because of shear, but it did erode. The motion of the ice blocks reduced the overall scouring forces and led to ice block sliding along the seabed. The sliding caused loss of buoyancy, which resulted in increased vertical loading on the seabed. The bearing capacity may have played a more significant role than was previously thought.

Scour depths measured in a gravel seabed were insignificant. The resistance forces were estimated from empirical relationships developed using regression analysis. The results achieved a good match between the measured and predicted forces.

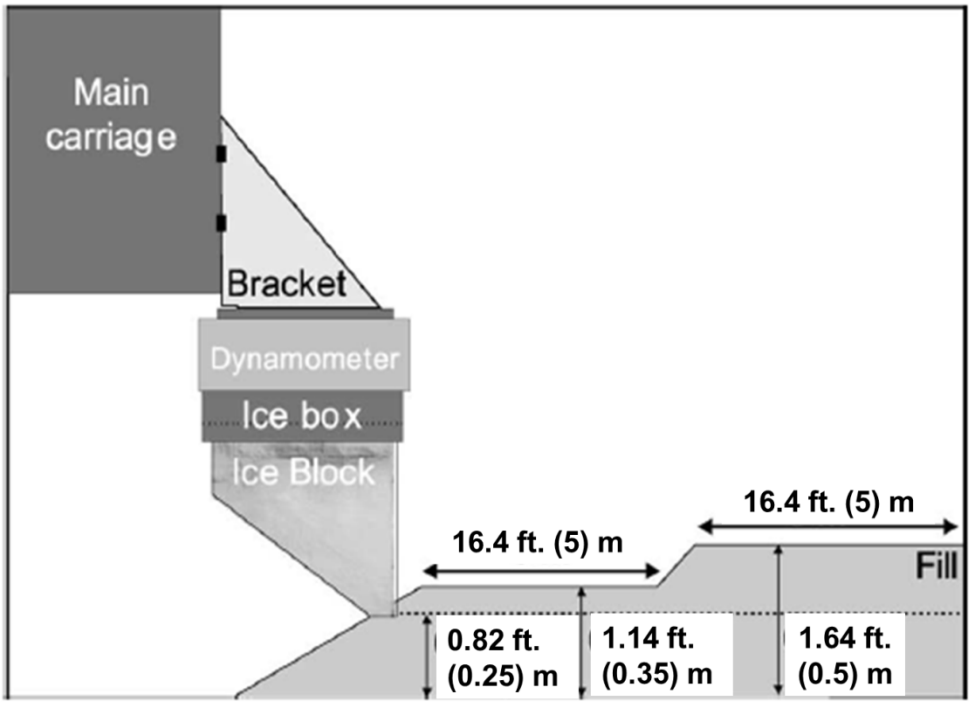

Figure 6.10: Schematic of Experimental Setup (Barker and Timco, 2002 [7])

6.3.9 Liferov et al. (2002), Liferov and Høyland (2004)

Liferov et al. [77] conducted an in situ program in the Van Mijen fjord in Spitsbergen, Norway, to study the keel destruction, investigate the process of scouring, and observe the ice ridges throughout their lifetimes. During pull tests, the keel of the ice ridge was sheared off by the sidewall of the trench. Figure 6.11 presents the in situ field condition observed by Liferov et al. Figure 6.12 illustrates a cross section that represents the test setup.

Two ice scour tests and one shear–off test were performed during the test program. The tests measured the pulling force, displacements, failure of the keel, and the resulting plough. The observed magnitude of the keel destruction was in the order of the scour depth and the ridge heave. The researchers observed a progressive failure of the keel as the ice ridge moved forward. The ice ridge failure follows the mode of the least resistance while scouring the seabed. The collected data was used to verify and justify existing ice ridge gouge models and to develop an improved ice ridge scour model.

Figure 6.11: In Situ Test Setup (Liferov and Høyland, 2004 [76])

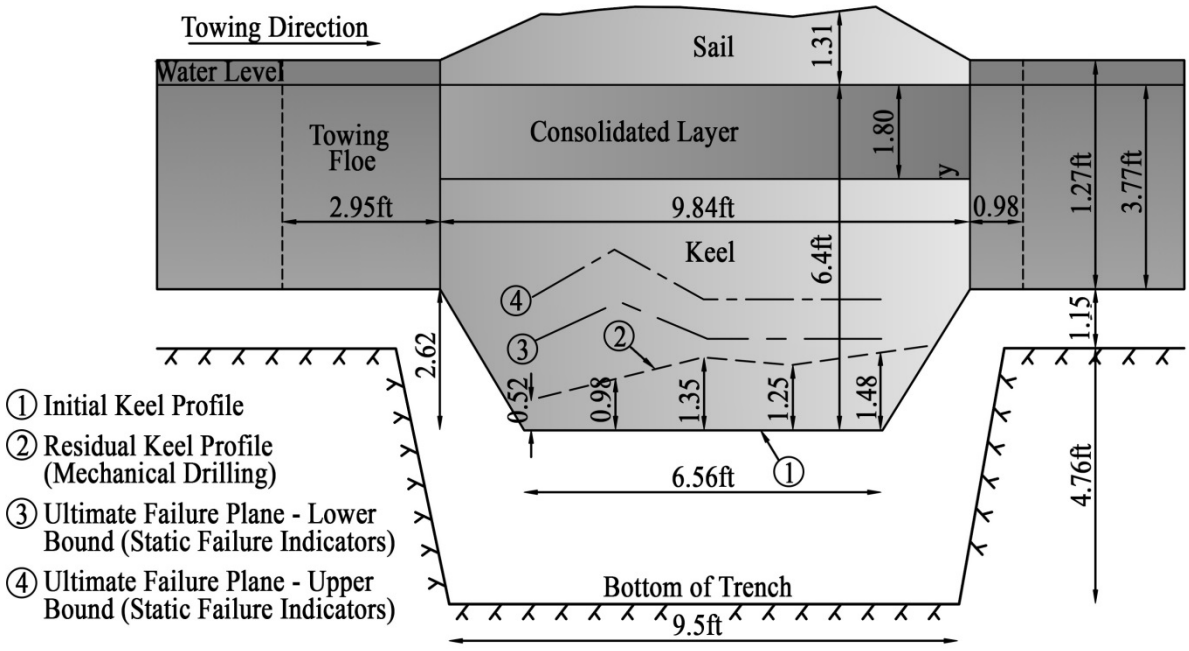

Figure 6.12: Cross Section of Ice Ridge Along Centerline (Liferov and Høyland, 2004 [76])

6.3.10 Vikse et al. (2007)

Vikse et al. [127] performed small–scale laboratory tests to investigate the pressure distribution and soil deformation around a buried pipe segment. The tests were performed using sand and sandy silt in the testbed. Vikse et al. discussed the dependence of subgouge soil deformations on several gouge–related parameters. The model setup was rather simplistic. A steel plate was used to limit keel motion only in the horizontal plane.

Vikse et al. observed that the buried pipe segments experienced cyclic movements, being first dragged forward and downward as the model keel approached the pipeline and then rebounding as the keel passed the pipeline. The maximum pipe displacement decreased exponentially with the pipe burial depth. The naturally formed soil mound in front of the keel influenced vertical pipeline displacements. Furthermore, horizontal pipe movements were larger at the lower attack angles of the ice keel.

6.3.11 Barrette et al. (2008, 2009)

The purpose of the Barrette et al., 2008 and 2009 [12] [13] test program was to investigate the sliding resistance of grounded level ice and rubble on sand and clay under full–scale stress conditions. The experiments were performed in a laboratory using a 19.7 ft. (6 m) long flume. Instruments were used to measure the stress distributions in the sediment and acquire deformation profiles of the sediment column. The instruments used for data acquisition included a displacement transducer to measure the vertical motion of the ice, a pore pressure transducer, and a few cameras to study keel dynamics.

The observations recorded during the full–scale test to support the assumption of a three–stage scouring process, as documented by Blasco et al. 1998 [15] were:

- Stage 1 – The ice penetrated the seabed to a given depth.
- Stage 2 – The ice went through a transition.
- Stage 3 – The ice scour became parallel to the seabed.

The test results indicated stabilization of the horizontal load, suggesting a steady–state behavior during scouring.

Barrette et al., 2009 [13] reported that friction between the ice and the sediment controls the sliding resistance. Their analysis shows that sliding resistance is a function of the effective shear response of the clay. The seabed freezing around the ice keel was observed for sand soils but not for clay soils.

The undrained shear strength for clay, which was measured with a shear testing device, was consistently higher than the sliding resistance of the ice in all tests. A method was proposed to estimate sliding resistance by determining the effective internal friction angle of the clay, monitoring pore water pressure, and determining effective normal stresses. Using ice rubble instead of level ice indicated that ice rubble can promote clay consolidation (attributed to shorter drainage paths for pore pressure dissipation) and yield a potentially significant gain in shear resistance over the pipeline's operational life span.

6.3.12 Sancio et al. (2011)

Sancio et al. [117] performed a testing program consisting of 17 large–scale ice gouging events. During each test, a composite steel and concrete indenter was pushed through an engineered soil bed of compacted clay or sand (a test 'basin'). The test was performed outdoors in saturated soils, and the keel was pulled for several feet. The test incorporated a buried pipe 40 ft. (12.2 m) long, 0.55 ft. (0.168 m) in diameter, and 0.43 in. (11 mm) thick. The pipe was outfitted with 60 strain gauges installed at four diametrically opposite locations. Figure 6.13 shows the pipeline in the trench before testing.

The keel was pulled the entire length of the basin while measuring several parameters:

- The position of the keel was measured with a potentiometer.
- The force required to pull the keel was measured using a dynamometer.
- The pitch and roll of the keel was measured with a biaxial tilt–meter installed on the keel.
- The inclination was measured with an inclinometer on the pull cable.

In addition, the researchers measured the displacements in the soil, strains on a pipe section, and pore water pressure response in the sand.

The shape of the gouge after the test is shown in Figure 6.14.

For sands tests, the subgouge displacements measured do not exhibit a direct relationship with the gouge depth, width, and soil density.

In clay tests, subgouge displacements do not exhibit a direct relationship with undrained shear strength.

Four piezometers were used to measure the induced pore water pressures during testing (see Figure 6.15). The magnitude of the induced pore water pressure was not included in the plot.

Figure 6.13: View of the Pipe (Sancio et al., 2011 [117])

Figure 6.14: Typical Gouge Produced in Sand Test (Sancio et al., 2011 [117])

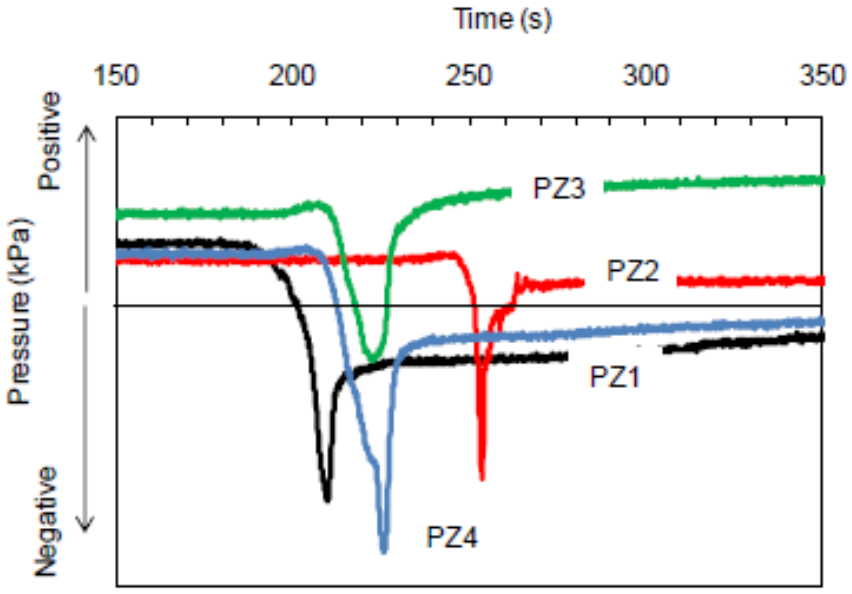

Figure 6.15: Pore Water Pressure Response in the Piezometers Installed in Saturated Sand Test (Sancio et al., 2011 [117])

6.4 Centrifuge Testing

6.4.1 Paulin et al. (1991,1992), C–CORE (1995,1997,1999)

In the 1990s, the Pressure Ridge Ice Scour Experiment (PRISE) joint industry program led by C–CORE [18] [19] [20] [21] [23] highlighted the importance of subgouge soil deformations on buried offshore pipelines in ice gouge regions (Woodworth–Lynas et al., 1996 [134]). The C–CORE test program included a series of small–scale physical ice gouging tests. The objective of the small-scale tests, which were conducted in a geotechnical centrifuge, was to enhance the understanding of soil deformations and ice loads produced during ice gouging events. Experimental procedures were divided between two physical studies, and 29 simulations were performed.

The first study involved eight model tests conducted at 1–g in dry, partially saturated, and submerged sands. The sand conditions, iceberg model dimensions, and scour cut depths varied. The tests were conducted to:

- Measure forces and pressures on the iceberg model during scouring.
- Monitor pore water pressures and total stresses in the sand.
- Measure the resultant forces and subscour deformations.

Tests confirmed that the deformations were greater in sand with a relative low density. In addition, increasing the attack angle from 15° to 30° degrees reduced the amount of subscour deformation and changed the dominant force acting on the iceberg model from vertical to horizontal.

In general, the scour process was similar in both the dry and the submerged tests. In both cases, soil builds up in front of the model, and failure surfaces appear in the sides and front of the model. However, the submerged tests had a greater amount of infill and smaller berms. The presence of water substantially reduced the horizontal and vertical forces required to create scour.

The second study involved two model tests performed on the centrifuge at an acceleration of 100–g in two saturated submerged clay samples with different soil stress histories. Soil deformations below the scour were evident in both tests. Soft soil tests produced soil movements that were opposite to the direction of travel. It was concluded that centrifuge tests closely simulated a full–scale prototype.

PRISE was the first extensive proprietary program designed to develop the engineering framework to allow pipeline installation in Arctic regions. The program led to the development of a semi–empirical equation for horizontal subgouge soil deformations in clay soils, commonly referred to as the PRISE equation. The PRISE program provided the stimulus and a knowledge basis to develop and validate numerical simulations.

6.4.2 Lach (1996)

Lach [66] performed nine centrifuge model tests at the level of 100–g gravity. The objective of the experiments was to investigate the effect of test variations in initial soil stress conditions (stress history), the model attack angle (15° to 25°), width, and vertical stiffness. The model tests allowed for two unrestrained motion degrees of freedom—lift along a vertical axis and rotation around a lateral axis. These unrestrained motions represent a partially buoyant model, which allows a more realistic representation of field events. However, the unrestrained motions reduce control over the input parameters. The data acquired from the experiments was compared to numerical data. Lach observed a good match between testing data and numerical data. Subsequent research has referred to Lach's experiments and has compared his results to numerical simulations.

6.4.3 Allersma and Schoonbeek (2005)

Allersma and Schoonbeek [4] performed their tests in a geotechnical centrifuge of the University of Delft in the Netherlands. Their objective was to determine how the subgouge soil deformation is influenced by measurable soil parameters such as the

undrained shear strength (Su). Other test parameters measured were scour speed, scour depth, keel angle, and keel surface roughness. Additionally, the scale effects were examined by performing one test at 150–g instead of 100–g. During the test program, some preliminary tests were performed on multiple scouring sites.

The program also performed tests on layered seabeds where soft soil overlaid overconsolidated soil. During the tests, the horizontal and vertical loads were measured by instrumentation. Soil deformation was measured using image processing. Figure 6.16 presents the observed shear planes and a visualization of the soil deformation. Horizontal soil disturbances extend up to four times the gouge depth in softer clay and up to two times the gouge depth in overconsolidated clay with a higher undrained shear strength. The magnitude of vertical soil displacements was relatively smaller, but they extended deeper than the horizontal displacements. Deep cracks and large shear bands were observed.

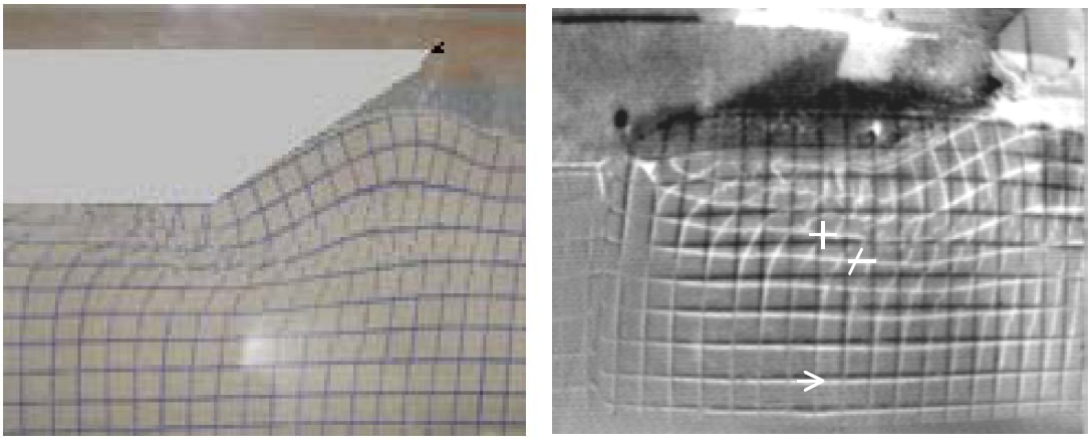

Figure 6.16: Shear Planes Observed in Test (left) and Visualization of Soil Deformation by Subtraction of Images (right) (Allersma and Schoonbeek, 2005 [4])

The deformation mechanism seemed to be sensitive to deformation rate, keel angle, and keel roughness. It was particularly sensitive to the undrained shear strength of clay soils. Researchers developed an empirical formula to predict subgouge deformation from the undrained shear strength and density of the soil (parameters that are measured in standard soil investigation for pipeline trenching).

The benefit from these experiments is the use of remolded soil because no other research has focused on the effect of multiple scouring. In addition, the program investigated scale effects and the sensitivity of subgouge deformation to soil strength.

6.4.4 Phillips et al. (2005)

Phillips et al., 2005 [103] summarized the PRISE experimental program results published in 2004. The centrifuge tests were performed with an instrumented, rough–faced, rigid, rectangular indenter at a fixed elevation, which could travel only horizontally. A sand seabed was used for the tests. Gouge forces and local bearing pressures on the indenter were monitored. The vertical–to–horizontal force ratio was equal to unity. Tests showed that the scour depth was directly proportional with keel bearing pressure.

For gouge depths representative of the Canadian Beaufort Sea, this implies a prototype keel bearing pressure of 14.50 to 29.01 psi (100 to 200 kPa). Base shear, as opposed to passive resistance and side shear, was thought to be the main contributor in horizontal resistance. The vertical extent of subscour deformation varied as a function of sand state (i.e., dilatancy). The seabed failure mechanisms, assuming drained shear response, included the formation of a triangular dead wedge below the inclined keel surface, with passive failure ahead of it.

6.4.5 Ralph et al., C–CORE (2011)

Ralph et al. [109] performed a series of physical model tests using C–CORE's geotechnical centrifuge facility to assess the feasibility of protecting multiple wellhead systems against gouging iceberg keels by housing them in a buried caisson. The physical tests simulated keel–soil–structure interactions that were representative of the design gouge features and soil conditions typically encountered in the Grand Banks. The objectives were to observe and study the global response of the protection structure in terms of stresses and deformations. Figure 6.17 illustrates the experimental setup. Various interaction scenarios were tested, and the results were used to calibrate a numerical finite element (FE) model.

The distance from the base of the keel to the top of the caisson played a major role in the stress magnitudes observed in the caisson. In addition, this distance influenced how the dead wedge interacted and flowed over the top of the caisson. Tests and simulations investigated the dead wedge interaction with the caisson cover and its effects on the cover. Apart from its primary function to prevent debris from entering the caisson, it was proven that the top of the caisson affects the keel–soil–structure interaction and the transfer of forces and stresses to the structure.

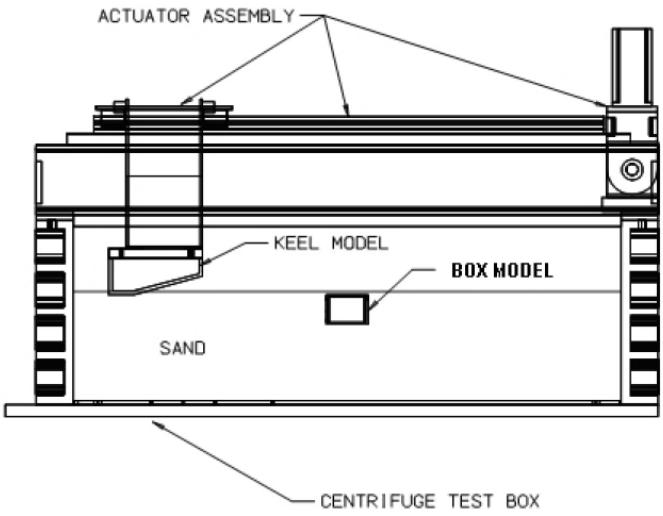

Figure 6.17: Illustration of Centrifuge Test Setup (Ralph et al., 2011 [109])

6.5 Gap Analysis

6.5.1 Overview

Several parameters control the physical testing of ice gouging (soil type, friction between keel and soil, and keel characteristics). Different types of soils present different responses to scour events because of the complex interactions between a number of aspects (keel geometry, soil strength, and gouge characteristics). As has been discussed in Sections 4.0 and 5.0 of this report, the influence of each parameter on gouge characteristics can be isolated and independently investigated in tailored experimental setups and under controlled conditions. Further complexity is introduced when the structure of interest (pipe or wellhead) is integrated into the model. At the same time, some simplification and idealization of testing parameters, conditions, or both are essential to producing physically sound and repeatable test results.

6.5.2 Soil

The area of greatest model uncertainty is related to the characterization of soil response, commonly described as a soil constitutive model. Soil is a complex material that shows nonlinear, time–dependent, and often anisotropic behavior when loaded. This behavior can be generally attributed to non–constant soil stiffness, irreversible deformations, and changes in soil strength because of the loading history and pore pressure build–up under loading.

Physical tests were performed for cohesive and cohesionless soils under dry and saturated conditions. In most of the physical tests (427 tests out of 487), approximately 91% were performed under normal gravity conditions. Sixty tests were performed in centrifuge to represent conditions under higher soil confinement stresses. The highest gravity test recorded was 100–g.

During testing, the soil layer was assumed to be homogenous, with a thickness that varied significantly among the tests. The typical soil layer thickness filling the test tank was 3.2 ft. (1.0 m).

6.5.3 Keel

The keel was usually made of a steel or concrete mass that varied in shape and size, depending on the purpose of the test. The shape of the iceberg keel was usually irregular. However, during experiments, the keel was idealized to common shapes. Investigation of the keel shape on the pressure imposed on the surface of soils was presented in several testing programs.

6.5.4 Attack Angle

Barrette et al., 2012 [11] summarized the number of simulation tests for each keel attack angle. Figure 6.18 presents this information. The attack angle was measured between the keel face and soil surface. In the past, the block–shape keel was used in most of the experiments conducted using an attack angle between 86° and 90°. No experiments were conducted for angles between 0° and 10°, 31° and 40°, and 76° and 85°. A large percentage of the experiments were tested at an attack angle between 26° and 60° and between 86° and 90°.

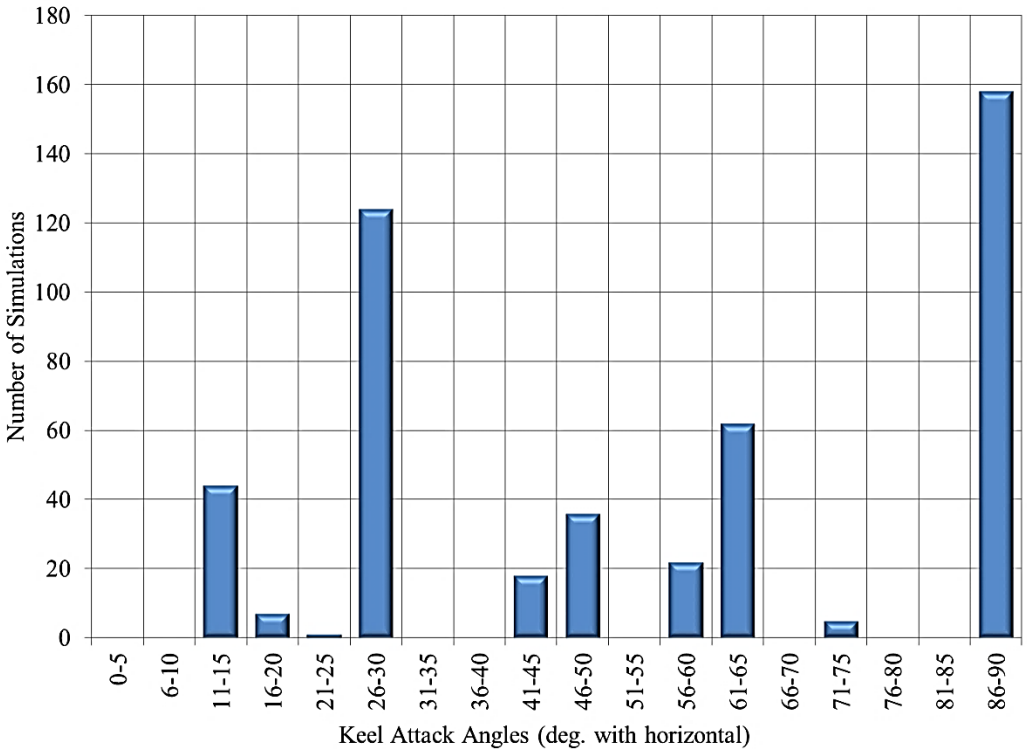

Figure 6.18: Number of Simulations (Barrette et al., 2012 [11])

6.5.5 Ice Keel Properties

A limited number of studies used ice keels for physical testing. The work done by Liferov et al., 2002; 2004 [77] [76] and Barker and Timco, 2003; 2008 [7] [8], included only 18 tests. The number of experiments performed with real ice represents only 3% of the total number of experiments, which is a relatively low percentage of tests to draw any meaningful conclusion. Liferov's work restated that the failure of the gouging ice feature could be the limiting mechanism. In addition, using an ice keel may induce freezing in cohesive soils during gouging. It is recommended that more experiments using ice keels be conducted.

6.5.6 Pipe

A limited number of tests were performed using buried pipes. Soil deformation around the pipe and the pressure induced on the pipe are important parameters when investigating displacement and the local buckling effect of the pipe. Additional research on ice gouging including pipe segments is essential to estimate the minimum required burial depth for pipelines.

6.5.7 Wellhead

Only one experimental study (Ralph et al., 2011 [109]) examined the response of a wellhead arrangement housed in a caisson for protection against an ice gouge event. Further analyses are required to achieve a better understanding of the wellhead–ice keel interaction.

6.6 Summary

Several field and laboratory–based approaches were adopted to study the seabed response to possible gouging events. Physical testing was given special attention because it allows for full control of most gouging test parameters. Physical testing is a low–cost and time–efficient approach to improving the ice gouge knowledge base.

Physical testing can be conducted under normal gravity and centrifuge gravity conditions. Normal gravity tests can be performed indoors or outdoors, depending on the size of the keel. The keel is pushed into the soil bed to induce gouge under its self–weight, which mimics real gouging events. However, soil mechanical properties are governed by the effective confining stress and stress history. Soils that are tested under normal gravity experience confinement stress caused by self–weight. Depending on the size of the facility and experimental setup, a soil failure can be tested within or outside the range of the confinement stresses that are experienced in situ. An issue related to the selection of the appropriate confining stress range is the uncertainty of the scaling laws.

For example, results from 1–g physical models must be extrapolated to full–scale for extreme ice gouge events, and there are technical challenges to simulating the bearing pressure, interface behavior, strain localization, and soil deformations. This is especially true in dense, cohesionless seabeds.

The centrifuge applies an increased gravitational acceleration to physical models to produce identical self–weight stresses in the model and prototype. The one–to–one scaling of stress enhances the similarity of geotechnical models and makes it possible to obtain accurate data to help solve complex problems. In simple terms, soil can be tested under higher confinement stresses (same magnitude as in the field).

Simulating an ice gouging event is rather complicated because several parameters influence the experiment. Soil types, ice–keel, and subsea structure characteristics must be considered in the ice gouging experiments. Most of the tests have focused on estimating the induced subgouge deformations and reaction forces acting on the keel during gouging. The load transfer to the pipeline is directly related to these parameters, but the relative stiffness of the pipe to the soil dictates the pipe response. With better

instrumentation, a better distribution of stresses and strains in the pipeline can be obtained. This would help to establish an Arctic–pipeline–specific design and operation method for offshore pipelines operating in cold climates. The design and operation method should account for expected loading conditions and should be compliant with the limit state design approach.

7.0 Numerical Simulations

7.1 Overview

The ice gouging process is a multi–faceted, non–linear problem. Advanced numerical analysis plays a significant role in addressing the complexity of the ice keel–soil–structure interaction. The development and validation of numerical models that can fully simulate this interaction have proven to be quite demanding because of the complex interactions between the modeling aspects involved and the challenges related to numerical simulations. The following sub–sections present a brief overview of these aspects and challenges.

7.1.1 Modeling Aspects

In the early 1990s, physical simulations of ice gouging processes provided researchers with the input data basis for numerical simulations. Parametric studies identified the parameters that strongly affect the keel–soil–pipeline response. These parameters are attack angle, keel geometry (width and depth), gouge depth, ice strength, soil type, and pipeline and wellhead properties.

7.1.2 Ice Attack Angle

The influence of the keel attack angle is particularly important to the gouging process. Steeper keels move greater soil volumes into the frontal mound, while shallower keels force most of the soil below and to the side of the indenter. For the same gouge depth and width, a shallow keel will generally result in greater subgouge displacement than a steeper shaped keel.

7.1.3 Ice Keel Geometry (Gouge Depth and Width)

Estimates of ice gouging keel depth and width can be obtained from direct measurements or inferred from seabed surveys. However, repetitive surveys of gouge events in different areas have not been reliable enough to establish correlations between several parameters, including gouge depth, keel geometry, and water depth. The effect of the keel geometry on gouge depth is fundamental to understanding the physical processes involved in ice gouging. Numerical studies have focused on simulating laboratory or field testing results, assuming constant gouge depths. The common practice used to investigate the effect of keel geometry is to use an idealized ice keel shape and vary its dimensions.

7.1.4 Ice Strength

Ice is a finite strength material, and the shear failure or fracture of the gouging ice feature itself could be the limiting mechanism for the gouge depth reached. The selection of an appropriate constitutive law for the continuum ice rubble to be integrated into a numerical model presents a challenging task. In general, when simulating a steady state gouging process, the ice indenter is generally considered to be rigid.

7.1.5 Soil Type – Constitutive Model

When assessing the deformation of a pipeline or wellhead caused by ice gouging, determining the response of the soil to the passing ice is critical. Simplified numerical models are used to simulate real–world phenomena by attempting to capture the most relevant mechanisms.

The soil itself is a non–simple, multi–phase material consisting of soil grains and voids. The soil grains make contact with each other, forming a porous medium where the voids are usually filled with water.

Two principal approaches have been adopted to predict the soil response:

- Calibrated functions based on laboratory scaled tests
- Constitutive models

7.1.6 Pipeline

The ultimate goal of all numerical ice gouge simulations is to assess the ductility demands on the pipeline. Because of the soil–pipe interaction, the predicted burial depth is sensitive to the gouge depth, pipe diameter, relative stiffness, and operating conditions (e.g., temperature, pressure).

7.1.7 Wellheads

Literature reviews have identified a shortage of numerical models that include wellheads in the analysis. This is an important gap which needs to be bridged with further numerical efforts that include wellheads.

7.2 Numerical Modeling Challenges

Ice gouging problems can be very complex because they involve large deformations, contact definitions, material nonlinearity, and strain–dependent behavior. The finite element (FE) method provides a rigorous solution to complex problems where analytical

solutions cannot be easily obtained. Although a considerable research effort has been devoted to improve solution algorithms, challenges still need to be addressed.

7.2.1 Large Deformation Problems

Conventional geotechnical numerical modeling has not focused adequately on processes that involve large deformations and strains such as those encountered in an ice gouging event. It is evident that the FE approach includes many difficulties when solving geotechnical problems with large deformations. For example, contact problems and large mesh distortions may occur that can hinder convergence of the numerical solution. Mesh distortions associated with Lagrangian approaches prevent engineers from obtaining reliable solutions.

Consequently, new formulations that combine Eulerian and Lagrangian methods have been proposed during the last decade. These formulations include the Coupled Eulerian–Lagrangian (CEL) method and the Arbitrary Lagrangian–Eulerian (ALE) method. In addition, meshless methods, including the Smoothed Particle Hydrodynamics (SPH) method, have also been proposed in recent years.

Adaptive FE analysis is a methodology that automatically refines, coarsens, or relocates elements in an FE mesh to obtain improved solution accuracy and resolution. Although a significant amount of research has been devoted to adaptive FE analysis, this method remains complex and has not been widely used in nonlinear geotechnical problems.

7.2.2 Implicit and Explicit Schemes

The selection of an iterative scheme is crucial for the convergence of the numerical solution and the validity of the acquired results. The decision depends heavily on analysis type and model characteristics because the two types of iterative schemes available in commercial software—implicit and explicit—are not supported in all solutions.

The implicit method uses a non–iterative time integration procedure using very small time steps and does not check for solution convergence after every step. An appropriately selected time step (either calculated by the FE program or specified by the user) generally ensures stability and accuracy of the solution but may yield inaccurate results without any warning. Careful model setup, including appropriate mesh refinement and solution control parameters and post–analysis checks, are necessary to ensure the accuracy of the results.

Because of their formulations, explicit solutions provide opportunities to solve problems with a large number of degrees of freedom. In contrast to implicit schemes, which must

iterate to determine the solution to a nonlinear problem, the explicit scheme determines the solution without iterating by explicitly advancing the kinematic state from the previous increment. Even though a given analysis may require a large number of time increments, using an explicit scheme can be more efficient compared to the implicit scheme, which requires a large number of iterations.

Advanced Eulerian (mesh–based) continuum models typically use an explicit FE method because of its ability to handle very large deformations and complex contacts (e.g., ice–soil and soil–pipe). Another advantage of an explicit scheme is that it requires much less space and memory than the implicit scheme for the same simulation.

7.2.3 Contact Mechanics

In addition to the large mesh distortions discussed previously, contact problems may occur so that a convergent solution often cannot be found. Two types of widely used contact interactions are the kinematic contact method and the general method. The general contact algorithm enforces the use of the penalty methods and is less stringent when compared to the kinematic contact method. Another difference between kinematic and penalty contact is that the critical time increment is unaffected by kinematic contact, but it can be affected by penalty contact. The contact surfaces between the Eulerian and Lagrangian domains in numerical simulations are usually discretized using a general contact method.

7.2.4 Constitutive Modeling

Many disciplines have developed constitutive material models and, as a result, many different constitutive models have been proposed for different applications. Each model can be valid within its own realm of applicability but invalid in others. Regardless of the application, constitutive models must reasonably represent material behavior and contain a realistic number of parameters for calibration.

7.2.4.1 Soil

The area of greatest model uncertainty is that related to the characterization of soil response, commonly described as a soil constitutive model. Soil is a complex material that shows nonlinear, time–dependent, and often anisotropic behavior when loaded. This behavior can be generally attributed to non–constant stiffness, irreversible deformations, and changes in soil strength because of the loading history and pore pressure build–up under loading.

In an ice gouge event, large deformations occur, particularly within the shallow soil layers beneath the ice keel, which historically is the area where the greatest discrepancy between measured data and numerical prediction has been observed.

7.2.4.2 Ice

The selection of an appropriate constitutive law to model the behavior of ice rubble as a continuum medium, and its integration into a numerical model are major challenges. In addition, models used to characterize strong ice (e.g., iceberg) interactions with soft soils may not be appropriate for loosely bonded ice (e.g., first–year ice ridges) interactions with strong soils.

Glacier or sea ice is a highly heterogeneous material. At low strain rates, it behaves as a ductile material and is characterized by strain–rate hardening and thermal softening. At high strain rates, it behaves as a brittle material with the potential for sudden material collapse (Jordaan, 2001 [53]; Liferov, 2005 [75]). Envelopes and surfaces describing both ductile and brittle failure are difficult to incorporate in constitutive models for ice. To avoid the difficulties associated with material modeling, most numerical simulations treat ice as a rigid body.

7.3 Empirical Structural Approach

Engineering practice has often simplified the complex reality of soil structure interaction down to an equivalent set of springs. The structural approach is based on a representation of soil as a set of discrete springs and the pipe as specialized beam elements.

The deformation of the soil mass is modeled by the deformation of three springs with the equivalent stiffness in the axial longitudinal, transverse horizontal, and transverse vertical directions, as described by American Society of Civil Engineers (ASCE), 1984 [5]; and O'Rourke and Liu, 1995 [93]. This simplification is derived from the concept of subgrade reaction presented by Winkler, 1867 [132]. Refer to Figure 7.1 for an illustration of soil–pipeline interaction using the Winkler–type model.

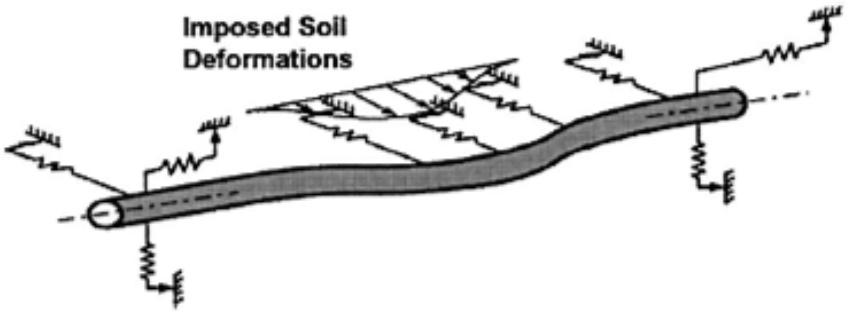

Figure 7.1: Soil–Pipeline Interaction using Winkler–type Model (ASCE, 1984 [5])

The nonlinear, stress–dependent, load–deformation characteristics of the springs are denoted as t–x, p–y, and q–z curves, representing the behavior of soil in the axial, transverse horizontal, and transverse vertical directions, respectively. The force displacement relationships are dependent on soil type and strength parameters, and they account for additional stress effects caused by the weight of the ice keel during the gouging process.

The most widely used force–displacement relationships have a hyperbolic or a bilinear form. The characterization of soil loads on pipelines is performed using three approaches:

- Use of theoretical soil mechanics to derive equivalent simplified relationships
- Use of numerical modeling of soil media through FE methods
- Use of physical models to develop empirical relationships

The pipeline can be modeled using suitable elements to simulate the effects of hoop stress caused by internal pressure and thermal expansion. The pipeline stress strain constitutive relationship can be defined by isotropic, elastoplastic behavior with a von Mises yield surface and isotropic hardening rule with appropriate material parameters. Ramberg–Osgood relationships can also be used.

The springs impart discrete reaction loads on the pipeline to represent the response of the soil continuum. The reaction loads are distributed along the longitudinal and circumferential pipeline axes. The soil spring formulations assume independent load–displacement behavior. This means that the springs do not account for pipeline/soil contact mechanisms (e.g., shear load transfer), and they lack physical significance with realistic, continuum soil behavior (e.g., load–dependent soil response).

The assumption of independent behavior may not be accurate under some conditions, such as limited clearance between the ice keel and the pipe crown or when the

subgouge deformation pattern is affected by the presence of the pipe. Reasonable agreement has been obtained between results from reduced scale physical model tests and simplified structural model prediction for pipe response to ice gouging.

7.4 Empirical Formulations of Subgouge Deformation

Pipeline deformation is mainly governed by soil displacement, soil stiffness, pipeline stiffness, and pipeline operating conditions. The first parameter, soil displacement, is the most critical factor. The prediction of subgouge deformation is usually based on empirical equations inferred from centrifuge model tests, specifically from the Pressure Ridge Ice Scour Experiment (PRISE) test program. Physical and numerical simulation results indicate that these empirical equations are conservative and overestimate the soil deformations produced by ice gouging. Refer to Figure 7.2.

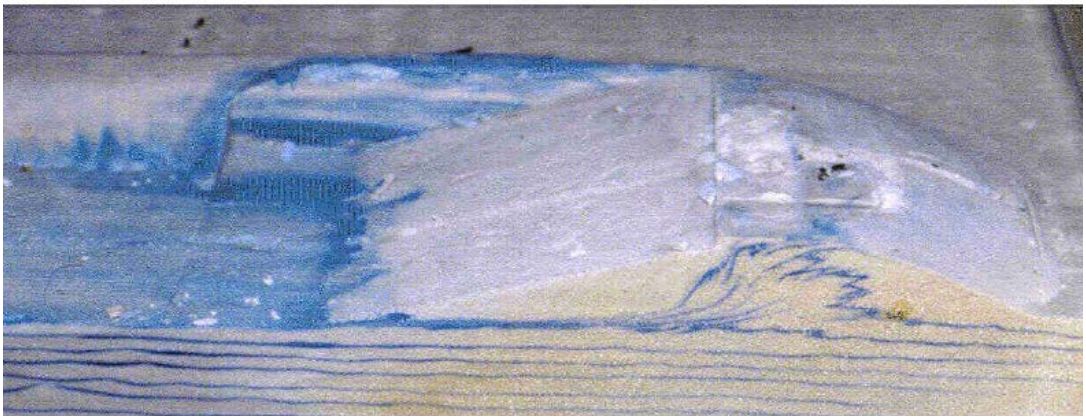

Figure 7.2: Typical Subgouge Failure Mechanism in Sand from PRISE (Phillips et al., 2005 [102])

7.4.1 Pressure Ridge Ice Scour Experiment

The PRISE joint industry research program investigated the stresses and soil deformations during ice gouging events (Phillips et al., 2005 [102]). This proprietary program was designed to develop the engineering framework to allow pipeline installation in Arctic regions. The program included a series of small–scale physical tests conducted in a geotechnical centrifuge to enhance the understanding of soil deformations and ice loads that occur during ice gouging events. This combined research effort provided the stimulus and a framework for the development and validation of numerical simulations.

A semi–empirical equation for horizontal subgouge soil deformations, commonly referred to as the PRISE equation, was derived from centrifuge tests in clay (Woodworth–Lynas et al., 1996 [134]).

The PRISE equation has three components:

- An equation for soil horizontal displacement at the base of the ice
- An equation for the reduction of horizontal displacement with depth
- An equation for the distribution of horizontal displacement in the transverse direction (horizontal and perpendicular to the axis of the gouge)

Subgouge deformations consist of horizontal and vertical soil displacements that vary with depth below the ice keel and with horizontal distance from the edge of the gouge. Soil horizontal displacement at the base of the ice is characterized by:

$$u(0,0,0) = 0.6\,(BD)^{0.5}$$

The displacement of the soil decreases as horizontal distance from the centerline of the gouge increases according to:

$$u(0,y,z) \,/\, u(0,0,z) = \begin{cases} 1 & if \;\; y/B < ¼ \\ ½(1 + cos(2y/B - ½)\pi) & if \;\; ¼ < y/B < ¾ \\ 0 & if \; y/B > ¾ \end{cases}$$

The displacement of the soil decreases as the vertical distance below the ice keel increases according to:

$$u(0,0,z) \,/\, u(0,0,0) = exp\,(-2z/3D)$$

The magnitude of vertical soil displacement below a gouging keel is similar to the gouge depth. The vertical soil movement decreases more slowly than the horizontal soil movement. The proposed vertical soil deformations are given by:

$$v(0,0,0) = D$$

$$v(0,0,z) \,/\, D = exp\,(-z/3D)$$

Where:

u (x,y,z) is horizontal soil deformation as a function of distance from the midpoint of the keel base along the gouge line, across the gouge line, and below the gouge base

v (x,y,z) is vertical soil deformation as a function of distance from the midpoint of the keel base along the gouge line, across the gouge line, and below the gouge base

D is gouge depth

B is gouge width

It must be noted that limited data is available on subgouge deformations in sand soils; therefore, no conclusion can be drawn on the subgouge deformation of sand. Available test data shows that the horizontal deformation is greater in dense sand than in loose sand. This is a result of the stress levels and the dilation experienced by the different soil types.

7.4.2 C–CORE (1995), Nixon et al. (1996)

The structural FE software package PIPSOL was used in the PRISE studies to analyze pipeline/soil interaction events and to predict load effects on the pipeline. The software is based on an idealized pipeline/soil interaction method that incorporates a nonlinear Winkler–type foundation model to define soil reaction loads. The model uses specialized beam elements to account for internal pressure, temperature, axial force, and nonlinear flexural behavior.

The PIPSOL model was adapted for the PRISE study to include the characterization of free field subgouge deformations, nonlinear soil load–deformation relationships, and lateral pipeline/soil interaction behavior (C–CORE, 1995 [18] and Nixon et al. 1996 [89]).

7.4.3 Kenny et al. (2004)

Kenny et al. (2004) [59] developed a three–dimensional structural FE model to idealize the continuum pipeline/soil interaction behavior. The pipeline was modeled using 3–node quadratic elements (assuming constant hoop stress), and the soil response was modeled by 2–node nonlinear spring elements. Soil response was defined by nonlinear, hyperbolic relationships based on the guidelines of ASCE, 1984 [5]. The force–displacement relationships were defined at the pipeline spring line and accounted for an increased effective burial depth caused by ice feature overburden pressure. The pipeline stress–strain constitutive relationship was defined by isotropic, elastoplastic behavior with a von Mises yield surface and isotropic hardening rule. The stress–strain relationship was defined using the Ramberg–Osgood formulation.

The work of Kenny et al. established a probabilistic methodology to optimize burial depth requirements for the mitigation of ice gouge hazards.

The authors recommend that future work should:

- Quantify and reduce data and model uncertainty with respect to ice keel–seabed interaction to define geotechnical loads.
- Define load transfer mechanisms for pipeline–soil interaction.
- Establish limit state criteria for a reliability–based design methodology.

7.4.4 Peek and Nobahar (2012)

Peek and Nobahar [99] used a coupled model and an uncoupled model to investigate the necessary burial depth of pipelines. In the uncoupled model, the soil is represented by a set of nonlinear Winkler springs attached to the pipe at one end while the displacement is applied at the other end of the springs. In the coupled models, soil is treated as a 3D continuum medium, and the ALE Abaqus Explicit scheme is employed, similar to previous efforts of the same author (Nobahar et al., 2007 [90]).

The benefit of this work lies in the comparison of the soil deformation and pipeline response predictions derived from the two different approaches. The authors highlighted that the superposition error caused by adding the subgouge deformations to the soil displacements because of the pipe loads was more influential than the coupling errors resulting from directional coupling of Winkler springs in axial, lateral, and vertical directions.

7.5 Continuum Approach

7.5.1 Overview

Continuum models resolve the coupled interactions between ice, soil, and pipe more accurately; therefore, they allow a more realistic representation of the ice gouging process. These models usually predict lower subgouge soil displacements and lower pipeline strain demand compared to spring–based soil–structural models, which have the effect of reducing burial depth requirements significantly.

7.5.2 Lagrangian

In the Lagrangian formulation, the time and material coordinates are independent, but the mesh deforms with the material. The Lagrangian coordinate of each mesh node moves with the material (Figure 7.3). Material coordinates of material points are time invariant, and no material passes between elements. Element quadrature points remain coincident with material points, and boundary nodes remain on the boundaries. Therefore, boundary conditions and interface conditions are easily applied. The characteristics of the Lagrangian formulation enable easy free–surface (interface) tracking between different materials and simplify the application of boundary conditions. Furthermore, time independency facilitates the treatment of materials with history–dependent constitutive relations. This formulation makes the modeling of history–dependent materials (e.g., soil) possible. On the other hand, when a large deformation occurs, the Lagrangian formulation distorts the mesh. Some extensions of the traditional Lagrangian formulation, such as the Total Lagrangian, the Updated Lagrangian, and the

Corotational formulations, have been developed to tackle large deformations. These formulations use mesh update techniques, where computations refer to previous configurations. However, when large deformations occur, the use of a distorted mesh as the reference domain is problematic.

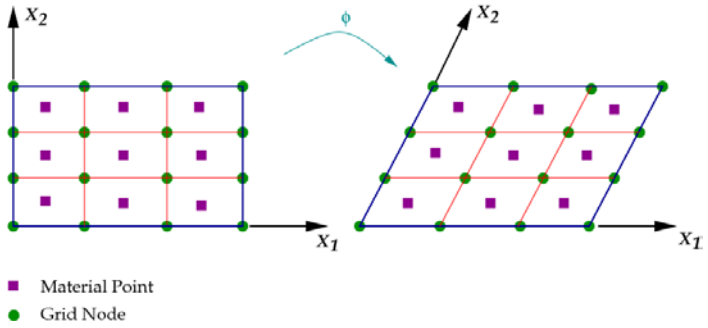

Figure 7.3: Lagrangian Mesh Description

7.5.3 Early Studies

Investigations in the 1990s examined the application of continuum FE methods to analyze ice gouge events. These studies encountered numerical problems such as poor convergence and solution instability caused by severe mesh distortion.

Several studies that were part of the PRISE research program developed 2D continuum FE modeling procedures for ice gouging , as presented in

- C–CORE, 1993 [17] and 1995 [19]
- Lach, 1996 [66]
- Lach and Clark, 1996 [67]
- Yang et al.,1993 [137]
- Yang and Poorooshasb, 1997 [136]).

The preliminary numerical investigations considered an elastic–perfectly plastic soil material model with the Drucker–Prager yield criterion (e.g., C–CORE, 1993 [17]; Yang et al., 1993 [137]; Yang and Poorooshasb, 1997 [136]). The ice keel to seabed interaction was defined by displacement boundary conditions with the assumption of a frictionless interface. These studies evaluated seabed reaction forces, pore water pressure, soil displacement vectors, and plastic strain contours. Surface horizontal displacements that were less than 50% of the gouge depth were mobilized before numerical instability halted the analysis. Despite these shortcomings, the analysis provided evidence that Lagrangian, 2D continuum FE analysis modeling was a reasonable engineering tool to model the magnitude and distribution of subgouge deformation profiles when compared with the PRISE centrifuge experimental data.

C–CORE and Lach and Clark implemented improvements to the numerical modeling procedure to include finite strain formulation and two–phase material behavior based on a modified Cam–Clay model. In addition, they used rigid surface interface elements to account for the ice keel/seabed boundary effects (C–CORE, 1995 [19]; Lach and Clark, 1996 [67]).

7.5.4 Yang and Poorooshasb (1997)

One of the early studies on ice gouging used 2D and 3D FE models to understand the free field response and pipe response during ice gouging on drained sand.

The pipeline deflection profiles obtained from both 2D and 3D analyses did not differ significantly. This is because of the assumption that the pipe moves with the soil without relative slip and that the stiffness of the pipe is relatively small compared to that of soil.

Yang and Poorooshasb observed that the presence of pipeline with a cover depth equal to the gouge depth did not influence the free field gouge displacements for small gouge movements. The analysis assumed perfect pipeline/soil contact with no slippage. The 3D FE analysis identified issues of surcharge clearance mechanisms, but steady–state conditions were not achieved because of limited mesh size and numerical instability. The analysis, however, provided an indication of the extent and the shape of lateral deformation profiles. The shape and size of the deformation zones is illustrated in Figure 7.4 and Figure 7.5. The authors questioned the numerical accuracy because of the severe mesh distortion, and they identified the need for a re–meshing technique.

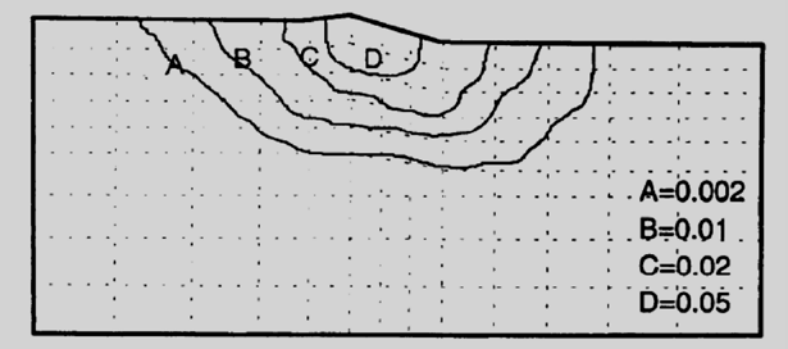

Figure 7.4: Equivalent Plastic Strains Contours (Yang and Poorooshasb, 1997 [136])

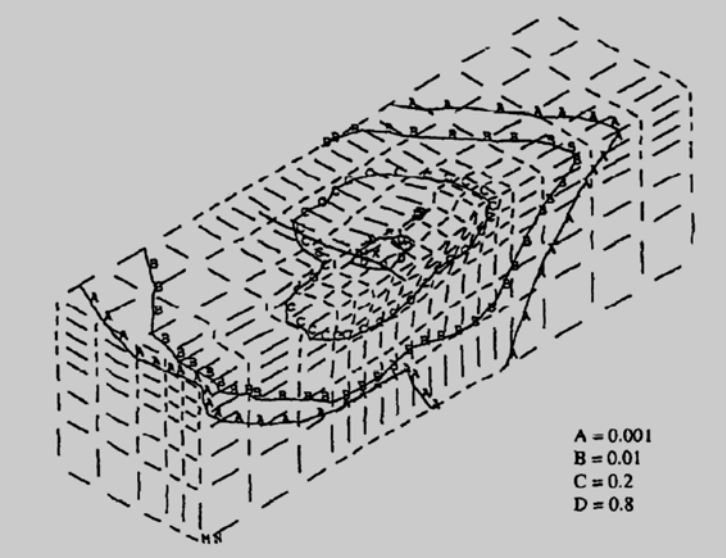

Figure 7.5: Equivalent Plastic Strains Contours (Yang and Poorooshasb, 1997 [136])

7.5.5 C–CORE (1997a, 1997b,1998), Phillips et al. (2004)

C–CORE [20] [21] [22] and Phillips et al. [104] extended the earlier PRISE investigations using 2D FE analysis to include the simulation of ice gouge events in dilatant soil such as sand or compact silt. (Figure 7.6 shows the configuration of the model.) Ice keel horizontal translations of 10 gouge depths were achieved. A Mohr–Coulomb soil model was adopted for a parametric study that examined the variation of elastic modulus with confining stress, friction angle, dilatancy angle, gouge depth, soil cohesion, permeability, and ice keel interface friction angle. The study concluded that the elastic modulus of the soil strongly influenced the subgouge deformation results.

Numerical analyses revealed trends that confirmed the magnitude and extent of subgouge deformations observed in the centrifuge tests. The plastic deformation zone extended to a few gouge depths and was consistent with other studies conducted under PRISE. When compared with the previous FE studies on soft clays conducted by the same researchers, the numerical analysis for dilatant materials was less successful in supporting the PRISE centrifuge experimental data.

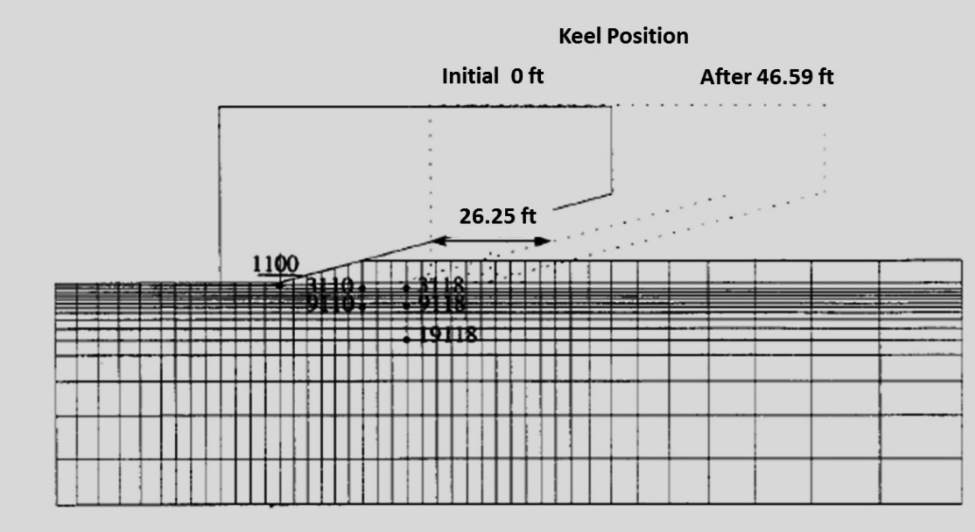

Figure 7.6: Finite Element Mesh for Scour Depth (C–CORE, 1998 [22])

7.5.6 Nobahar et al. (2004)

Nobahar (2004) [91] performed two–dimensional (2D) simulations of seabed scour using the commercial FE package, Abaqus Explicit. The seabed was modeled as undrained clayey material using the total stress concept with a simple von Mises yield criterion as the plasticity model. A constant undrained shear strength of 3.63 psi (25 kPa) and an initial embedment depth to reach the required scour depth were assumed. Simulations of scour in the absence of a buried pipe as well as scour with soil–pipe interaction were performed in two dimensions.

The objective of the research was to compare monolithic coupled versus staggered analyses results with respect to the keel–soil–pipe interaction. The analyses indicated that an ice gouge event with keel depth approaching or even exceeding pipeline cover depth does not necessarily lead to a catastrophic failure of the pipeline.

7.6 Arbitrary Lagrangian–Eulerian

7.6.1 Overview

During the ice gouging process, the soil medium undergoes very large deformations in front of and underneath the ice feature. Performing finite–element analyses without the mesh adaptive technique resulted in severe numerical difficulties as reported by Kenny et al., 2005 [58]; Lach, 1996 [66]; Lach and Clark, 1996 [67]; and Yang and Poorooshasb, 1997 [136]. The most important difficulty was associated with element distortion that occurs because of large deformations, 2D model idealizations, or both.

Researchers have used the Arbitrary Lagrangian–Eulerian (ALE) approach to solve complex technical problems in a variety of engineering fields such as fluid–structure interaction, large deformation solid mechanics (Donea et al., 2004 [32] and Wang and Gadala, 1997 [128]), and geomechanics with respect to nonlinear, large deformation problems involving strain localization (e.g., Zienkiewicz et al., 1995 [138]).

In the ALE formulation, the nodes of the computational mesh may be moved with the continuum in normal Lagrangian fashion or held fixed in the Eulerian manner. The nodes can also be moved in some arbitrarily specified way to give a continuous rezoning capability. Because of this freedom in nodes movement, the computational mesh offered by the ALE description provides better handling of the large distortions of the continuum than a pure Lagrangian method and more resolution than is afforded by a pure Eulerian method (Donea et al., 2004 [32]).

However, these advanced numerical procedures have some restrictions with respect to element selection (e.g., type, order) for non–adaptive mesh interfaces where there is a change in the material properties (e.g., native and backfilled soil at a trench interface). In addition, soil plasticity models are limited to single–phase material behavior (i.e., no pore pressure effects).

In the ALE method, the analysis undergoes three major steps:

1. First, a standard Lagrangian FE analysis is conducted.
2. Next, the FE mesh is remapped, based on smoothing criteria. The remapping algorithms can be based on the stresses and the deformations obtained in the previous time step or on the mesh topology.
3. The third step is the advection phase. In this step, the discretized strain, mass, and momentum parameters are computed for each node of the new mesh using the laws of conservation of mass and momentum.

Figure 7.7 shows an example of ALE remapping in comparison to the Lagrangian and Eulerian schemes.

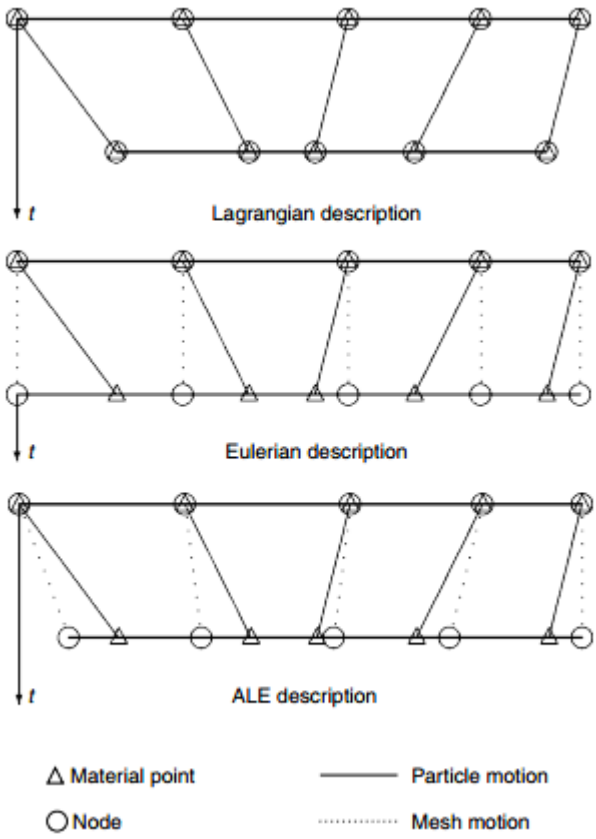

Figure 7.7: One–dimensional Example of Lagrangian, Eulerian, and ALE Mesh and Particle Motion (Donea et al., 2004 [32])

7.6.2 Kenny et al. (2007)

Kenny et al. [57] implemented an ALE modeling approach using the software package Abaqus Explicit to assess the magnitude and extent of subgouge deformations. This study modeled soil plasticity using von Mises criterion and total stress analysis. The test conditions consisted of a rigid ice keel gouging through a deformable clayey seabed with an undrained shear strength of 3.63 psi (25 kPa). (Refer to Figure 7.8.)

In the Kenny et al. study, the gouge depth and width were 4.79 ft. (1.46 m) and 32.81 ft. (10 m), respectively, with an attack angle of 15° to the horizontal.

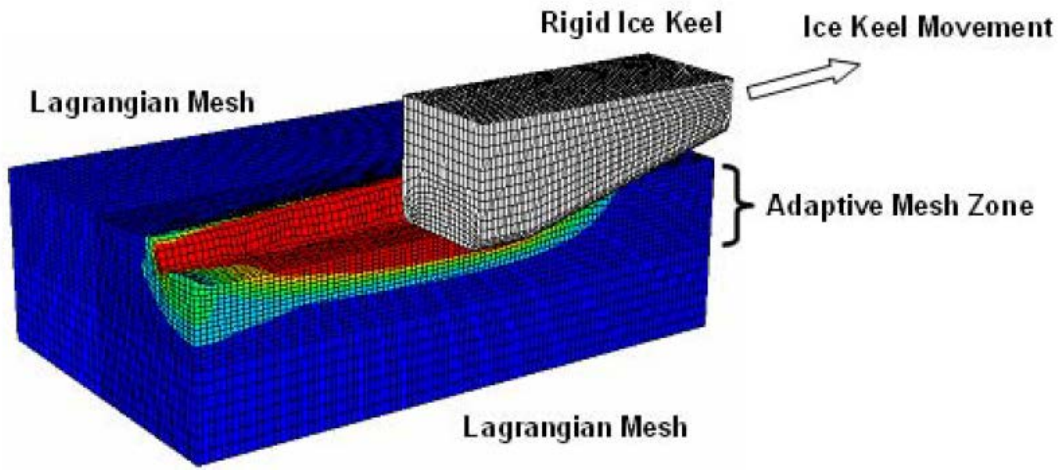

Figure 7.8: Finite Element Model of an Ice Gouge Event (Kenny et al., 2007 [57])

The magnitude and extent of subgouge deformations was monitored by defining an array of tracer particles as presented in Figure 7.9.

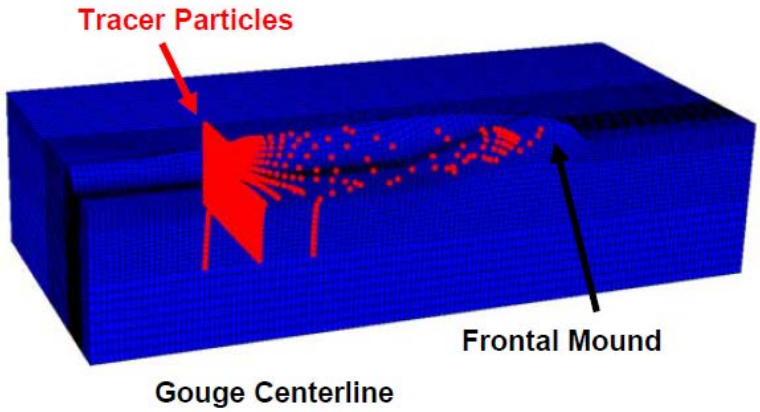

Figure 7.9: Tracer Particle Array Used to Characterize Subgouge Deformations (Kenny et al., 2007 [57])

Figure 7.10 presents a comparison of the vertical profile of subgouge deformations with depth beneath the ice keel as predicted by the ALE procedures with the centrifuge modeling data.

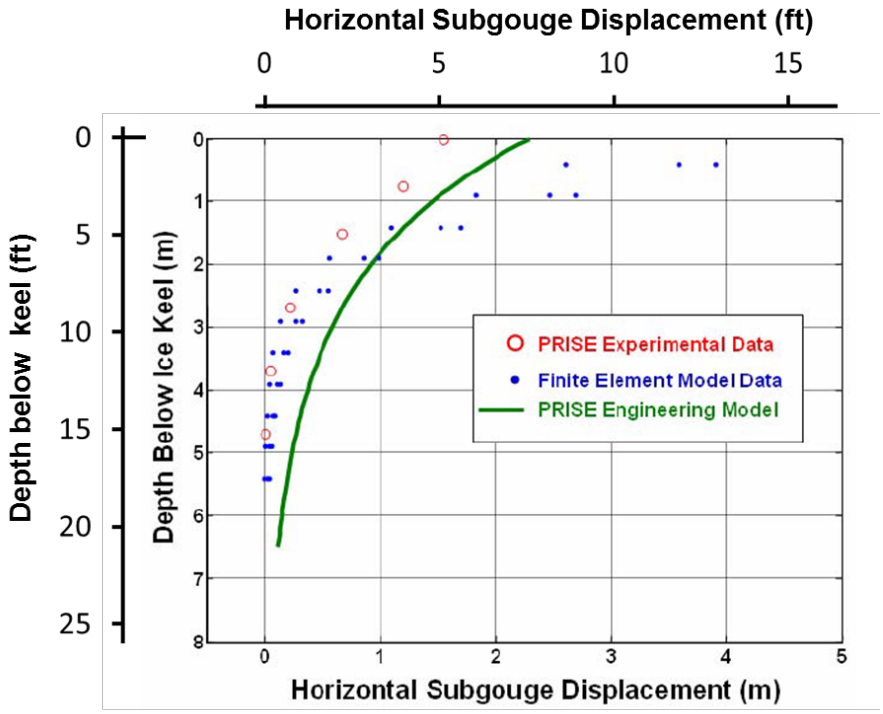

Figure 7.10: Profile of Subgouge Deformations from Numerical and Reduced Scale Centrifuge Modeling Studies (Kenny et al., 2007 [57])

The soil failure mechanism observed in the numerical solutions [57] involved:

- The build–up of soil surcharge in front of the advancing ice keel
- A rupture surface through the seabed penetrating the mud line
- A dead wedge trapped adjacent to the inclined ice keel face
- Subgouge deformations extending beneath the base of the ice keel.

These findings were consistent with the soil failure mechanism as described by Been et al., 1990 [14].

Figure 7.11 shows the distribution of equivalent plastic strains.

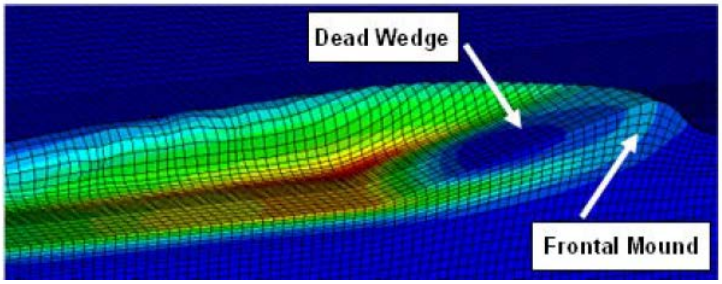

Figure 7.11: Distribution of Equivalent Plastic Strains (Kenny et al., 2007 [57])

7.6.3 Nobahar et al. (2007)

The Nobahar et al. study [90] presents an explicit continuum FE analysis of pipe/soil and pipe/soil/ice keel and compares the results from continuum finite element analysis with Winkler–type analysis for the same analyzed problem. The study considers ice features with an attack angle of 30° crossing the pipeline path in the transverse direction (refer to Figure 7.12). The pipe/soil contact interface was evaluated through a frictional contact surface allowing finite sliding and separation between the two surfaces based on Coulomb frictional criterion.

The report notes that the ice feature attack angle and the interface friction affected the failure mechanism of the soil and the depth of the failure plastic wedges. The authors observed that soil failure occurs at lower load levels for undrained loading of cohesive clayey soil when it is loaded simultaneously in various directions compared with independent loading in a single direction. The pipeline responses in terms of stresses and strains were lower than those estimated using a conventional Winkler type structural approach and the decoupled pipe/soil/ice keel interaction approach. Figure 7.13 shows an estimate of the horizontal and vertical forces mobilized during gouging through two clayey seabeds (one soft and one stiffer). Nobahar et al. concluded that the structural approach provided reasonably conservative results for the studied parameters and soil inputs, but the coupled pipe/soil behavior requires additional studies and verification.

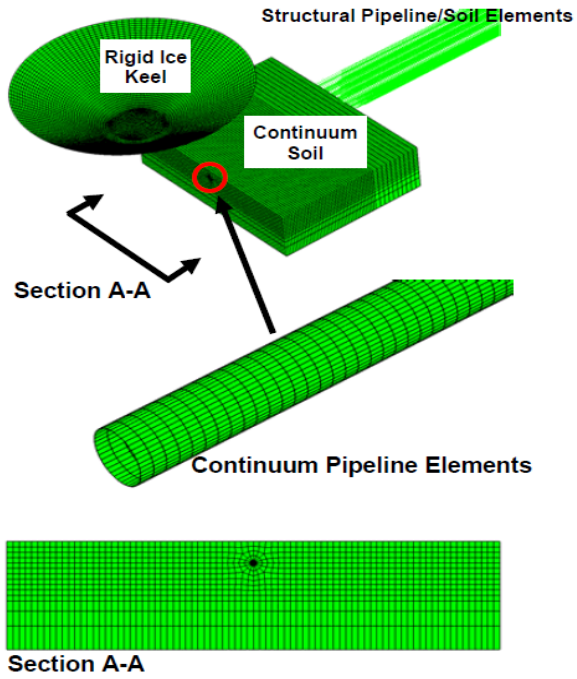

Figure 7.12: Fully Coupled Ice Keel/Seabed/Pipeline Interaction Model (Nobahar et al., 2007 [90])

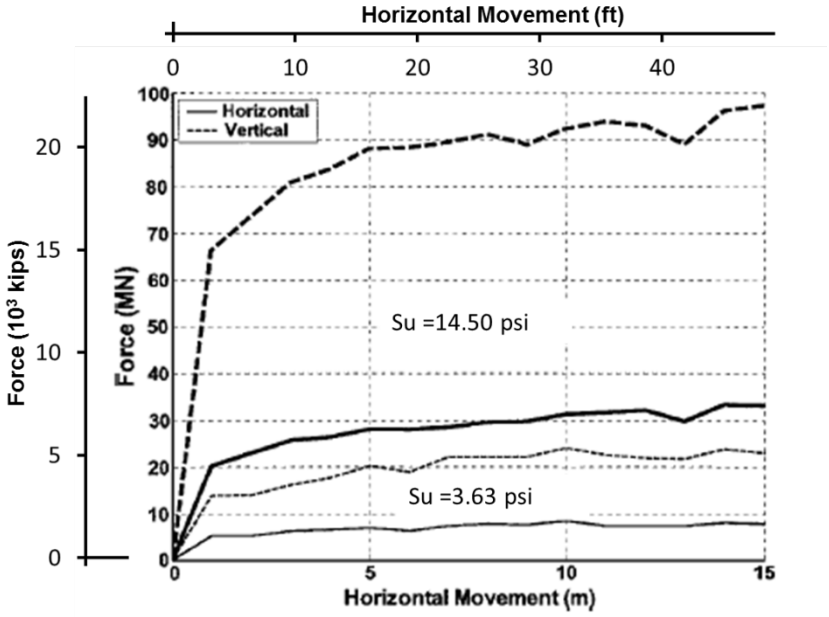

Figure 7.13: Horizontal and Vertical Gouging Forces for 4.92 ft. (1.5 m) Deep Gouge for Soil Types I and II (Nobahar et al., 2007 [90])

7.6.4 Konuk and Gracie (2004a)

Konuk and Gracie [61] developed an FE model using an LS–DYNA® explicit method. The researchers used a Cap model (a constitutive model where shear and compaction surfaces are combined to form a smooth, continuous surface) for the soil, assuming undrained conditions. The ice ridge was idealized as a rigid conical indenter with the ridge angle varying from 15° to 45° (see Figure 7.14). Scour width was 49.21 ft. (15 m), and the size of the model ensured negligible boundary effects and steady state.

The results indicated a logarithmic relationship between the subscour deformation and the ridge angle because the change in subscour deformation from 30° to 15° (angle) was exponentially higher than the change from 45° and 30° (angle). Figure 7.15 provides a snapshot of the deformed mesh for the 45° (angle) case.

On the other hand, the subscour deformation magnitude increased proportionally with the scour depth. The vertical reaction force on the indenter increased by a rate similar to the rate of increase in subscour deformations, suggesting that the reaction force applied by the ice sheet was independent of ridge geometry and that the buoyancy contribution was relatively small.

The results showed that at lower ridge angles, the subscour deformations and the ice–soil reaction forces were very sensitive to the ice ridge angle. The authors implied that there is a correlation between the scour depths and the ridge angles (deeper scours are formed by higher slope ridges), but they highlighted the need to verify their findings against field testing.

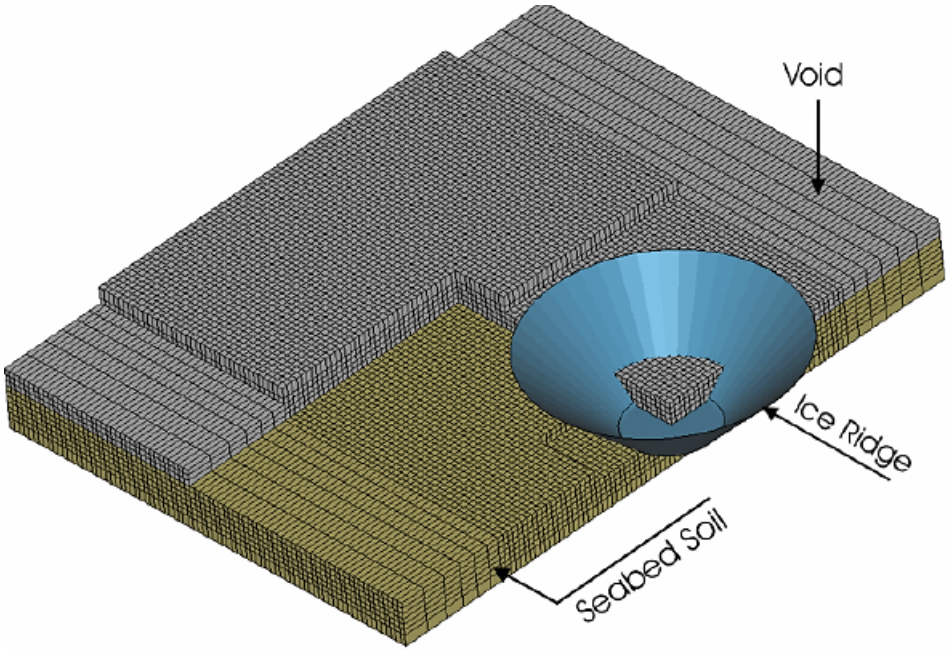

Figure 7.14: Illustration of the FE Model (Konuk and Gracie, 2004a [61])

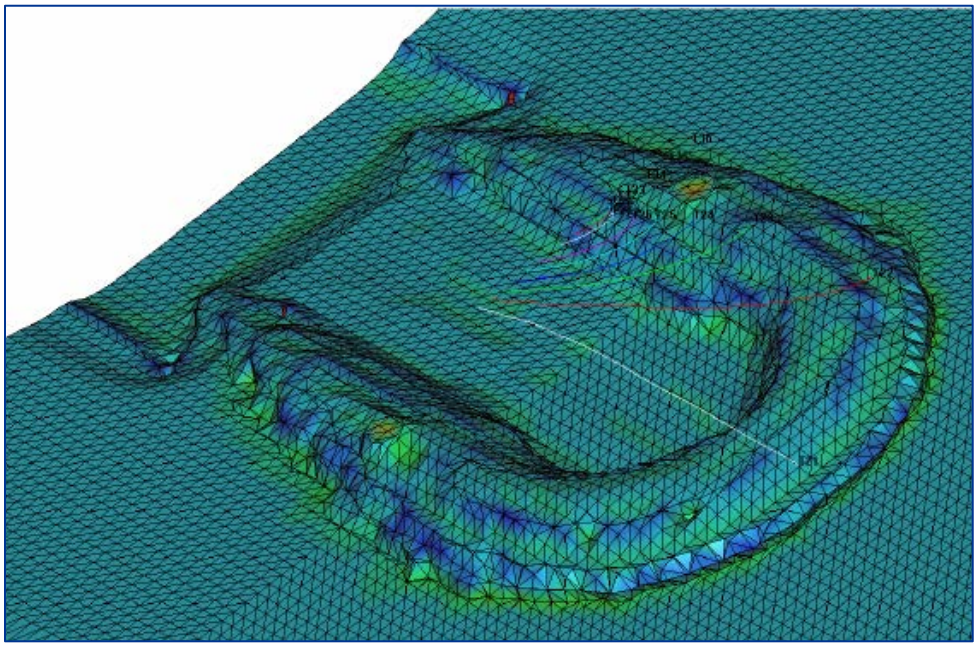

Figure 7.15: Typical Output from FE Model with 45° Ice Ridge (Konuk and Gracie, 2004a [61])

7.6.5 Konuk and Fredj (2004b)

Konuk and Fredj [63] conducted another study that focused on the effects of the pipeline trench on the scour process and the forces transmitted to the pipeline.

The authors used two versions of a conical indenter in the study: an indenter width of 49.21 ft. (15 m) and ridge angles of 30° and 45°, respectively. The 36–inch diameter pipe was modeled as a rigid structure and was kept stationary at its original position. Soil–pipe contact was defined, similar to the soil–ice contact using penalty functions. Two types of soils that were somewhat softer than the ambient seabed soils were used to cover the pipeline and fill the trench modeled with a Cap soil constitutive model.

Konuk and Fredj observed the significance of the trench in the soil deformation profile (refer to Figure 7.16), which generated a very different discontinuity in the presence or absence of the pipe and trench. Horizontal loads were cyclic, varied gradually, and were not significantly affected by the ridge angle. The force on the pipe increased until the front of the ice ridge reached the pipeline axis, and then it decreased at the same rate as the increase, eventually becoming negative. The horizontal loads pushed the pipeline forward and then backward by about the same magnitude (peak average force per unit length of pipe is about 0.67 kips/ft (1 ton/m)). Refer to Figure 7.17.

In the Konuk and Fredj study, the pipe was fixed and rigid, implying that peak calculated loads in the ALE FE model were an ‘upper limit,’ depending on the soil properties. However, these loads were somewhat lower than the loads calculated by the Winkler (structural) models. Intuitively, the stiffer the infill soil is, the higher the horizontal loads experienced by the pipeline will be. Similarly, vertical pipeline loads were significantly higher for the stiffer soil.

The authors recommended that a more detailed study of infill properties and the analysis of unburied flexible pipe could be beneficial for optimum design protection purposes.

Figure 7.16 presents the deformation profiles produced by the 30° and 45° (angle) angle indenter, with and without the trench and using two different type of soil for trenching material. The effect of the trench to the pipe response is apparent.

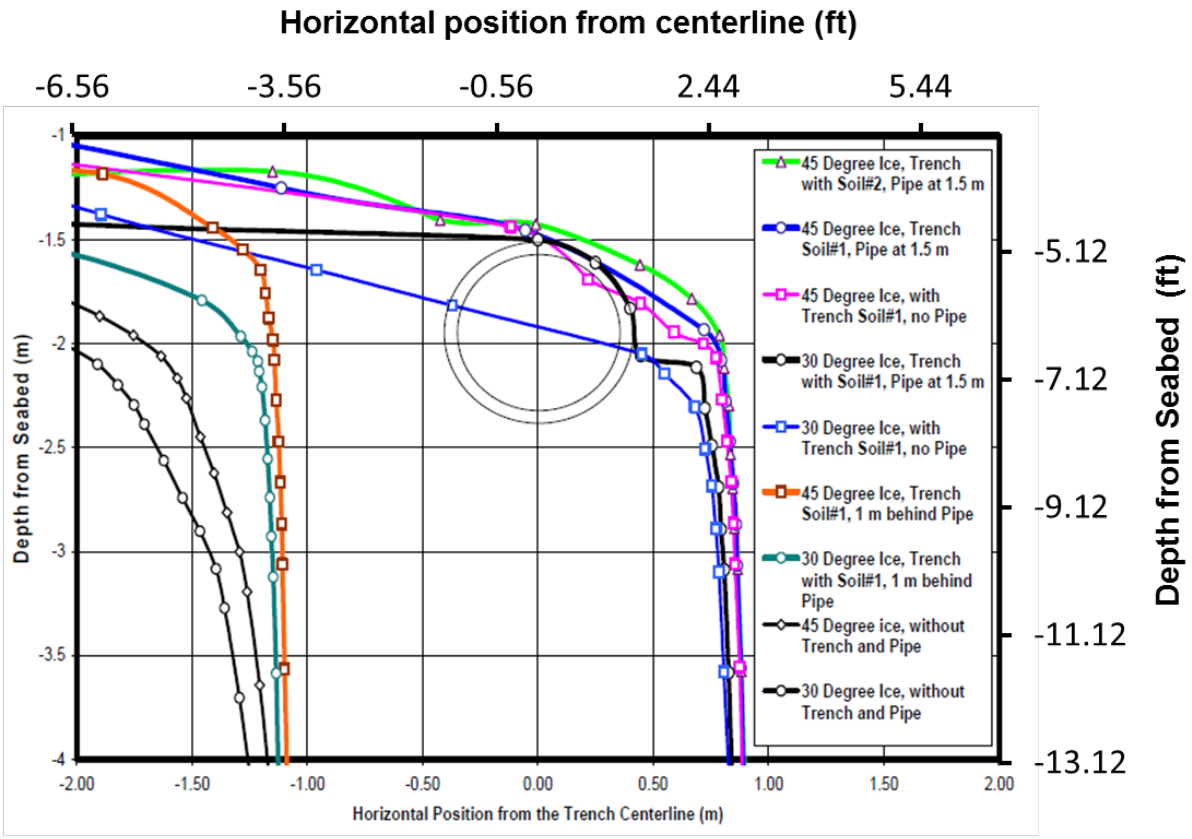

Figure 7.16: Comparison of Soil Deformation Profiles (Konuk and Fredj, 2004b [63])

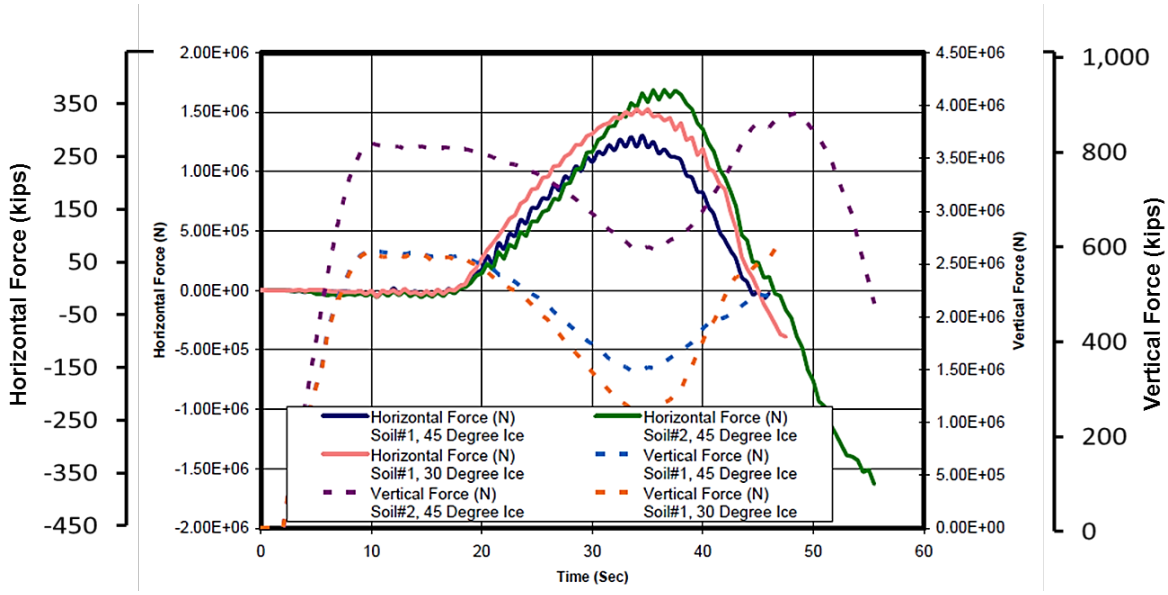

Figure 7.17: Vertical and Horizontal Pipe Forces (Konuk and Fredj, 2004b [63])

7.6.6 Fredj et al. (2008)

Fredj et al. conducted a parametric study to define the governing parameters for High Pressure/High Temperature (HP/HT) pipeline design. The study focused on the effects of the operating pressure and thermal loads on the pipeline response.

Comparison of the two scenarios indicates differences in the maximum pipe displacement. In the case of an operating pipe, this displacement is greater than for the cold unpressurized pipe (130% in the vertical direction and 150% in the lateral). Bending moment and curvature showed the same trend. Explicitly, axial forces developed in an operating pipe caused by pressure and thermal loads have an important influence on the pipeline's response in terms of stresses and strains. The results presented in Figure 7.17 show that the maximum pipeline displacement increases with the gouge width. However, plastic strains do not follow the same trend.

The study used the ALE model and two Winkler springs models to simulate a single ice scour event. One spring model used pipe elements, while the other used shell elements. The results derived from the two different formulations were in good agreement with each other. However, compared to the continuum model, both formulations predicted higher displacements for narrower gouge width (refer to Figure 7.18).

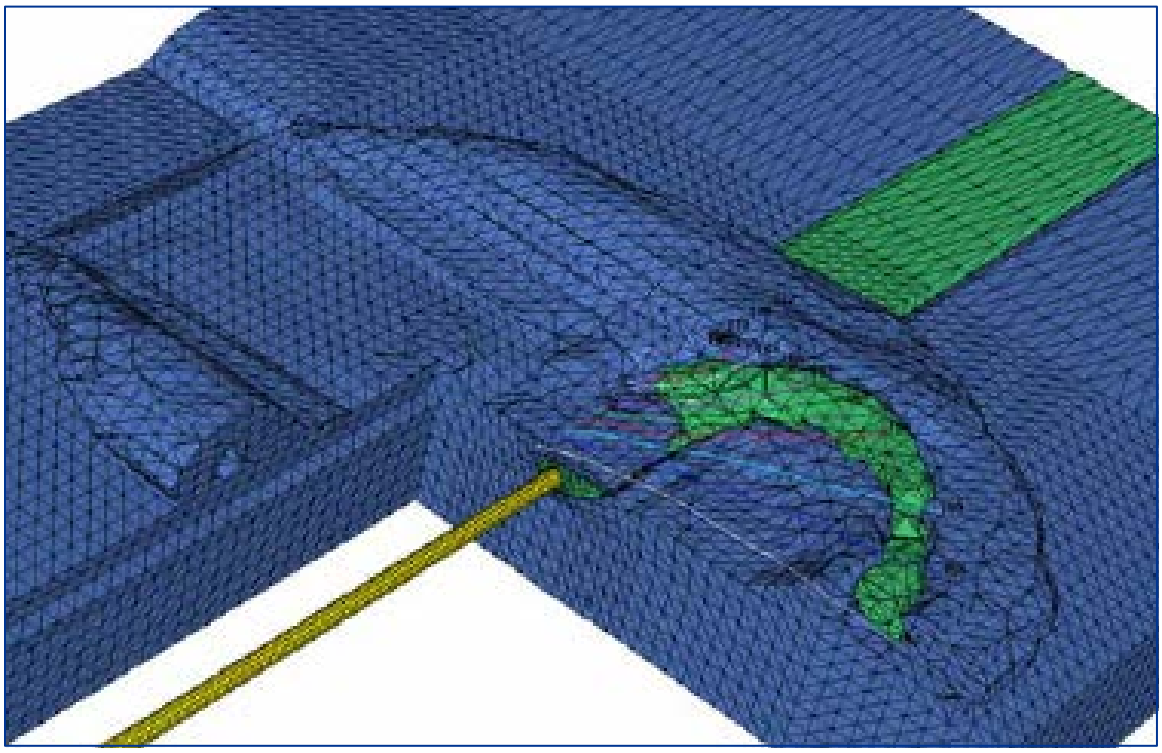

Figure 7.18: Visualization of Typical Output from the ALE FE Model – 45–degree Ice Ridge (Konuk and Fredj, 2004b [63])

The research concluded that for a given pipe geometry and operating condition, there is a critical gouge width that maximizes pipe bending moments and strains. The study also assessed the influence of trench bottom imperfections, indicating that pipeline misalignments of 0.98 ft. (0.3 m) in the vertical or lateral directions have a significant impact on pipe response. Refer to Figure 7.19 and Figure 7.20.

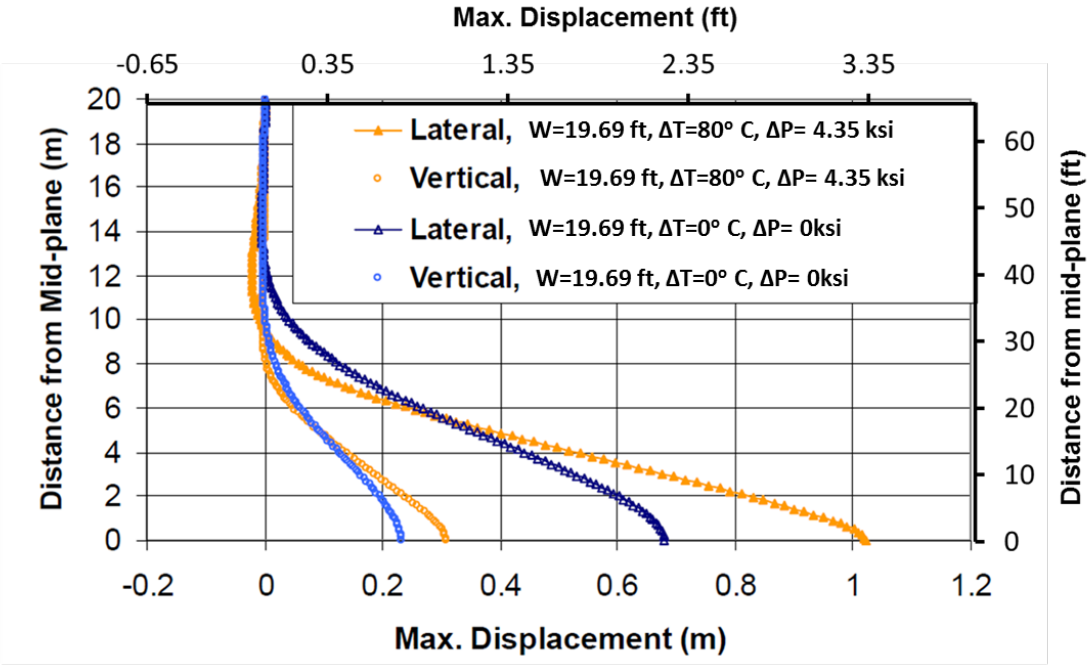

Figure 7.19: Comparison of Lateral and Vertical Displacement Pressurized vs. Unpressurized (Fredj et al., 2008 [40])

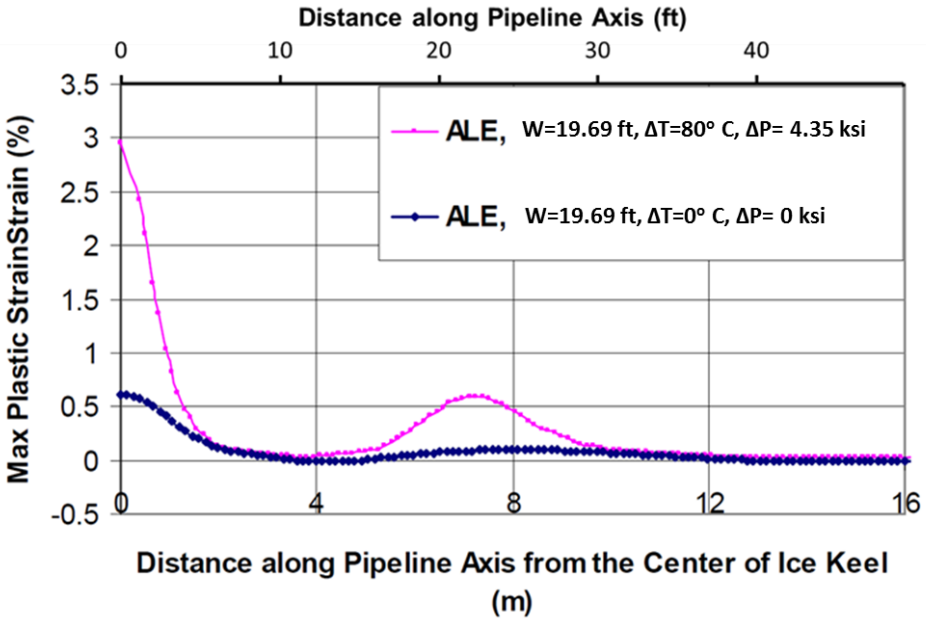

Figure 7.20: Comparison of Plastic Strain Pressurized vs. Unpressurized (Fredj et al., 2008 [40])

7.6.7 Eskandari et al. (2010, 2011)

Eskandari et al., 2010, 2011 [36] [38] developed a three–dimensional (3D) FE model in Abaqus Explicit to simulate the ice gouging events in sand as part of the Pipeline Ice Risk Assessment and Mitigation (PIRAM) Joint Industry Project (JIP). The focal point was a realistic stress–strain behavior based on the critical state soil mechanics using the NorSand constitutive model.

The NorSand model applies two principles:

- A unique locus exists for critical state in the void ratio–stress space.
- The soils move toward the critical state as the shear strain evolves.

This study used the volume constraint method and extended the NorSand critical state model to simulate the undrained behavior of soils. The rigid keel was idealized as a conical frustum with a diameter of 32.81 ft. (10 m) at the base and an attack angle of 30° (Figure 7.21). The soil had a maximum shear stress of 21.75 psi (150 kPa). For the keel roughness, a friction coefficient μ of 0.2 was chosen, and the keel base was at a depth of 3.28 ft (1 m). The deformations and associated reaction forces (vertical, horizontal) were different from those of Phillips and Barrett, 2011 [100], mainly because of the difference in the assumed keel roughness. The results of the analyses are in good agreement with triaxial laboratory tests as published by Jefferies and Been, 2006 [52].

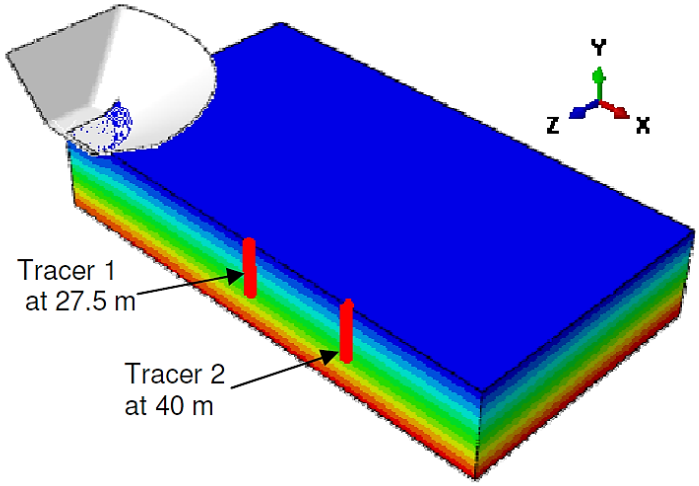

Figure 7.21: Keel and Soil Assembly in FE Model (Eskandari et al., 2011 [38])

The study investigated mesh dependency of the ice gouging model using the NorSand critical state model and the two mesh densities. The results observed were scarcely dependent on the selected levels of discretization (Figure 7.22).

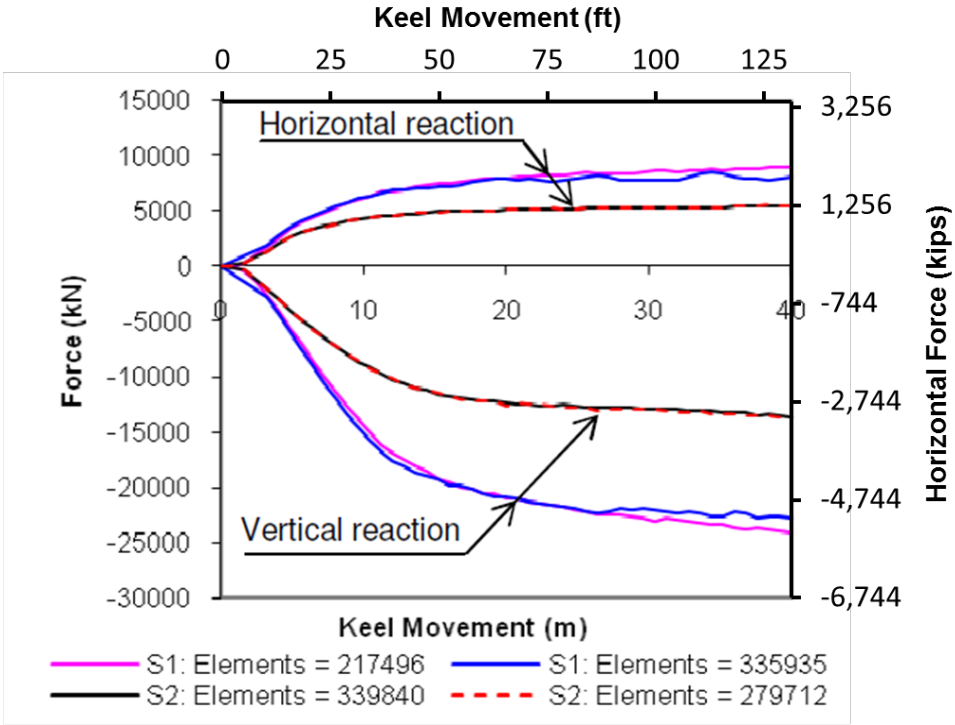

Figure 7.22: Mesh Dependency in NorSand (Eskandari et al., 2011 [38])

Figure 7.23 shows the response in terms of vertical keel reaction after 131.23 ft. (40 m) of keel displacement, depending on the critical state ratio, M_{tc} and state parameter, ψ. The reactions increase with both soil strength and initial sand density.

The preliminary analyses of Eskandari et al. showed that the NorSand model is capable of predicting ice gouging behavior, but further study is required to calibrate the model performance.

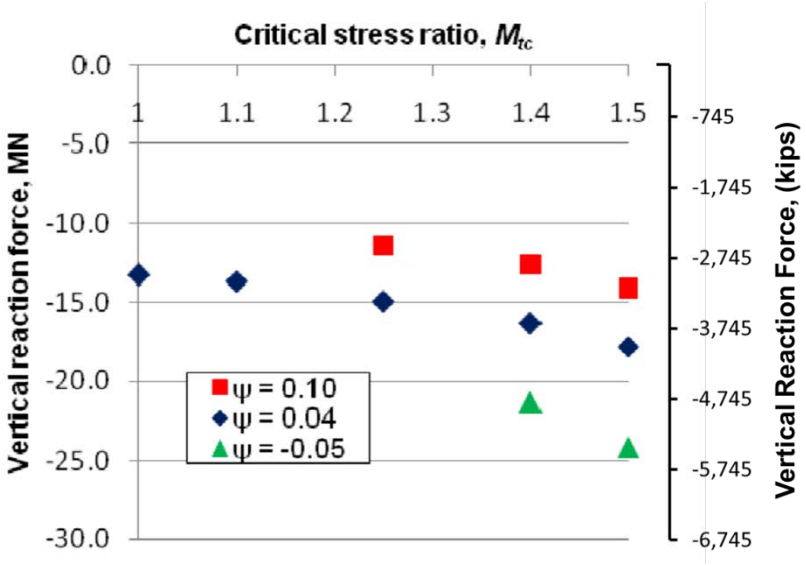

Figure 7.23: Variation of Vertical Force with Critical State Ratio M_{tc} and State Parameter ψ (Eskandari et al., 2011 [38])

7.6.8 Eskandari et al. (2012)

This Eskandari et al. (2012) [37] study focused on the model output results such as keel reaction forces, subgouge deformation, frontal mound height, and failure mechanism. Among these outputs, the subgouge deformation is consequential because the main target of the ice/soil study was the development of a categorical understanding to determine the optimum burial depth of offshore pipelines.

The Eskandari et al. model is identical to the medium–sized meshed model of the Phillips and Barrett, 2011 [100] study with the exception that the Eskandari model used an ALE formulation rather than the CEL formulation.

The state parameter and the critical friction angle are the soil parameters chosen for sensitivity analyses. Other parameters whose significance were also assessed are keel attack angle and gouging depth. An increase of the gouging depth directly affected the subgouge deformation, extending it deeper into the seabed.

The study emphasized that critical stress ratio becomes more influential for deeper gouges in contrast to the shallower gouging depths, and likewise for denser soils compared to loose soils. Eskandari et al. concluded that the combination of the critical stress ratio and the state parameter has an evident influence on the seabed subgouge deformation rather than the effect of the critical stress ratio alone.

These analyses were used to propose an equation to estimate the horizontal reaction forces for the conditions studied.

7.6.9 Peek and Nobahar (2012)

The Peek and Nobahar (2012) [99] study used two types of models, a coupled and an uncoupled, to investigate the necessary burial depth of pipelines. In the uncoupled model, the soil was modeled by a set of nonlinear Winkler springs attached to the pipe at one end with displacement applied at the other end of the springs. In the coupled models, the soil was treated as a 3D continuum medium and the ALE Abaqus Explicit scheme was employed, which is similar to previous efforts of the same author (Nobahar et al., 2007 [90]). The value of this work lies in comparing the soil deformation and the pipeline response predicted by the two different approaches. Adding the subgouge deformations to the soil displacements, which are caused by the pipe load exerted on the soil, produces a superposition error. It was shown that this error is more influential than the coupling errors resulting from the directional coupling of Winkler springs in axial, lateral, and vertical directions.

7.7 Coupled Eulerian–Lagrangian

The Coupled Eulerian–Lagrangian (CEL) method attempts to capture the strength of the Lagrangian and the Eulerian methods. A Lagrangian mesh is used to discretize structures (in this case the iceberg and the pipeline), while a Eulerian mesh is used to discretize the domain subjected to large deformations (in this case, the soil).

In Eulerian formulations, the coordinates of nodes are fixed and coincide with spatial points, but the spatial coordinates of the material points vary with time. There is no mesh distortion because the mesh is fixed in space (Figure 7.24). The material point at a given element quadrature point changes with time because material flows through the mesh. This makes the definition of history–dependent materials difficult.

Boundary nodes and the material boundary may not coincide. Therefore, boundary conditions and interface conditions are difficult to apply.

In the Eulerian formulation (initially used in fluid mechanics), spatial coordinates are used to track the flow of the material in time through points that are fixed in space.

Hence, large deformations can be easily simulated. Unfortunately, a fine mesh at the interface of Lagrangian and Eulerian domains is required to obtain high quality results. In addition, the Eulerian domain needs to be modeled to a larger extent so that no material leaves the specified domain.

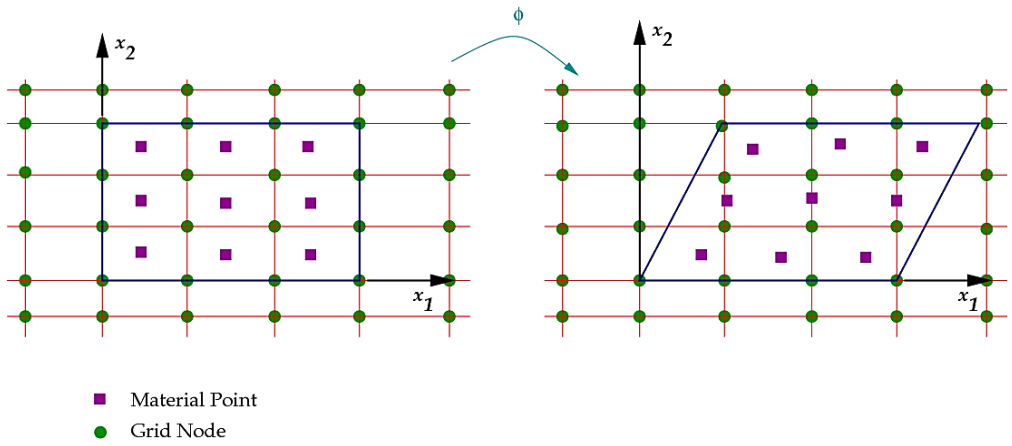

Figure 7.24: Eulerian Mesh Description

The interface between the structure (ice) and the soil is defined using the boundary of the Lagrangian domain. Interface models use the velocity of the Lagrangian boundary as a kinematic constraint in the Eulerian calculation, and the stress from the Eulerian cell is used to calculate the resulting surface stress on the Lagrangian domain.

7.7.1 Konuk and Gracie (2004)

Konuk and Gracie [61] presented numerical simulations comparable to the PRISE studies on subgouge deformations using LS–DYNA. The authors refer to the approach as Eulerian, but the approach is actually similar to the Coupled Eulerian–Lagrangian that is available in Abaqus software because the ice keel is a Lagrangian domain.

The results presented in this study indicated that the PRISE function could be overly conservative for the selected ice keel geometry, attack angle, and soil strength parameters. Konuk and Gracie also recognized the direct influence of these parameters on the magnitude and extent of subgouge deformations. Consequently, the authors suggested that future numerical analysis should mimic the cases evaluated during the PRISE studies by using equivalent parameters to those recorded, including ice keel attack angle, geotechnical conditions (e.g., soil strength, effective stress path, drained and undrained loading), and interface friction.

Konuk and Gracie noted that, although the Eulerian approach does not suffer from element distortion, numerical difficulties such as dissipation and dispersion problems

associated with inter–element mass flux may be encountered. The work underlined the necessity of verification through comparison with centrifuge data and Lagrangian continuum FE analysis.

7.7.2 Jukes et al. (2008), Abdalla et al. (2009)

The models of Jukes et al. [54] [55] [56] and Abdalla et al. [1] use the CEL formulation that is available in Abaqus/Explicit software. The Eulerian domain labeled 'VOID' in Figure 7.25 encloses all materials and the Lagrangian parts, and it is divided into three parts: the initial seabed material, the initial trench backfill material, and the absence of material (or void). The pipeline extends outside the seabed and trench material, but not beyond the Eulerian domain. The pipe was modeled as a 3D deformable homogenous general–purpose shell. The ice indenter was modeled as a 3D solid rigid shape Lagrangian part that moves through the Eulerian mesh.

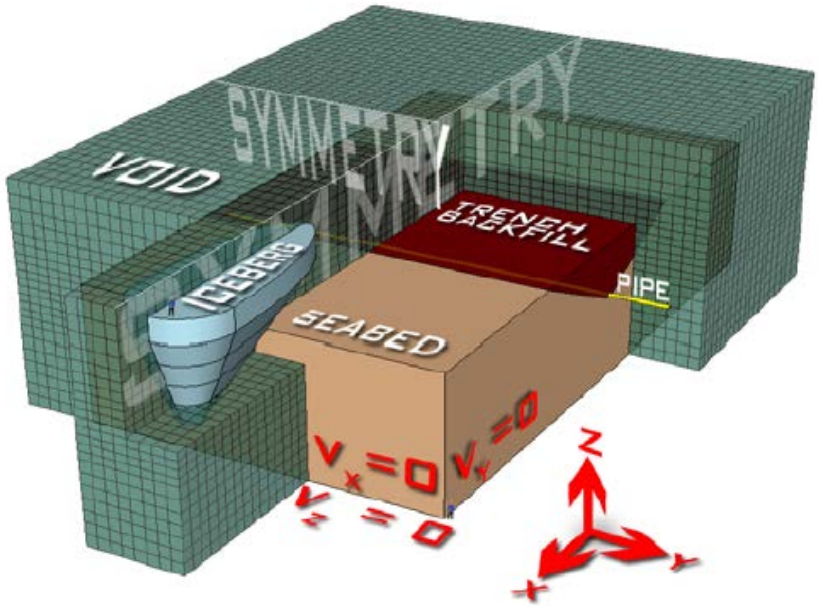

Figure 7.25: CEL Model Schematic (Abdalla et al., 2009 [1])

The soil, which was modeled as a single–phase material, presented the undrained conditions using the modified Drucker–Prager/Cap constitutive model. The developed model was used to examine the effect of keel configurations (depth, width, attack angle). In this effort, the results from the developed CEL model, although limited to subgouge predictions in soft clay, were compared to selected PRISE centrifuge experimental data and the empirical PRISE function. The selected comparison data was obtained from the centrifuge testing performed by Lach, 1996 [68] and the results presented by two FE models: Konuk and Gracie, 2005 [65] and Kenny et al., 2007 [57] (refer to Figure 7.26).

The soil parameters, gouge depth, gouge width, keel geometry, attack angles, and gouge speed were matched with Konuk's (2005) model. The soil parameters used in the comparison study with Kenny et al. (2007) and the PRISE test were reasonably assumed because of the limited availability of the presented data.

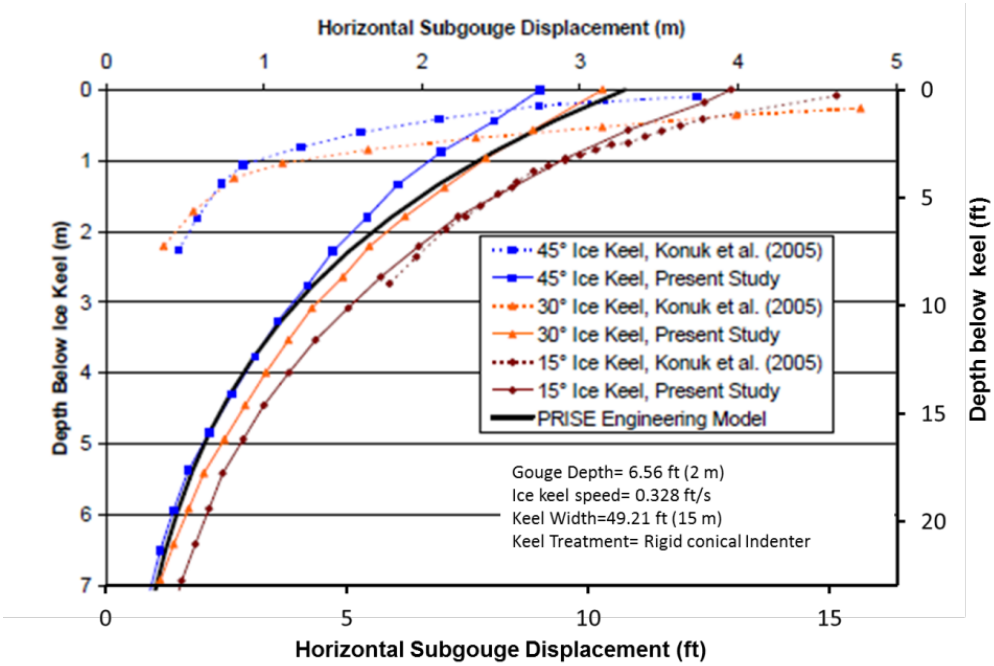

Figure 7.26: Comparison of Horizontal Subgouge Deformation Predictions with Konuk (Abdalla et al., 2009 [1])

The study concluded that for the same soil, deeper gouging keels produce larger subgouge soil deformations (Figure 7.27). This is consistent with the observations in the available literature.

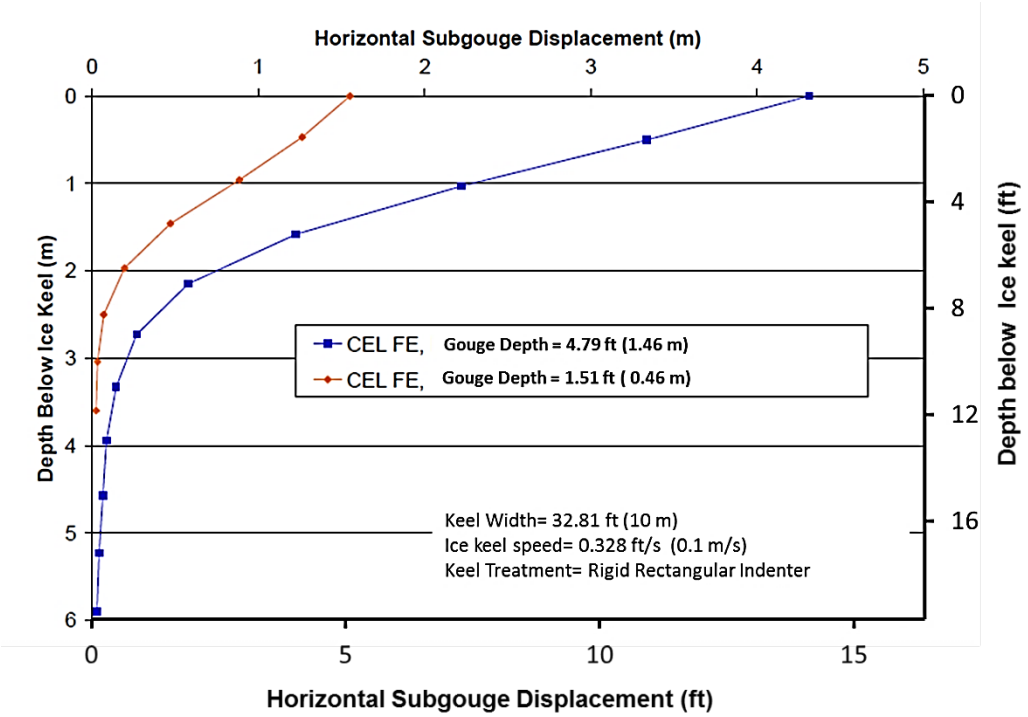

Figure 7.27: Effect of Gouge Depth on Subgouge Deformation (Abdalla et al., 2009 [1])

For shallow keel angles (15°), the soil is compressed below the keel and then squeezed upwards, forming a low mound along the gouge sides. This side mound is higher in conical shape keels than in rectangular keels. On the other hand, for higher keel angles (30° and 45°), the soil is lifted upwards ahead of the keel, forming a mound immediately in front of the keel, which subsequently clears to the gouge sides (Figure 7.28).

In addition, it can be noted that the sharp edges of the rectangular keel produce higher stresses in the soil mass just beneath the keel–soil contact as compared to the conical keel.

When compared to the PRISE data, the FE model predicted higher soil displacements immediately below the gouge base and within one to two gouge depths. The predicted soil displacements are smaller below this region. In general, the FE results generally agreed with the PRISE Engineering Model.

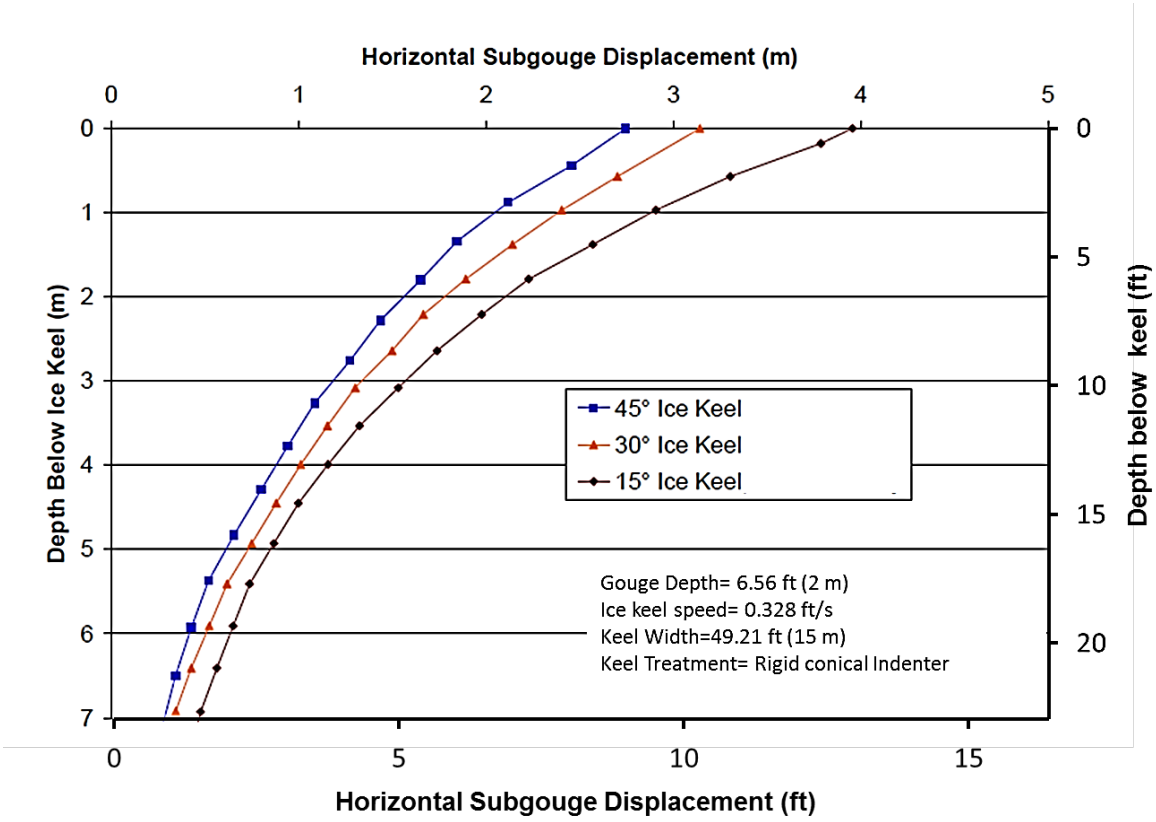

Figure 7.28: Effect of Keel Angle on Subgouge Deformation (Abdalla et al., 2009 [1])

7.7.3 Phillips et al. (2010, 2011)

Phillips et al. [100] [101] presented a numerical ice–soil interaction model that was developed for sand with an emphasis on improving solution mesh dependency and sand constitutive behavior.

As part of the PIRAM JIP, a more realistic, effective stress analysis was attempted using a Drucker–Prager Cap variant with suppression of the dilatancy on the shear failure surface under high shear strains. The dilation angle varies with a user–defined subroutine between a minimum of 0° and a peak value of 11° to capture the effects of variable dilation.

The ice keel was generally modeled as a rough, inverted truncated conical frustum of 49.2 ft. (15 m) minimum diameter (basal gouge width) and 30° side slope, embedded to a gouge depth of 4.92 ft. (1.5 m). The sensitivity of the deformations and keel reaction forces to mesh size was investigated by three levels of discretization

(refer to Figure 7.29). A comparison of numerical results to the physical subgouge deformation trend indicated that the mesh density refinement was adequate.

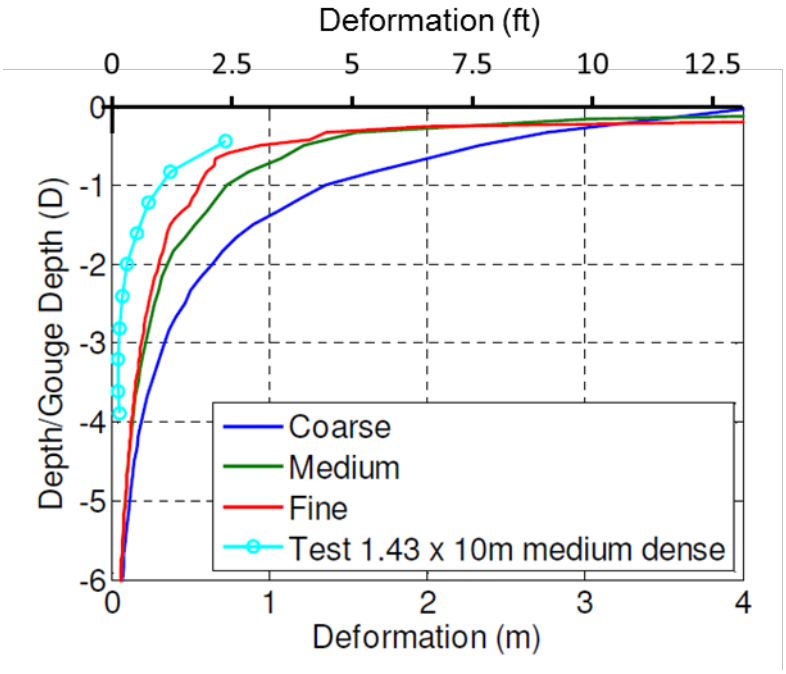

Figure 7.29: Subgouge Displacement Profiles (Phillips et al., 2011 [100])

FE analysis results for gouging in saturated sand conditions were validated against the PRISE physical model data for similar conditions.

Figure 7.30 illustrates the plastic shear strain contours by percentage.

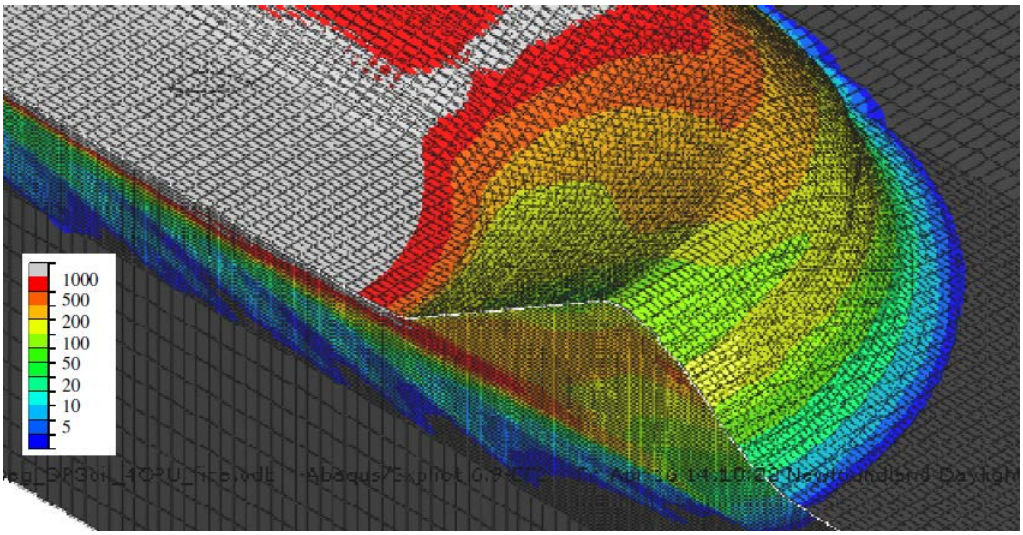

Figure 7.30: Percentage of Plastic Shear Strain Contours (Phillips et al., 2011 [100])

Keel reaction force with varying mesh size and dilation angle is illustrated in Figure 7.31 and Figure 7.32, respectively.

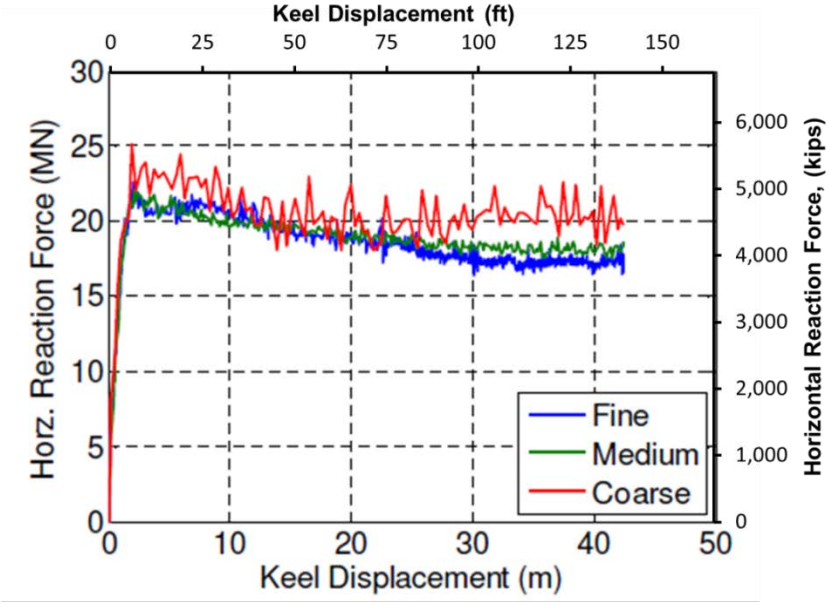

Figure 7.31: Keel Reaction Force Development with Varying Mesh Size (Phillips et al., 2011 [100])

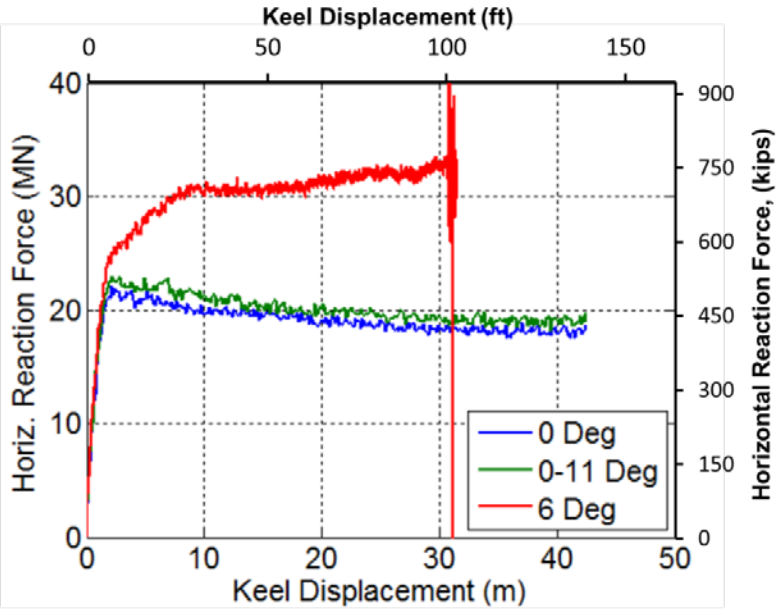

Figure 7.32: Keel Reaction Force with Varying Dilation (Phillips et al., 2011 [100])

Figure 7.33 shows how the variable dilation gives rise to a modest increase in subgouge deformation (SGD) over the entire profile. The excessive plastic strains arising from the fixed dilation case (6 Degrees) give rise to excessive and unrealistic SGD, which is shown by the large plastic strains.

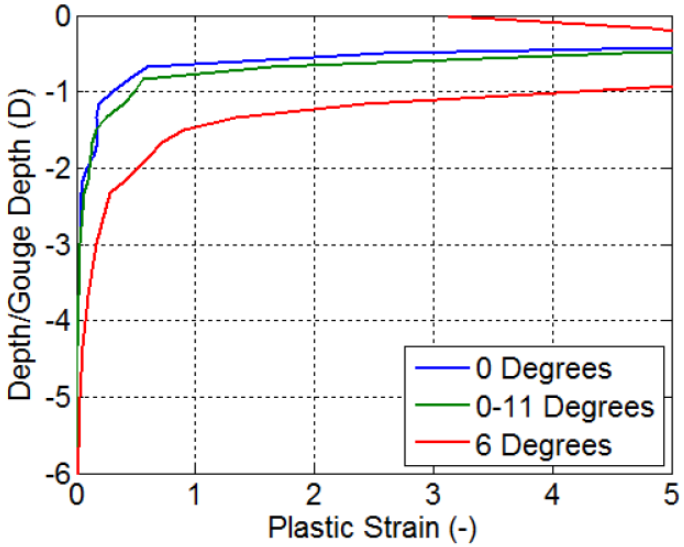

Figure 7.33: Plastic Strains Profiles Variation with Dilation (Phillips et al., 2011 [100])

The analyses highlighted the importance of dilation and stress level on the vertical extent and magnitude of subgouge displacements under gouges of differing scales. The soil constitutive models need to be improved to capture the appropriate effective stress behavior within a single–phase continuum.

7.7.4 Banneyake et al. (2011)

As contributors to the ice–pipeline JIP, Banneyake et al. [6] conducted a series of ice gouging simulations where the effects of ice keel movement on the surrounding soil and on the pipeline were studied for a range of pre–specified modeling parameters. A soil model calibration subtask with two selected PRISE tests (one for clay and another for sand) preceded the simulations. Figure 7.34 illustrates the Eulerian and Lagrangian components of the ice–soil–pipeline CEL FE analysis model.

Banneyake et al. used comparisons of the numerically simulated triaxial compression tests and T–bar test results with the actual test data to verify the accuracy of the material model implementation. For the clay case, the simulated horizontal subgouge displacements results compared very well with those from the PRISE test, but the vertical subgouge displacements showed some disagreement. For the sand case, the authors observed several discrepancies between the simulation and tests results, possibly because of the lack of details in the sand parameters used in the PRISE tests.

Increase in the gouge depth, the keel attack angle, and the keel width caused an increase in the height of the side berms and frontal mounds (Figure 7.35). Side berms in sandy seabeds were higher than those in clayey seabeds (Figure 7.36). Larger keel angle resulted in scraping–like removal of the soil, reducing the subgouge soil deformation and hence pipe displacement.

Sandy seabeds resulted in subgouge deformation and pipe curvature that were greater than those observed in clayey seabed. Decrease in pipe diameter showed detrimental effects on the pipe deformation as anticipated. Soil movement in the upper soil zone remained similar for the two pipe diameters. However, the soil around the pipe showed a significantly higher range of motion when the pipe diameter was reduced. Change in pipeline stiffness will affect the extent of pipe deformation under soil pressure and the resistance offered to soil deformation by the pipe.

The lateral subgouge soil movement had a very high gradient in the vertically upward direction in sand compared to that in clay. Therefore, pipeline lateral deformation appeared to be higher in the normally consolidated sand than in the medium dense clay

modeled. Sand experiences more of scraping like removal by the keel and is less susceptible to squeezing into side berms. Hence, in sandy seabed the pipe does not demonstrate the level of lifting that was observed in clayey seabeds.

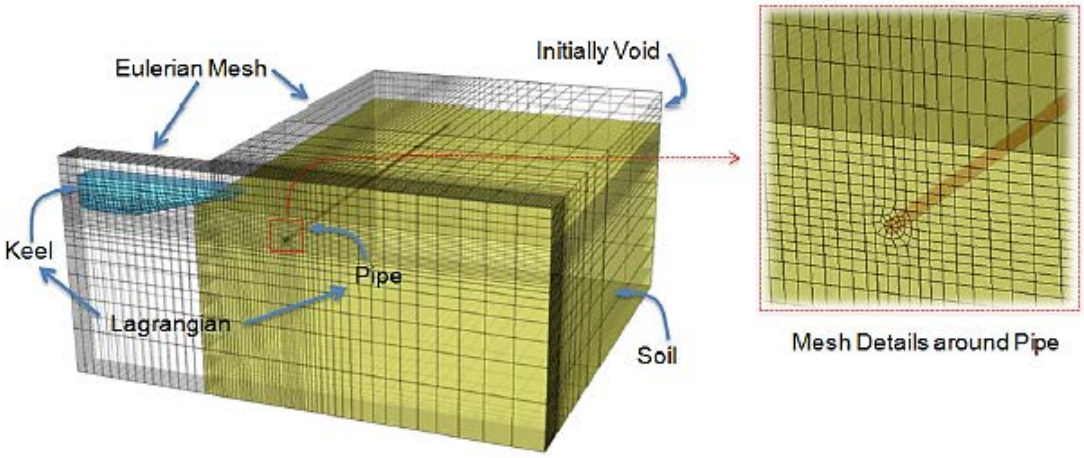

Figure 7.34: Eulerian and Lagrangian Components of the Ice–Soil–Pipeline CEL Model (Banneyake et al., 2011 [6])

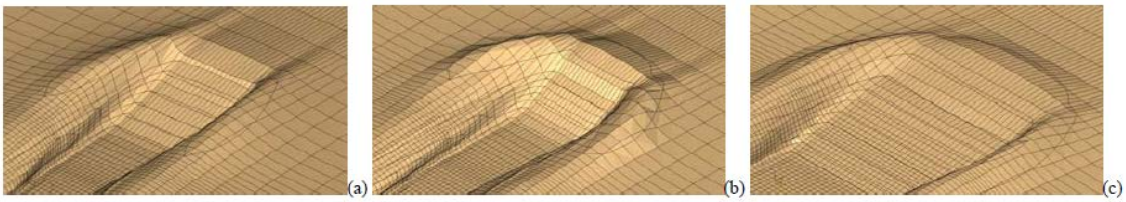

Figure 7.35: Effect of Keel Size and Angle (DOG–11.5 ft.) a) Width=32.8 ft. and Angle 15^o, b) Width=32.8 ft. and Angle 30^o, c) Width=98.5 ft. and Angle 15^o (Banneyake et al., 2011 [6])

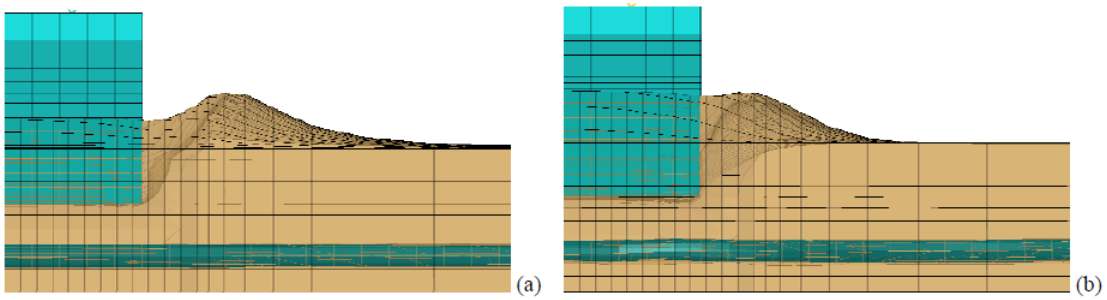

Figure 7.36: Side Berm Formation in Clayey (a) and Sandy (b) Seabed (Banneyake et al., 2011 [6])

7.7.5 Lele et al. (2011a, 2011b)

Lele et al. [72] [73] developed a CEL model to evaluate its capability to characterize the ice gouging process and to accurately estimate pipeline strain demand. The authors modeled the soil using a Eulerian mesh, and the pipe and rigid ice keel were modeled in the Lagrangian domain. Figure 7.37 illustrates the model, and the mesh refinement details are available in Figure 7.38.

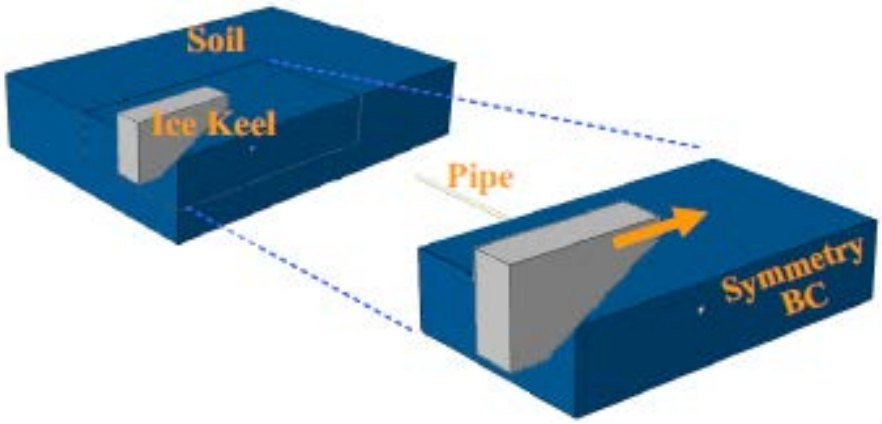

Figure 7.37: Finite Element Model (Lele et al., 2011 [72])

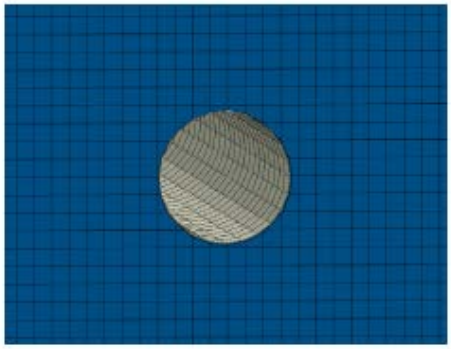

Figure 7.38: Mesh Refinement in the Pipe–Soil Contact Region (Lele et al., 2011 [72])

The authors used the von–Mises elastic–plastic material model for modeling clay and the Drucker–Prager model for sand. Because software in–built Drucker–Prager models (with and without cap) may lead to unrealistic excessive dilation in large deformation analysis, especially when using finer meshes, Lele et al. implemented a user subroutine that prevents this excessive dilation in this work.

The authors conducted a limited parametric study to determine the effect of gouge depth, gouge width, pipe diameter, and pipe wall thickness on pipeline strain demand. They also assessed the effect of pipe burial depth for a constant gouge depth.

Figure 7.39 provides a comparison of the results produced by this study and the PRISE experiment.

Lele et al. were confident that learnings from the continuum approach results could be used to improve the accuracy of soil–spring based models so as to avoid the cost of continuum model parametric studies in the conceptual design phase.

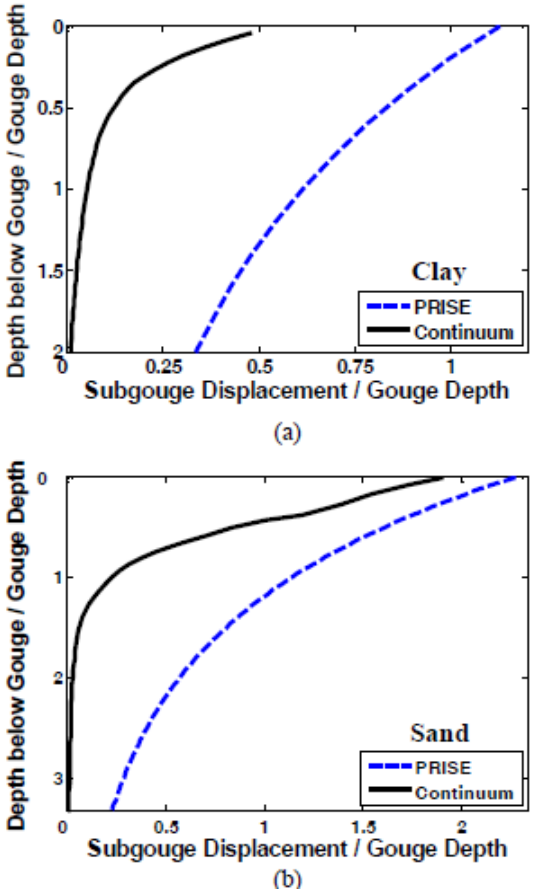

Figure 7.39: Comparison of Subgouge Soil Deformation Predicted by Continuum Model and PRISE Equation: a) Clay; b) Sand (Lele et al., 2011 [72])

7.7.6 Panico et al. (2012)

Panico et al [96] extended the scope of Lele et al., 2011 [72] and investigated the effect of sand frictional properties on gouge forces and subgouge displacements by implementing two sand friction models. The two friction models, one with constant friction and the other with varying friction, can be seen in Figure 7.40. The authors concluded that in sand, the ice gouging response is mainly controlled by critical state behavior, with a limited effect of the peak friction angle on gouge force and subgouge displacements (Figure 7.41).

A comparison between centrifuge tests showed that the continuum model can reasonably estimate gouge forces, with a maximum error in the order of 30% magnitude. Given the uncertainties associated with sand properties characterization and testbed preparation in centrifuge experiments, the comparison of results is satisfactory.

The comparison conducted between centrifuge tests, the continuum approach, and the soil–spring approach for both a thick and thin–walled pipe scenario showed that continuum models can adequately predict the pipe strain demand (Figure 7.42). In both cases, the soil–spring approach predicted much larger pipe strains than the continuum approach.

The authors showed some preliminary validation of the continuum approach using small–scale centrifuge tests. Full validation requires a comparison of ice gouging continuum models with large–scale test data, which are currently limited. Once full validation is completed, the authors are confident that continuum models can be effectively used to improve the reliability and cost effectiveness of the design.

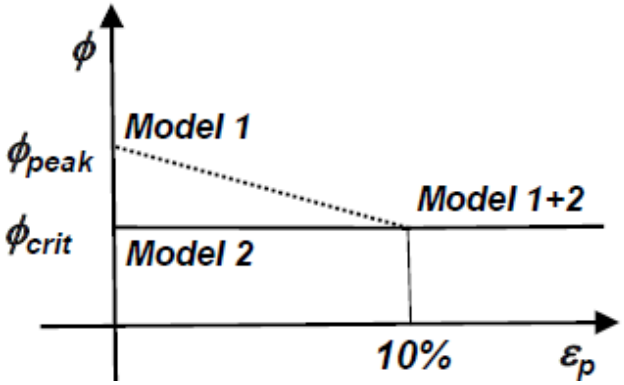

Figure 7.40: Dependence of Sand Friction Angle on Equivalent Plastic Strain for Model 1 and Model 2 (Panico et al., 2012 [96])

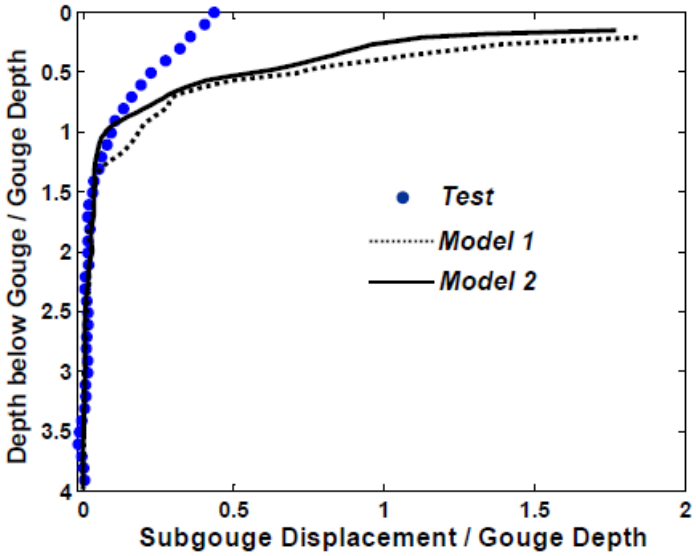

Figure 7.41: Comparison of Subgouge Displacement Profile for Model 1 and 2 with Centrifuge Experiment (Panico et al., 2012 [96])

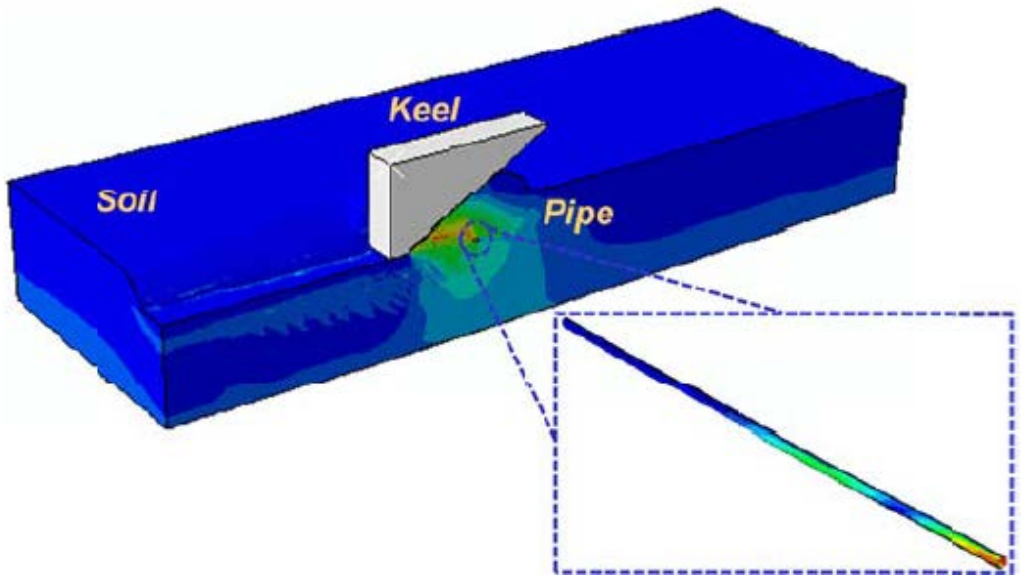

Figure 7.42: Continuum Simulation of Ice Gouging Process and Induced Strains on Pipeline (Panico et al., 2012 [96])

7.7.7 Rossiter and Kenny (2012)

Rossiter and Kenny [116] conducted a parametric study to examine the influence of attack angle and interface properties on soil behavior and pipeline mechanical response. The initial intention was to use the CEL formulation because of its robust modeling capabilities. However, technical issues related to interface shear strength behavior and contact mechanics were identified within the Abaqus/CEL modeling framework. This work used ALE formulations in LS–DYNA to simulate both free field and coupled ice gouge events.

From analysis of the contact stress developed at the ice keel/seabed interface, the authors observed that the interface frictional forces did not correctly account for the equivalent shear stress limit (τmax). The shear stresses developed to a value much lower than the defined τmax, which resulted in greater clearing and subduction of the soil, causing incorrect estimation of the seabed reaction forces. It was illustrated that weaker interface properties allow for greater subduction below the keel, resulting in less material building in front of the keel.

Horizontal to vertical force ratios were within the range of Lach's (1996, [66]) and PRISE's centrifuge data (Figure 7.43). Plots of horizontal subgouge deformations revealed an increase in deformation with an increase in keel width. However, because the model tends toward a plane strain–type condition, there is a potential trend in the data that suggests a limiting keel width.

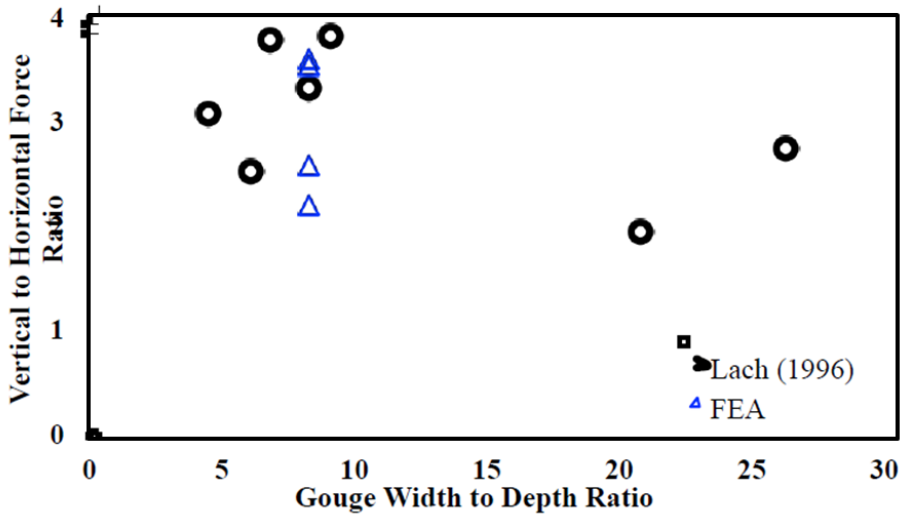

Figure 7.43: Comparison of Results with Lach's Experimental Data (Rossiter and Kenny, 2012 [116])

For the investigated ice keel attack angles (results shown in Figure 7.44), the side berm elevations were not as sensitive to changes in Su and τ_{max}, with only slightly decreasing trends for decreasing values of these properties. These results suggest that higher strength soils have higher frontal mound elevation and less material being cleared to side berms, while weaker soils have less resistance to subduction and clearing mechanisms and therefore have less material developing in front of the gouging keel.

(Refer to Table 7.1 for specifics of the cases that Rossiter and Kenny studied.)

Table 7.1: Cases Examined in the Study (Rossiter and Kenny, 2012 [116])

	Keel Attack Angle (degrees)	Width to Depth Ratio	Gouge Width (feet)
Case 5	15	5	24.61
Case 6	15	10	49.21
Case 7	15	15	73.82
Case 8	15	20	98.43
Case 9	30	10	24.61
Case 10	30	10	49.21

The Rossiter and Kenny (2012) paper illustrates the importance of soil representation and interface conditions on the soil response. Abaqus/CEL numerical models that have been partially calibrated with reduced–scale centrifuge data may not produce realistic results, outside the calibration domain, with respect to clearing mechanisms, interface conditions, and contact mechanics. This perspective introduces a significant uncertainty when examining free–field or fully coupled ice gouge events outside the calibration data set conditions.

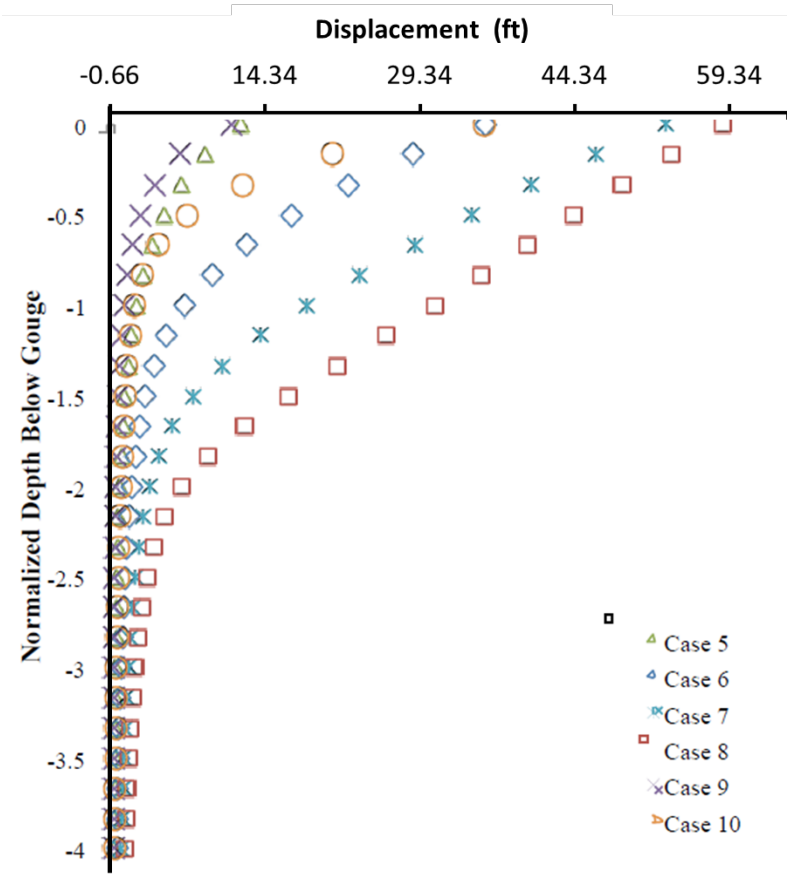

Figure 7.44: Horizontal Subgouge Deformation for Varying Gouge Widths and Keel Attack Angles (Rossiter and Kenny, 2012 [116])

7.7.8 Pike and Kenny (2012)

Pike and Kenny [106] developed a prototype numerical model of Lach's centrifuge test in clay (see Figure 7.45). Lach, 1996 [66] provided the model details, variability of undrained shear strength with depth (Su), variation of overconsolidation ratio (OCR) and common Speswhite kaolin index properties.

Horizontal and vertical keel reaction forces and subgouge soil displacements were in good agreement with the physical data set as well as the numerical predictions of horizontal subgouge soil deformations by a semi–empirical equation derived from centrifuge tests in clay (Woodworth–Lynas et al., 1996 [134]), commonly referred to as the PRISE equation.

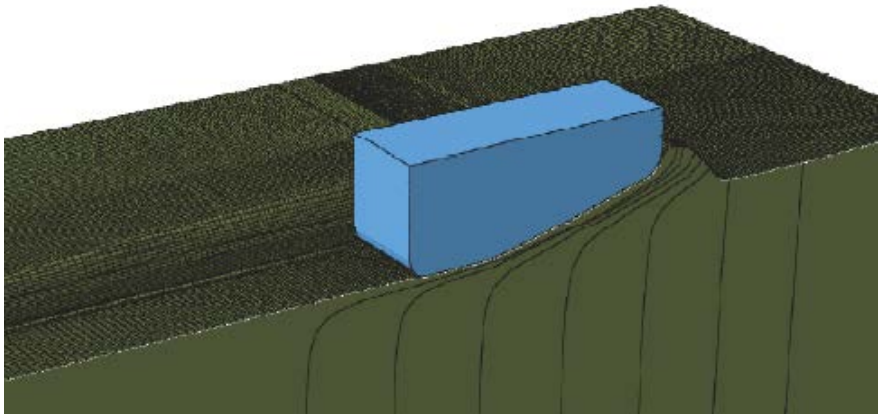

Figure 7.45: CEL Model Output (Pike and Kenny et al., 2012 [106])

The agreement between the numerical and centrifuge test data tends to diverge in the upper 3.28 ft. (1 m) beneath the base of the gouge. This was explained by a shift from a continuum mechanical response to a localized zone of high shear that is difficult to capture with the current mesh resolution. Furthermore, the element formulation is such that the strain is constant within each element, thus presenting difficulty in capturing sharp strain gradients. When assessing the effect of ice keel shape on subgouge soil deformation, it was shown that steep keels produce less severe subgouge deformations.

The Pike and Kenny study showed the variability of soil strength profiles in the Canadian Beaufort as provided by Crooks et al., 2007 [31] and Rogers et al., 1993 [115], for the Amauligak F24 and Tarsuit P45 sites. Figure 7.46 presents the shear strength profiles in the aforementioned locations. As expected, soil strength profile was shown to have a profound effect on subgouge deformation fields (refer to Figure 7.47).

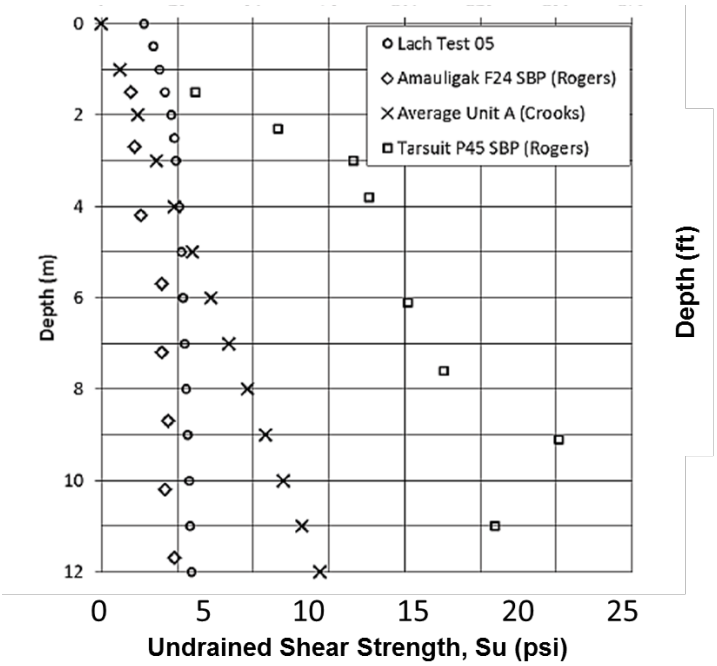

Figure 7.46: Undrained Shear Strength Profiles of Some Beaufort Sea Clays (Pike and Kenny et al., 2012 [106])

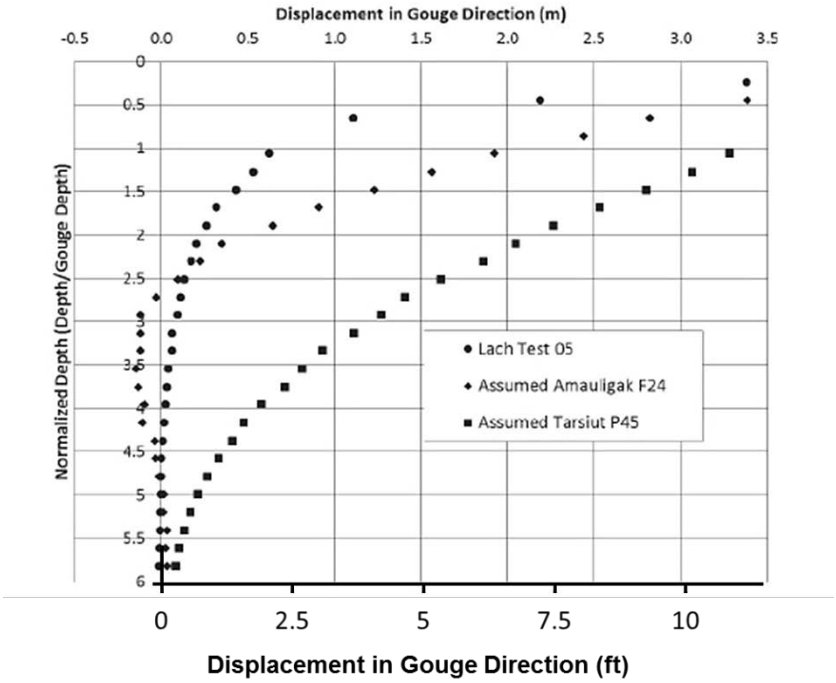

Figure 7.47: Effect of Varying Soil Strength Profiles on Horizontal Subgouge Deformations (Pike and Kenny et al., 2012 [106])

7.7.9 King et al. (2012)

King et al. [60] developed a 3D seabed model with a rectangular sub–surface caisson using Abaqus FE modeling and a Coupled Eulerian–Lagrangian (CEL) scheme. The intention was to assess the feasibility of such structures, as an alternative to placing them inside EDCs, based on the conditions encountered on the Grand Banks in offshore Newfoundland Canada.

The scenario considered was an ice keel scouring over a buried caisson, avoiding direct contact but with minimal clearance (see Figure 7.48). A centrifuge testing program, consisting of five tests, formed the basis for the calibration of an FE model. The results indicated that (1) the proposed numerical model performed satisfactorily when simulating the centrifuge tests and (2) a caisson system can potentially provide the protection needed for subsea installations. Based on authors' recommendation, future work should involve evaluating various ice keel–soil–structure interaction scenarios and attack angles as well as assess in detail the construction and installation issues.

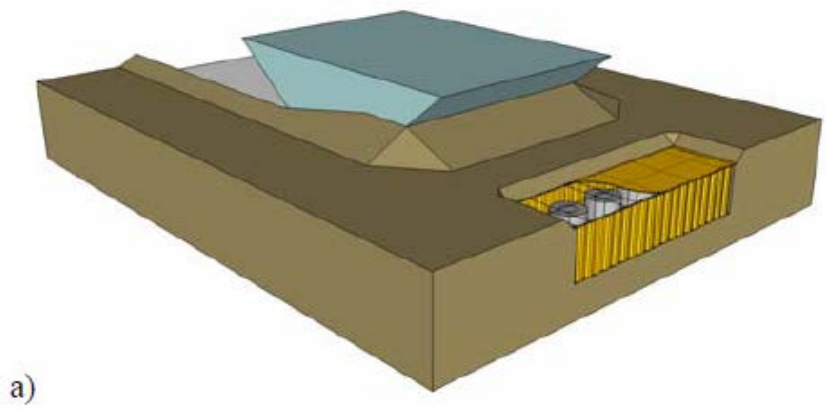

Figure 7.48: Illustration of Protection Caisson and Keel–Soil Interaction (King et al., 2012 [60])

Figure 7.49 shows the effect of the keel roughness in the displacement patterns observed as the keel progresses.

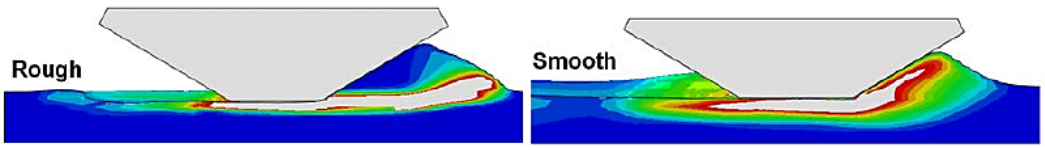

Figure 7.49: Numerical FE Analysis on the Effect of Keel Roughness on Soil Displacement (King et al., 2012 [60])

Figure 7.50 illustrates how the presence of the caisson interferes with the subgouge soil clearance mechanisms obstructing free flow beneath the keel.

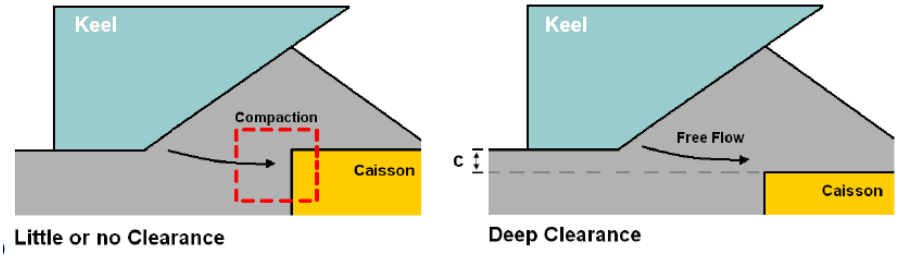

Figure 7.50: Numerical FE Analysis on the Influence of Clearance on Soil Forces Experienced by the Caisson (King et al., 2012 [60])

7.8 Mesh–free

Smoothed Particle Hydrodynamics (SPH) Methods

The advantage of mesh–free methods is that nodes and elements are not defined; instead, only a collection of points is necessary to represent a given body. Wu et al. [135] first used a mesh–free method in 2001 to study geotechnical materials. However, mesh–free methods have not been popular, as they have not been widely adopted by commercial software developers. In addition, assessing nodal interactions without an explicit mesh appears to make mesh–free methods computationally expensive.

Smoothed particle hydrodynamics (SPH) is a numerical method that is part of the larger family of mesh–less (or mesh–free) methods. The coordinates move with the fluid, and the resolution of the method can easily be adjusted with respect to variables such as density. The SPH method works by dividing the fluid into a set of discrete elements, referred to as particles or pseudo–particles. These particles have a spatial distance (known as ‘smoothing length’), over which their properties are ‘smoothed’ by a kernel function. This means that the physical quantity of any particle can be obtained by summing the relevant properties of all the particles that lie within the range of the kernel.

SPH is based on a fully Lagrangian modeling scheme, which permits the discretization of a prescribed set of continuum equations by interpolating the properties directly at a discrete set of points distributed over the solution domain without the need to define a spatial mesh. The method's Lagrangian nature, combined with the absence of a fixed mesh, is its main strength.

Pike et al. [106] and the Abaqus documentation guide (2012) noted that the SPH method is less accurate than the CEL method in high deformation regimes. Note that if a large percentage of nodes in the model are associated with SPH, the analysis may not scale well over multiple CPUs. Because there is currently no capability to compute the volume

associated with these particles automatically, it is necessary to distribute the particle elements uniformly. Hence, bias meshing in elastic regions of the problem domain to reduce the number of particles is not currently an option. This, combined with poor parallel scalability and the need for small particle spacing to capture strain localization, may make the SPH method less effective for the extension of structure–soil interaction problems to coupled ice keel–soil–structure interaction scenarios.

Fredj et al. 2010 [39] does not directly refer to an ice gouge event; however, the study does describe the application of a 3D continuum modeling technique for assessing the performance of a pipeline system that is subjected to large soil displacements. This work makes use of the LS–DYNA SPH modeling capability to consider a wide range of soil types and soil movement scenarios. The results are compared with published experimental data of large–scale tests to verify the numerical method. Note that test data come from a large–scale tank experiment investigating pipe–soil load transfer caused by large lateral soil movements, and not an ice gouge event. A comparison between numerical predictions and full–scale experimental results showed a good agreement, which indicates that SPH can simulate pipeline response and soil deformation in certain pipe–soil interaction scenarios.

7.9 Other Continuum Methods

The Particle–In–Cell (PIC) model is based on the ideas of approximating saturated soil as an incompressible viscous fluid and generalizing the formulation to soil–structure/object interaction in a large deformation framework. Within this approach, the soil–ridge and soil–pipe interactions are treated as fluid–object and fluid–structure interaction problems, respectively. The arbitrarily large topological changes in the soil are accommodated by representing the water–soil interface as a single dynamic implicit surface.

Sayed and Timco (2009) [118] presented an alternative approach for the numerical modeling of the soil gouging process by treating the soil as a highly viscous non–Newtonian fluid, thereby converting deformation to viscous flow. Deformation of the seabed material is considered to be elastic–plastic and follows a Mohr–Coulomb criterion. Compressibility was introduced through a pressure–solids volume fraction relationship. The numerical scheme employed a PIC advection method where the soil was represented by discrete particles, making it possible to handle discontinuities and large deformations. Numerical analyses considered 2D deformation of seabed soil against a vertical moving indenter that represented an iceberg keel. Sayed and Timco simulated a buoyant iceberg response and compared the results with experimental data. The resulting deformation patterns were similar to the slip (shear) planes that are

considered in plastic limit analyses (e.g., Schoonbeek et al., 2006 [119]). The authors further noted that displacements took place mostly in wedges that formed in front of the rigid indenter, near the free surface. Vertical profiles of the velocities and normal stresses (Figure 7.51) provided quantitative measures of the disturbance of the soil beneath the scour depth.

The Sayed and Timco simulation showed that stresses in front of the iceberg are higher than the values corresponding to passive earth pressure because of the inertia of the moving soil. The resulting deformation patterns as seen in Figure 7.52 display failure zones and the development of shear zones as described by other researchers (e.g., Schoonbeek et al., 2006 [119]). The simulations examined the dependence of stresses on scour depth, soil properties, compaction, and scour velocity and were compared with experimental data. The results show that the mean normal stress on the iceberg increased with deeper scours and higher angles of internal friction in sands.

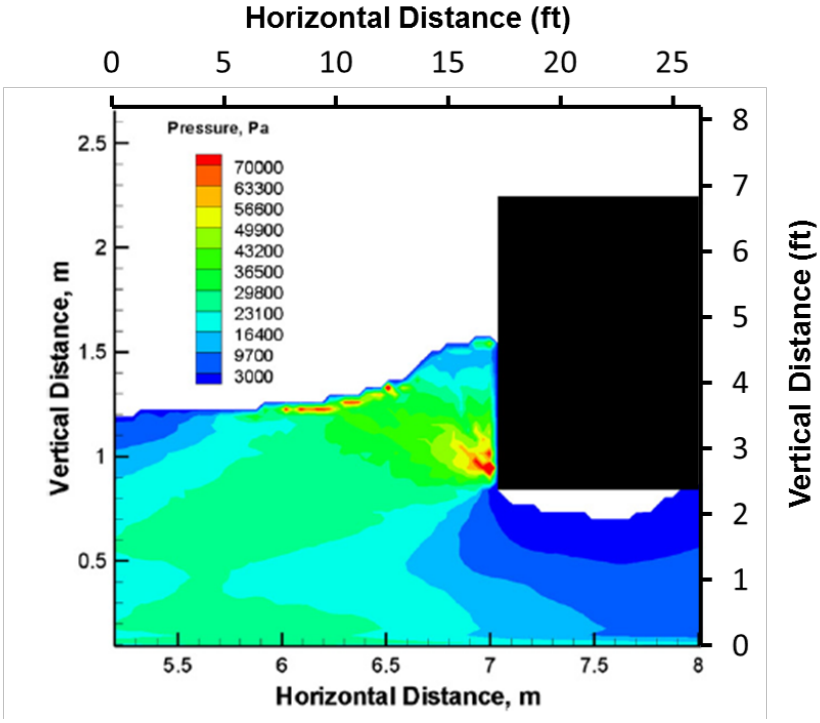

Figure 7.51: Contour Plot of the Pressure for the Reference Case (Sayed and Timco, 2009 [118])

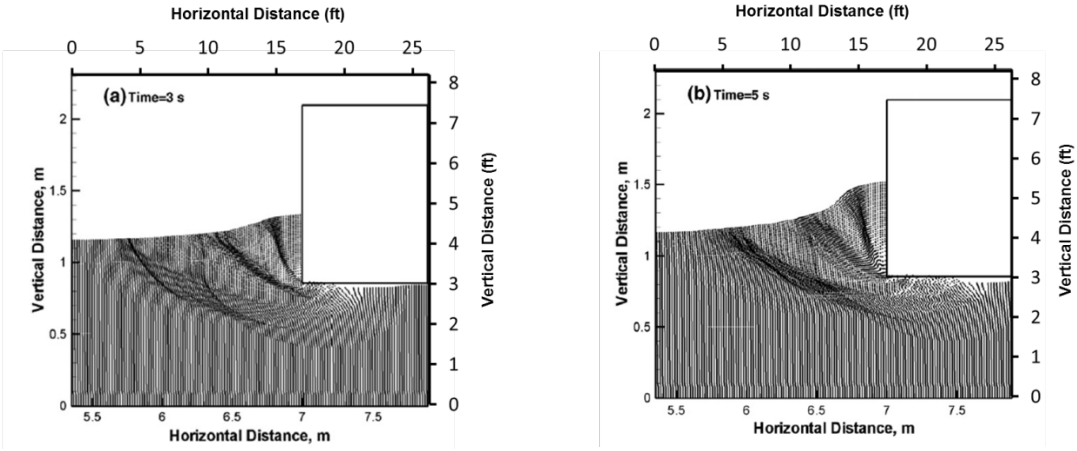

Figure 7.52: Snapshots of Particle Positions:
a) 3 s After the Start of the Simulation for the Reference Case;
b) 5 s After the Start of the Simulation for the Reference Case
(Sayed and Timco, 2009 [118])

8.0 Recommendations for Future Work

In the past two decades, the advancement of research activity related to ice gouging has been aligned with the needs of the offshore oil and gas industry and its regulators. Assessing the risk of ice interaction with oil production and transportation systems (such as wells and pipelines) requires multidisciplinary efforts.

These combined efforts should address the following needs:

1. Reduce uncertainty in input parameters.
2. Improve the numerical processes through advancements in software package capabilities.
3. Reduce uncertainty in output parameters through validation using large–scale data.

8.1 Input Parameters

8.1.1 Ice Gouge Features

Knowledge of the geometric properties of the ice keel (including ice keel width, depth, attack angle, and spatial variation of these parameters within the ice feature) is vital to improve simulation efficiency and evaluate the performance of subsea structures against realistic ice gouging scenarios. Studying actual ice gouge processes in their environments can offer great insight for understanding the phenomenon and can address the question, “What are we designing for?”

The United States Geological Survey (USGS) has collected significant ice gouge data through a number of seabed survey programs conducted in the American Beaufort and one in the Chukchi Sea.

Surveys of the OCS are costly in terms of resources and time, but they are the only means to develop a database of ice gouge features (e.g., depth, width). Numerous surveys that have provided information on maximum gouge depths and widths and occurrence rates have been performed in the Beaufort Sea. However, inconsistencies in record methodology have prevented comparisons between repetitive surveys in some cases.

Surveys should record data in a consistent way, considering the following:

1. The importance of gouge depth and width measurements along the gouge track line (Current surveys list only the maximum values of these ice gouge features.)
2. Orientation of the gouging tracks relative to pipelines (This feature was usually neglected in previous surveys.)
3. Locations of gouge tracks using Global Positioning System (GPS)

4. The distinction between single and multiplet events
5. Soil properties along the ice gouge track

Surveys should be performed in a repetitive fashion to provide information on:

1. Occurrence rates – Because only one survey (in the Chukchi Sea) has been performed so far, it is impossible to draw conclusions on occurrence rates.
2. Infilling models and sediment transport processes – This will aid in developing accurate models to monitor how the features of relic gouge tracks change with time.

Wellhead structures are vulnerable to damage from near gouge events. Because near gouge events leave no traces, the risk they might impose on wellheads cannot be easily assessed.

In the absence of near ice gouge event data, alternative methods can be used, such as keel draft to sail height ratio models or measurements from upward looking sonar.

The burial depth required to protect subsea structures against interaction with gouging ice keels is a function of the maximum gouge depth, the rate of ice gouge occurrence in a specific area, and the specified level of acceptable risk. In simple terms, the burial depth depends on the design ice gouge depth and the design gouge depth return period.

Probabilistic analyses and the application of optimization techniques on data collected from surveys can establish the following parameters, which are critical to the design process:

- Burial depth, which has the potential to balance cost (i.e., burial depth, trenching volume) with pipeline integrity and safety
- Governing parameters associated with the distribution tails because of limited data
- Design event return period, which may be a function of a number of factors governing the system demand (e.g., magnitude and distribution of subgouge soil deformations), including characteristics of the ice feature (e.g., depth, width, angle of attack, ice keel strength), soil conditions (e.g., type, strength properties), and pipeline (e.g., diameter, burial depth).

8.1.2 Soil Properties

The response of clay to ice gouging has been studied extensively using experimental and numerical simulations. The behavior of sand is far more complicated than clay. Further investigation is needed on the effects of constitutive parameters such as dilation angle and critical state parameters on the sandy soil response.

Previous research efforts tended to idealize the soil conditions. A common assumption is that the seabed consists of a single layer (clay or sand). In reality, the field ice gouge is

more complex and includes layered profiles and soil strengths that vary significantly with depth. Future investigations are needed, mimicking actual field soil conditions.

Relative to this need are the trench geometry and infill soil properties. When a pipe is buried in a trench to avoid direct contact with gouging keels, the properties of the trench and infill material affect the ice gouge response; this requires further study.

8.1.3 Ice Properties

Most of the experiments performed so far have assumed that the ice keel is rigid. In reality, the ice strength appears to be a decisive factor that is worthy of consideration. Fracture of the keel may be beneficial in a real ice gouge scenario.

8.2 Numerical Processes

Advancements in the software package capabilities are required to incorporate:

- Two–phase material within an effective stress analysis to account for the effects of pore pressure and associated volumetric changes caused by plastic shear strain (e.g., modified Cam–Clay plasticity model).
- Improvements of constitutive models for ice and soil (e.g., effective stress analysis, nonlinear subyield behavior, strain softening/hardening response) through calibration of the numerical procedures to physical experimental and laboratory testing data.

8.3 Validation of Results

Researchers have conducted a large number of laboratory (1–g) and centrifuge experiments to date. Primary issues are associated with:

- The range of confining stresses
- Uncertainties involving:
  - Scaling laws
  - Interface properties and contact mechanics
  - Failure mechanisms observed
  - Strain localization
  - Clearing mechanisms

This report has identified that only a small number of experiments include a pipe segment and monitor the induced stresses on the pipeline. In addition, only one experiment has been performed focusing on the response of wellheads during a gouge event. Future experimental efforts should take these issues into consideration.

Researchers have calibrated numerical models using results from small–scale testing. Currently, the availability of large–scale data to validate numerical models is extremely limited, which is attributed to the following facts:

- The implementation of large–scale experiments can be costly.
- Preparation of the testbed (e.g., consolidation of cohesive seabeds, placement of cohesionless seabeds, saturation) can require a great deal of time.
- Acquiring measurements during tests (e.g., real–time monitoring of subgouge soil deformations, pipe strain, pore pressures) can be challenging.

Large–scale testing should be conducted, which would address issues related to:

- Understanding ice keel kinematics. Depending on the characteristics of the ice feature and seabed, the ice mass may rotate, tilt, or lift during the scouring process. The ice keel itself may be subject to breakage and abrasion; vertical stiffness; and heave, pitch, or rotation.
- Scaling laws when extrapolating:
  - Deformation patterns.
  - The magnitude of seabed reaction forces (pull or tow forces) derived from a small–scale experiment to the full–scale reality.
- Contact mechanics.

When full validation is completed, continuum models can be effectively used to improve the reliability and cost effectiveness of the design of subsea structures that are subjected to ice gouging hazards such as pipelines and wellheads.

Continuum models should be used for parametric analyses to assess the effect of the following:

- Attack angle
- Gouge geometry
- Layered soil
- Trench geometry
- Demand on the pipeline
- Orientation of the gouge relative to the pipeline

The outcome of the parametric analyses will aid in improving empirical relations.

A comprehensive review of the available literature has identified the scarcity of numerical models that included wellheads. This important gap should be bridged with further numerical efforts.

Figure 8.1 provides a design methodology flow chart for ice gouge actions on offshore pipelines and highlights the importance of survey input, experimental investigations, and numerical validation in the offshore pipeline design process.

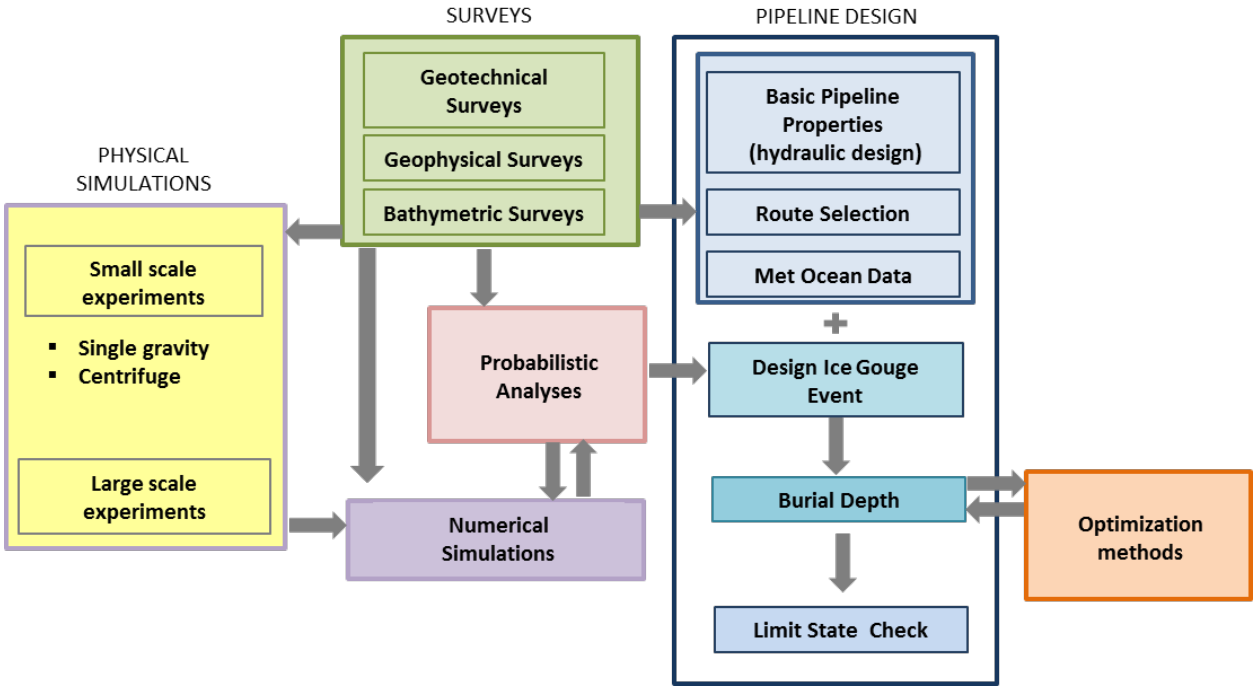

Figure 8.1: Design Methodology for Ice Gouge Actions on Offshore Pipelines

9.0 References

1. Abdalla, B., Pike, K., Eltaher, A., Jukes, P., and Duron, B. (2009). Development and Validation of a Coupled Eulerian–Lagrangian Finite Element Ice Scour Model. 28th International Conference on Ocean, Offshore and Arctic Engineering, OMAE2009, pp. 87–95.
2. Abdelnour, R. and Graham, B. (1984). Small Scale Tests of Sea Bottom Ice Scouring. Proceedings of the 7th International Symposium on Ice, Association of Hydraulic Engineering and Research, Hamburg, Germany, Vol 3, pp. 267–279.
3. Abdelnour, R., Lapp, D., Haider, S., Shinde, S.B., and Wright, B. (1981). Model Test of Sea Bottom Scouring. Proceedings of the 6th International Conference on Port and Ocean Engineering under Arctic Conditions, Quebec City, Canada, Vol. 2, pp. 688–705.
4. Allersma, H.G.B. and Schoonbeek, I.S.S. (2005). Centrifuge Modeling of Scouring Ice Keels in Clay. Proceedings of the 15th International Offshore and Polar Engineering Conference, The International Society of Offshore and Polar Engineers, Seoul, Korea, ISOPE, Vol 1, pp. 404–409.
5. ASCE, (1984). Guidelines for the Seismic Design of Oil and Gas Pipeline Systems. Committee on Gas and Liquid Fuel Lifelines, Technical Council on Lifeline Earthquake Engineering, New York.
6. Banneyake, R., Hossain, M.K., Eltaher, A., Nguyen, T., and Jukes, P. (2011). Ice–soil–pipeline Interactions Using Coupled Eulerian–Lagrangian (CEL) Ice Gouge Simulation: Extracts from Ice Pipe JIP, Arctic Technology Conference, Houston, TX, U.S.
7. Barker, A. and Timco, G. (2002). Laboratory Experiments of Ice Scour Processes: Rigid Ice Indentor. Cold Regions Science and Technology, Vol 35, pp. 195–206.
8. Barker, A. and Timco, G. (2003). Laboratory Experiments of Ice Scour Processes: Buoyant Ice Model. Cold Regions Science and Technology, Vol 36, pp. 103–114.
9. Barnes, P.W. and Rearic, D.M. (1985). Rates of Sediment Disruption by Sea Ice as Determined from Characteristics of Dated Ice Gouges Created Since 1975 on the Inner Shelf of the Beaufort Sea, Alaska. U.S. Geological Survey Open–File Report 85–473, 38 p.
10. Barnes, P.W. and Reimnitz, E. (1974). Sedimentary Processes on Arctic Shelves off the Northern Coast of Alaska. In J.C. Reed and J.E. Sater, eds. The Coast and Shelf of the Beaufort Sea, The Arctic Institute of North America, Arlington, Virginia.

11. Barrette, P. and Sudom, D. (2012). Physical Simulations of Seabed Scouring by Ice: Review and Database. Proceedings of the Twenty–second (2012) International Offshore and Polar Engineering Conference Rhodes, Greece, June 17–22, 2012.
12. Barrette, P. and Timco, G. (2008). Ice Scouring in a Large Flume: Test Setup and Preliminary Observations. Proceedings of the 8th International Conference on Ships and Marine Structures in Cold Regions, Banff, Canada, 1–8.
13. Barrette, P., Marquardt, J. and Timco, G. (2009). Test Data from Scour Simulations with Rigid Indentors and Real ice Rubble. CHC–NRC Technical Report CHC–CTR–103, 31 pp.
14. Been, K., Kosar, K., Hachey, J., Rogers, B.T., and Palmer, A.C. (1990). Ice Scour Models. Proceedings of the Ninth International Conference on Offshore Mechanics and Arctic Engineering Conference. Houston, TX, U.S., Vol 5, pp. 179–188.
15. Blasco, S.M., Shearer, J.M., and Myers, R. (1998). Seabed Scouring by Sea–ice: Scouring Process and Impact Rates: Canadian Beaufort Shelf. Proceedings of the 13th International Symposium on Okhotsk Sea and Sea Ice, 1st Ice Scour and Arctic Marine Pipelines Workshop, Mombetsu, Hokkaido, Japan, pp. 53–58.
16. Campbell, R. How Does an Iceberg Start Scouring and What Happens to the Iceberg? MadSci Network: Earth Sciences. ID: 1102609783.Es, December 11, 2004. http://www.madsci.org/posts/archives/2004-12/1103249519.Es.r.html.
17. C–CORE (1993). Pressure Ridge Ice Scour Experiment (PRISE) Phase 2: Progress Report. C–CORE Report 93–C4, March, 105p.
18. C–CORE (1995). Pressure Ridge Ice Scour Experiment (PRISE) Phase 3c: Extreme Ice Scour Event – Modeling and Interpretation. St. John's, Canada. C–CORE Publication 97–C34, 198 pp.
19. C–CORE (1995). Pressure Ridge Ice Scour Experiment (PRISE) Phase 3: Engineering Model Application. C–CORE Report 95–C12, August 1995.
20. C–CORE (1997a). Pressure Ridge Ice Scour Experiment (PRISE) Phase 3c: Extreme Ice Scour Event – Modeling and Interpretation. St. John's. C–CORE Publ 97–C34, 36 pp.
21. C–CORE (1997b). Pressure Ridge Ice Scour Experiment (PRISE) Phase 3C: Extreme Ice Scour Event – Modeling and Interpretation, Review and Development of Finite Element Modeling. C–CORE Report 97–C20, April 1997, 27p.
22. C–CORE (1998). Safety and Integrity of Arctic Marine Pipelines. Report for the Minerals Management Service, C–CORE Report 98–C15, June, 41p.

23. C–CORE (1999) Alaskan Arctic Pipeline Workshop Proceedings, Captain Cook Hotel. Anchorage, Alaska, November 8–9, 1999. http://www.mms.gov/tarworkshops/WorkshopPages/PipelineWorkshops/workshop%2025/proceedings.pdf.
24. C–CORE (2000). Risk Assessment of Ice Damage to Buried Marine Pipelines. C–CORE Report 00–C31, October, 192p.
25. Chari, T.R. (1975). Some Geotechnical Aspects of Iceberg Grounding. Ph.D. Thesis, Memorial University of Newfoundland, St. John's, 181 pp.
26. Chari, T.R. (1980). A Model Study of Iceberg Scouring in the North Atlantic. Journal of Petroleum Technology, 32, 2247–2252.
27. Chari, T.R. and Green, H.P. (1981). Iceberg Scour Studies in Medium Dense Sand. Proceedings of the 6th International Conference on Port and Ocean Engineering under Arctic Conditions (POAC), Quebec City, Canada, Vol. 2, 1012–1019.
28. Chari, T.R., (1979). Geotechnical Aspects of Iceberg Scours on Ocean Floors. Canadian Geotechnical Journal, Vol. 16, No. 2: 379–390.
29. Chari, T.R., Green, H.P. and Reddy, A.S. (1982). Some Geotechnical Aspects of Iceberg Furrows. Proceedings of the 2nd Canadian Conference on Marine Geotechnical Engineering, Halifax, Canada.
30. Chen, W.F. and Rosenfarb, J.L., (1973). Limit Analysis Solutions of Earth Pressure Problems. Soils Found, 13(4): pp. 45–60.
31. Crooks, J., Been, K., Becker, D., and Jefferies, M. (2007). Geology, Characterization and Properties of Beaufort Sea clays. In Characterization and Engineering Properties of Natural Soils. Taylor and Francis. doi:doi:10.1201/NOE0415426916.ch7.
32. Donea, J., A. Huerta, J.–Ph. Ponthot and A. Rodrıguez–Ferran (2004). Arbitrary Lagrangian–Eulerian Methods. Encyclopedia of Computational Mechanics, Erwin Stein, René de Borst and Thomas J.R. Hughes Editors. Volume 1: Fundamentals. John Wiley & Sons.
33. Drescher A. and Vardoulakis I. (1982). Geometric Softening in the Triaxial Test on Granular Material. Geotechnique, 32, 291–303.
34. Emmerson, C. and Lahn, G. (2012) Lloyd's Report Arctic Opening: Opportunity and Risk in the High North, Chatham House. http://www.lloyds.com/~/media/Files/News%20and%20Insight/360%20Risk%20Insight/Arctic_Risk_Report_webview.pdf
35. Environmental Response Management Application (ERMA) for Arctic https://erma.noaa.gov/arctic/erma.html

36. Eskandari, F., Phillips, R., and Hawlader, B. (2010). A State Parameter Modified Drucker–Prager Cap Model. Canadian Geotechnical Conference.
37. Eskandari, F., Phillips, R., and Hawlader, B. (2012) Finite Element Analyses of Seabed Response to Ice Keel Gouging, Proc. 65th Canadian Geotechnical Conference Winnipeg, Manitoba, 2012.
38. Eskandari, Farzad, Ryan Phillips, and Bipul Hawlader.(2011) Ice Gouging Analysis Using NorSand Critical State Soil Model. 2011 Pan–Am CGS Geotechnical Conference, paper# 995.
39. Fredj, A. and Dinovitzer, A. (2010). Three–dimensional Response of Buried Pipeline Subjected to Large Soil Deformation Effects– Part I: 3D Continuum Modeling Using ALE and SPH Formulations, 8th Int. Pipeline Conf., Calgary, Alberta, Canada.
40. Fredj, A., Comfort, G., and Dinovitzer, A. (2008). A Case Study of High Pressure/High Temperature Pipeline for Ice Scour Design Using 3D Continuum Modeling. In ASME 2008 27th International Conference on Offshore Mechanics and Arctic Engineering (pp. 563–572). American Society of Mechanical Engineers.
41. Freeman, R., King, T., and Zakeri, A. (2011). Alternative Concepts to Gloryholes for Protection of Subsea Infrastructure in Ice Prone Regions. Offshore Technology Conference. doi:10.4043/22137–MS
42. Golder and Associates Ltd. (1989). Laboratory Indentor Testing to Verify Ice/Soil/Pipe Interaction Models – Phase II. Joint Industry Partnership, Calgary, Canada. Report 882–20488, 59 pp.
43. Green, H.P. and Chari, T.R. (1981). Sediment Compaction Below Iceberg Furrows. OCEANS 1981 IEEE Proceedings, Boston, U.S., Vol. 1, 223–227.
44. Green, H.P., Reddy, A.S. and Chari, T.R. (1983). Iceberg Scouring and Pipeline Burial Depth. Proceedings of the 7th International Conference on Port and Ocean Engineering under Arctic Conditions, Helsinki, Finland, Vol. 1, 280–288.
45. Harrison, W.L. (1972). Soil Failure Under Inclined Loads. Cold Regions Research and Engineering Laboratory, 303, 95 pp.
46. Hettiarachi D.R.P and Reece A.R. (1975) Boundary Wedges in Two–dimensional Passive Soil Failure. Geotechnique 20, 1 pp.17–37.
47. Holmes, M.L., (1975). Tectonic Framework and Geologic Evolution of the Southern Chukchi Sea Continental Shelf. Ph.D. dissertation, University of Washington.
48. Iceberg Finder Website, (2007) http://www.icebergfinder.com/
49. Institute of Energy Research article. U.S. Government Shuts Out Increased Alaskan Oil Production, 23 February, 2011.

50. International Ice Patrol IIP (2006).
51. James, R.G. and Bransby, P.L. (1970). Experimental and Theoretical Investigations of a Passive Earth Pressure Problem, Geotechnique, 20(1), 17–36.
52. Jefferies, M. G., and Been, K. (2006). Soil Liquefaction: a Critical State Approach, Taylor and Francis.
53. Jordaan, I. J. (2001). Mechanics of Ice–structure Interaction. Eng. Fract. Mech., 68, 1923–1960.
54. Jukes, P., Eltaher, A., Abdalla, B. and Duron, B, (2008a), The Design and Simulation of Arctic Subsea Pipelines, Russia Offshore, 3rd Annual Meeting, Moscow.
55. Jukes, P., Eltaher, A., Abdalla, B. and Duron, B., (2008b), The Design and Simulation of Arctic Subsea Pipelines – Ice Gouging Formulations, 4th annual Arctic Oil & Gas Conference, Oslo, Norway.
56. Jukes, P., Eltaher, A., Abdalla, B., Duron, B. (2008c), The Design and Simulation of Arctic Subsea Pipelines, DNV Conference on Arctic activities, Høvik.
57. Kenny S, Barrett J, Phillips R and Popescu R (2007) Proceedings of the Seventeenth 2007 International Offshore and Polar Engineering Conference, ISOPE 2007.
58. Kenny, S., A. Nobahar, R. Phillips and J.I. Clark (2005) PRISE Studies on Sub–Gouge Deformations and Pipeline/Soil Interaction Analysis. Proc. 18th. Int. Conf. POAC.
59. Kenny, S., J. Bruce, T. King, R. McKenna, A. Nobahar and R. Phillips (2004). Probabilistic Design Methodology to Mitigate Ice Gouge Hazards for Offshore Pipelines. Proc., IPC, IPC04 0527, 9p.
60. King, T., Ralph, F., Barrett, J., and Zakeri, A. (2012). Physical and Numerical Modeling of a Sub–Surface Caisson for Protection of Subsea Facilities against Scouring Icebergs. Offshore Technology Conference. doi:10.4043/23789–MS
61. Konuk, I. and R. Gracie (2004a) A 3–dimensional Eulerian Finite Element Model for Ice Scour. Proceedings of IPC 2004, Calgary, Alberta. Paper IPC04–0075.
62. Konuk, I., 2009. Arctic Pipeline Design Challenges and Current Practices — Ice Scour. Proceedings of the 28th International Conference on Ocean, Offshore and Arctic Engineering (OMAE) Honolulu, Hawaii, pp. 155–162.
63. Konuk, I.S., Fredj, A. (2004b). A FEM model for pipeline analysis of ice scour. Proc., OMAE, OMAE2004–51477.
64. Konuk, I.S., Yu, S. (2007). A Pipeline Case Study for Ice Scour Design. Proc., OMAE, OMAE 2007–29375.

65. Konuk, I.S., Yu, S. Gracie, R. (2005). An ALE FEM Model of Ice Scour. Proc., IACMAG, Vol.3, pp.63–70.
66. Lach, P.R. (1996). Centrifuge Modeling of Large Soil Deformation Due to Ice Scour Ph.D. Thesis. Memorial University of Newfoundland, St. John's, Newfoundland, 685p.
67. Lach, RR. and Clark, J.I. (1996). Numerical Simulation of Large Soil Deformation Due to Ice Scour. The 49th Canadian Geotechnical Conference of the Canadian Geotechnical Society, Vol.1 pp. 189–198.
68. Lach, RR.,Clark, J.K., and Poorooshasb, R (1993). Centrifuge Modeling of Ice Scour. 4th Canadian Conference on Marine Geotechnical Engineering, St. John's, Newfoundland, pp. 356–374.
69. Lanan, G. A., Niedoroda, A. W., and Weeks, W. F. (1986). Ice Gouge Hazard Analysis. Offshore Technology Conference. doi:10.4043/5298–MS.
70. Lanan, G.A., Cowin, T.G., Hazen, B., Maguire, D.H., Hall, J.D., Perry, C., 2008 Oooguruk offshore Arctic flowline design and construction. Offshore Technology Conference (OTC), pp. 1180–1192.
71. Lanan, G.A., Ennis, J.O., (2001). Northstar Offshore Arctic Pipeline Design and Construction Proceedings of the 33rd Offshore Technology Conference. Offshore Technology Conference (OTC), Houston, pp. 621–628.
72. Lele, S.P., Hamilton, J.M., Panico, M., Arslan, H. (2011a), Advanced Continuum Modeling to Determine Pipeline Strain Demand due to Ice Gouging, Int. Conference on Offshore and Polar Engineering, Maui, Hawaii, ISOPE, Vol 4. ISBN 978–1–880653–96–8.
73. Lele, S.P., Hamilton, J.M., Panico, M., Arslan, H., Minnaar, K. (2011b), 3D Continuum Simulations to Determine Pipeline Strain Demand due to Ice–Gouge Hazards, Proc. Arctic Technology Conference, Houston, Texas.
74. Lewis, C.F.M. (1977). Beaufort Sea Tech. Rept. 23. Department of the Environment, Victoria.
75. Liferov, P. (2005). First–year Ice Ridge Scour and Some Aspects of Ice Rubble Behavior. Ph.D. thesis, Norwegian Univ. of Science and Technology, Trondheim, Norway.
76. Liferov, P. and Høyland, K.V. (2004). In–Situ Ice Ridge Scour Tests: Experimental Set Up and Basic Results. Cold Regions Science and Technology, 40, 97–100.

77. Liferov, P., Løset, S., Moslet, P.O., Bonnemaire, B. and Høyland, K.V. (2002). Medium Scale Modeling of Ice Ridge Scouring of the Seabed – Part I: Experimental Setup and Basic Results. Proceedings of the 16th International Symposium on Ice, Association of Hydraulic Engineering and Research, Dunedin.
78. McManus, D.A., Kelley, J.C., and Creager, J.S., (1969), Continental Shelf Sedimentation in an Arctic Environment: Geol. Soc. America Bull., v. 80, p. 1961–1984.
79. Meadows, B. W., and Gilbert, D. C. (1989). Drilling and Installing Large–Diameter Caissons for Wellhead Protection. Offshore Technology Conference. doi:10.4043/6128–MS
80. Miley, J.M. and Barnes, P.W. (1986). Field Studies, Beaufort and Chukchi Seas, Conducted from the NOAA ship Discoverer USGS Report 86–202.
81. Miller, D. L. and Bruggers, D. E. (1980). Soil and Permafrost Conditions in the Alaskan Beaufort Sea, Offshore Technology Conference OTC 3887.
82. Minerals Management Service (1990). Outer Continental Shelf Beaufort Sea Planning Area Oil and Gas Lease Sale 124: Final Environmental Impact Statement.
83. Minerals Management Service (2002). Evaluation of Sub–Sea Physical Environmental Data for the Beaufort Sea OCS and Incorporation into a Geographic Information System (GIS) Database. OCS Study MMS 2002–017.
84. Minerals Management Service (2006). Chukchi Planning Area Oil and Gas Lease Sale 193 and Seismic Surveying Activities in the Chukchi Sea: Draft Environmental Impact Statement. OSC EIS/EA, MMS 2006–060.
85. Minerals Management Service (2008). Design Options for Offshore Pipelines in the US Beaufort and Chukchi Seas Report R–07–078–519.
86. Myers, R., Blasco, S., Gilbert, G. and Shearer, J. (1996). 1990 Beaufort Sea Ice Scour Repetitive Mapping Program. Environmental Studies Research Funds, Report No. 129.
87. National Snow and Ice Center (NSIDC) Data. http://nsidc.org/data.
88. Nessim, M. and Hong, H. (1992). Statistical Data Analysis of New Scour Characteristics in the Beaufort Sea, Report prepared by the Centre for Frontier Engineering Research.
89. Nixon, J.R, Palmer, A., and Phillips, R. (1996). Simulations for Buried Pipeline Deformations Beneath Ice Scour. Offshore Marine and Arctic Engineering, Florence, Italy.

90. Nobahar, A., Kenny, S., and Phillips, R. (2007). Buried Pipelines Subject To Sub–Gouge Deformations. ASCE International Journal of Geomechanics GM/2005/000235, Vol. 7, No. 3, pp.206–216.
91. Nobahar, A., Phillips, R., and Zhou, J., (2004). Trench Effects on Pipe–Soil Interaction. Proc., 5th IPC, Paper No. IPC04–0141.
92. Nogueira, A.C., Paulin, M., 1999. Limit State Design for Northstar Offshore Pipeline. Offshore Magazine 59 (9), 146–196.
93. O'Rourke, M. J., and Liu, X. (1995). Lifeline Earthquake Engineering: Proc., 4th U.S. Conf., San Francisco, Technical Council on Lifeline Earthquake Engineering, New York.
94. Palmer, A., Konuk, I., Love, J., Been, K. and Comfort, G., (1989) Ice Scour Mechanics, A Research Paper prepared for Canada Oil and Gas Lands Administration and Gulf Canada Resources Ltd.
95. Palmer, A.C., Konuk, I., Comfort, G. and Been, K. (1990) Ice Gouging and Safety of Marine Pipelines. In Proceedings of the 22nd Annual Offshore Technology Conference 235–244.
96. Panico, M., Lele, S. P., Hamilton, J. M., Arslan, H., and Cheng, W. (2012). Advanced Ice Gouging Continuum Models: Comparison With Centrifuge Test Results. International Society of Offshore and Polar Engineers.
97. Paulin, M.J. (1992). Physical Model Analysis of Iceberg Scours in Dry and Submerged Sand. M.Eng. Thesis, Memorial University of Newfoundland, St. John's, 183 pp.
98. Paulin, M.J., Lach, P.R., Poorooshasb, F. and Clark, J.I. (1991). Preliminary Results of Physical Model Tests of Ice Scour. Proceedings of the 11th International Conference on Port and Ocean Engineering under Arctic Conditions, St. John's, Canada, 1017–1036.
99. Peek, R., Nobahar, A., (2012). Ice Gouging over a Buried Pipeline: Superposition Error of Simple Beam–And–Spring Models. Int. J. Geomech. 12 (4), 508–516.
100. Phillips, R., and Barrett, J. (2011). Ice Keel–Seabed Interaction: Numerical Modeling for Sands. Paper presented at the Port and Ocean Engineering under Arctic Conditions, Montreal.
101. Phillips, R., Barrett, J.A., Al–Showaiter, A., (2010), Ice Keel–Seabed Interaction: Numerical Modeling Validation. Proc.Offshore Technology Conference, Houston, Texas.
102. Phillips, R., Clark, J. I. and Kenny, S., (2005). PRISE studies on Gouge Forces and Sub–Gouge Deformations. 18th Int Conf Port and Ocean Engineering under Arctic Conditions, Vol. 1, p75–84.

103. Phillips, R., Clark, J.I. and Kenny, S. (2005). PRISE Studies on Gouge Forces and Sub–Gouge Deformations. Proceedings of the 18th International Conference on Port and Ocean Engineering under Arctic Conditions, Potsdam, New York, U.S., Vol. 1, 75–84.
104. Phillips, R., Nobahar, A. and Zhou, J., (2004). Combined Axial and Lateral Pipe–Soil Interaction Relationships. Proc., 5th IPC, Paper No. IPC04–0144.
105. Phillips, R.L., Barnes, P.W., Hunter, R.E., Reiss, T.E. and Rearic, D.M. (1988). Geologic Investigations in the Chukchi Sea, 1984, NOAA Ship Surveyor Cruise. USGS Report 88–25.
106. Pike, K., and Kenny, S. (2012). Advanced Continuum Modeling of the Ice Gouge Process: Assessment of Keel Shape Effect and Geotechnical Data. Proc., ISOPE, 6p.
107. Poorooshasb, F., Clark, J.I. and Woodworth–Lynas, C.M.T. (1989). Small Scale Modeling of Iceberg Scouring of the Seabed. Proceedings of the 10th International Conference on Port and Ocean Engineering under Arctic Conditions, Lulea, Sweeden, 133–145.
108. Prasad, K.S.R. (1985). Analytical and Experimental Modeling of Iceberg Scours. M.Eng. Thesis, Memorial University of Newfoundland, St. John's, Canada, 170 pp.
109. Ralph, F., King, T., and Zakeri, A. (2011). Alternative Concepts to Glory Holes for Protection of Subsea Infrastructure in Ice Prone Regions. Arctic Technology Conference, Houston, Texas, U.S., 7–9 February 2011.
110. Ralph, F., Soper, S., Stuckey, P., McNeil, A., and Barrett, J. (2012). Impact Loads and Protection of Subsea Structures on the Seabed from Floating Iceberg Keels. Offshore Technology Conference. doi:10.4043/23788–MS
111. Rearic, D.M., and McHendrie, A.G. (1983). Ice Gouge Data Sets from the Alaskan Beaufort Sea. Magnetic Tape and Documentation for Computer Assisted Analyses and Correlation. USGS Report 83–706.
112. Rearic, D.M., Barnes, P.W., and Reimnitz, E. (1981). Ice Gouge Data, Beaufort Sea, Alaska, 1972–1980. U.S. Geological Survey Open–File Report #81–950, 8 microfiche cards.
113. Reimnitz, E., Barnes, P.W., Rearic, D.M., Minkler, P.W., Kempema, E.W., and Reiss, T.E. (1982). Marine geological investigations in the Beaufort Sea in 1981 and Preliminary Interpretations from Regions from the Canning River to the Canadian Border. U.S. Geological Survey Open–File Report #82–974, 46 p.
114. Reimnitz, E., Maurer, D., Barnes, P. and Toimil, L. (1977). Some physical properties of shelf surface sediments, Beaufort Sea, Alaska. USGS Report 77–416.

115. Rogers, B., Blasco, S., and Jefferies, M. (1993). Pressuremeter Testing in Beaufort Shelf Surficial Sediments. 4th Canadian Conference on Marine Geotechnical Engineering, Vol. 1, (pp. 208–228). St. John's, Newfoundland, Canada.
116. Rossiter, C. P., and Kenny, S. P. (2012). Assessment of Ice/Soil Interactions: Continuum Modeling in Clays. Proc., ISOPE2012, 10p.
117. Sancio, R., Been, K. and Lopez, J. (2011). Large Scale Indenter Test Program to Measure Sub Gouge Displacements. Proceedings of the 21st International Conference on Port and Ocean Engineering under Arctic Conditions, Montreal, Canada.
118. Sayed, M. and Timco, G., (2009). A Numerical Model of Iceberg Scour. Cold Regions Sci. Tech., 55(1):103–110.
119. Schoonbeek I.S.S. and Allersma H.G.B. (2006) Centrifuge Modeling of Scouring Ice Keels in Clay. Physical Modeling in Geotechnics – 6th ICPMG '06 – Ng, Zhang and Wang 2006 Taylor and Francis Group, London, ISBN 0–415–41586–1
120. Schoonbeek, I.S.S. and Allersma, H.G.B. (2006). Centrifuge Modeling of Scouring Ice Keels in Clay. Proceedings of the 6th International Conference on Physical Modeling in Geotechnics, Vol. 2, 1291–1296.
121. Schoonbeek, I.S.S., Xin, M.X., Van Kesteren, W.G.M. and Been, K. (2006). Slip Line Field Solutions As an Approach to Understand Ice Sub–Gouge Deformation Patterns. Proceedings of the 16th International Offshore and Polar Engineering Conference, The International Society of Offshore and Polar Engineering, San Francisco, U.S., ISOPE, Vol 1, 628–633.
122. Serré, N. (2011). Numerical Modeling of Ice Ridge Keel Action on Subsea Structures. Cold Regions Science and Technology, 67(3), 107–119.
123. Sokolovski V.V. (1965) Statistics of Granular Media (74th edn.) Pergamon, London
124. Toimil, L. J. (1978). Ice–gouged Microrelief on the Floor of the Eastern Chukchi Sea, Alaska: A Reconnaissance Survey. USGS Report 78–693.
125. University of Alaska. Chukchi & Western Beaufort Circulation Study. Objectives & Background. Available from http://dm.sfos.uaf.edu/chukchi-beaufort/background.php.
126. USGS Circum–Arctic Resource Appraisal Fact Sheet 2008. http://pubs.usgs.gov/fs/2008/3049/fs2008–3049.pdf

127. Vikse, N., Gudmestad, O.T., Nystrøm, P.R. and Liferov, P. (2007). Small Scale Model Tests on Sub–Gouge Soil Deformations. Proceedings of the 26th International Conference on Offshore Mechanics and Arctic Engineering, The American Society of Mechanical Engineers, San Diego, U.S., 1–6.
128. Wang, J. and M.S. Gadala (1997). Formulation and Survey of ALE Method in Nonlinear Solid Mechanics. Finite Elem. Anal. Des., 24, pp.253–269.
129. Weber, W.S., Barnes, P.W., and Reimnitz, E. (1989). Data on the Characteristics of Dated Gouges on the Inner Shelf of the Beaufort Sea, Alaska; 1977–1985. USGS Open–File Report 89–151, 1989.
130. Weeks, W.F., Barnes, P.W., Rearic, D.M. and Reimnitz, E., (1983). Statistical Aspects of Ice Gouging on the Alaskan Shelf of the Beaufort Sea. USA Cold Regions Research and Engineering Laboratory, CRREL Report 83–21.
131. Wilson D.E. (1982) Nearshore Coastal Currents–Chukchi Sea. Kinetic Laboratories Int. Report to Arctic Project Office, Geophysical Institute, University of Alaska
132. Winkler, E., (1867), Die Leher von der Elastizitat und Festigkeit, Dominicus, Prague Dominicus, Prague.
133. Winters, W. J. and Lee, H. J. (1984). Geotechnical Properties of Samples from Borings Obtained in the Chukchi Sea, Alaska. USGS Report 85–23.
134. Woodworth–Lynas C., Nixon D., Phillips R., Palmer A. (1996) Sub–gouge Deformations and the Security of Arctic Marine Pipelines, Proceedings of the 28th Offshore Technology Conference (OTC), Houston, pp. 657–664.
135. Wu, C–T, Chen, J. S., Huck, Frank, (2001). Lagrangian Meshfree Formulation for Analysis of Geotechnical Materials. Journal of Engineering Mechanics, Volume 127, Number. 5, Pages 440–449.
136. Yang, Q.S. and Poorooshasb, H.B. (1997). Numerical Modeling of Seabed Ice Scour. Computers and Geotechnics, Vol.21, No. 1, pp. 1–20.
137. Yang, Q.S., Poorooshasb, F. and Poorooshasb, H.B. (1993). Analysis of Subscour Deformation by Finite Element Method. 4th Canadian Conference on Marine Geotechnical Engineering. Vol.2, pp. 739–754.
138. Zienkiewicz, O.C., M. Huang and M. Pastor (1995). Localization Problems in Plasticity Using Finite Elements with Adaptive Remeshing. Intl J Numerical and Analytical Methods in Geomechanics, 19(2), pp.127–148.

-o0o--o0o--o0o-

Appendix A Glossary

Terms used throughout this document include the following:

Abaqus: A software suite for Finite Element (FE) Analysis and computer–aided engineering.

Adaptive mesh technique: A local mesh refinement strategy to improve the convergence of solution in problematic areas.

Advection: A transport mechanism of a substance or conserved property (e.g., energy) by a fluid caused by the fluid's bulk motion.

Attack angle: The angle between the keel face and the contacting soil surface.

Bearing capacity: In geotechnical engineering, the capacity of soil to support the loads applied to the ground. The bearing capacity of soil is the maximum average contact pressure transferred from the foundation to the soil without soil shear failure.

Boundary condition: The set of conditions specified for the behavior of the solution to a set of differential equations at the boundary of its domain. In FE analysis simulations, it is the restriction of a certain degree of freedom applied at the set of nodes.

Cam–Clay (CC) and **Modified Cam–Clay (MCC)**: The first critical state models for describing the behavior of soft soils such as clay. The Cam–Clay (CC) and Modified Cam–Clay (MCC) were formulated by researchers at Cambridge University. Both models describe three important aspects of soil behavior: (1) Strength, (2) Compression or dilatancy (the volume change that occurs with shearing), and (3) Critical state at which soil elements can experience unlimited distortion without any changes in stress or volume. A major advantage of Cap plasticity models, a class to which the CC and MCC formulations belong, is their ability to model volume changes more realistically.

Cap Model (LS–DYNA): A constitutive model where shear and compaction surfaces are combined to form a smooth, continuous surface.

C–CORE: Centre for Cold Ocean Resources Engineering, a Canadian research and development corporation.

Centrifuge modeling: Involves testing of small–scale models in the enhanced gravity field of a geotechnical centrifuge. This technique is particularly useful in testing materials such as soils that exhibit non–linear stress–strain behavior and can suffer significant plastic strains.

Constitutive modeling: The mathematical description of how materials respond to various loadings so that any increment of strain applied on a material will cause a stress increment.

Continuum approach: A material is modeled as a continuous mass, meaning the matter in the body is continuously distributed and fills the entire region of space it occupies.

Convergence: In FE analysis, convergence is achieved when the output from the FE program is converging on a single correct solution. To check the convergence of the solution, at least two solutions to the same problem are required. The solution from the FE program is checked with a solution of increased accuracy. If the more accurate solution is dramatically different from the original solution, then the solution is not converged. However, if the solution does not change much (less than a few percentage points of difference), then the solution is considered converged.

Critical state: This state is reached when the soil distorts at a constant state of stress with no volume change. This state is characterized by the critical state line.

Dead wedge: Soil mass in the frontal mount that does not undergo significant displacements during ice gouging and remains 'attached' to the keel.

Dilatancy: The observed tendency of a compacted granular material to dilate (expand in volume) as it is sheared. This occurs because the grains in a compacted state are interlocking and therefore do not have the freedom to move around one another. When stressed, a lever motion occurs between neighboring grains, which produces a bulk expansion of the material. On the other hand, when a granular material starts in a very loose state, it may initially compact instead of dilating under shear.

Dilation angle: Controls an amount of plastic volumetric strain developed during plastic shearing and is assumed constant during plastic yielding.

Drained condition: Occurs when there is no change in pore water pressure due to external loading. In a drained condition, the pore water can drain out of the soil easily, causing volumetric strains in the soil.

Drucker–Prager: A failure criterion that is a three–dimensional, pressure–dependent model to estimate the stress state at which soil reaches its ultimate strength.

Friction angle φ: The strength of sand is usually characterized by the peak friction angle φ and the critical state friction angle φ_c. It is generally understood that the peak friction angle depends not only on density but also on the stress path.

Iceberg: Ice that has broken off from glaciers or shelf ice and is floating in open water. To be classified as an iceberg, the height of the ice must be greater than 16 ft. above sea level, the thickness must be 98–164 ft., and the ice must cover an area of at least 5,382 sq ft.

Isoparametric formulation: Allows elements to be created that are nonrectangular and have curved sides.

Keel: The submerged counterpart of an ice ridge/iceberg.

Lach's experiment: Lach conducted centrifuge experiments in Cambridge University's geotechnical centrifuge in 1992. He is thought to be one of the pioneers in the study of ice gouging. Test 05 was the base case for the experimental program, where the keel attack angle was set to 15°, keel width was 0.328 ft. (100 mm) or 32.8 ft. at prototype scale, and the steady state gouge depth attained was 0.039 ft. (12.1 mm) or 0.39 at prototype scale. Many later researchers have referred to Lach's experiments and compared results of numerical simulations with his.

Limit State Design (LSD): Also known as Load and Resistance Factor Design (LRFD), refers to a design method used in structural engineering. A limit state is a condition of a structure beyond which it no longer fulfils the relevant design criteria. The condition may refer to a degree of loading or other actions on the structure, while the criteria refer to structural integrity, fitness for use, durability, or other design requirements.

Mesh distortion: Deformations alter the FE mesh, often to the point where the mesh cannot provide accurate results or the analysis terminates for numerical reasons. In such simulations, it is necessary to use adaptive meshing tools to periodically minimize the distortion in the mesh. Mohr Coulomb describes a linear relationship between normal and shear stresses (or maximum and minimum principal stresses) at failure and combines Hooke's Law with Coulomb's failure criteria for shear strength.

Nonlinear spring: An element that has a defined nonlinear load–displacement function.

Penalty methods: A certain class of algorithms for solving constrained optimization problems. A penalty method replaces a constrained optimization problem by a series of unconstrained problems whose solutions ideally converge to the solution of the original constrained problem. The unconstrained problems are formed by adding a term, called a penalty function.

PRISE (Pressure Ridge Ice Scour Experiment): This joint industry research program investigated the stresses and soil deformations during ice gouging events. It was a proprietary program designed to develop the engineering framework to allow pipeline installation in Arctic regions. The program included a series of small–scale physical tests conducted in a geotechnical centrifuge to enhance the understanding of soil deformations and ice loads that occur during ice gouging events.

Ramberg–Osgood: This equation was created to describe the nonlinear relationship between stress and strain—that is, the stress–strain curve—in materials near their yield points. It is especially useful for metals that harden with plastic deformation (strain hardening), showing a smooth elastic–plastic transition.

Reliability: Theoretically defined as the probability of success (Reliability = 1 – Probability of Failure); as the frequency of failures; or in terms of availability, as a probability derived from reliability and maintainability. Reliability engineering deals with the estimation and management of high levels of 'lifetime' engineering uncertainty and risks of failure.

Shell elements: Four– to eight–node isoparametric quadrilaterals or three– to six–node triangular elements in any 3–D orientation.

Soil resistance: The pressure exerted by the soil against a structure on a surface of a surrounding soil mass. It can be classified as earth pressure at rest, active resistance, and **passive resistance**. When a soil mass pushes against a structure, the pressure is known as active pressure. On the other hand, if the retaining structure pushes against the soil mass, the resulting pressure is known as passive pressure.

Strain gradient: An increase or decrease in the magnitude of strain observed in passing from one point or moment to another.

Steady state gouging: A gouging ice keel is thought to have reached steady state when the frontal mount and side berms have reached their ultimate sizes.

Strain contour: Mapping of points with the same amplitude of strain in a continuous line or surface.

Strain localization/Shear band: A narrow zone of intense shearing strain, usually of plastic nature, developing during severe deformation of ductile materials.

Subgouge deformation profile: The magnitude and extent of deformations taking place underneath the gouging keel.

T–bar test: Test used in site investigations to obtain accurate intact and remolded undrained strength profiles of soft sediments.

Total stress analysis: Analysis that uses the undrained shear strength of the soil. The total stress analysis is typically only used for cohesive soil. The total stress analysis is often used for the evaluation of foundations and embankments to be supported by cohesive soil. The actual analysis is performed for rapid loading or unloading conditions often encountered during the construction phase or just at the end of construction. This analysis is applicable to field situations where there is a change in shear stress that occurs quickly enough that the cohesive soil does not have time to consolidate, or in the case of heavily overconsolidated cohesive soils, the negative pore water pressures do not have time to dissipate.

Undrained condition: Condition that occurs when the pore water is unable to drain out of the soil. In an undrained condition, the rate of loading is much quicker than the rate at which the pore water can drain out of the soil. As a result, most of the external loading is taken by the pore water, resulting in an increase in the pore water pressure. The tendency of soil to change volume is suppressed during undrained loading.

Undrained Shear strength (Su): A term used in soil mechanics to describe the magnitude of the shear stress that a soil can sustain under undrained conditions.

Von Mises criterion: This constitutive model considers piecewise, linear, elasto–perfectly plastic soil behavior with yield strength independent of hydrostatic pressure. In terms of simulating cohesive soil behavior, the classical plasticity model assumes fully saturated conditions with undrained loading (i.e., total stress). The von Mises yield surface in principal stress space is a right cylinder and is represented by the equation of a circle in the deviatoric plane.

Winker springs: The first springs used for foundation design. The soil was treated as a row of independent springs called Winker springs, implying that the soil resistance to a settlement y would be proportional to a spring constant (stiffness). This method is also called p–y curve and is mentioned in American Petroleum Institute and DNV GL codes.

Appendix B Reference Tables

Table B–1: Summary of Borehole Locations (Miller and Bruggers, 1980 [81])

Boring Number	Water Depth (ft.)	Boring Depth (ft.)	Thickness of Holocene (ft.)		Depth to Top of Pleistocene (ft.)		Depth to Bonded Permafrost (ft.)
			Fine–grain	Sand	Stiff Clay	Gravel	
1	16.5	81	33	—	NE	33	NE
2	22.8	101	19	—	NE	19	NE
3	4.2	95	10	—	NE	10	NE
4	27.9	102	—	12	12	53	40
5	42.1	300	15	—	NE	15	190
6	36.4	103	39	—	39	60	NE
7	25.4	100	39	—	39	51	NE
8	46.0	100	—	—	0	85	63
9	17.4	130	—	—	0	63	23
10	21.2	108	—	7	7	95	76
11	24.7	95	—	10	10	83	54
12	50.0	301	—	—	0	112	2
13	18.3	101	—	—	0	37	32
14	21.6	101	33	—	53	33 & 62	53
15	18.0	300	32	—	NE	32	42
16	30.3	110	—	4	4	97	72
17	47.7	103	—	—	0	—	85
18	37.0	303	—	—	0	—	42
19	34.5	116	43	—	43	102	73
20	37.0	114	—	—	0	112	21

Table B–2: Boring Locations (Winters and Lee, 1984 [133])

Boring	Latitude	Longitude	Water Depth (ft.)	Location
2	70°40.014'N	167°19.594'W	176.83	Southern margin of North Chukchi Basin
3	70°40.014'N	167°19.594'W	176.83	Southern margin of North Chukchi Basin
4	70°27.676'N	167°05.205'W	167.98	Northern flank of Herald Arch
5	69°59.146'N	168°04.943'W	159.12	On Herald Arch
6	69°37.901 'N	168°51.785'W	162.07	Extreme Northern margin of Hope Basin
7	69°50.506'N	168°22.205'W	154.20	On Herald Arch
8	69°37.91 1'N	168°51.776'W	173.89	Extreme Northern margin of Hope Basin
Borings 2 and 3 are spaced approximately 23 ft. apart Borings 7 and 8 are spaced approximately 23 ft. apart				

Table B–3: Summary of Data Sets – MMS, 2008 [85]

Parameter	Rearic and McHendrie (1983)	Weber et al. (1989)
Dates surveyed	1972–1981	1977–1985
Repetitive mapping used?	No	Yes
Total length surveyed	1518.01 mi (2443 km)	196.35 mi (316 km)
Total no. of gouges recorded (single keel/multiple)	132183	19327 (s + m)
Seabed soil type identified?	Yes	No
Gouge depths recorded	Yes (s/m not differentiated)	Yes (new gouges only)
Zone A		
Water depth covered	32.81–196.85 ft. (10–60 m)	49.21–98.43 ft. (15–30 m)
Length surveyed	382.14 mi (615 km)	9.94 mi (16 km)
Total number of gouges recorded	46885	2091
Number of new gouges recorded	–	33/31
Zone B		
Water depth covered	0–82.02 ft. (0–25 m)	16.40–65.62 ft. (5–20 m)
Length surveyed	72.70 mi (117 km)	54.06 mi (87 km)
Total number of gouges recorded	8534	5725
Number of new gouges recorded	–	254/124
Zone C		
Water depth covered	0–98.43 ft. (0–30 m)	16.40–82.02 ft. (5–25 m)
Length surveyed	288.32 miles (464 km)	67.11 miles (108 km)
Total number of gouges recorded	2583	2675
Number of new gouges recorded		286/88
Zone D		
Water depth covered	0–32.80 ft. (0–10 m)	–
Length surveyed	234.25 miles (377 km)	–
Total number of gouges recorded	1197	–
Number of new gouges recorded	–	–

Table B–4: Summary of Rearic and McHendrie, 1983 [111] Gouge Depths – MMS, 2008 [85]

Water Depth ft.		Gouge Depth ft. (m)					
	Zone	A	B	C	D.1	D.2	ALL
0–16.40 (0–5)	No. Gouges		6	3	4	9	22
	Mean (ft.)		0.98 (0.3)	1.31 (0.4)	1.31 (0.4)	0.98 (0.3)	0.98 (0.3)
	Max (ft.)		0.98 (0.3)	1.64 (0.5)	1.64 (0.5)	2.30 (0.7)	2.30 (0.7)
	Std (ft.)		0	0.33 (0.1)	0.33 (0.1)	0.33 (0.1)	0.33 (0.1)
	Λ (ft.$^{-1}$)		10 (32.8)	6 (19.7)	6.7 (22)	6.9 (22.6)	7.4 (24.3)
16.40–32.81 (5–10)	No. Gouges		153	52		15	220
	Mean (ft.)		0.98 (0.3)	1.31 (0.4)		0.98 (0.3)	0.98 (0.3)
	Max (ft.)		2.95 (0.9)	3.61 (1.1)		1.64 (0.5)	3.61 (1.1)
	Std (ft.)		0.33 (0.1)	0.66 (0.2)		0.33 (0.1)	0.33 (0.1)
	Λ (ft.$^{-1}$)		7.2 (23.6)	5.9 (19.4)		8.9 (29.2)	6.9 (22.6)
32.81–49.21 (10–15)	No. Gouges	186	357	598			1141
	Mean (ft.)	1.31 (0.4)	1.31 (0.4)	0.98 (0.3)			1.31 (0.4)
	Max (ft.)	2.30 (0.7)	3.61 (1.1)	3.61 (1.1)			3.61 (1.1)
	Std (ft.)	0.66 (0.2)	0.33 (0.1)	0.33 (0.1)			
	Λ (ft.$^{-1}$)	6.5 (21.3)	5.1 (16.7)	7 (23)			6.2 (20.3)
49.21–65.62 (15–20)	No. Gouges	1910	258	1652			3820
	Mean (ft.)	1.64 (0.5)	1.31 (0.4)	1.31 (0.4)			1.31 (0.4)
	Max (ft.)	6.89 (2.1)	2.95 (0.9)	5.57 (1.7)			6.89 (2.1)
	Std (ft.)	0.98 (0.3)	0.33 (0.1)	0.66 (0.2)			0.66 (0.2)
	Λ (ft.$^{-1}$)	3.5 (11.5)	6.5 (21.3)	5.8 (19)			4.4 (14.4)
65.62–82.02 (20–25)	No. Gouges	7784	83	2383			10250
	Mean (ft.)	1.64 (0.5)	1.31 (0.4)	1.31 (0.4)			1.31 (0.4)
	Max (ft.)	7.55 (2.3)	2.95 (0.9)	5.57 (1.7)			7.55 (2.3)
	Std (ft.)	0.98 (0.3)	0.33 (0.1)	0.66 (0.2)			0.66 (0.2)
	Λ (ft.$^{-1}$)	3.9 (12.8)	5.7 (18.7)	4.6 (15.1)			4 (13.1)
65.62–98.43 (20–30)	No. Gouges	5694		516			6210
	Mean (ft.)	1.64 (0.5)		1.64 (0.5)			1.64 (0.5)
	Max (ft.)	11.48 (3.5)		4.92 (1.5)			11.48 (3.5)
	Std (ft.)	0.98 (0.3)		0.98 (0.3)			0.98 (0.3)

Water Depth ft.		Gouge Depth ft. (m)					
	Zone	A	B	C	D.1	D.2	ALL
	Λ (ft.$^{-1}$)	2.9 (9.5)		3.3 (10.8)			2.9 (9.5)
98.43–114.83 (30–35)	No. Gouges	2165					2165
	Mean (ft.)	1.97 (0.6)					1.97 (0.6)
	Max (ft.)	12.8 (3.9)					12.8 (3.9)
	Std (ft.)	1.31 (0.4)					1.31 (0.4)
	Λ (ft.$^{-1}$)	2.5 (8.2)					2.5 (8.2)
114.83–131.23 (35–40)	No. Gouges	298					298
	Mean (ft.)	2.95 (0.9)					2.95 (0.9)
	Max (ft.)	12.8 (3.9)					12.8 (3.9)
	Std (ft.)	1.97 (0.6)					1.97 (0.6)
	Λ (ft.$^{-1}$)	1.5 (4,9)					1.5 (4.9)
131.23–147.64 (40–45)	No. Gouges	163					163
	Mean (ft.)	1.97 (0.6)					1.97 (0.6)
	Max (ft.)	8.20 (2.5)					8.20 (2.5)
	Std (ft.)	0.66 (0.2)					0.66 (0.2)
	Λ (ft.$^{-1}$)	2.4 (7.9)					2.4 (7.9)
147.64–164.04 (45–50)	No. Gouges	139					139
	Mean (ft.)	1.97 (0.6)					1.97 (0.6)
	Max (ft.)	4.92 (1.5)					4.92 (1.5)
	Std (ft.)	0.66 (0.2)					0.66 (0.2)
	Λ (ft.$^{-1}$)	2.4 (7.9)					2.4 (7.9)
164.04–180.45 (50–55)	No. Gouges	51					51
	Mean(ft.)	2.30 (0.7)					2.30 (0.7)
	Max (ft.)	4.92 (1.5)					4.92 (1.5)
	Std (ft.)	0.98 (0.3)					0.98 (0.3)
	λ(ft.$^{-1}$)	2.1(6.9)					2.1(6.9)
180.45–196.85 (55–60)	No. Gouges	2					2
	Mean (ft.)	3.28 (1)					3.28 (1)
	Max (ft.)	3.61 (1.1)					3.61 (1.1)
	Std (ft.)	0.33 (0.1)					0.33 (0.1)
	Λ (ft.$^{-1}$)	1.3 (4.3)					1.3 (4.3)

Water Depth ft.		Gouge Depth ft. (m)					
	Zone	A	B	C	D.1	D.2	ALL
Total	No. Gouges	18392	857	5204	4	24	24481
	Mean (ft.)	1.64 (0.5)	1.31 (0.4)	1.31 (0.4)	1.31 (0.4)	0.98 (0.3)	1.64 (0.5)
	Max (ft.)	12.8 (3.9)	3.61 (1.1)	5.58 (1.7)	1.64 (0.5)	2.30 (0.7)	12.80 (3.9)
	Std (ft.)	0.98 (0.3)	0.33 (0.1)	0.66 (0.2)	0.33 (0.1)	0.33 (0.1)	0.98 (0.3)
	Λ (ft.$^{-1}$)	3.2 (10.5)	5.9 (19.4)	4.9 (16.1)	6.7 (22)	8 (26.3)	3.5 (11.5)

Table B–5: Single Gouge Depths (Weber et al., 1989 [129]) – MMS, 2008 [85]

Water Depth ft. (m)	Gouge Depth, ft. (m)				
	Zone	A	B	C	ALL
16.40–32.81 (5–10)	No. Gouges		7	2	9
	Mean (ft.)		1.31 (0.4)	1.97 (0.6)	1.31 (0.4)
	Max (ft.)		2.30 (0.7)	2.30 (0.7)	2.30 (0.7)
	Std (ft.)		0.33 (0.1)	0.33 (0.1)	0.66 (0.2)
	Λ (ft.$^{-1}$)		1.80 (5.9)	0.76 (2.5)	1.37 (4.5)
32.81–49.21 (10–15)	No. Gouges		17	1	18
	Mean (ft.)		1.97 (0.6)	1.31 (0.4)	1.97 (0.6)
	Max (ft.)		9.84 (3)	1.31 (0.4)	9.84 (3)
	Std (ft.)		2.30 (0.7)	0	1.97 (0.6)
	Λ (ft.$^{-1}$)		0.82 (2.7)	1.52 (5)	0.86 (2.8)
49.21–65.62 (15–20)	No. Gouges	2	3	12	17
	Mean (ft.)	1.31 (0.4)	0.98 (0.3)	1.64 (0.5)	1.64 (0.5)
	Max (ft.)	1.64 (0.5)	0.98 (0.3)	4.59 (1.4)	4.59 (1.4)
	Std (ft.)	0.33 (0.1)	0	0.98 (0.3)	0.98 (0.3)
	Λ (ft.$^{-1}$)	1.52 (5)	3.05 (10)	0.94 (3.1)	1.12 (3.7)
65.62–82.02 (20–25)	No. Gouges	4			4
	Mean (ft.)	0.98 (0.3)			0.98 (0.3)
	Max (ft.)	0.98 (0.3)			0.98 (0.3)
	Std (ft.)	0			0
	Λ (ft.$^{-1}$)	3.04 (10)			3.04 (10)
Total	No. Gouges	6	27	15	48
	Mean (ft.)	0.98 (0.3)	1.64 (0.5)	1.64 (0.5)	1.64 (0.5)
	Max (ft.)	1.64 (0.5)	9.84 (3)	4.59 (1.4)	9.84 (3)
	Std (ft.)	0.33 (0.1)	1.64 (0.5)	0.98 (0.3)	1.31 (0.4)
	Λ (ft.$^{-1}$)	2.29 (7.5)	1.07 (3.5)	0.95 (3.1)	1.09 (3.6)
Measurements in parenthesis are in meters (m)					

Table B–6: Multiple Gouge Depths (Weber et al., 1989 [129])

Water Depth ft. (m)	Gouge Depth, ft. (m)				
	Zone	A	B	C	ALL
32.81–49.21 (10–15)	No. Gouges		12	1	13
	Mean (ft.)		1.31 (0.4)	9.84 (3)	1.97 (0.6)
	Max (ft.)		1.97 (0.6)	9.84 (3)	9.84 (3)
	Std (ft.)		0.33 (0.1)	0	2.30 (0.7)
	Λ (ft.$^{-1}$)		1.74 (5.7)	0.12 (0.4)	0.82 (2.7)
49.21–65.62 (15–20)	No. Gouges	8	5	3	16
	Mean (ft.)	1.64 (0.5)	1.64 (0.5)	1.31 (0.4)	1.64 (0.5)
	Max (ft.)	3.93 (1.2)	2.62 (0.8)	1.64 (0.5)	3.93 (1.2)
	Std (ft.)	0.98 (0.3)	0.66 (0.2)	0.33 (0.1)	0.66 (0.2)
	Λ (ft.$^{-1}$)	1.10 (3.6)	1.10 (3.9)	1.31 (4.3)	1.16 (3.8)
65.62–82.02 (20–25)	No. Gouges	7		1	8
	Mean (ft.)	1.97 (0.6)		0.98 (0.3)	1.64 (0.5)
	Max (ft.)	2.62 (0.8)		0.98 (0.3)	2.62 (0.8)
	Std (ft.)	0.66 (0.2)		0	0.66 (0.2)
	Λ (ft.$^{-1}$)	0.85 (2.8)		3.05 (10)	0.95 (3.1)
65.62–98.43 (20–30)	No. Gouges	1			1
	Mean (ft.)	2.62 (0.8)			2.62 (0.8)
	Max (ft.)	2.62 (0.8)			2.62 (0.8)
	Std (ft.)	0			0
	Λ (ft.$^{-1}$)	0.52 (1.7)			0.52 (1.7)
Total	No. Gouges	16	17	5	38
	Mean (ft.)	1.64 (0.5)	1.31 (0.4)	2.95 (0.9)	1.64 (0.5)
	Max (ft.)	3.93 (1.2)	2.62 (0.8)	9.84 (3)	9.84 (3)
	Std (ft.)	0.98 (0.3)	0.33 (0.1)	3.93 (1.2)	1.64 (0.5)
	Λ (ft.$^{-1}$)	0.91 (3)	1.52 (5)	0.43 (1.4)	0.95 (3.1)
Measurements in parentheses are in meters (m)					

Table B–7:Single Gouge Depths (Weber et al., 1989) – MMS (2008)

Water Depth (m)	Gouge Depth, ft. (m)				
	Zone	A	B	C	ALL
16.40–32.81 (5–10)	**No. Gouges**		7	2	9
	Mean (ft.)		1.31 (0.4)	1.97 (0.6)	1.31 (0.4)
	Max (ft.)		1.38 (0.7)	1.38 (0.7)	1.38 (0.7)
	Std (ft.)		0.33 (0.1)	0.33 (0.1)	0.66 (0.2)
32.81–49.21 (10–15)	**No. Gouges**		17	1	18
	Mean (ft.)		1.97 (0.6)	1.31 (0.4)	1.97 (0.6)
	Max (ft.)		9.84 (3)	1.31 (0.4)	9.84 (3)
	Std (ft.)		1.38 (0.7)	0	1.97 (0.6)
49.21–65.62 (15–20)	**No. Gouges**	2	3	12	17
	Mean (ft.)	1.31 (0.4)	0.98 (0.3)	1.64 (0.5)	1.64 (0.5)
	Max (ft.)	1.64 (0.5)	0.98 (0.3)	4.59 (1.4)	4.59 (1.4)
	Std (ft.)	0.33 (0.1)	0	0.98 (0.3)	0.98 (0.3)
65.62–82.02 (20–25)	**No. Gouges**	4			4
	Mean (ft.)	0.98 (0.3)			0.98 (0.3)
	Max (ft.)	0.98 (0.3)			0.98 (0.3)
	Std (ft.)	0			0
Total	**No. Gouges**	6	27	15	48
	Mean (ft.)	0.98 (0.3)	1.64 (0.5)	1.64 (0.5)	1.64 (0.5)
	Max (ft.)	1.64 (0.5)	9.84 (3)	4.59 (1.4)	9.84 (3)
	Std (ft.)	0.33 (0.1)	1.64 (0.5)	0.98 (0.3)	1.31 (0.4)

Table B–8: Multiplet Gouge Depths (Weber et al., 1989)

Water Depth (m)	Gouge Depth, ft. (m)				
	Zone	A	B	C	ALL
16.40–32.81 (10–15)	**No. Gouges**		12	1	13
	Mean (ft.)		1.31 (0.4)	9.84 (3)	1.97 (0.6)
	Max (ft.)		1.97 (0.6)	9.84 (3)	9.84 (3)
	Std (ft.)		0.33 (0.1)	0	2.30 (0.7)
49.21–65.62 (15–20)	**No. Gouges**	8	5	3	16
	Mean (ft.)	1.64 (0.5)	1.64 (0.5)	1.31 (0.4)	1.64 (0.5)
	Max (ft.)	3.94 (1.2)	2.62 (0.8)	1.64 (0.5)	3.94 (1.2)
	Std (ft.)	0.98 (0.3)	0.66 (0.2)	0.33 (0.1)	0.66 (0.2)
65.62–82.02 (20–25)	**No. Gouges**	7		1	8
	Mean (ft.)	1.97 (0.6)		0.98 (0.3)	1.64 (0.5)
	Max (ft.)	2.62 (0.8)		0.98 (0.3)	2.62 (0.8)
	Std (ft.)	0.66 (0.2)		0	0.66 (0.2)
82.02–98.43 (25–30)	**No. Gouges**	1			1
	Mean (ft.)	2.62 (0.8)			2.62 (0.8)
	Max (ft.)	2.62 (0.8)			2.62 (0.8)
	Std (ft.)	0			0
Total	**No. Gouges**	16	17	5	38
	Mean (ft.)	1.64 (0.5)	1.31 (0.4)	2.14 (0.9)	1.64 (0.5)
	Max (ft.)	3.94 (1.2)	2.62 (0.8)	9.84 (3)	9.84 (3)
	Std (ft.)	0.98 (0.3)	0.33 (0.1)	3.94 (1.2)	1.64 (0.5)

Table B–9: Summary of Weber et al., 1989 [129] Gouge Crossing Density – MMS, 2008 [85]

Water Depth ft. (m)	Crossing Density (gouge/mile)				
	Zone	A	B	C	ALL
0–16.40 (0–5)	No. mile Intervals	0	0	111.85	111.85
	Mean (gouge/mile)	0	0	0.11	0.11
	Max (gouge/mile)	0	0	0.21	0.21
	Std (gouge/mile)	0	0	0.11	0.11
16.40–32.81 (5–10)	No. mile Intervals	0	782.93	894.78	1677.70
	Mean (gouge/mile)	0	0.64	0.43	0.51
	Max (gouge/mile)	0	1.72	1.45	1.72
	Std (gouge/mile)	0	0.51	0.46	0.48
32.81–49.21 (10–15)	No. mile Intervals	0	2125.09	1938.68	4063.77
	Mean (gouge/mile)	0	2.09	0.48	1.34
	Max (gouge/mile)	0	4.59	1.66	4.59
	Std (gouge/mile)	0	1.02	0.43	1.13
49.21–65.62 (15–20)	No. mile Intervals	260.98	335.54	745.65	1342.16
	Mean (gouge/mile)	3.19	2.31	0.80	1.64
	Max (gouge/mile)	5.04	3.17	3.54	5.04
	Std (gouge/mile)	0.99	0.51	1.02	1.34
65.62–82.02 (20–25)	No. mile Intervals	186.41	0	298.26	484.67
	Mean (gouge/mile)	4.43	0	2.25	3.08
	Max (gouge/mile)	7.19	0	3.41	7.19

Water Depth ft. (m)	Crossing Density (gouge/mile)				
	Zone	A	B	C	ALL
	Std (gouge/mile)	1.61	0	0.78	1.56
82.02–98.43 (25–30)	No. mile Intervals	186.41	0	0	186.41
	Mean (gouge/mile)	2.31	0	0	2.31
	Max (gouge/mile)	3.46	0	0	3.46
	Std (gouge/mile)	1.31	0	0	1.31
Measurements in parenthesis are in meters (m)					

Table B–10: Summary of Toimil, 1978 [124] Data Set Used in MMS, 2008 [85]

Parameter	Toimil (1978)
Dates surveyed	1974
Repetitive mapping used	No
Total length surveyed	847.55 miles (1,364 km)
Total number of gouges recorded	436
Seabed soil type identified	No
Gouge depths recorded	584
Gouge widths recorded	245
Zone A	
Water depth covered	65.62–246.06 ft. (20–75 m)
Length surveyed	257.86 mi (415 km)
Total number of gouges recorded	2825
Zone B	
Water depth covered	82.02–164.04 ft. (25–50 m)

Parameter	Toimil (1978)
Length surveyed	16.16 mi (26 km)
Total number of gouges recorded	6
Zone C	
Water depth covered	65.62–360.89 ft. (20–110m)
Length surveyed	349.21 mi (562km)
Total number of gouges recorded	6,522

Table B–11: Summary of Gouge Depths (Toimil, 1978 [124])

Water Depth ft. (m)	Gouge Depth, m				
	Zone	A	B	C	ALL
65.62–82.02 (20–25)	No. Gouges	2	0	34	36
	Mean	2.62	0	2.30	2.30
	Max	3.28	0	3.28	3.28
	Std	1.31	0	0.66	0.66
82.02–98.43 (25–30)	No. Gouges	21	0	48	69
	Mean	1.97	0	2.62	2.30
	Max	4.92	0	6.56	6.56
	Std	0.66	0	1.31	0.98
98.43–114.83 (30–35)	No. Gouges	56	0	62	118
	Mean	1.97	0	2.62	2.30
	Max	4.92	0	16.40	16.40
	Std	0.98	0	1.97	1.64
114.83–131.23 (35–40)	No. Gouges	62	0	68	130
	Mean	2.95	0	2.30	2.62
	Max	14.76	0	4.92	14.76
	Std	2.30	0	0.98	1.97
131.23–147.64 (40–45)	No. Gouges	42	0	36	78
	Mean	3.61	0	2.62	3.28
	Max	9.84	0	4.92	9.84
	Std	1.97	0	0.98	1.64

Water Depth ft. (m)	Gouge Depth, m				
	Zone	A	B	C	ALL
147.64–164.04 (45–50)	No. Gouges	36	0	16	52
	Mean	2.30	0	2.62	2.62
	Max	9.84	0	4.92	9.84
	Std	1.64	0	0.98	1.31
164.04–180.45 (50–55)	No. Gouges	0	0	9	9
	Mean	0	0	2.30	2.30
	Max	0	0	4.92	4.92
	Std	0	0	1.31	1.31
180.45–196.85 (55–60)	No. Gouges	0	0	2	2
	Mean	0	0	1.64	1.64
	Max	0	0	1.64	1.64
	Std	0	0	0	0
> 196.85 (> 60)	No. Gouges	0	0	0	0
	Mean	0	0	0	0
	Max	0	0	0	0
	Std	0	0	0	0

Table B–12: Summary of Gouge Widths (Toimil, 1978 [124])

Water Depth ft. (m)	Gouge Width, m				
	Zones	A	B	C	ALL
65.62–82.02 (20–25)	No. Gouges	0	0	14	14
	Mean	0	0	39.37	39.37
	Max	0	0	98.43	98.43
	Std	0	0	26.25	26.25
82.02–98.43 (25–30)	No. Gouges	2.00	0	27.00	29.00
	Mean	49.21	0	45.93	45.93
	Max	82.02	0	196.85	196.85
	Std	45.93	0	42.65	39.37
98.43–114.83 (30–35)	No. Gouges	32.00	0	35.00	67.00
	Mean	108.27	0	42.65	75.46
	Max	246.06	0	196.85	246.06
	Std	75.46	0	32.81	65.62
114.83–131.23 (35–40)	No. Gouges	31.00	0	32.00	63.00
	Mean	114.83	0	45.93	78.74
	Max	311.68	0	164.04	311.68
	Std	75.46	0	42.65	68.90
131.23–147.64 (40–45)	No. Gouges	5.00	0	13.00	18.00
	Mean	180.45	0	59.06	95.14
	Max	262.47	0	196.85	262.47
	Std	85.30	0	45.93	78.74

Water Depth ft. (m)	Gouge Width, m				
	Zones	A	B	C	ALL
147.64–164.04 (45–50)	No. Gouges	16.00	0	4.00	20.00
	Mean	62.34	0	68.90	62.34
	Max	82.02	0	82.02	82.02
	Std	19.69	0	16.40	19.69
164.04–180.45 (50–55)	No. Gouges	0	0	3.00	3.00
	Mean	0	0	52.49	52.49
	Max	0	0	82.02	82.02
	Std	0	0	29.53	29.53
180.45–196.85 (55–60)	No. Gouges	0	0	0	0
	Mean	0	0	0	0
	Max	0	0	0	0
	Std	0	0	0	0
> 196.85 (> 60)	No. Gouges	0	0	0	0
	Mean	0	0	0	0
	Max	0	0	0	0
	Std	0	0	0	0

Table B–13: Summary of Gouge Density (Toimil, 1978 [124])

Water Depth ft. (m)	Gouge Density gouge/mile				
	Zone	A	B	C	ALL
65.62–82.02 (20–25)	No. mile Intervals	74.56	0	3877.36	3951.92
	Mean	0.86	0	0.21	0.21
	Max	1.18	0	3.59	3.59
	Std	0.46	0	0.59	0.59
82.02–98.43 (25–30)	No. mile Intervals	1528.57	0	3280.84	4809.42
	Mean	0.64	0	0.40	0.48
	Max	3.76	0	6.38	6.38
	Std	1.02	0	0.78	0.86
98.43–114.83 (30–35)	No. mile Intervals	3914.64	0	2982.58	6897.23
	Mean	0.11	0	0.40	0.24
	Max	1.02	0	2.79	2.79
	Std	0.21	0	0.54	0.40
114.83–131.23 (35–40)	No. mile Intervals	3877.36	0	3019.87	6897.23
	Mean	0.13	0	0.56	0.32
	Max	1.90	0	1.90	1.90
	Std	0.24	0	0.54	0.46
131.23–147.64 (40–45)	No. mile Intervals	2274.22	298.26	2013.24	4585.72
	Mean	0.16	0	0.32	0.21
	Max	1.80	0	1.74	1.80
	Std	0.32	0	0.40	0.35

Water Depth ft. (m)	Gouge Density gouge/mile				
	Zone	A	B	C	ALL
147.64–164.04 (45–50)	No. mile Intervals	2087.81	298.26	1342.16	3728.23
	Mean	0.19	0	0.11	0.13
	Max	1.02	0	0.80	1.02
	Std	0.24	0	0.19	0.21
164.04–180.45 (50–55)	No. mile Intervals	0.00	0	1081.19	1081.19
	Mean	0.00	0	0.05	0.05
	Max	0.00	0	0.35	0.35
	Std	0.00	0	0.11	0.11
180.45–196.85 (55–60)	No. mile Intervals	111.85	0	410.11	521.95
	Mean	0.00	0	0.03	0.00
	Max	0.00	0	0.13	0.13
	Std	0.00	0	0.05	0.03
> 196.85 (> 60)	No. mile Intervals	149.13	0	820.21	969.34
	Mean	0	0	0	0
	Max	0	0	0	0
	Std	0	0	0	0
Unknown Depth	No. mile Intervals	223.69	186.41	1118.47	1528.57
	Mean	0.21	0.03	0.05	0.08
	Max	0.48	0.08	0.86	0.86
	Std	0.19	0.03	0.16	0.16

Water Depth ft. (m)	Gouge Density gouge/mile				
	Zone	A	B	C	ALL
Total	No. mile Intervals	14241.84	782.93	19946.03	34970.80
	Mean	0.19	0	0.30	0.24
	Max	3.76	0.08	6.38	6.38
	Std	0.43	0.03	0.54	0.51
Measurements in parentheses are in meters (m)					

Appendix C Reference Figures

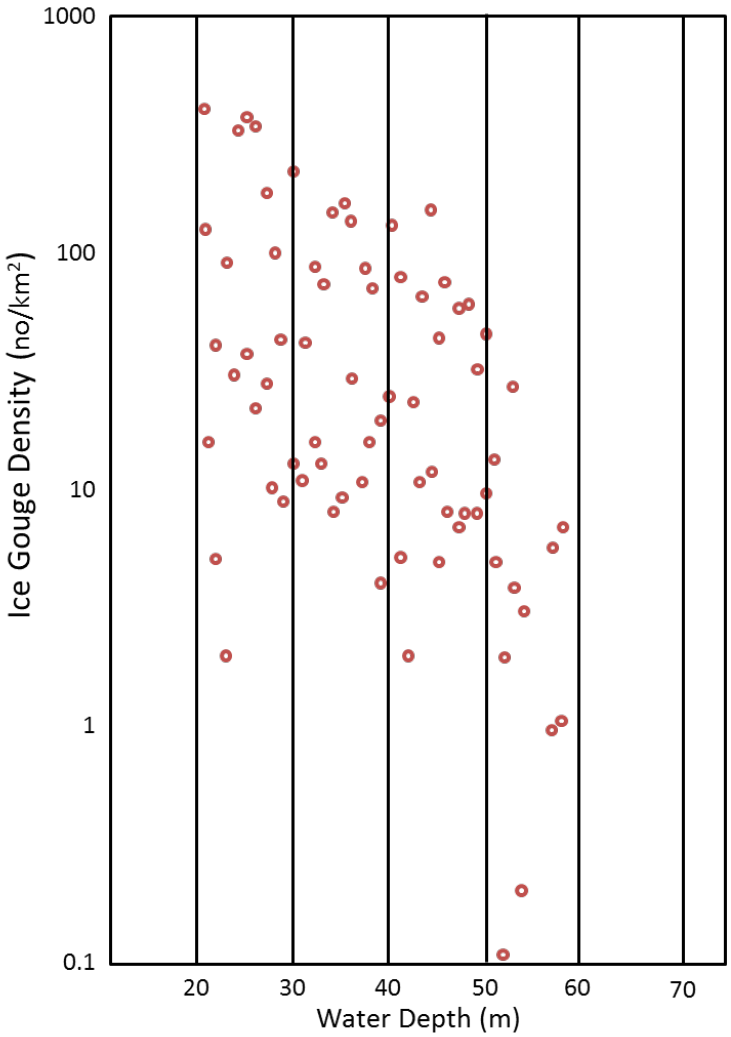

Figure C–1: Normalized Maximum Ice Gouge Mean Ice Gouge Density Values Plotted Over One Meter Water Depth Intervals (Toimil, 1978 [131])